On the Phonon Interactions and Terahertz Excitations among Coulomb-correlated Charge Carriers of Semiconductors

DISSERTATION

zur
Erlangung des Doktorgrades
der Naturwissenschaften
(Dr. rer. nat.)

dem
Fachbereich Physik
der Philipps-Universität Marburg
vorgelegt von

Dipl.-Phys.
Christoph N. Böttge

aus Gelnhausen
geboren in Hanau

Marburg an der Lahn
2013

BÖTTGE, Christoph N.:
On the Phonon Interactions and Terahertz Excitations among Coulomb-correlated Charge Carriers of Semiconductors.
Marburg, Philipps-Universität Marburg,
Fachbereich Physik und wissenschaftliches Zentrum für Materialwissenschaften,
Dissertation, 2013.

Satz: LaTeX unter Verwendung der Makropakete PSfrag und PSTricks
Druck und Bindung: Görich & Weiershäuser, Deutschhausstraße 42, 35037 Marburg

Vom Fachbereich Physik
der Philipps-Universität Marburg
(Hochschulkennziffer: 1180)
als Dissertation angenommen am 23. August 2013.

Erstgutachter: Prof. Dr. tech. Mackillo Kira
Zweitgutachter: Priv.-Doz. Sangam Chatterjee, PhD

Datum und Ort der mündlichen Prüfung: Freitag, 30. August 2013, 10:00 Uhr
Philipps-Universität Marburg
Fachbereich Physik
– Kleiner Hörsaal –
Renthof 5
35032 Marburg an der Lahn

Prüfungskommission: Prof. Reinhard M. Noack, PhD *(Vorsitzender)*
Prof. Dr. tech. Mackillo Kira
Priv.-Doz. Sangam Chatterjee, PhD

On the Phonon Interactions and Terahertz Excitations among Coulomb-correlated Charge Carriers of Semiconductors

DISSERTATION

submitted in partial fulfillment
of the requirements
for the degree of
Doctor of natural sciences
(Dr. rer. nat.)
in the subject of Physics

to the
Department of Physics
at the
Philipps-Universität Marburg, Germany

by

Christoph N. Böttge

from Gelnhausen, Germany
born in Hanau, Germany

Marburg an der Lahn, Germany
2013

Christoph N. Böttge,
On the Phonon Interactions and Terahertz Excitations among Coulomb-correlated Charge Carriers of Semiconductors,
Marburg (Germany),
Philipps-Universität Marburg,
Department of Physics and Material Sciences Center,
PhD thesis (2013).

Typesetting: LaTeX using the PSfrag and PSTricks macropackages
Print and bookbinding: Görich & Weiershäuser, Deutschhausstraße 42, 35037 Marburg, Germany

Accepted as dissertation on August 23, 2013
by the Department of Physics
at the Philipps-Universität Marburg, Germany
(university-code number: 1180).

First reviewer: Prof. Dr. tech. Mackillo Kira
Second reviewer: Priv.-Doz. Sangam Chatterjee, PhD

Date and place of oral examination: Friday, August 30, 2013, 10:00 a.m.

Philipps-Universität Marburg
Department of Physics
– Small lecture hall –
Renthof 5
35032 Marburg an der Lahn
GERMANY

Board of examiners: Prof. Reinhard M. Noack, PhD *(board chairman)*
Prof. Dr. tech. Mackillo Kira
Priv.-Doz. Sangam Chatterjee, PhD

Everything remains (as it never was)

Eluveitie

See page XLIV for reference.

The Inner Horizon I

See page XLIV for reference.

Zusammenfassung

Halbleiter sind ein unverzichtbarer und wesentlicher Bestandteil unserer Welt geworden. Die schnelle Entwicklung der Halbleitertechnologie hat zu einer reichhaltigen und breit gefächerten Fülle an Anwendungsvariationen dieser Materialien geführt. Aufgrund der spezifischen Kristallstruktur sind das höchste besetzte Energieband (Valenzband) und das nächsthöhere Energieband (Leitungsband) durch die sogenannte *Energielücke* oder *Bandlücke* getrennt [1, 2]. Üblicherweise befindet sich diese Energielücke im Bereich von einigen wenigen Elektronenvolt (eV) und somit in einem Bereich der elektromagnetischen Strahlung, die vom menschlichen Auge wahrgenommen werden kann, was Absorption und Emission von Strahlung im sichtbaren Bereich ermöglicht. Die Möglichkeit, Halbleiterstrukturen mit höchster Reinheit und Präzision produzieren zu können, macht diesen Festkörper zu einem äußerst geeigneten Material für die Grundlagenforschung sowie viele Bereiche von anwendungsorientierten und -optimierten Produkten des täglichen Lebens. Beispielsweise decken Halbleiter elementare Bedürfnisse der Menschen ab, wie etwa Raumausleuchtung, Kommunikation, und Mikroelektronik, aber auch Speicherung und Übertragung von Information.

In Hinsicht auf Anwendungen von Halbleitermaterialien im kommerziellen und privaten Bereich des heutigen Lebens lassen sich selbstverständlich Computerchips wie Prozessoren, darunter Hauptprozessoren (CPUs, vom Englischen *central-processing units*), und Speichermodule nennen. Halbleiter bieten die Möglichkeit elektronische Schaltungen und Komponenten, wie beispielsweise Transistoren, zu miniaturisieren, was mit einem geringeren Energie- und Platzverbrauch und dabei schnelleren Schaltzeiten einhergeht. Erst kürzlich wurde über flüssigkeitsbasierte Transistoren berichtet, welche Daten wie das menschliche Gehirn verarbeiten können [3–5]. Eine Besonderheit hierbei ist, dass ein bestimmter Zustand ohne Energieversorgung beibehalten werden kann. Weiterhin können die Schaltungen dynamisch rekonfiguriert, das heißt reprogrammiert werden. Diese Eigenschaften statten diese neue Methode mit vielen variationsreichen Möglichkeiten wie Kontrolle von Schaltkreisen oder Informationsspeicher – in einem Gerät – aus. Darüber hinaus kann nicht bestritten werden, dass moderne Datenspeicherung auf digitalen Speichern basiert und diese die analogen Speichermedien größtenteils verdrängt haben. Eines der prominentesten Beispiele ist sicherlich die *Compact Disc* (CD). Dieses optische Speichermedium [6] lässt sich kontaktlos mit einem auf Aluminiumgalliumarsenid (AlGaAs) basierten Halbleiterlaser, der im nahen Infrarot bei einer Wellenlänge von 780 Nanometern (nm) emittiert, auslesen und beschreiben. Definitionsgemäß ist ein Nanometer gleich dem milliardsten Teil eines Meters, das heißt $1\,\mathrm{nm} \equiv 10^{-9}\,\mathrm{m}$. Unter Verwendung anderer Halbleitermaterialien lässt sich die Wellenlänge des Lichts verringern, was wiederum zu höheren Datendichten auf dem optischen Medium führt. Auf diese Weise werden hohe Datenkapazitäten und hochauflösende Videos auf DVDs (vom Englischen *Digital Versatile Disc*) und *Blu-Ray Discs*[1] gespeichert. Für letztere finden auf Indiumgalliumnitrid (InGaN) basierte Halbleiterlaser mit großer Bandlücke Anwendung, die im blau/ultravioletten Spektralbereich [7] emittieren. Allerdings werden Daten nicht nur auf optischen Medien gespeichert. Schnellere Kerne und die Multikern-Architektur moderner CPUs erschweren eine weitere Leistungssteigerung herkömmlicher Festplatten (HDDs, vom Englischen *hard-disk drives*), da diese unter der Limitierung einer Erhöhung der Rotationsgeschwindigkeit der magnetischen Scheiben leiden. Mit dem Ursprung in den 1950er Jahren ist die Entwicklung von Halbleiterlaufwerken [8, 9]

[1] Handelsmarke der *Blu-ray Disc Association*.

(SSDs, vom Englischen *solid-state drives*) im letzten Jahrzehnt schnell vorangeschritten. SSDs sind auf Halbleitern basierende Permanentspeicher, welche Lese- und Schreibleistungen bieten, die bereits Geschwindigkeiten aktueller Computerschnittstellen entsprechen. Nach anfänglicher Kritik und Startschwierigkeiten [10] stellt dieses unmechanische Datensicherungsgerät heutzutage eine echte Alternative und wettbewerbsfähige Variante zu herkömmlichen Festplatten dar.

Moderne Laserdioden und Leuchtdioden (LEDs, vom Englischen *light-emitting diodes*) bieten eine große Vielfalt an Farben und extrem hohe Helligkeit. Im Vergleich zu weißglühenden Lichtquellen weisen LEDs unter anderem physikalische Robustheit, geringen Energieverbrauch, kleine Baugrößen, lange Lebenszeiten und schnelle Schaltzeiten auf. Im Zuge der Weiterentwicklung ist die Herstellung organischer Leuchtdioden (OLEDs) [11] möglich geworden. Diese dünnschichtigen und flexiblen Halbleitermaterialien wurden erstmals 1987 von Tang und Van Slyke vorgestellt [12] und bieten neben hoher Brillanz und Leuchtkraft auch die Möglichkeit auf drucktechnischem Wege kostengünstig und großflächig hergestellt werden zu können. Vornehmlich finden OLEDs heutzutage Anwendung in Mobiltelefonen, Medienabspielgeräten und Digitalkameras [13]. Der aktuelle Fortschritt und die wachsende Verbreitung von LEDs in der Raumausleuchtung [14] rücken die Ersetzung gewöhnlicher, fluoreszierender Lichtquellen durch höchst effiziente LEDs in greifbare Nähe [15, 16]. Unter Ausnutzung der hohen Schaltraten, die LEDs bieten, sowie der breit gefächerten Anwendungsmöglichkeiten von LED-Lampen können superschnelle Datentransferraten mit bis zu 3 Gigabit pro Sekunde [17, 18] mittels Kommunikation durch sichtbares Licht (VLC, vom Englischen *visible-light communication*) realisiert werden [19, 20]. Zweifelsohne ermöglicht auch eine Blitzlampe die Möglichkeit der Datenübertragung wie beispielsweise Morsesignale, allerdings kann diese sicher nicht als brauchbare Beleuchtungsquelle angesehen werden. Die superschnellen Schaltfähigkeiten, welche LEDs mit sich bringen, bieten jedoch die Möglichkeit sowohl Beleuchtung als auch Kommunikation miteinander zu kombinieren. Dies bringt den großen Vorteil, dass jede LED-basierte Lichtquelle, wie etwa Deckenlampen, Autobahnbeleuchtungen, oder Bildschirme und Fernsehgeräte, dazu verwendet werden können, zum einen Licht zu produzieren, aber auch Netzwerkfähigkeiten, sozusagen als Nebeneffekt, bereitzustellen. Gleichzeitig sind diese Lichtquellen allgegenwärtig und unbedenklich für den menschlichen Körper und elektronische Geräte. Aufgrund der Tatsache, dass diese Lichtquellen bei hohen Frequenzen von einigen hundert Terahertz betrieben werden, ermöglichen sie weiterhin einen Ausweg aus Schwierigkeiten wie etwa durch Radiofrequenzen verursachte Störungen sowie dem Problem, dass nur ein bestimmter Teil des Strahlenspektrums für die Übertragung von Daten nutzbar ist und dieser Teil zunehmend weniger freie Frequenzen bereitstellen kann (Englisch: *spectrum crunch*). Nicht zuletzt ist die lizenzfreie Anwendbarkeit der entsprechenden Frequenzen ein weiterer großer Vorteil.

Die Herstellung und fortlaufende Verbesserung von solchen Geräten ist das Ergebnis langer und ausgiebiger Entwicklungsprozesse sowie der Grundlagenforschung. Die starke Nachfrage nach neuen und immer effizienteren Geräten betont die unverminderte Wichtigkeit von Wissenschaft und fortwährender Forschung. Moderne Kristallzüchtungs- und Dotierungstechniken ermöglichen die Produktion von hochreinen Halbleiterproben, die individuell gefertigt und maßgeschneidert für spezielle Anforderungen produziert werden können [21]. In diesem Zusammenhang lassen sich Heterostrukturen unterschiedlicher Dimensionalität fertigen, die von dreidimensionalen Proben bis hin zu allen Arten von Systemen, in denen die Ladungsträger in ihrer Bewegungsfreiheit eingeschränkt sind, reichen. Hier lassen sich eingeschlossene Systeme in zwei Dimensionen als Quantentöpfe (QWs, vom Englischen *quantum wells*), in einer Dimension als Quantendrähte (QWIs, vom Englischen *quantum wires*) und in null Dimensionen als Quantenpunkte (QD, vom Englischen *quantum dots*), bei denen die Elektronenbewegung in allen drei räumlichen Dimensionen eingeschränkt ist, herstellen. In der Grundlagenforschung benutzen Wissenschaftler solche Strukturen, um mittels optischer Experimente die zugrunde liegenden optischen und elektronischen Eigenschaften von wechselwirkenden Vielteilchensystemen zu untersuchen, zu kontrollieren und zu manipulieren. Die rasche Entwicklung experimenteller Techniken und Laseraufbauten ermöglicht die Durchführung ultraschneller Experimente auf der Zeitskala von Femtosekunden [22]. Die Anregung eines Halbleiters mit einem klassischen Laserpuls, dessen Frequenz energetisch nahe an der fundamentalen Absorptionskante, also an der Energielücke, liegt, befördert ein Elektron aus dem Valenzband ins Leitungsband und induziert somit eine kohärente Polarisation im Halbleitermaterial. Das Fehlen dieses Elektrons im Valenzband führt zum Konzept von Elektronen und Löchern in Halbleitern, wobei ein Loch ein

positiv geladenes Teilchen und somit das konzeptuelle Gegenteil eines Elektrons beschreibt. In einer semiklassischen Behandlung hat sich die Einführung effektiver Massen als vorteilhaft herausgestellt. Diese beschreiben die geladenen Teilchen in einem Kristall, als würden sie sich frei, allerdings mit einer Masse, die von der Masse des freien Elektrons abweicht, bewegen. Diese effektiven Massen bestimmen die Krümmung der Energiebänder am Leitungsbandminimum und Valenzbandmaximum. Die effektive Masse ist im Allgemeinen ein Tensor und kann anisotrope Effekte aufweisen [23]. Die Coulomb-Wechselwirkung zwischen den geladenen Teilchen führt zu einer Vielzahl von Vielteilchenkorrelationen, welche wiederum Energierenormalisierungen verursachen, sodass auch Zustände unter der gewöhnlichen Energielücke erlaubt sind [1,2]. Unter diesen Bedingungen beeinflusst die Phase des anregenden Pulses die Systemeigenschaften und nimmt Einfluss auf alle damit in Verbindung stehenden Prozesse, was eine wohldefinierte Phasenbeziehung untereinander schafft. Dies führt zum Konzept des *kohärenten Exzitons*, welches im Wesentlichen einen einzelnen Ladungsträger in einem Superpositionszustand zwischen Valenz- und Leitungsband beschreibt [24]. Allerdings zerstören Unordnung [25–28] sowie unvermeidbare Streuprozesse unter den Ladungsträgern [29] und Gitterschwingungen [30,31] diese Phasenbeziehungen (Dephasierung), was zum schnellen Zerfall der kohärenten Polarisation auf der Zeitskala von Pikosekunden ($1\,\mathrm{ps} = 10^{-12}\,\mathrm{s}$) führt [24]. Das System geht dann in das sogenannte *inkohärente Regime* über, in welchem alle Interbandkohärenzen verschwinden und lediglich inkohärente Größen bestehen bleiben. Die einfachste Form solcher inkohärenter Größen sind die Ladungsträgerdichten von Elektronen und Löchern, welche gewöhnlicherweise im System für sehr lange Zeiten im Bereich von Nanosekunden vorherrschen [24]. Somit ist ein Halbleiter zu spontaner Emission in der Lage, selbst wenn der anregende Puls bereits lange vorüber ist [2]. Aufgrund der Licht–Materie-Wechselwirkung und Streumechanismen zerfällt die kohärente Polarisation entweder radiativ oder wird in inkohärente Quasiteilchenanregungen umgewandelt. Abhängig von den Anregebedingungen können Elektronen und Löcher entweder als ungebundene Paare (Plasma) vorliegen oder, aufgrund komplizierter Streuprozesse von Ladungsträgern mit Ladungsträgern sowie Gitterschwingungen, ein neues Quasiteilchen bilden, das als *inkohärentes Exziton* [29] bezeichnet wird. Dieses Gebilde stellt ein korreliertes Elektron–Loch-Paar dar, welches echt durch Coulomb-Anziehung gebunden ist. Es lässt sich in Analogie zum Wasserstoffproblem beschreiben. Allerdings können Exzitonpopulationen auch gleichzeitig neben Plasma vorhanden sein, sodass eine Mischung aus beiden Konfigurationen im System vorherrscht. Da alle Untersuchungen in dieser Dissertation im inkohärenten Regime stattfinden, verweist der Ausdruck *Exziton* ausschließlich auf das Konstrukt des echt gebundenen Elektron–Loch-Paares.

Unter Berücksichtigung der Tatsache, dass ein klassisches Lichtfeld im inkohärenten Regime verschwindet, erscheint die Quantennatur des Lichts eine wichtige Rolle zu spielen. Um die komplizierten Streumechanismen und das Zusammenspiel mit elektromagnetischen Feldern zu modellieren, wird eine vollkommen mikroskopische Quantentheorie benötigt, welche die verschiedenen Beiträge des quantisierten Lichtfeldes, der Streuung zwischen Ladungsträgern durch Coulomb-Wechselwirkung sowie der Streuung von Ladungsträgern mit Gitterschwingungen konsistent beinhaltet und vereint. Abhängig von den experimentellen Bedingungen und dem untersuchten Problem können entweder verschiedene Annahmen eingeführt oder auch die Theorie erweitert werden, um zusätzliche Beiträge, wie beispielsweise die Einwirkung eines Terahertz (THz)-Pulses oder magnetischen Feldern, zu beschreiben. Zur Konstruktion des theoretischen Rahmens stellt die Methode der Heisenberg-Bewegungsgleichungen [1] eine geeignete Grundlage dar, um alle wichtigen Prozesse auf der gleichen Stufe zu beschreiben. Die Methode der Cluster-Entwicklung [2, 32–38] ermöglicht den konsistenten Abbruch des bekannten Hierarchieproblems, was in einem geschlossenen Satz von Gleichungen resultiert, welche das System und seine spezifischen Vielteilchenkonfigurationen beschreiben. Auf diese Weise ist die Theorie in der Lage, die experimentellen Ergebnisse zu erklären oder neue physikalische Effekte zu prognostizieren.

Der erste Teil dieser Dissertation behandelt die elementaren Wechselwirkungen zwischen Ladungsträgern und Gitterschwingungen in Halbleitern. Die Untersuchungen sind unterteilt in zwei Projekte, welche in den Kapiteln 3 und 4 zusammengefasst sind und die Effekte von Gitterschwingungen auf die Lumineszenz von Halbleitern beschreiben. Im quantenmechanischen Sinn können diese delokalisierten, angeregten Zustände der Schwingungsmoden innerhalb der Kristallstruktur durch ein Quasiteilchen beschrieben werden, das *Phonon* genannt wird. Neben der bereits erwähnten Dephasierung der kohärenten Anregungen [39–41] spielen Phononen eine zentrale Rolle im Zusammenhang mit der Kühlung eines heißen Ladungsträgersystems [42–44], der

Licht–Materie-Wechselwirkung [45,46] und der Bildung von Exzitonen [29]. Allerdings können longitudinal-optische (LO) Phononen auch zur Elektron–Loch-Rekombination beitragen, was zur Entstehung ausgeprägter Repliken, den sogenannten Phononseitenbändern (PSBs, vom Englischen *phonon sidebands*), im Photolumineszenzspektrum (PL-Spektrum) eines Halbleiters führt. Frühere Arbeiten haben bereits die Berechnung von phonon-assistierten Lumineszenzgleichungen ausführlich sowohl mit störungstheoretischen [47] als auch nicht-störungstheoretischen [48, 49] Ansätzen behandelt. Hierbei ist vor allem die Frage untersucht worden, ob und zu welchem Grad unkorreliertes Elektron–Loch-Plasma und echt gebundene Exzitonpopulationen zur phonon-assistierten PL beitragen [47,50] – eine wichtige Erweiterung zu früheren Studien [51], welche sich auf die $1s$-Exzitonresonanz konzentriert haben. Im Rahmen dieser Arbeiten über Phononen sind stationäre Lösungen der Halbleiter-Lumineszenzgleichungen unter Einbeziehung von Phononseitenbändern beliebiger Ordnung präsentiert worden; allerdings beinhalteten diese Lösungen keine stimulierten Emissionseffekte. Es ist wohlbekannt, dass eine dielektrisch strukturierte Umgebung (dielektrische Spiegel) wesentlich zur Veränderung von Lumineszenzspektren und den auftretenden Resonanzen beiträgt, sobald eine Halbleiter-Nanostruktur, wie beispielsweise ein Quantenfilm, in den Schwingungsbauch des intrakavitären Feldes positioniert wird. Wird die Resonanz der Mikrokavität so eingestellt, dass sie mit der $1s$-Exzitonresonanz übereinstimmt, sodass die Resonanz des Resonators und des aktiven Materials entartet sind, führt dies zu dem berühmten Szenario der Normalmodenkopplung (NMC, vom Englischen *normal-mode coupling*), bei welcher die Resonanz in zwei Resonanzen aufspaltet [52–58]. Auf Grundlage dieses ausgiebig untersuchten Systems werden die oben erwähnten Untersuchungen an Phononen in Kapitel 3 dieser Dissertation erweitert und sich eingehend mit der Frage befasst, wie eine dielektrische Umgebung die phonon-assistierte Photolumineszenz modifiziert und beeinflusst. Hierbei wird nicht nur eine Kavität untersucht, deren Resonanzfrequenz mit der $1s$-Exzitonenergie übereinstimmt, sondern vor allem auch eine Kavität, die so verstimmt ist, dass sie mit dem ersten Phononseitenband des Halbleiter-Emissionsspektrums resonant ist. Nach einer detaillierten numerischen Studie der verschiedenen Kavitätskonfigurationen wird die Analyse durch ein streng analytisches Modell abgerundet.

Das zweite Projekt, welches sich mit Phononen befasst, ist in Kapitel 4 beschrieben. Hier wird der Ursprung der Streumechanismen zwischen Ladungsträgern und Phononen detailliert untersucht. Aufgrund ihrer Kristallstruktur können Halbleitermaterialien stark polares Verhalten aufweisen. Hierdurch bedingt können, abhängig von der Struktur und der Systemkonfiguration, entweder die polare Wechselwirkung oder die nicht-polare Streuung zwischen Ladungsträgern und Phononen im Halbleitermaterial vorherrschend sein. Darüber hinaus verändert die Coulomb-Anziehung das Wechselwirkungsverhalten zwischen Ladungsträgern und Gitterschwingungen, sodass sich einzelne Ladungsträger anders verhalten als ein wechselwirkendes Vielteilchensystem. Dies wirft die Frage auf, unter welchen Umständen und aufgrund welcher Basis ein immanent polares Material von nicht-polarer Streuung zwischen Ladungsträgern und Phononen dominiert werden kann. Unterstützt von experimentell gemessenen phonon-assistierten Photolumineszenzspektren wird eine systematische Vielteilchentheorie vorgestellt, um den Ursprung der Exziton–Phonon-Wechselwirkung in polaren Halbleitern zu erklären und die Rolle eines wechselwirkenden Vielteilchensystems zu identifizieren.

Die Coulomb-Wechselwirkung in Vielteilchensystemen ist nicht nur zur Vermittlung der Kopplung zwischen Exzitonen und LO-Phononen von essentieller Bedeutung, sondern spielt auch für intra-exzitonische Übergänge eine wesentliche Rolle, bei welchen diffusive Coulomb-Streuung zur Erweiterung der gewöhnlichen Dipolauswahlregeln führt. Als direkte Weiterführung kürzlich veröffentlichter Arbeiten [59] behandelt der zweite Teil dieser Dissertation ein sehr zentrales Feld aktueller Forschung. Im Gegensatz zu Interbandübergängen, bei welchen ein Absorptions- oder Emissionsprozess ein Elektron–Loch-Paar erzeugt bzw. vernichtet, verändern Intrabandübergänge die Anzahl der Elektron–Loch-Paare nicht. Erst kürzlich sind die herkömmlichen Interbandstudien durch die Entwicklung kohärenter Terahertzquellen, wie beispielsweise dem Freie-Elektronen-Laser [60–63], dem Quantenkaskadenlaser [64, 65] oder Quellen zur Differenzfrequenzerzeugung, ergänzt und erweitert worden. Die Energien des ferninfraroten (FIR) Feldes bei Terahertzfrequenzen liegen im Bereich von Millielektronenvolt (meV), das heißt $1\,\mathrm{THz} = 10^{-12}\,\mathrm{Hz}$ entspricht ungefähr $4\,\mathrm{meV}$, und sind damit drei Größenordnungen kleiner als typische Bandlückenenergien. Da die interne Energiestruktur von korrelierten Halbleiter-Vielteilchenzuständen in den meV-Bereich fällt, ist THz-Spektroskopie eine eindeutige und geeignete Methode, um diese Systeme zu untersuchen, also Exzitonpopulationen zu identifizieren [66, 67] und kon-

trollierte Übergänge zwischen den angeregten Quasiteilchenzuständen zu induzieren [66, 68–71]. Terahertzstrahlung findet jedoch nicht nur in der Physik Anwendung, sondern bietet auch sehr gute Abtast- und Erfassungsfähigkeiten in einem breiten Bereich von Forschungsfeldern und Wissenschaften wie etwa Pharmazie, Biologie und Medizin [72]. Darüber hinaus wird Terahertzstrahlung zur zerstörungsfreien Untersuchungen und Materialcharakterisierung verwendet [73]. In Hinblick auf Halbleiter ist die Energie von Terahertzstrahlung deutlich nicht-resonant in Bezug auf Interbandübergänge in typischen GaAs-ähnlichen Halbleitern [74, 75], sodass die Wechselwirkung von Licht und Materie in diesem spektralen Bereich durch Zwei- und Mehrteilchenkorrelationen beherrscht ist. Folglich ermöglicht die Kombination von gepulsten, optischen Feldern und Terahertzfeldern nicht nur die Erzeugung von Vielteilchenanregungen, sondern auch die Charakterisierung ihrer dynamischen Entwicklung sowie die kontrollierte Manipulation der beteiligten Quantenzustände. Unter Anwendung eines magnetischen Feldes können sowohl die Exzitoneigenschaften als auch die terahertz-induzierten intra-exzitonischen Übergänge modifiziert werden. In Kapitel 5 wird das Augenmerk auf die Effekte gerichtet, die ein Magnetfeld auf die Kontrolle und die Manipulation des intra-exzitonischen Ladungsträgertransfers hat. Die experimentellen Ergebnisse werden durch eine theoretische Beschreibung untermauert, in welcher der Hamilton-Operator des Gesamtsystems durch die Berücksichtigung linearer und nichtlinearer Beiträge des Magnetfeldes wesentlich erweitert wird.

Diese Arbeit ist wie folgt aufgebaut. In Kapitel 2 wird der allgemeine Rahmen gesetzt, indem der theoretische Hintergrund erläutert und die damit verbundenen Hamilton-Operatoren und theoretischen Konzepte kurz eingeführt werden. In Kapitel 3 werden die Effekte, die eine Mikrokavität auf die phonon-assistierte Lumineszenz eines Halbleiters hat, präsentiert, gefolgt von den Studien zum Ursprung der Exziton–Phonon-Wechselwirkung in polaren Halbleitern in Kapitel 4. Der Einfluss eines magnetischen Feldes in Verbindung mit Terahertzfeldern wird in Kapitel 5 diskutiert. In Kapitel 6 werden die Resultate dieser Arbeit zusammengefasst und ein Ausblick gegeben. Die Anhänge beinhalten einige zusätzliche, jedoch erwähnenswerte Herleitungen, welche allerdings für ein umfassendes Verständnis der vorangegangen physikalischen Resultate nicht unbedingt vonnöten sind. Die bisher veröffentlichten Publikationen, die mit den Ergebnissen aus den Kapiteln 3–5 in Verbindung stehen, sind auf Seite XLV f. zusammengefasst, gefolgt von den entsprechenden Veröffentlichungen. Eine Liste aller Publikationen mit meiner Beteiligung als Erst- oder Koautor sowie Manuskripte in Vorbereitung ist auf Seite IX zu finden.

The Inner Horizon II

See page XLIV for reference.

Acknowledgments

This thesis and my entire research would not have been possible without the support of several persons who contributed with ideas, conversations, guidance, and care. In the end, I gratefully look back to a great time full of memorable moments which I shared with many friendly people. In particular, my sincere thanks is owed to...

... my parents Gabriele Böttge and Lothar Böttge for their encouragement for my plan and wish to do my doctorate, and for permanent support during my studies in Marburg.

... Prof. Dr. Mackillo Kira for valuable input, constructive criticism, and extensive support concerning our projects. Additionally, for the CCC (Cluster Crunching Club) meetings as well as helpful typographical hints and *The Beauty Rules*;
and Prof. Dr. Stephan W. Koch for kind and obliging advisory support in all project-related and personal matters as well as for always offering a sympathetic ear.

I thank both for accepting me as a doctoral candidate and for perfectly organized supervision. Additionally, I want to thank for the opportunity to participate in several conferences (NOEKS 2010 in Paderborn, DPG 2011 in Dresden, and NOEKS 2012 in Stuttgart), workshops (GPU programming in CUDA at the HLRS Stuttgart), and the CORK SCHOOL 2013 at the University College Cork, Ireland.

... Priv.-Doz. Sangam Chatterjee, PhD for providing the second opinion on this thesis, for excellent cooperation and support in the second project of my PhD-student time, and for a pleasant atmosphere in our session at the DPG spring conference in Dresden, Germany (March 2011).

... Prof. Reinhard M. Noack, PhD for his interest in my thesis and for chairing the thesis defense.

... the *DFG–OTKA International Research Training Group "Electron–Electron Interactions in Solids" (Marburg–Budapest) (RTG 790)*, in particular the speaker Prof. Dr. Florian Gebhard and deputy speaker Prof. Dr. Dr. h. c. Peter Thomas, for financial support during the period from 02/2010 to 03/2012.

... the *DFG Research Training Group "Functionalization of Semiconductors" (RTG 1782)*, in particular the speaker Prof. Dr. Kerstin Volz and deputy speaker Prof. Dr. Stefanie Dehnen, to admit me to the Research Training Group to join as an associate during the period from 10/2012 to the end of my PhD-student time.

... all my colleagues of the *Semiconductor Theory Group*, especially Benjamin Breddermann and Dr. Lukas Schneebeli for the excellent collaboration in the second part of my work (and Lukas, in particular, for his clairvoyant skills), Dr. Tineke Warncke and Martin Mootz for many extremely helpful hints, Phillip Springer for explaining (parts of) the world through the eyes of an experimentalist, and Christian Berger for many funny and (to some extent) disillusioning attempts of installing Linux properly, vivid exchange of information about computer systems and programming, as well as Hessian pleasure, food, and lifestyle.

... Dr. Martin Schäfer for providing me with the `FORTRAN` code of his computer program which is the basement of parts of my work.

... Steven Youngkin, Dr. Tineke Warncke, Dr. Lukas Schneebeli, and Dr. Thomas Feldtmann for proofreading and looking closely at the final version of this thesis for English style and grammar.

... my love Melody ♫ for wonderful moments at all times as well as unlimited support and unreserved backing especially in the final stage of writing this thesis. *Gina higugma ko ikaw!*

... Prof. John E. Sipe, PhD for fruitful and stimulating discussions on new interesting fields of theoretical physics, but also pudding and German language, during his stays in Marburg as well as the NOEKS 11 conference.

... Renate Schmid for guiding into the right way through the maze of bureaucracy, and for sympathetic and caring conversations.

... Annegret Webel, Ute Schilhabl, Gudrun Schäfer-Lehnhoff, and Marina Koch for helpful support concerning contracts of employment as well as the Research Training Groups.

... Denise Berger (sis), Ilja Stettler, Rabea Reußwig, Isabell Heise, Michaela Will, David Löffler, Christoph Klotz, Alissa Zouari, Albrecht Wienß, Tabea Holmer, Myriam Goldtstedt, John Wais Khairi-Taraki, Bertil-Austen Abel, Melissa Engel, Sebastian Peil, Dr. Manuel Marks, Jan Ulrich Heinemann, Sina Wüthrich, Tina Dallmeier, Janne van Aswegen, and many more for unforgettable experiences and great memories of Marburg.

... Prof. Dr. Dr. h. c. Peter Thomas for organizing the marvelous hiking holidays every fall.

... Jens Lausen for allowing me to print his artwork on the blank pages of this thesis.

... 张杨、彭兰、高雁、王蕾、梁世军，谢谢你们帮助我学习中文！你们非常有耐心。我真的很感谢你们的帮助。在你们的帮助下，我的中文已经改善了很多。

I thank all of you very much!

Christoph

Marburg an der Lahn
August 2013

Author's contributions

This dissertation consists of a review part introducing the main ideas, and also the project results in which I was involved in during my doctoral studies, followed by the related research publications that have been published up until the submission of this thesis. The abstracts are presented in the preface to the appended papers on page XLV.

Publications in peer-reviewed journals

[I] A. Chernikov, **C. N. Böttge**, T. Feldtmann, S. Chatterjee, M. Koch, M. Kira, and S. W. Koch, "Plasma-related phonon-sideband emission in semiconductors", Phys. Status Solidi C **8**, 1129 (2011).

[II] **C. N. Böttge**, T. Feldtmann, M. Kira, and S. W. Koch, "Phonon sidebands in the semiconductor microcavity luminescence", Phys. Status Solidi C **8**, 1220 (2011).

[III] A. Chernikov, V. Bornwasser, M. Koch, S. Chatterjee, **C. N. Böttge**, T. Feldtmann, M. Kira, S. W. Koch, T. Wassner, S. Lautenschläger, B. K. Meyer, and M. Eickhoff, "Phonon-assisted luminescence of polar semiconductors: Fröhlich coupling versus deformation-potential scattering", Phys. Rev. B **85**, 035201 (2012).

[IV] **C. N. Böttge**, M. Kira, and S. W. Koch, "Enhancement of the phonon-sideband luminescence in semiconductor microcavities", Phys. Rev. B **85**, 094301 (2012).

[V] **C. N. Böttge**, B. Breddermann, L. Schneebeli, M. Kira, S. W. Koch, J. Bhattacharyya, H. Schneider, and M. Helm, "Terahertz-induced effects on excitons in magnetic field", Phys. Status Solidi C **10**, 1218 (2013).

[VI] **C. N. Böttge**, S. W. Koch, L. Schneebeli, B. Breddermann, A. C. Klettke, M. Kira, B. Ewers, N. S. Köster, and S. Chatterjee, "Terahertz-induced exciton signatures in semiconductors", Phys. Status Solidi B **250**, 1768 (2013).

Publications submitted to peer-reviewed journals

[VII] J. Bhattacharyya, S. Zybell, F. Eßer, M. Helm, H. Schneider, L. Schneebeli, **C. N. Böttge**, B. Breddermann, M. Kira, S. W. Koch, A. M. Andrews, and G. Strasser, "Magnetic control of Coulomb scattering and terahertz transitions among excitons", submitted (2013).

Poster contributions

- **C. N. Böttge**, T. Feldtmann, M. Kira, and S. W. Koch, "Phonon sidebands in the semiconductor microcavity luminescence", Poster presented at the 10^{th} international workshop on Nonlinear Optics and Excitation Kinetics in Semiconductors (NOEKS 10) in Paderborn (Germany) (2010).
- A. Chernikov, **C. N. Böttge**, T. Feldtmann, S. Chatterjee, M. Koch, M. Kira, and S. W. Koch, "Plasma-related phonon-sideband emission in semiconductors", Poster presented at the 10^{th} international workshop on Nonlinear Optics and Excitation Kinetics in Semiconductors (NOEKS 10) in Paderborn (Germany) (2010).
- **C. N. Böttge**, T. Feldtmann, M. Kira, and S. W. Koch, "Numerical and analytical studies on phonon-assisted luminescence in the semiconductor microcavity", Poster presented at the "Materialforschungstag Mittelhessen 2011" (Material Sciences Conference) in Gießen (Germany) (2011).
- **C. N. Böttge**, B. Breddermann, L. Schneebeli, M. Kira, S. W. Koch, J. Bhattacharyya, H. Schneider, and M. Helm, "Terahertz-induced exciton scattering and influence of magnetic fields", Poster presented at the "Materialforschungstag Mittelhessen 2012" (Material Sciences Conference) in Marburg (Germany) (2012).
- **C. N. Böttge**, B. Breddermann, L. Schneebeli, M. Kira, S. W. Koch, J. Bhattacharyya, H. Schneider, and M. Helm, "Terahertz-induced exciton scattering and influence of magnetic fields", Poster presented at the 11^{th} international workshop on Nonlinear Optics and Excitation Kinetics in Semiconductors (NOEKS 11) in Stuttgart (Germany) (2012).
- B. Breddermann, L. Schneebeli, **C. N. Böttge**, M. Kira, S. W. Koch, B. Ewers, N. S. Köster, S. Chatterjee, W. D. Rice, S. Zybell, S. Winnerl, H. Schneider, M. Helm, and J. Kono, "Exciton shelving and intra-excitonic scattering via terahertz fields", Poster presented at the 11^{th} international workshop on Nonlinear Optics and Excitation Kinetics in Semiconductors (NOEKS 11) in Stuttgart (Germany) (2012).
- J. Bhattacharyya, S. Zybell, S. Winnerl, L. Schneebeli, **C. N. Böttge**, B. Breddermann, M. Kira, S. W. Koch, M. Helm, and H. Schneider, "Control of Coulomb-mediated excitonic $2s$ emission by an external magnetic field", Poster presented at the International Workshop on Optical Terahertz Science and Technology (OTST) 2013 in Kyoto (Japan) (2013).
- **C. N. Böttge**, M. Kira, and S. W. Koch, "On the Phonon Interactions and Terahertz Excitations among Coulomb-correlated Charge Carriers of Semiconductors", Poster presented at the CORK SCHOOL 2013 (School on Theory and Mathematics Modeling of Ultrashort Pulse Propagation) at the University College Cork (Ireland) (2013).

Talks

- **C. N. Böttge**, T. Feldtmann, M. Kira, and S. W. Koch, "Microscopic theory of phonons in the semiconductor microcavity luminescence", Contributed talk, DPG (German Physical Society) spring conference in Dresden (Germany) (March 2011).
- A. Chernikov, V. Bornwasser, M. Koch, W. W. Rühle, S. Chatterjee, T. Wassner, B. Laumer, S. Lautenschläger, B. K. Meyer, M. Eickhoff, **C. N. Böttge**, T. Feldtmann, M. Kira, and S. W. Koch, "Many-body effects in phonon-sideband luminescence", Contributed talk, DPG (German Physical Society) spring conference in Dresden (Germany) (March 2011).
- **C. N. Böttge**, L. Schneebeli, B. Breddermann, M. Kira, and S. W. Koch, "Magnetic-field control of terahertz excitations and Coulomb interactions among excitons", Contributed talk, kick-off event of the Research Training Group RTG 1782 "Functionalization of Semiconductors", Rauischholzhausen Castle (Germany) (October 2012).

- J. Bhattacharyya, S. Zybell, S. Winnerl, L. Schneebeli, **C. N. Böttge**, B. Breddermann, M. Kira, S. W. Koch, M. Helm, and H. Schneider, "THz free-electron laser spectroscopy of magnetoexcitons in semiconductor quantum wells", Contributed talk, 38$^{\text{th}}$ International Conference on Infrared, Millimeter and Terahertz Waves (IRMMW-THz) 2013, Mainz (Germany) (September 2013).

Original contributions

When I started my doctoral studies in February 2010, an extension to the semiconductor luminescence equations (SLEs) involving phonon sidebands (PSBs) of arbitrary order had already been established in our workgroup by Dr. Thomas Feldtmann[1] *et al.* Since these previous studies concentrated on a free-space configuration, it was interesting to study phonon-assisted photoluminescence (PL) in a microcavity where coupling to a dielectric environment must be considered. Therefore, I derived the phonon-assisted SLEs, including stimulated-emission effects, and rigorously extended an existing computer program which was capable to compute semiconductor PL of quantum-well systems including dielectric environments. The original version of this program was written by Dr. Martin Schäfer within the scope of his doctoral studies. However, the program did not include any phonon-related contributions. In the framework of this first project, I combined existing knowledge of semiconductor microcavities with substantial extensions involving phonon-assisted processes. The possibility to design all different kinds of refractive-index profiles was already implemented in the program. However, the cavity resonance was fixed to the $1s$ resonance of the respective quantum-well material. Therefore, I systematically expanded the computer program to offer the option of detuning the cavity away from the $1s$ resonance to any arbitrary frequency. This extension not only allowed me to investigate phonon-assisted PL of a quantum well in free space, i.e., without a dielectric environment, but also with microcavities arbitrarily tailored with respect to their resonance frequency. All investigations were performed in the low-density regime where excitons prevail. Even though the scenario where the cavity is resonant with the $1s$-exciton peak has been thoroughly studied in the past and published in many pioneering articles, it was nonetheless interesting to investigate the impact of a microcavity whose resonance energy is detuned to coincide with the first phonon sideband of the semiconductor emission. Known from previous studies, the $1s$-exciton peak splits into two peaks leading to the scenario of normal-mode coupling (NMC) when the cavity resonance coincides with the $1s$-exciton resonance. In this configuration, the $1s$-peak intensity first increases due to the Purcell effect but starts to decrease once the system enters the nonperturbative regime, i.e., when the peak starts to split. A very interesting result arose when I used the new cavity configuration by tuning the cavity resonance to coincide with the first phonon sideband. No splitting occurred here no matter how large the cavity quality was but, interestingly, the phonon sideband was highly enhanced. Simultaneously, the intensity of the first phonon sideband first increased but stayed constant instead of decreasing like the $1s$-peak configuration had done. Additionally, I found that the phonon-sideband emission is clearly favored over the $1s$-exciton emission in the strong-cavity limit.

To gain more insight into these findings, I developed an *analytic model* to describe phonon-assisted semiconductor luminescence including cavity effects. Without the stimulated part, an analytic expression results from a straightforward derivation, especially for the phonon-free SLEs, leading to an extended Elliott formula that describes semiconductor luminescence with plasma and exciton contributions. Including these cavity effects, however, leads to serious complications regarding the stimulated parts which eventually may be solved analytically in the so-called *strong-cavity approximation*. After these preliminary steps, I also included effects of the first phonon sideband, which resulted in a complicated interplay of many different, coupled equations that had to be solved simultaneously. If only the correlated-emission source contributes, the analysis may be simplified by transforming into the exciton picture. Having derived all involved equations of motion and transforming these into the exciton picture, I was able to find a closed, analytic expression for the description of the $1s$-exciton resonance and the first phonon sideband. This expression also offered the possibility to investigate a system in free space but also inside a cavity whose resonance frequency can be set and tuned freely. Both analytic and numerical derivations have been published in Papers [II] and [IV]. In both of them, I contributed significantly

[1] If no university or workgroup is stated explicitly, all people mentioned here were members of the *Semiconductor Theory Group* at the Philipps-Universität Marburg (Germany) during the time of our collaboration.

to the research and the paper writing. I presented the results as posters at the NOEKS 10 conference in 2010 in Paderborn (Germany) and at the "Materialforschungstag Mittelhessen 2011" (Material Sciences Conference) in Gießen (Germany). Furthermore, I gave a contributed talk on this topic at the DPG (German Physical Society) spring conference in 2011 in Dresden (Germany). In this thesis, this project is discussed in Chap. 3.

Almost simultaneously to the first project, I had started a collaboration with the groups of Professor Martin Koch[2] and Priv.-Doz. Sangam Chatterjee, PhD.[2] Lattice-temperature-dependent first and second PSB-emission spectra of three different polar materials were measured, namely zinc oxide (ZnO), zinc sulfide (ZnS), and cadmium sulfide (CdS). The groups of Professors Martin Eickhoff[3] and Bruno K. Meyer[3] provided the samples. Previous literature studies of confined quantum-dot systems indicated that polar interaction between phonons and excitons may partially be canceled. In our studies, we explored the origin of exciton–phonon interaction in polar semiconductors and the role of a many-body system configuration in this context. To microscopically compute PL spectra in the stationary limit, I utilized the exciton-picture representation of the phonon-sideband emission, established by Dr. Thomas Feldtmann, and explicitly derived the contributions of the $1s$-exciton resonance as well as the first and second phonon sideband. For a consistent description, I additionally derived the corrections arising from these sidebands to lower-order sidebands (including the $1s$-exciton resonance). Having worked out all equations, I wrote a completely new computer program in FORTRAN where I implemented all relevant contributions for the derivation of steady-state PL spectra including sidebands up to the second order. I used the material parameters from the literature but also had to convert some of them since we investigated wurtzite-structure materials while the literature mostly provided zincblende-type parameters. Then, I analyzed the respective contributions of the first and second phonon sideband, where especially the temperature-dependent second-to-first phonon-sideband ratio has been scrutinized. Experiments and theory independently reveal that the polar Fröhlich interaction may become ineffective in case of excitons, and deformation-potential scattering may even prevail in polar semiconductors like ZnO. This is a very interesting result since in all investigated materials the interaction of phonons with *single* charge carriers is clearly dominated by Fröhlich interaction. Using the microscopic theory in the exciton picture, I could descriptively show that in an interacting many-body system, the exciton–phonon coupling may be dominated by deformation-potential scattering, even though polar carrier–phonon interaction dominates in uncorrelated systems. Even without any concrete computation, the representation of the derived matrix elements directly allows this conclusion and interpretation of the origin of exciton–phonon coupling. By this means, Fröhlich interaction may be strongly suppressed for small phonon momenta whereas deformation-potential scattering does not show this selectivity. The results of this project are published in Paper [III] and presented in Chap. 4 of this thesis. In this paper, I was responsible for the theory, computations, and writing the theory part.

In the second part of my doctoral studies, I was involved in an experiment–theory collaboration between the groups of Priv.-Doz. Dr. Harald Schneider[4] and Professor Manfred Helm,[4,5] Professor Gottfried Strasser,[6] and the *Semiconductor Theory Group* in Marburg (Germany). The theory part has been a collaboration with Dr. Lukas Schneebeli and Benjamin Breddermann. Recent investigations have provided abundant evidence that THz radiation can efficiently induce transitions between exciton states. As a result of Coulomb interaction among excitons, a THz pulse resonant with the $1s$–$2p$-energy separation may lead to pronounced population transfer to the $2s$ state [59]. Based on these studies that have also been a collaboration between Marburg and Dresden, we were encouraged to investigate how this Coulomb-induced symmetry breaking and population transfer may be modified and controlled by an external magnetic field. For this investigation, I rigorously expanded the existing theory by linear and nonlinear contributions to the total-system Hamiltonian to consistently include effects induced by an external magnetic field. As it turned out, a separation of relative- and center-of-mass coordinates was not easily feasible which is why an additional transformation had to be performed. Afterwards, I transformed the resulting equations from the real-space representation into the momentum-space representation and implemented the additional terms into the excitonic eigenvalue solver provided by Dr. Martin

[2]Philipps-Universität Marburg (Germany).
[3]Justus-Liebig-Universität Gießen (Germany).
[4]Institute of Ion Beam Physics and Materials Research, Helmholtz-Zentrum Dresden–Rossendorf (HZDR), Dresden (Germany).
[5]Technische Universität Dresden (Germany).
[6]Institute of Solid State Electronics, Technische Universität Wien (Austria).

Schäfer's computer program. I computed excitonic wavefunctions and eigenvalues including center-of-mass movement of the excitons. Together with Benjamin Breddermann, I worked out the correct normalization of the eigenfunctions and implemented the option for excitation-induced dephasing effects via a diffusive scattering model to the computer program; an extension to the already implemented second-Born scattering. The dynamical computation of exciton populations was mainly performed by Dr. Lukas Schneebeli. For this, I provided him with scattering-matrix elements and THz-transition elements computed from the eigenfunctions. As the exciton scattering was only formulated in Cartesian coordinates to this point, Benjamin Breddermann and I derived this mechanism in polar coordinates as well and found interesting and helpful analytic relations concerning the different symmetries of the eigenfunctions. The results of this project are presented in Chap. 5 and Apps. A and B, even though it is intended to mention that the project has not been completely finished when printing this thesis. The results of the exciton wavefunction and eigenvalue computations including magnetic-field effects are presented in Paper [V] as the main author. This contribution is a conference proceeding of the NOEKS 11 conference in 2012 in Stuttgart (Germany) where I also presented the results as a poster. Additionally, I presented a poster about this project at the "Materialforschungstag Mittelhessen 2012" in Marburg (Germany).

Besides these topics, I contributed to a study by Dr. Alexey A. Chernikov *et al.* on the "Intra-excitonic relaxation dynamics in ZnO" (published in Appl. Phys. Lett. **99**, 231910 (2011)) by evaluating the radiative recombination times for several exciton states. In Ref. [59] (published in Phys. Rev. Lett. **110**, 137404 (2013)), I contributed by computing exciton eigenfunctions and eigenvalues needed for the exciton-scattering elements and the terahertz-transition elements.

I have presented a poster with an overview of my research topics at the CORK SCHOOL 2013 (School on Theory and Mathematics Modeling of Ultrashort Pulse Propagation) at the University College Cork (Ireland).

All projects and investigations were associated with frequent and intensive group meetings where results have been discussed and further action was coordinated. The actual programming, implementation of new code (as stated above), and evaluation of the results was performed by me.

In Paper [I], I contributed parts of the theoretical description. I wrote Paper [II] and substantially contributed to the theory part and theoretical description of Paper [III]. I wrote most parts of Paper [IV], with assistance and supervision of Prof. Dr. Mackillo Kira and Prof. Dr. Stephan W. Koch. Paper [V] was written by Dr. Lukas Schneebeli, Benjamin Breddermann, Prof. Dr. Mackillo Kira, Prof. Dr. Stephan W. Koch, and me. I contributed the basic structure, assembled the manuscript, and computed and generated the figures. Paper [VI] was mainly written by Dr. Andrea Klettke, Dr. Lukas Schneebeli, Benjamin Breddermann, Prof. Dr. Mackillo Kira, Prof. Dr. Stephan W. Koch, and me. Also, I contributed the basic structure and most text parts, assembled the manuscript, and created Figs. 2 and 3. In Paper [VII], I contributed by writing text and generating figures.

Apart from direct participation in research projects, I administrated the computer and network systems in our workgroup and contributed several supporting scripts and hints for the members.

The Inner Horizon III

See page XLIV for reference.

Table of Contents

List of Figures

The Inner Horizon IV

See page XLIV for reference.

1 Introduction

Semiconductors have become a vital and integral part of our world. The rapid development of semiconductor technology has generated a manifold and diverse wealth of application variants of these materials. Owing to the specific crystal structure, the highest occupied energy band (valence band) and the next-higher energy band (conduction band) are separated by the so-called *energy gap* or *band gap* [1, 2]. Usually, this energy gap is in the range of some few electron volts (eV), thus allowing absorption and emission of radiation in the visible range [76], i.e., in a domain of electromagnetic radiation which is perceptible by the human eye. The possibility to produce semiconductor structures with highest purity and precision renders this solid-state material to be highly suitable for fundamental research and also in many fields of application-oriented and -optimized products of everyday life. For example, semiconductors cover elementary needs of humankind like ambient lighting, communication, and microelectronics, but also record and transfer of information.

With regard to applications of semiconductor materials on the commercial and private sector in today's life, clearly, parade examples are computer chips such as central-processing units (CPUs) and memory. Semiconductors offer the possibility to miniaturize electronic circuits and components, e.g., transistors, which is associated with less energy and space consumption but yet faster processing times. Recently, liquid-based transistors have been reported that could process data like the human brain [3–5]. Especially the feature of maintaining a certain state without supplying power and the dynamically reconfigurable, i.e., reprogrammable, circuits provide this new method with many variational possibilities such as switching-circuit control or information storage in one device. Besides this, it cannot be denied that modern data storage is based on digital memory devices that largely superseded analog storage media. One of the most prominent examples is certainly the compact disc (CD). This optical storage medium [6] may be read and written without contact by an aluminum–gallium–arsenide (AlGaAs)-based semiconductor laser emitting in the near-infrared range at a wavelength of 780 nanometers (nm). By definition, one nanometer is equal to one billionth of a meter, i.e., $1\,\mathrm{nm} \equiv 10^{-9}\,\mathrm{m}$. Utilizing other semiconductor materials, the wavelength of the laser light may be decreased, leading to higher data densities on the optical medium. With this, high data capacities and high-resolution videos are saved on digital versatile discs (DVDs) and Blu-ray discs.[1] For the latter, indium–gallium–nitride (InGaN)-based wide-gap semiconductor lasers emitting in the blue/ultraviolet range are used [7]. However, data is not only stored on optical memory devices. Faster cores and the multi-core architecture of modern CPUs impede the performance augmentation of common hard-disk drives (HDDs) as these suffer from limitations in increasing the rotational speed of the magnetic media. Having its origin in the 1950s, the development of solid-state drives (SSDs) [8] advanced much in the last decade. SSDs are semiconductor-based, non-volatile memories offering reading and writing performance which already measures up to current computer-interface speeds. After initial criticism and start-up difficulties [10], this unmechanical data-storage device represents nowadays a genuine alternative and a competitively viable option to HDDs.

[1] Trademark owned by the *Blu-ray Disc Association*.

Modern laser diodes and light-emitting diodes (LEDs) offer a large variety of colors and extremely high brightness. Compared to incandescent light sources, LEDs exhibit, e.g., physical robustness, low energy consumption, smaller size, long lifetimes, and fast switching times. As a further development, organic LEDs (OLEDs) [11], first introduced in 1987 by Tang and Van Slyke [12], are thin-layered and flexible semiconductor materials offering high brilliance and the possibility to be manufactured using printing technologies. Mostly, OLEDs are used in cell phones, media players, and digital cameras today [13]. Current developments and the growing prevalence of LEDs utilized for ambient lighting [14] move into a direction where common fluorescent-light sources are intended to be replaced by highly efficient LED tubes [15, 16]. Taking advantage of the high switching rates of LEDs and the widespread use of LED-light bulbs, high-speed data transfer via *visible-light communication* (VLC) is within reach [19, 20] offering data-transfer rates up to 3 gigabits per second [17, 18]. Clearly, also a flash lamp provides the possibility to transfer data such as a Morse-code signal. However, it obviously cannot be considered to be a useful illumination source. High-speed switching capabilities that come with LEDs, however, allow for a combination of both illumination and communication. This offers the great advantage to adopt every LED-based light source such as ceiling lamps, highway lighting, or displays and television sets to provide light and, additionally, networking capabilities as a side benefit. At the same time, these light sources are ubiquitous and harmless for the human body and electronic devices. By virtue of operating at high frequencies of hundreds of terahertz, it furthermore offers a way around the problems of the wireless-spectrum crunch, and disturbances due to radio-frequency noise. Not least, the license-free applicability of the respective frequencies is another great advantage.

The fabrication and ongoing improvement of such devices is a result of long and extensive development processes and fundamental research. The strong demand for new and more efficient devices underlines the undiminished significance of the contribution of science and ongoing research. Modern crystal-growth and doping techniques allow to produce high-purity semiconductor samples customized and tailored to specific and individual requirements [21]. In this context, fabrication of heterostructures with different dimensionality is possible, reaching from three-dimensional bulk samples to all kinds of quantum-confined systems such as quantum wells (QWs) in two dimensions and quantum wires (QWIs) in one dimension up to quantum dots (QDs) where the electron movement is confined in all three spatial directions. In fundamental research, scientists utilize such structures to investigate, control, and manipulate the underlying optical and electronic properties of interacting many-body systems by performing optical experiments. The rapid development of experimental techniques and laser setups allows to perform ultrafast experiments on a femtosecond time scale [22]. Exciting a semiconductor sample by a classical laser pulse whose frequency is energetically close to the fundamental absorption edge, i.e., the energy gap, induces a coherent polarization in the semiconductor material by lifting an electron from the valence band into the conduction band. The absence of this electron in the valence band leads to the concept of electrons and holes in semiconductors where a hole describes a positively charged particle and thus the opposite of an electron. In a semiclassical treatment, it has proved beneficial to introduce effective masses which describe the charged particles in a crystal as if they would move freely but with a mass deviating from the free-electron mass. These effective masses determine the curvatures of the energy bands at the conduction-band minimum and the valence-band maximum. Generally, the effective mass is a tensor and may show anisotropic effects [23]. The Coulomb interaction among charged particles leads to a variety of many-particle correlations giving rise to energy renormalizations where states also below the usual energy gap are allowed [1, 2]. Under coherent conditions, the phase of the exciting pulse affects the system properties and influences all related processes yielding a well-defined phase dependence among each other. This leads to the concept of the *coherent exciton* which essentially describes a single carrier in a superposition state between the valence and the conduction band [24]. However, disorder and inevitable scattering processes among charged particles [29] and lattice vibrations [30, 31] destroy these phase relations (dephasing) leading to a fast decay of the coherent polarization on a picosecond time scale [24] ($1\,\mathrm{ps} = 10^{-12}\,\mathrm{s}$). The system then enters the so-called *incoherent regime* where all interband coherences vanish and only incoherent quantities remain. The simplest form of such an incoherent quantity are the carrier densities of electrons and holes which usually remain in the system for a long time in the range of nanoseconds [24]. Thus, a semiconductor is able to spontaneously emit radiation even if the exciting pulse is long gone [2]. Owing to the light–matter interaction and scattering mechanisms, the coherent

polarization decays either radiatively or is converted into incoherent quasi-particle excitations. Depending on the excitation conditions, electrons and holes may exist as unbound pairs (plasma) or, owing to complicated carrier–carrier and carrier–lattice-vibration scattering processes, may form a new quasiparticle called *incoherent exciton* [29]. This entity represents a correlated electron–hole pair, truly bound via Coulomb attraction, and may be described in analogy to the hydrogen problem. However, exciton populations may also coexist to plasma such that a mixture of both configurations is present in the system. As all investigations presented in this thesis are performed in the incoherent regime, the term *exciton* exclusively refers to the construct of the truly bound electron–hole pair.

Considering that the classical light field vanishes in the incoherent regime, the quantum nature of light appears to play an essential role. To microscopically model the complex scattering mechanisms and interplay with electromagnetic fields, a fully microscopic quantum theory is needed which consistently includes and combines the different contributions of the quantized light field, carrier–carrier scattering via the Coulomb interaction, and scattering of charge carriers with lattice vibrations. Depending on experimental conditions and the investigated problem, different assumptions may be introduced or the theory is to be expanded by additional contributions including, e.g., the influence of a terahertz (THz) pulse or magnetic-field effects. To construct the theoretical framework, the Heisenberg equations-of-motion method [1] constitutes an appropriate foundation to describe all important processes on the same level. The cluster-expansion approach [2, 32–38] allows for a consistent truncation of the well-known hierarchy problem, resulting in a closed set of equations which describe the system and its specific many-body configuration. That way, theory is capable of explaining experimental findings or predicting new physical effects.

The first part of this thesis deals with the elementary interaction between charge carriers and lattice vibrations in semiconductors. The investigations are separated into two projects presented in Chaps. 3 and 4 where the effects of lattice vibrations on the semiconductor luminescence are discussed. In a quantum-mechanical sense, these delocalized excited states of vibrational modes in the crystal structure may be described by a quasiparticle called *phonon*. Besides the already mentioned dephasing of coherent excitations [39–41], phonons also play a central role in the context of cooling a hot carrier system [42–44], light–matter interaction [45, 46], and the formation of excitons [29]. Yet, longitudinal-optical (LO) phonons may also participate in electron–hole recombination giving rise to pronounced replicas, so-called *phonon sidebands* (PSBs), in the photoluminescence (PL) spectrum of a semiconductor. Earlier works have addressed the derivation of phonon-assisted luminescence equations in depth following both perturbative [47] and non-perturbative approaches [48, 49]. Here, especially the question of whether and to which extent uncorrelated electron–hole plasma and truly bound exciton populations contribute to the phonon-assisted PL has been examined [47, 50] – an important extension to earlier works [51] which concentrated on the $1s$-exciton resonance. Within the scope of these phonon-related works, steady-state solutions for semiconductor luminescence including phonon sidebands of arbitrary order have been presented, albeit without the participation of stimulated-emission effects. It is well-known that a dielectrically structured environment substantially alters the luminescence spectra and appearing resonances if a semiconductor nanostructure such as a quantum well is placed at an antinode of the intracavity field. Tuning the microcavity resonance to coincide with the $1s$-exciton resonance such that the resonance of the resonator and of the active material are degenerate leads to the famous scenario of normal-mode coupling (NMC) where the resonance splits into two peaks [52–58]. On the basis of this thoroughly investigated system, the above-mentioned phonon-related studies are extended in Chap. 3 of this thesis. The discussion delves into the question how a dielectric environment modifies and influences the phonon-assisted photoluminescence. Here, not only a cavity whose resonance frequency coincides with the $1s$-exciton resonance is explored but, in particular, a cavity which is detuned to be resonant with the first phonon sideband of the semiconductor emission. After a detailed numerical study of the different cavity configurations, the analysis is topped off by a rigorous analytic model.

The second phonon-related project is presented in Chap. 4 where the origin of scattering between carriers and phonons is scrutinized in detail. Set by the crystal structure, a semiconductor material may exhibit strong polar behavior. Thus, depending on the structure and system configuration, either polar carrier–phonon interaction or non-polar carrier–phonon scattering prevails in the semiconductor material. Additionally, the Coulomb attraction modifies the interaction behavior between charge carriers and lattice vibrations such that single car-

riers behave differently than an interacting many-body system. This raises the question under which conditions and on which basis an intrinsically polar material may be dominated by non-polar carrier–phonon scattering. Supported by experimentally measured phonon-assisted photoluminescence spectra, a systematic many-body theory is presented to explain the origin of exciton–phonon interaction in polar semiconductors and identify its role in an interacting many-body system.

The Coulomb interaction in many-body systems is not only of particular importance for mediating the coupling among excitons and LO phonons but also plays a crucial role in intra-exciton transitions where diffusive Coulomb scattering gives rise for extensions of the usual dipole-selection rules. As a direct continuation of recent works [59], the second part of this thesis addresses a very central field of current research. In contrast to interband transitions where an absorption or emission process creates or destroys an electron–hole pair, respectively, intraband transitions do not alter the number of electron–hole pairs. Recently, the traditional interband studies have been supplemented and expanded due to the development of coherent THz sources such as the free-electron laser [60–63], quantum-cascade lasers [64, 65], or sources using difference-frequency generation [77, 78]. The energies of far-infrared (FIR) fields at terahertz frequencies are in the range of milli-electron volts (meV), i.e., $1\,\mathrm{THz} = 10^{-12}\,\mathrm{Hz}$ corresponds roughly to $4\,\mathrm{meV}$, and thus three orders of magnitude smaller than typical band-gap energies. Since the internal energy structure of correlated semiconductor many-body states falls in this meV range, THz spectroscopy is an unambiguous method to probe these systems, i.e., identify exciton populations [66,67], and to induce controlled transitions [66,68–71] between the excited quasi-particle states. However, terahertz radiation is not only applicable in physics but provides sensing capabilities in a wide range of research fields and sciences such as pharmacy, biology, and medicine [72]. Additionally, it is used for nondestructive testing and material characterization [73]. With regard to semiconductors, the THz energy is far off-resonant with respect to the interband transitions in typical GaAs-like semiconductors [74, 75] such that the light–matter coupling in this spectral regime is governed by two- or more-particle correlation contributions. Consequently, the combination of pulsed optical and THz fields allows not only for the creation of many-body excitations but also for the characterization of their dynamic evolution and the controlled manipulation of the involved quantum states. Applying an external magnetic field, both the exciton properties and THz-induced intra-exciton transitions may be modified. Chapter 5 focuses on the control and manipulation of the intra-exciton carrier transfer by magnetic-field effects. Experimental findings are corroborated by a theoretical description, rigorously expanded by fully including linear and nonlinear magnetic-field contributions to the total-system Hamiltonian.

This thesis is structured as follows. In Chap. 2, the general framework is set by briefly discussing the theoretical background and introducing the related Hamiltonians and theoretical concepts. In Chap. 3, the effects of a microcavity on the phonon-assisted semiconductor luminescence are presented, followed by the studies on the origin of exciton–phonon interaction in polar semiconductors in Chap. 4. The impact of a magnetic field in connection with THz fields is discussed in Chap. 5. In Chap. 6, the results of this thesis are summarized and an outlook is given. The appendices contain some supplementary and noteworthy derivations which, however, are not necessarily needed for a comprehensive understanding of the preceding physical results. The hitherto published papers associated with the results presented in Chaps. 3–5 are summarized on page XLV et seq., followed by the respective publications. A list of all papers with my participation as first author or coauthor, including manuscripts in preparation, is given on page IX.

2 Theoretical approach

This first chapter sets the general framework for the results presented in Chaps. 3–5 and related Papers. After briefly discussing the theoretical background, the theoretical approach will be introduced. The subsequent concepts are mainly based on the thorough theoretical descriptions and meticulous derivations presented in the literature [1, 2, 24, 79–81] and previous theses [47, 82, 83].

In this work, both bulk semiconductors and structures of reduced dimensionality are investigated. While in bulk semiconductors the electron is genuinely a three-dimensional entity, the movement of electrons may be restricted in one (quantum well, QW), two (quantum wire, QWI), or all three (quantum dot, QD) spatial directions for confined systems. Of these, exclusively quasi-two-dimensional systems are considered. In general, a quantum well is a potential well thought of as low-dimensional heterostructures where the carriers occupy a planar region embedded within layers of different band-gap energies. Owing to reduced dimensionality, the charge carriers exhibit strong confinement, leading to changes of the effective masses and lifting of degeneracies of the valence bands [84, 85], the so-called *heavy-* and *light-hole bands*. Furthermore, the translational symmetry is broken in direction perpendicular to the growth plane [57, 86] and the density of states shows distinct steps in contrast to a square-root-like behavior in case of bulk systems. These effects lead to fundamentally different behaviors of the many-body properties.

In this chapter, the different constituents needed for a consistent description of the results presented in the subsequent chapters are delineated in Sec. 2.1. In Sec. 2.2, an equation-of-motion approach to derive the system dynamics is presented. All derivations suffer from the obstacle of the operator-dynamics coupling to higher-order correlations due to the many-body interaction which, eventually, evokes an infinite hierarchy of coupled equations. To obtain a self-contained solution, a consistent truncation scheme is needed.

In the remainder of this work, three-dimensional momentum-space vectors, e.g., $\mathbf{q}_{3\mathrm{D}} = (\mathbf{q}, q_\perp)$, will be decomposed into their in-plane and perpendicular components, denoted by $\mathbf{q}$ and $q_\perp$. For the sake of better readability, the parallel index is omitted here. Real-space vectors, however, mainly represent three-dimensional quantities $\mathbf{r} = (\mathbf{r}_\parallel, r_\perp)$ and parallel as well as perpendicular components will be labeled explicitly if needed. If not otherwise stated, vectors $\mathbf{k}$, $\mathbf{q}$, $\mathbf{Q}$, and $\mathbf{p}$ always denote momentum-space vectors whereas $\mathbf{r}$, $\mathbf{x}$, $\mathbf{R}$, $\mathbf{S}$, and $\boldsymbol{\kappa}$ are in real space. Without explicitly given limits, all sums and integrals are assumed to cover the full space or, in the case of angular integrals, a full turn. The derivations in this chapter are presented for quantum wells, but can be easily assigned for bulk systems.

2.1 System Hamiltonian

In solids, mainly three important (quasi)particles are of major interest: electronic states, phonons, and photons. While photons show a linear dispersion relation connecting the speed of light with the momentum of the elementary particle, phonons can be divided into two main categories which can either show a linear dispersion for small momenta (acoustic phonons) or a nearly constant dispersion over the complete spectral range (optical phonons). In contrast, the energies of the electronic states exhibit a nontrivial dependency on the electron

momentum, which has to be determined carefully. The single-particle energies then constitute the energetic band structure of the solid. This section briefly condenses the basics of solid-state theory and the fundamental considerations for the description of charge carriers, lattice vibrations, and photons in a crystal structure. The mathematical tool for this purpose is the generic Hamilton operator (Hamiltonian) which constitutes the cornerstone of the description of quantum-mechanical systems.

Lattice vibrations constitute a very fundamental mechanism to the description of interacting many-body systems. Even though the microscopic description of lattice vibrations is mainly important in Chaps. 3 and 4, its theoretical framework is comprised in the context of the following general theoretical approach. The effects arising when a semiconductor is subjected to a magnetic field, however, describe a special configuration with regard to the results presented in Papers [V] and [VII]. Accordingly, the corresponding extensions to the basic-system Hamiltonian are presented separately in Chap. 5.

2.1.1 Quantization of the carrier system

In typical semiconductors, electrons move in a lattice-periodic potential while interacting with each other via the Coulomb interaction. A typical starting point for the description of these basic concepts is the single-particle Schrödinger equation which in first quantization is given by

$$\left[-\frac{\hbar^2\nabla^2}{2m_0}+V_0(\mathbf{r})\right]\phi_{\lambda,\mathbf{k}}(\mathbf{r})=\epsilon^{\lambda}_{\mathbf{k}}\,\phi_{\lambda,\mathbf{k}}(\mathbf{r}) \tag{2.1}$$

with the single-particle wavefunction $\phi_{\lambda,\mathbf{k}}(\mathbf{r})$. The effective, translation-invariant lattice potential $V_0(\mathbf{r}) = \sum_{\mathbf{R}_i} V_{0,i}(\mathbf{r}-\mathbf{R}_i)$ is assumed to offer symmetry and periodicity properties reflecting the structure of the perfect crystal lattice. Here, $\mathbf{R}_i$ denotes the position of the i^{th} ion core. Equation (2.1) can be solved by choosing Bloch states [79, 80, 87] as a single-particle basis of the problem. Then, the states $(\lambda, \mathbf{k}, \sigma)$ build a complete set of single-particle quantum numbers including band index λ, wavevector $\mathbf{k}$, and spin index σ which is implicitly included in $\mathbf{k}$ in the remainder of this work. Since this particular notation is restricted to a state of fixed particle number, it is convenient to use the occupation-number representation which is often referred to as the *second quantization* [1, 2, 88]. States of different particles are then connected by introducing creation and annihilation operators $\hat{a}^{\dagger}_{\lambda,\,\mathbf{k}}$ and $\hat{a}_{\lambda,\,\mathbf{k}}$, respectively. Here, $\hat{a}^{\dagger}_{\lambda,\,\mathbf{k}}$ creates a particle with crystal momentum $\hbar\mathbf{k}$ (and spin σ) in band λ whereas $\hat{a}_{\lambda,\,\mathbf{k}}$ annihilates the same particle. They obey the Fermionic anticommutation relations

$$\left[\hat{a}_{\lambda,\,\mathbf{k}},\hat{a}_{\lambda',\,\mathbf{k}'}\right]_+ = 0 = \left[\hat{a}^{\dagger}_{\lambda,\,\mathbf{k}},\hat{a}^{\dagger}_{\lambda',\,\mathbf{k}'}\right]_+ \quad \text{and} \quad \left[\hat{a}_{\lambda,\,\mathbf{k}},\hat{a}^{\dagger}_{\lambda',\,\mathbf{k}'}\right]_+ = \delta_{\lambda,\lambda'}\,\delta_{\mathbf{k},\mathbf{k}'} \tag{2.2}$$

where $\left[\hat{A},\hat{B}\right]_+ \equiv \hat{A}\hat{B}+\hat{B}\hat{A}$. The Coulomb interaction between Bloch electrons can equally be expressed in terms of this basis. With this, the Hamiltonians for the electronic system of free carriers $\hat{H}_{\text{kin}}$ and Coulomb interaction $\hat{H}_{\text{el–el}}$ among the Bloch electrons take the second-quantized form

$$\hat{\boldsymbol{H}}_{\mathbf{kin,\,el\text{–}el}} = \sum_{\boldsymbol{\lambda},\mathbf{k}} \boldsymbol{\epsilon}^{\boldsymbol{\lambda}}_{\mathbf{k}}\hat{\boldsymbol{a}}^{\dagger}_{\boldsymbol{\lambda},\,\mathbf{k}}\hat{\boldsymbol{a}}_{\boldsymbol{\lambda},\,\mathbf{k}} + \frac{\mathbf{1}}{\mathbf{2}}\sum_{\boldsymbol{\lambda},\boldsymbol{\lambda}'}\sum_{\substack{\mathbf{k},\mathbf{k}',\\ \mathbf{q}\neq\mathbf{0}}} \boldsymbol{V}^{\boldsymbol{\lambda},\boldsymbol{\lambda}'}_{\mathbf{q}}\hat{\boldsymbol{a}}^{\dagger}_{\boldsymbol{\lambda},\,\mathbf{k}}\hat{\boldsymbol{a}}^{\dagger}_{\boldsymbol{\lambda}',\,\mathbf{k}'}\hat{\boldsymbol{a}}_{\boldsymbol{\lambda}',\,\mathbf{k}'+\mathbf{q}}\hat{\boldsymbol{a}}_{\boldsymbol{\lambda},\,\mathbf{k}-\mathbf{q}} \tag{2.3}$$

System Hamiltonian of the charge-carrier system

with the single-particle energies $\epsilon^{\lambda}_{\mathbf{k}}$ for an electron with momentum $\hbar\mathbf{k}$ in band λ. To describe excitations near the extrema of the bands, it is customary to assume parabolic bands $\epsilon^{\lambda}_{\mathbf{k}} = \frac{\hbar^2\mathbf{k}^2}{2m_\lambda}$ with effective masses m_λ. The Coulomb-matrix element for confined carrier systems is given by

$$V_{\mathbf{q}}^{\lambda,\lambda'} = V_{\mathbf{q}}^{\mathrm{2D}} \int \mathrm{d}r_\perp \int \mathrm{d}r'_\perp \; |\zeta_\lambda(r_\perp)|^2 \, |\zeta_{\lambda'}(r'_\perp)|^2 \; \mathrm{e}^{-|\mathbf{q}\,(r_\perp - r'_\perp)|} \tag{2.4}$$

with confinement function $\zeta_\lambda(r_\perp)$ and Coulomb-matrix element $V_{\mathbf{q}}^{\mathrm{2D}} = \frac{e^2}{2\epsilon_\mathrm{r}\varepsilon_0\mathcal{L}^2}\frac{1}{|\mathbf{q}|}$ for a strictly two-dimensional system, where ϵ_r is the relative permittivity. For bulk systems, the confinement function is constant for all spatial positions such that $\zeta_\lambda(r_\perp) \equiv 1$. For strongly confined systems, the Coulomb potential approaches the matrix element $V_{\mathbf{q}}^{\mathrm{2D}}$. The operator representation (2.3) shows that the Coulomb interaction expresses an annihilation of the incoming particles with wavevectors $\mathbf{k}' + \mathbf{q}$ and $\mathbf{k} - \mathbf{q}$, respectively, followed by a creation of two particles with wavevectors $\mathbf{k}$ and $\mathbf{k}'$. In other words, the Coulomb interaction exchanges the momentum $\hbar\mathbf{q}$ between two electrons conserving the in-plane momentum of the Bloch electrons. The momentum exchange is mediated by the Coulomb-matrix element. Within the scope of the Jellium-model approach [1,2] the vanishing $\mathbf{q} = \mathbf{0}$ contribution in Eq. (2.3) is explained as being compensated by the Coulomb self-energy of the uniformly charged background of the ions. From the physical point of view, it is meaningful that the scattering process induced by the Coulomb interaction must be accompanied by a momentum exchange; otherwise no scattering would take place.

2.1.2 Quantization of the electromagnetic field

The presence of oscillating dipoles allows for the emission of electro-magnetic waves. To describe the quantum dynamics of the coupled light–matter system, it it essential to expand the classical fields in terms of quantum-mechanical operators. Here, the contributions resulting from the electro-magnetic field are divided into a free-field part and the interaction with the semiconductor. The plain field is usually derived by mode-expanding a vector potential $\mathbf{A}(\mathbf{r},t)$ and transforming it to an operator representation via the canonical-quantization scheme [88, 89]. The light–matter coupling can either be expressed in the $\hat{\mathbf{p}}\cdot\hat{\mathbf{A}}$ picture or the $\hat{\mathbf{x}}\cdot\hat{\mathbf{E}}$ picture, depending on the respective problem and physical effect.

Free transverse light field

The derivation of the quantum dynamics of light starts from the vector potential of a classical electromagnetic field propagating in a structure described by a space-dependent background refractive index $n(\mathbf{r})$. The solutions must obey the homogeneous part of the transversal wave equation

$$\left[\triangle - \frac{n^2(\mathbf{r})}{c_0^2}\frac{\partial^2}{\partial t^2}\right]\mathbf{A}(\mathbf{r},t) = -\mu_0\,\mathbf{J}_\mathrm{T}(\mathbf{r},t) \tag{2.5}$$

where the generalized Coulomb gauge $\nabla\cdot[n^2(\mathbf{r})\,\mathbf{A}(\mathbf{r},t)] = 0$ is adopted. Thus, only the purely transversal component $\mathbf{J}_\mathrm{T}(\mathbf{r},t)$ of the current remains here. The quantity $c_0 = 1/\sqrt{\mu_0\varepsilon_0}$ is the speed of light in vacuum, μ_0 is the vacuum permeability, and ε_0 the vacuum permittivity.

A single or multiple quantum well, as investigated in large part in this thesis, may either be placed between two dielectric barriers or be embedded in an optically passive, planar environment consisting of $\lambda/4$ Bragg layers where λ is the wavelength of the propagating mode within the structure. These microcavity structures are called *distributed Bragg reflectors* (DBRs) [57, 90–92]. Between such DBR layers, a single or multiple quantum well is typically positioned within a spacer layer. For large spatial extension perpendicular to the growth plane, the refractive-index profile $n(\mathbf{r}) = n(r_\perp)$ is constant within each grown layer and changes abruptly at the border to the next layer. The mode functions parallel to the quantum well, i.e., in the x–y plane of each planar region, are then described via plane waves while the perpendicular solutions are related to boundary conditions at the interfaces of each layer via Maxwell's equations [81, 93–96]. Such a microcavity structure is the crucial point of the investigations presented in Chap. 3. Fourier-transforming the homogeneous part of Eq. (2.5) into the frequency domain, $t \to \omega_{\mathbf{q}_\mathrm{3D}} = c_0|\mathbf{q}_\mathrm{3D}|$, results in the (generalized) Helmholtz equation. The solutions are stationary eigenmodes $\mathbf{U}_{\mathbf{q}_\mathrm{3D}}(\mathbf{r})$ where the polarization of each eigenmode is implicitly included in $\mathbf{q}_\mathrm{3D}$. These solutions build a complete orthogonal basis for the Helmholtz equation. In other words, these eigenmodes are eigenfunctions of the Laplace operator with eigenvalues $-\mathbf{q}_\mathrm{3D}^2$.

Transverse displacement field $\mathbf{D}_\mathrm{T}(\mathbf{r},t) = -\varepsilon_0\, n(\mathbf{r})\, \frac{\partial \mathbf{A}(\mathbf{r},t)}{\partial t}$ and magnetic field $\mathbf{B}(\mathbf{r},t) = \nabla \times \mathbf{A}(\mathbf{r},t)$ are connected to the vector potential $\mathbf{A}(\mathbf{r},t)$ via Maxwell's equations. Using the eigenmodes $\mathbf{U}_{\mathbf{q}_\mathrm{3D}}(\mathbf{r})$, these quantities may be expressed in second-quantized form by introducing Bosonic creation and annihilation operators $\hat{B}^\dagger_{\mathbf{q}_\mathrm{3D}}$ and $\hat{B}_{\mathbf{q}_\mathrm{3D}}$ for photons. These unitless operators obey the Bosonic commutation relations

$$\left[\hat{B}_{\mathbf{q}_\mathrm{3D}}, \hat{B}_{\mathbf{q}'_\mathrm{3D}}\right]_- = 0 = \left[\hat{B}^\dagger_{\mathbf{q}_\mathrm{3D}}, \hat{B}^\dagger_{\mathbf{q}'_\mathrm{3D}}\right]_- \quad \text{and} \quad \left[\hat{B}_{\mathbf{q}_\mathrm{3D}}, \hat{B}^\dagger_{\mathbf{q}'_\mathrm{3D}}\right]_- = \delta_{\mathbf{q}_\mathrm{3D},\mathbf{q}'_\mathrm{3D}}\,. \tag{2.6}$$

As a consequence, the mode expansion of the vector potential and the transversal electric field allows to identify the particle aspects associated with light waves. The contribution of the longitudinal part of the electric field, i.e., the scalar potential, is a function of the carrier density itself and yields the instantaneous Coulomb interaction discussed above. The vector potential takes the form

$$\hat{\mathbf{A}}(\mathbf{r},t) = \sum_{\mathbf{q}_\mathrm{3D}} \frac{\mathscr{E}_{\mathbf{q}_\mathrm{3D}}}{\omega_{\mathbf{q}_\mathrm{3D}}} \left[\mathbf{U}_{\mathbf{q}_\mathrm{3D}}(\mathbf{r}) \hat{B}_{\mathbf{q}_\mathrm{3D}} + \mathrm{h.\,c.}\right] \tag{2.7}$$

with photon dispersion relation $\omega_{\mathbf{q}_\mathrm{3D}} = c_0|\mathbf{q}_\mathrm{3D}|$ and the expansion coefficient $\mathscr{E}_{\mathbf{q}_\mathrm{3D}} = \sqrt{\frac{\hbar\omega_{\mathbf{q}_\mathrm{3D}}}{2\varepsilon_0}}$ which is often referred to as the *vacuum-field amplitude*. The abbreviation $\mathrm{h.\,c.}$ denotes the Hermitian conjugate of the preceding part. The solutions $\mathbf{U}_{\mathbf{q}_\mathrm{3D},\sigma}(\mathbf{r})$ are orthogonalized, leading to a complete set of transverse eigenstates. The product $\mathscr{E}_{\mathbf{q}_\mathrm{3D}}\mathbf{U}_\mathbf{q}(\mathbf{r})$ determines the strength of the electric field at a given position. With the mode-expanded vector potential (2.7) and Maxwell's equations, the transverse electric field, $\hat{\mathbf{E}}_\mathrm{T}(\mathbf{r},t) = -\frac{\partial \hat{\mathbf{A}}(\mathbf{r},t)}{\partial t}$, and the magnetic field, $\hat{\mathbf{B}}(\mathbf{r},t) = \nabla \times \hat{\mathbf{A}}(\mathbf{r},t)$, express the energy of the transverse field

$$\hat{\boldsymbol{H}}_\mathbf{em} = \frac{\boldsymbol{\varepsilon_0}}{\mathbf{2}} \int \left[\boldsymbol{n}^\mathbf{2}(\mathbf{r})\, \hat{\mathbf{E}}^\mathbf{2}_\mathbf{T}(\mathbf{r},\boldsymbol{t}) + \boldsymbol{c}^\mathbf{2}_\mathbf{0}\, \hat{\mathbf{B}}^\mathbf{2}(\mathbf{r},\boldsymbol{t})\right] \mathbf{d}^\mathbf{3}\boldsymbol{r} = \sum_{\mathbf{q_{3D}}} \hbar\boldsymbol{\omega}_\mathbf{q_{3D}} \left(\hat{\boldsymbol{B}}^\dagger_\mathbf{q_{3D}} \hat{\boldsymbol{B}}_\mathbf{q_{3D}} + \tfrac{\mathbf{1}}{\mathbf{2}}\right). \tag{2.8}$$

Hamiltonian of the free transverse light field

Light–matter interaction

Besides the plain electro-magnetic field, the interaction of light and matter plays an essential role in the description of semiconductors. In order to microscopically model the interaction of the carrier system and the electro-magnetic field, the derivation starts from the free-particle Hamiltonian introduced by Eq. (2.1)

$$\hat{H}_\mathrm{free} = \sum_{j=1}^{N} \frac{\hat{\mathbf{p}}_j^2}{2m_0} + V_0(\mathbf{r}_j) \tag{2.9}$$

with the free-electron mass m_0, lattice-periodic potential $V_0(\mathbf{r}_j)$, position $\mathbf{r}_j$, and canonical-momentum operator $\hat{\mathbf{p}}_j = -\mathrm{i}\hbar\nabla_{\mathbf{r}_j}$ of particle j in the N-particle many-body system. Introducing the minimal substitution $\hat{\mathbf{p}}_j \to \hat{\mathbf{p}}_j + |e|\hat{\mathbf{A}}(\mathbf{r}_j,t)$ with electron charge given by $-|e|$ and applying the Coulomb gauge[1] ($\nabla \cdot \hat{\mathbf{A}} = 0$), results in the *minimal-substitution Hamiltonian* [81] in first-quantized form

$$\hat{H} = \sum_{j=1}^{N} \frac{\hat{\mathbf{p}}_j^2}{2m_0} + \frac{|e|}{m_0}\hat{\mathbf{A}}(\mathbf{r}_j,t)\cdot\hat{\mathbf{p}}_j + \frac{e^2\hat{\mathbf{A}}^2(\mathbf{r}_j,t)}{2m_0} + V_0(\mathbf{r}_j) + \frac{1}{2}\sum_{i\neq j} V(\mathbf{r}_i - \mathbf{r}_j) + \hat{H}_\mathrm{em}\,. \tag{2.10}$$

Equation (2.10) describes an interacting carrier system including coupling to an electro-magnetic field $\hat{\mathbf{A}}(\mathbf{r}_j,t)$. In this representation, the Coulomb interaction and the free electro-magnetic field (2.8) are added as well. For the derivation of the light–matter interaction, however, the terms containing the vector potential $\hat{\mathbf{A}}(\mathbf{r}_j,t)$ are the essential contributions. Since the mode basis and gauge may be chosen freely, it is customary to introduce new

[1] For large separations of quantum well and DBRs, the refractive index in the region of interest may be assumed to be position independent, i.e., $n(\mathbf{r}) = n_0$.

unitary operators $\hat{U}$ to transform the dipole interaction from the $\hat{\mathbf{p}} \cdot \hat{\mathbf{A}}$-picture to the $\hat{\mathbf{x}} \cdot \hat{\mathbf{E}}$-picture. For classical electric fields, the corresponding transformation is known as the *Göppert-Mayer transformation* [2, 97] given by $\hat{H}' = \hat{U}\hat{H}\hat{U}^\dagger$ where $\hat{U} = \exp[\frac{\mathrm{i}}{\hbar}|e|\sum_j \mathbf{r}_j \cdot \hat{\mathbf{A}}(\mathbf{r}_j, t)]$. By performing an expansion [2, 82, 98] of $\hat{H}'$, various contributions arise. In dipole approximation [2], where terms proportional to the spatial derivative of the vector potential are neglected, the carrier part of the transformed form of Hamiltonian (2.10) reproduces the free-carrier part Eq. (2.9). The Coulomb interaction remains unaffected by this procedure under the assumptions stated above. Transforming the free-field Hamiltonian (2.8) reproduces this part as the first contribution of the expansion but also generates additional terms, namely the dipole interaction

$$\hat{\boldsymbol{H}}_{\mathbf{D}} = -\sum_{\mathbf{k},\mathbf{q}_{3\mathrm{D}}} \mathrm{i}\left(\boldsymbol{\mathcal{F}}_{\mathbf{q}_{3\mathrm{D}}}\hat{\boldsymbol{a}}^\dagger_{c,\,\mathbf{k}+\mathbf{q}}\hat{\boldsymbol{a}}_{v,\,\mathbf{k}} + \boldsymbol{\mathcal{F}}^\star_{\mathbf{q}_{3\mathrm{D}}}\hat{\boldsymbol{a}}^\dagger_{v,\,\mathbf{k}}\hat{\boldsymbol{a}}_{c,\,\mathbf{k}-\mathbf{q}}\right)\hat{\boldsymbol{B}}_{\mathbf{q}_{3\mathrm{D}}} + \mathbf{h.\,c.} \tag{2.11}$$

Light–matter interaction Hamiltonian

and dipole self-energy. The latter may be neglected within the scope of the long-wavelength approximation [2] as it merely leads to energetic shifts in the optical spectra [82]. As can be shown, the transformation formally interchanges the role of electric- and displacement-field operators [81]. In Eq. (2.11), $\mathcal{F}_{\mathbf{q}_{3\mathrm{D}}} \equiv \mathscr{E}_{\mathbf{q}_{3\mathrm{D}}}\mathbf{u}_{\mathbf{q}_{3\mathrm{D}}} \cdot \mathbf{d}_{cv}$ defines the strength of light–matter interaction and contains the vacuum-field amplitude $\mathscr{E}_{\mathbf{q}_{3\mathrm{D}}}$, light-mode strength $\mathbf{u}_{\mathbf{q}_{3\mathrm{D}}}(r_\perp)$ at the QW position, and dipole-matrix element $\mathbf{d}_{cv}$. The latter determines the probability of optical interband transitions leading to strict selection rules for optical excitations in semiconductors.

Interaction of carriers with terahertz fields

Chapter 5 concentrates on the investigation of intra-exciton transitions where exciton populations are transferred from the $1s$ to the $2p$ state by a THz pulse resonant with the $1s$-to-$2p$ transition energy. The theoretical description of the THz-induced many-body dynamics follows from the $\mathbf{p} \cdot \mathbf{A}$ and $\mathbf{A}^2$ terms of Hamiltonian (2.10). A detailed derivation of the general procedure described here is presented in, e.g., Ref. [83]. By applying the second-quantization scheme, different matrix elements arise which may be solved by using a Fourier decomposition of the vector potential and performing a length-scale separation with respect to lattice-periodic wavefunctions and confinement functions. A second-order $\mathbf{k} \cdot \mathbf{p}$ ansatz, compare App. A of Ref. [83], eventually leads to interband and intraband contributions to the matrix elements. In typical investigations, homogeneous-excitation conditions are assumed where the field propagates perpendicular to the quantum-well plane. Then, the vector potential depends only on the z-component and $A(z_{\mathrm{QW}}, t)$ denotes the field at the position of the quantum well. It is straightforward to show that only the intraband contribution linear in the vector potential contributes to the singlet- and doublet dynamics [67, 83]. The corresponding Hamiltonian in Bloch basis is given by

$$\hat{\boldsymbol{H}}_{\mathbf{THz}} = -\sum_{\boldsymbol{\lambda},\mathbf{k}} \mathbf{j}_{\boldsymbol{\lambda},\mathbf{k}} \cdot \mathbf{A}(\boldsymbol{z_{\mathrm{QW}}}, \boldsymbol{t})\, \hat{\boldsymbol{a}}^\dagger_{\boldsymbol{\lambda},\,\mathbf{k}}\hat{\boldsymbol{a}}_{\boldsymbol{\lambda},\,\mathbf{k}} \tag{2.12}$$

Semiclassical light–matter Hamiltonian for interaction of carriers with terahertz fields

where $\mathbf{j}_{\lambda,\mathbf{k}} = -|e|\hbar\mathbf{k}/m_\lambda$ is the band-dependent current-matrix element with effective mass m_λ and electron charge $-|e|$. The terahertz interaction is treated in the semiclassical limit by defining the THz field as a classical pulse whereas carriers are described quantum-mechanically. The remaining terms resulting from the derivation are intraband contributions nonlinear in the vector potential and a term describing interband transitions. The $\mathbf{A}^2$ term gives rise to the so-called *ponderomotive energy* [99]. This part does not contribute to the semiconductor response or the many-body (doublet) dynamics induced by THz fields [83] but rather leads to a refractive-index change by means of a Drude-like response [100]. The influence of interband transitions and ponderomotive

contributions is not the focus of the investigations presented in Chap. 5. Instead, THz fields are utilized to induce intraband transitions between exciton states such that Hamiltonian (2.12) consistently describes the THz-induced effects investigated in Chap. 5.

2.1.3 Lattice-vibrations in solids

Typically, the lattice structure is assumed to be perfect and to consist of ions located at their equilibrium positions. Nevertheless, the ions are not absolutely fixed at these positions but can oscillate moderately. As a result of the collective Coulomb interaction with respect to the other ions in the solid, an ion is pulled back once it is displaced away from the equilibrium position. Under these conditions, the oscillations are described by a harmonic equilibrating force leading to collective lattice vibrations in the solid. In quantum-mechanical sense, these lattice vibrations are referred to as *phonons*. Thus, the displacement away from the equilibrium position perturbs the periodic potential acting on the electrons in the crystal, leading to the carrier–phonon-interaction energy. This constitutes a very important interaction mechanism for the realistic description of condensed-matter systems. When phonons are present, the electrons do not move in a perfect periodic potential anymore but in an effective potential of the displaced ions. The theory of lattice vibrations is similar to the derivation of the light quantization. An elaborated and self-contained description is presented in Ref. [47]. Therefore, the following part only briefly sketches the essential steps.

For a microscopic description of electrons and ions, it is convenient to consider the mass ratio $m_\mathrm{e}/M_\mathrm{ion} \approx 10^{-4}$ to 10^{-5} of both constituents. This large difference justifies to decouple both systems and regard the ions as ponderous compared to the electrons. With regard to the time scales, this decoupling is also justified if the ion movement is thought to be so slow that the electron system is able to follow the new ion positions. On the time scale of the electron motion, the ion system then behaves like a time-independent and static system. These basic considerations are referred to as the *Born–Oppenheimer* or *adiabatic approximation*.

Quantization of the lattice-vibration field

Considering $j = 1, \ldots, Z$ ions located at $\mathbf{S}_j(\mathbf{R})$ within a unit cell, the displacement of each ion from its equilibrium position $\mathbf{S}_j^0(\mathbf{R})$ is defined as $\boldsymbol{\kappa}_j(\mathbf{R}) = \mathbf{S}_j(\mathbf{R}) - \mathbf{S}_j^0(\mathbf{R})$ where the argument defines the corresponding unit cell at $\mathbf{R}$. Adopting the Born–Oppenheimer approximation, a Taylor expansion of the potential around the equilibrium energy can be performed. The zeroth-order element corresponds to the equilibrium energy. Without loss of generality, this term may be set to zero by means of renormalization of the energy scale. The linear term vanishes since first-order partial derivatives vanish at the equilibrium positions, i.e., at the absolute minimum of the potential. The third term introduces a harmonic force with respect to the relative distance between two lattice sites. For relatively low temperatures, the deviations from the equilibrium positions are small and the Taylor expansion may be truncated after the quadratic term [79, 80]. This is the so-called *harmonic approximation*. Expanding them in terms of normal modes, freely propagating lattice vibrations can thus be described in complete analogy to a set of *independent* harmonic oscillators. For equal displacement of all atoms within a unit cell, the complete crystal is displaced.

The quantized phonon field is obtained from the lattice displacements and canonical momenta $\mathbf{P}_j(\mathbf{R}) = M_j \dot{\boldsymbol{\kappa}}_j(\mathbf{R})$ where the dot indicates the derivative with respect to time, producing Canonical field operators which then are expanded in terms of the polarization and wavevector of each phonon mode. This leads to Bosonic phonon-creation and -annihilation operators $\hat{D}^\dagger_{\mathbf{p}_\mathrm{3D}}$ and $\hat{D}_{\mathbf{p}_\mathrm{3D}}$, respectively, which obey the commutation relations (2.6). The Hamiltonian of the free lattice-vibration field eventually reads

$$\hat{\boldsymbol{H}}_\mathbf{vib} = \sum_{\mathbf{p_{3D}}} \hbar \boldsymbol{\Omega}_\mathbf{p_{3D}} \left(\hat{\boldsymbol{D}}^\dagger_\mathbf{p_{3D}} \hat{\boldsymbol{D}}_\mathbf{p_{3D}} + \tfrac{\mathbf{1}}{\mathbf{2}} \right) \tag{2.13}$$

Hamiltonian of the lattice-vibration field

with phonon energy $\hbar\Omega_{\mathbf{p}_{3\mathrm{D}}}$. Since phonons are Bosons, the occupation numbers in equilibrium follow a Bose–Einstein distribution. Considering semiconductor structures of reduced dimensionality, normally, also phonons are affected by the confinement. Due to the differences of ion and electron masses, however, it is justified to neglect the size quantization for the lattice vibrations and model these as propagating bulk phonons which interact with an electron gas of reduced dimensionality [47, 101].

It is known that a linear dispersion relation is expected for the phonon branches for which the atoms within a unit cell are equally displaced. The phonon frequency then vanishes for long wavelengths, i.e., vanishing phonon momentum $\hbar\mathbf{p}_{3\mathrm{D}} \to \mathbf{0}$. Corresponding to d directions in real space for a fixed polarization direction, d such branches, which are called *acoustic phonons*, are expected. Since many semiconductor materials are compounds of several elements, they consequently have unit cells which consist of more than one atom, i.e., $Z > 1$. Then, there are also *optical phonon* excitations that exist. Here, the atoms within a unit cell do not vibrate in sync but against each other. In general, dZ phonon branches are expected from which d correspond to acoustic phonons and $d(Z-1)$ stem from optical phonons. The optical phonon energy only barely depends on the wavelength, $\hbar\Omega_{\mathbf{p}_{3\mathrm{D}}} \simeq \hbar\Omega$, and especially shows a non-vanishing value for small wavelengths and at the center of the Brillouin zone. For usual semiconductors it is in the range of 10 –100 meV. For example, in the case of gallium arsenide (GaAs) it is about 36 meV whereas the polar wide-gap semiconductors zinc oxide (ZnO) and gallium nitride (GaN) offer a much larger optical phonon energy of 72 meV and 93 meV, respectively. Cadmium sulfide (CdS) and zinc sulfide (ZnS) show intermediate energies of 38 meV and 44 meV.

Carrier–phonon interaction

Similar to the light field, phonons also interact with the entire charge-carrier system. The electron–phonon interaction [102] arises due to the attractive potential caused by the ions, i.e., the electrostatic Coulomb potential. The electron–phonon coupling is constructed from the change $\Delta V_{\mathrm{ion}}(\mathbf{r}) = V_{\mathrm{ion}}(\mathbf{r}) - V^0_{\mathrm{ion}}(\mathbf{r})$ of the potential compared to the lattice-periodic potential $V^0_{\mathrm{ion}}(\mathbf{r})$ in equilibrium configuration of the ion positions. To develop the electron–phonon interaction Hamiltonian in second quantization, $\Delta V_{\mathrm{ion}}(\mathbf{r})$ must be evaluated microscopically. If the ions are located at their equilibrium positions, the potential equals the unperturbed potential of the perfect lattice introduced in Hamiltonian (2.1). When phonons are present, the electrons do not move in a perfect periodic potential anymore but in an effective potential of the displaced ions. For weak perturbation, only the lowest non-vanishing order of $\Delta V_{\mathrm{ion}}(\mathbf{r})$ is included leading to

$$\Delta V_{\mathrm{ion}} = \sum_{\mathbf{R}} \sum_{j} \nabla V_j \left(\mathbf{r} - \mathbf{S}^0_j(\mathbf{R}) \right) \cdot \hat{\boldsymbol{\kappa}}_j (\mathbf{R}) \tag{2.14}$$

which additionally enters the matter part of Eq. (2.10). After a lengthy but straightforward derivation, similar to the quantization of the light–matter system, the Hamiltonian is cast into the form

$$\hat{\boldsymbol{H}}_{\mathbf{el\text{–}vib}} = \sum_{\boldsymbol{\lambda},\boldsymbol{\lambda'}} \sum_{\mathbf{k},\mathbf{p_{3D}}} \hbar\boldsymbol{\Omega}_{\mathbf{p_{3D}}}\, \boldsymbol{g}^{\boldsymbol{\lambda},\boldsymbol{\lambda'}}_{\mathbf{p_{3D}}} \left(\hat{\boldsymbol{D}}^{\dagger}_{-\mathbf{p_{3D}}} + \hat{\boldsymbol{D}}_{\mathbf{p_{3D}}} \right) \hat{\boldsymbol{a}}^{\dagger}_{\boldsymbol{\lambda},\mathbf{k}} \hat{\boldsymbol{a}}_{\boldsymbol{\lambda'},\mathbf{k-p}} \tag{2.15}$$

Hamiltonian of the carrier–phonon coupling

with phonon energy $\hbar\Omega_{\mathbf{p}_{3\mathrm{D}}}$ and the phonon-matrix element $g^{\lambda,\lambda'}_{\mathbf{p}_{3\mathrm{D}}}$. In the most general case, this coupling element depends on two band indices. Considering that typical phonon energies are about two orders of magnitude smaller than usual band-gap energies of semiconductors, however, the analysis may be restricted to pure intraband contributions, i.e., $\lambda = \lambda'$. The strength of the phonon interaction in a semiconductor is then defined by the phonon-matrix element which acts as a weighting of the coupled lattice-vibration–carrier system.

Within the scope of this work, the related investigations are performed exclusively with LO phonons. Therefore, acoustic phonons will not be discussed further. The different interaction mechanisms—Fröhlich interac-

tion and deformation-potential scattering—play a substantial role for the investigations presented in Paper [III] and will be discussed in more detail in Chap. 4.

2.2 Cluster-expansion representation

In this work, the Heisenberg equation-of-motion method [1] is adopted to develop the quantum-mechanical operator dynamics of the interacting many-body system. Here, different expectation values of all kinds of mixed Bosonic and Fermionic operators need to be evaluated consistently. Due to the many-body interaction, N-particle expectation values couple to $(N+1)$-particle expectation values, which is often referred to as the *hierarchy problem* [1, 2, 103]. This coupling offers direct access to calculate the entire and complex interaction mechanisms between, e.g., electrons, photons, and phonons. The infinite number of coupled equations renders it impossible to completely calculate the coupling mechanisms and correlations between all particles in the entire system. Solutions beyond the triplet level are numerically very demanding and limited by modern computing capacity and clock speed. Recently emerged techniques harnessing graphics-processing units (GPUs) to highly parallelize arithmetic operations, however, have promise to provide tremendous additional processing power for a variety of technical and scientific high-performance computing applications [104–106]. Yet, to consider all physical characteristics correctly, the arising hierarchy must be truncated consistently. A very beneficial method is the so-called *cluster-expansion approach* [2, 32–38] where a N-particle expectation value is methodically classified and prioritized into clusters with maximal order of N. With increasing complexity, the clusters contain independent single particles (singlets), coupled pairs (doublets), three-particle terms (triplets), contributions of four-particle interactions (quadruplets), as well as higher-order correlations. The approach consistently accounts for the completely (anti)symmetrized states of Bosonic (Fermionic) systems and limits the problem to a certain level of coupled clusters. In general, coupled clusters of a specific order act as sources for higher-order correlations. Once the current system configuration is accurately described by the particular cluster level, all higher clusters may be omitted. Actual computations show that clusters up to the doublet or triplet level accurately describe the properties of interacting many-body systems and quantum-optical correlations [107, 108]. The fast convergence of the expansion approach as function of the clusters corroborates the advantages of this method.

2.2.1 Quantum-dynamical hierarchy problem of expectation values

To express the temporal evolution of an arbitrary operator $\hat{\mathcal{O}}$ in an interacting many-body system, the Heisenberg equation-of-motion technique turns out to be a very useful tool. Here, the total Hamiltonian for the consistent description of the system is inserted into the Heisenberg equation of motion

$$\mathrm{i}\hbar\frac{\partial}{\partial t}\hat{\mathcal{O}} = \left[\hat{\mathcal{O}}, \hat{H}\right]_- = \hat{\mathcal{O}}\hat{H} - \hat{H}\hat{\mathcal{O}}\,. \tag{2.16}$$

The dynamics of $\hat{\mathcal{O}}$ is then obtained by evaluating the commutator between the operator and the Hamiltonian. Depending on the interaction mechanisms and the number of particles contained in the system, the derivation of the complete operator dynamics may be very easy, or can be very cumbersome. For the results presented in this thesis it is sufficient to include the Hamiltonians brought to attention in the preceding sections. All measurable expectation values of the many-body system can be expressed by an N-particle expectation value

$$\left\langle \hat{N} \right\rangle \equiv \left\langle \hat{a}^\dagger_{\lambda_N,\mathbf{k}_N} \ldots \hat{a}^\dagger_{\lambda_1,\mathbf{k}_1} \hat{a}_{\nu_1,\mathbf{l}_1} \ldots \hat{a}_{\nu_N,\mathbf{l}_N} \right\rangle \tag{2.17}$$

with $2N$ normally ordered Fermionic creation and annihilation operators. Formally, a single Boson operator contains a pair of Fermion operators. In general, a generic quantity is called *two-point quantity* if it contains two Fermion operators such that a pair of Fermion operators corresponds to a single-particle operator. Due to this connection, the Bosonic operators of, e.g., photons and phonons can easily be classified via clusters in the same way as the pure carrier expectation values [2]. The dynamics of a given N-particle operator is accessible

by evaluating Eq. (2.16) with the total Hamiltonian. This leads to contributions that involve the same order, i.e., without hierarchy problem, as the quantity for which the dynamics is derived, but also interaction contributions with hierarchical coupling to higher-order correlations. This infinite coupling to higher-order expectation values is caused by the many-body interaction and referred to as the hierarchy problem. This interminable hierarchy is schematically expressed via

$$\mathrm{i}\hbar\frac{\partial}{\partial t}\left\langle\hat{N}\right\rangle = T\left[\left\langle\hat{N}\right\rangle\right] + V\left[\left\langle\hat{N}+1\right\rangle\right] \tag{2.18}$$

where functional T contains those contributions which are of the same order as the left-hand side while the second term contains coupling to higher-order contributions.

2.2.2 Classification of correlations

Even though the hierarchy problem seems to display a relatively simple structure, it is the crucial point which complicates the calculations of interacting many-body systems. Theoretical investigations that offer an exact solution are only possible in very limited cases. Therefore, the hierarchy must be truncated at a certain level of complexity. Over the last decades, many different approaches have been developed [2]. Within the scope of the cluster expansion, equations of the correlation dynamics are solved instead of formulating equations for approximated wavefunctions or density matrices. Being a variant of the coupled-cluster approach [2, 107], the cluster expansion constitutes a description where the expectation values offer *direct* access to the operator dynamics and represent a very clear and descriptive structure, which involves a physically meaningful interpretation. The classification into particle clusters thus offers a great tool to develop efficient approximation schemes.

In the perspective of quantum mechanics, already the calculation of the second-simplest atom to model, namely helium following the hydrogen atom, shows that finding an exact solution of the Schrödinger equation for more than two electrons is very unpromising. For the description of interacting electron systems, the *Hartree–Fock approximation* (HF) [1, 80, 88] turned out to be a very beneficial approach. Here, an arbitrarily chosen electron is described in the potential of the nucleus and additionally experiences an effective potential of the remaining electrons. Therefore, this approach is also referred to as the *self-consistent field method* (SCF) because the particle is subjected to the mean field created by all other particles where every electron is described by a single-particle Schrödinger equation. The potential within these Schrödinger equations depends on the wavefunctions of the remaining electrons and must follow a self-consistent solution ansatz.

The Hartree–Fock method is mainly used for ab-initio calculations of the electronic Schrödinger equation of atoms and molecules in physics and quantum chemistry. The complete N-particle system is described by a single Slater determinant, i.e., a completely antisymmetrized product of single-particle wavefunctions

$$\left\langle\hat{N}\right\rangle_{\mathrm{S}} = \left\langle\hat{N}\right\rangle_{\mathrm{HF}} = \langle\hat{a}^\dagger_{\mathbf{k}_N}\ldots\hat{a}^\dagger_{\mathbf{k}_1}\hat{a}_{\mathbf{l}_1}\ldots\hat{a}_{\mathbf{l}_N}\rangle_{\mathrm{S}} = \sum_\pi(-1)^\pi\prod_{i=1}^{N}\left\langle\hat{a}^\dagger_{\mathbf{k}_i}\hat{a}_{\mathbf{l}_{\pi[i]}}\right\rangle = \det\left[\mathbf{N}\right] \tag{2.19}$$

which are chosen arbitrarily but orthonormalized. Here, the index S denotes the singlet contribution, i.e., the first factorization level of the cluster-expansion scheme. The permutation π ensures correct antisymmetrization and operates on the group of the coordinates $\{\mathbf{l}_1\ldots\mathbf{l}_N\}$ and with this builds the group the permutations $\{\mathbf{l}_j\}_{j=1}^{N!}$ of all $N!$ possible combinations. The Hartree–Fock method already yields very good results for simple electron systems where the single-particle properties prevail. Such systems are called *uncorrelated* whereas systems containing inseparable electron states are called *correlated* and need further treatment beyond Hartree–Fock. The correlated part of the expectation value is then denoted as $\Delta\langle\cdots\rangle$. For example, a two-particle expectation value is easily evaluated to $\langle\hat{a}^\dagger_{\mathbf{k}_2}\hat{a}^\dagger_{\mathbf{k}_1}\hat{a}_{\mathbf{l}_1}\hat{a}_{\mathbf{l}_2}\rangle = [\langle\hat{a}^\dagger_{\mathbf{k}_2}\hat{a}_{\mathbf{l}_2}\rangle\langle\hat{a}^\dagger_{\mathbf{k}_1}\hat{a}_{\mathbf{l}_1}\rangle - \langle\hat{a}^\dagger_{\mathbf{k}_2}\hat{a}_{\mathbf{l}_1}\rangle\langle\hat{a}^\dagger_{\mathbf{k}_1}\hat{a}_{\mathbf{l}_2}\rangle] + \Delta\langle\hat{a}^\dagger_{\mathbf{k}_2}\hat{a}^\dagger_{\mathbf{k}_1}\hat{a}_{\mathbf{l}_1}\hat{a}_{\mathbf{l}_2}\rangle$ where the expansion scheme (2.19) leads to the singlet part, i.e., the terms in the brackets. For completeness, the correlated part Δ is mentioned as well but can be neglected in case of the Hartree–Fock approximation. The build-up of the remaining many-particle contributions and correlations is structured very systematically. Beyond Hartree–Fock, genuine correlations appear with the two-particle expectation values (doublets). All other

N-particle clusters follow recursively such that the two-, three, up to N-particle clusters can be written as [2]

$$\langle \mathbf{2} \rangle = [\langle \mathbf{2} \rangle]_{\mathbf{S}} + \boldsymbol{\Delta} \langle \mathbf{2} \rangle \ , \tag{2.20}$$

$$\langle \mathbf{3} \rangle = [\langle \mathbf{3} \rangle]_{\mathbf{S}} + \langle \mathbf{1} \rangle \boldsymbol{\Delta} \langle \mathbf{2} \rangle + \boldsymbol{\Delta} \langle \mathbf{3} \rangle \ , \tag{2.21}$$

$$\begin{aligned} \langle \boldsymbol{N} \rangle = [\langle \boldsymbol{N} \rangle]_{\mathbf{S}} &+ [\langle \boldsymbol{N-2} \rangle_{\mathbf{S}} \boldsymbol{\Delta} \langle \mathbf{2} \rangle + \langle \boldsymbol{N-4} \rangle_{\mathbf{S}} \boldsymbol{\Delta} \langle \mathbf{2} \rangle \boldsymbol{\Delta} \langle \mathbf{2} \rangle]_{\mathbf{D}} \\ &+ [\langle \boldsymbol{N-3} \rangle_{\mathbf{S}} \boldsymbol{\Delta} \langle \mathbf{3} \rangle + \langle \boldsymbol{N-5} \rangle_{\mathbf{S}} \boldsymbol{\Delta} \langle \mathbf{3} \rangle \boldsymbol{\Delta} \langle \mathbf{2} \rangle \dots]_{\mathbf{T}} \\ &+ \sum_{\boldsymbol{J=4}}^{\boldsymbol{N-1}} [\langle \boldsymbol{N} \rangle]_{\boldsymbol{J}} + \boldsymbol{\Delta} \langle \boldsymbol{N} \rangle \ . \end{aligned} \tag{2.22}$$

***N*-particle cluster representation**

These clusters are separated into singlets (S), doublets (D), triplets (T), and higher-order particle correlations. The complete system is described by a sum of all classified clusters properly accounting for the mathematical requirements of Fermionic and Bosonic operators. In doing so, each N-particle expectation value contains products of all possibilities of factorized subclusters, i.e., clusters not exceeding the respective particle number N. The correlated part is denoted as $\Delta\langle N \rangle$. A recursive identification allows for the systematical formulation of the quantum dynamics of correlated clusters. Even though this does not directly remove the hierarchical coupling, a representation in terms of clusters reveals the nature of correlations: In contrast to the expectation-value representation (2.18) where, in general, all particle classes are nonvanishing, correlations are generated sequentially [109] by many-body and quantum-optical interactions such that the largest number of contributing clusters usually is considerably smaller than the largest particle number N [2]. This allows for the omission of the hierarchical-coupling terms, thus leading to a closed set of equations. Consult Ref. [2] for a more detailed approach. A wide variety of semiconductor properties can be treated within the singlet–doublet approximation of the cluster-expansion approach. Among other things, phonon-assisted effects in semiconductors are discussed in the following chapters. This introduces additional (Bosonic) operators necessitating the inclusion of three- and four-particle correlations based on Eq. (2.22).

2.3 Semiconductor luminescence equations

After optical excitation of an initially unexcited semiconductor, microscopic polarizations $P_{\mathbf{k}} = \langle \hat{a}^\dagger_{v,\mathbf{k}} \hat{a}_{c,\mathbf{k}} \rangle$ as well as carrier densities $f^{\mathrm{e}}_{\mathbf{k}} = \langle \hat{a}^\dagger_{c,\mathbf{k}} \hat{a}_{c,\mathbf{k}} \rangle$ for electrons in the conduction band and $f^{\mathrm{h}}_{\mathbf{k}} = 1 - \langle \hat{a}^\dagger_{v,\mathbf{k}} \hat{a}_{v,\mathbf{k}} \rangle$ for holes, i.e., valence-band vacancies, in the valence band build up. For low-excitation conditions, the optical polarization grows commensurately with the carrier densities as long as the exciting pulse is present. Due to microscopic scattering processes, however, the microscopic polarizations exist only transiently and decay on a picosecond timescale while the quasi-stationary excitation remains in the system in the form of carrier densities. At this stage, it is convenient to separate the arising quantities into coherent and incoherent: While coherent quantities decay on the timescale of the optical polarization, incoherent quantities remain long after the exciting pulse. This directly identifies $P_{\mathbf{k}}$ as coherent while $f^{\mathrm{e/h}}_{\mathbf{k}}$ describe the simplest form of incoherent quantities. On the singlet level of the cluster-expansion approach, the *semiconductor Bloch equations* (SBEs) [1, 110] connect the coherent amplitudes $\langle \hat{B}^\dagger_{\mathbf{q}_{3\mathrm{D}}} \rangle$ and $\langle \hat{B}_{\mathbf{q}_{3\mathrm{D}}} \rangle$ of the light field to the polarizations and carrier densities.

The studies presented in this thesis concentrate on the investigation of how truly bound excitons [24, 29, 37, 111–120], i.e., strongly correlated two-particle electron–hole-pair states [2], affect the semiconductor emission when interacting with phonons and terahertz fields. Since the optical polarization is fundamentally a single-particle quantity, it cannot describe atom-like electron–hole binding. The decay of the coherent polarizations may, however, yield simultaneous creation of exciton correlations via the so-called *polarization-to-population*

conversion initiated by scattering processes. For a detailed description of exciton-formation processes, see Refs. [24, 29, 121–124]. Yet, as a result of the long-lasting carrier densities, the optically generated semiconductor excitation can recombine spontaneously due to vacuum-field fluctuations [37]. To describe light emission in the incoherent regime where all coherent quantities $\langle \hat{B}^{(\dagger)}_{\mathbf{q}_{3\mathrm{D}}} \rangle$ and $P_{\mathbf{k}}$ vanish, the quantum nature of the light field must be incorporated. Applying the Heisenberg equation-of-motion method and truncating the arising hierarchy via the cluster-expansion approach, eventually shows that the incoherent light emission stems from photon-number-like correlations

$$\mathrm{i}\hbar\frac{\partial}{\partial t}\Delta\langle \hat{B}^{\dagger}_{\mathbf{q}_{3\mathrm{D}}}\hat{B}_{\mathbf{q},\,q'_{\perp}}\rangle = (\hbar\omega_{\mathbf{q},\,q'_{\perp}} - \hbar\omega_{\mathbf{q}_{3\mathrm{D}}})\Delta\langle \hat{B}^{\dagger}_{\mathbf{q}_{3\mathrm{D}}}\hat{B}_{\mathbf{q},\,q'_{\perp}}\rangle + \mathrm{i}\sum_{\mathbf{k}}\left[\mathcal{F}^{\star}_{\mathbf{q},\,q'_{\perp}}\Pi_{\mathbf{k},\mathbf{q}_{3\mathrm{D}}} + \mathcal{F}_{\mathbf{q}_{3\mathrm{D}}}\Pi^{\star}_{\mathbf{k},\mathbf{q},q'_{\perp}}\right] \tag{2.23}$$

which are coupled to *photon-assisted polarizations* $\Pi_{\mathbf{k},\mathbf{q}_{3\mathrm{D}}} \equiv \Delta\langle \hat{B}^{\dagger}_{\mathbf{q}_{3\mathrm{D}}}\hat{a}^{\dagger}_{v,\,\mathbf{k}-\mathbf{q}_{\mathrm{h}}}\hat{a}_{c,\,\mathbf{k}+\mathbf{q}_{\mathrm{e}}}\rangle$ where the photon momentum $\hbar\mathbf{q}$ is divided among the electron and hole according to $\mathbf{q}_{\mathrm{e}} = \frac{m_{\mathrm{e}}}{m_{\mathrm{e}}+m_{\mathrm{h}}}\mathbf{q}$ and $\mathbf{q}_{\mathrm{h}} = \frac{m_{\mathrm{h}}}{m_{\mathrm{e}}+m_{\mathrm{h}}}\mathbf{q}$. This defines the photon flux

$$I_{\mathrm{PL}}(\omega_{\mathbf{q}_{3\mathrm{D}}}) = \frac{\partial}{\partial t}\Delta\langle \hat{B}^{\dagger}_{\mathbf{q}_{3\mathrm{D}}}\hat{B}_{\mathbf{q}_{3\mathrm{D}}}\rangle = \frac{2}{\hbar}\,\mathrm{Re}\left[\sum_{\mathbf{k}}\mathcal{F}^{\star}_{\mathbf{q}_{3\mathrm{D}}}\Pi_{\mathbf{k},\mathbf{q}_{3\mathrm{D}}}\right] \tag{2.24}$$

which is proportional to the photoluminescence spectrum for quasi-stationary emission [81]. The photon-assisted polarizations describe correlations where an electron recombines with a hole under simultaneous emission of a photon. The corresponding equation of motion reads

$$\begin{aligned}\mathrm{i}\hbar\frac{\partial}{\partial t}\,\Pi_{\mathbf{k},\mathbf{q}_{3\mathrm{D}}} &= \left(\epsilon^{\mu}_{\mathbf{k}} + \epsilon^{M}_{\mathbf{q}} - \Sigma_{\mathbf{k},\mathbf{q}} - \hbar\omega_{\mathbf{q}_{3\mathrm{D}}}\right)\Pi_{\mathbf{k},\mathbf{q}_{3\mathrm{D}}} + \Pi^{\mathrm{phon}}_{\mathbf{k},\mathbf{q}_{3\mathrm{D}}} + T[\Pi] \\ &\quad - \left(1 - f^{\mathrm{e}}_{\mathbf{k}+\mathbf{q}_{\mathrm{e}}} - f^{\mathrm{h}}_{\mathbf{k}-\mathbf{q}_{\mathrm{h}}}\right)\left[\sum_{\mathbf{k}'}V_{\mathbf{k}-\mathbf{k}'}\,\Pi_{\mathbf{k}',\mathbf{q}_{3\mathrm{D}}} + \Delta\Omega_{\mathbf{q}_{3\mathrm{D}}}\right] + \Omega^{\mathrm{SE}}_{\mathbf{k},\mathbf{q}_{3\mathrm{D}}}\,.\end{aligned} \tag{2.25}$$

The free-propagation parts of Eqs. (2.23) and (2.25) show that both quantities rotate on an energy scale much smaller than the band-gap energy of typical semiconductors. In analogy to incoherent quantities like the carrier densities, this feature renders these dynamics to be incoherent – in contrast to, e.g., the optical polarizations in the SBEs. In many relevant semiconductors, the optically coupled bands are nearly parabolic. Then, the sum of the single-particle energies $\epsilon^{\mathrm{e}}_{\mathbf{k}+\mathbf{q}_{\mathrm{e}}} + \epsilon^{\mathrm{h}}_{\mathbf{k}-\mathbf{q}_{\mathrm{h}}} = \epsilon^{\mu}_{\mathbf{k}} + \epsilon^{M}_{\mathbf{q}}$ can be decomposed into $\epsilon^{\mu}_{\mathbf{k}} = \frac{\hbar^2\mathbf{k}^2}{2\,\mu}$ and $\epsilon^{M}_{\mathbf{q}} = \frac{\hbar^2\mathbf{q}^2}{2\,M}$ where $\mu = \left(\frac{1}{m_{\mathrm{e}}} + \frac{1}{m_{\mathrm{h}}}\right)^{-1}$ is the reduced mass and $M = m_{\mathrm{e}} + m_{\mathrm{h}}$ is the total mass. These energy terms appear in Eq. (2.25) together with the Coulomb renormalization $\Sigma_{\mathbf{k},\mathbf{q}} \equiv \sum_{\mathbf{k}'} V_{\mathbf{k}-\mathbf{k}'}\left(f^{\mathrm{e}}_{\mathbf{k}'+\mathbf{q}_{\mathrm{e}}} + f^{\mathrm{h}}_{\mathbf{k}'-\mathbf{q}_{\mathrm{h}}}\right)$ whenever carriers are excited in the system. Equations (2.23)–(2.25) constitute the principal structure of the *semiconductor luminescence equations* (SLEs) [2, 24, 54, 81] where the explicit Coulomb sum yields excitonic resonances in the luminescence or photoluminescence (PL). The phonon-assisted triplets $\Pi^{\mathrm{phon}}_{\mathbf{k},\mathbf{q}_{3\mathrm{D}}}$ are included only symbolically at this stage and will be discussed in more detail in Chap. 3. The triplet scattering is modeled either microscopically or at the level of a dephasing approximation via $T[\Pi] = -\mathrm{i}\gamma_0\,\Pi_{\mathbf{k},\mathbf{q}_{3\mathrm{D}}}$ defined by γ_0. When a cavity is present, the stimulated feedback of light

$$\Delta\Omega_{\mathbf{q}_{3\mathrm{D}}} = \mathrm{i}\sum_{q'_{\perp}}\mathcal{F}_{\mathbf{q},\,q'_{\perp}}\Delta\langle \hat{B}^{\dagger}_{\mathbf{q}_{3\mathrm{D}}}\hat{B}_{\mathbf{q},\,q'_{\perp}}\rangle \tag{2.26}$$

also enters which yields the coupling between the different photon modes via Eq. (2.23). This contribution especially produces the well-known normal-mode splitting [52–58] of excitonic resonances in high-quality cavities, which is investigated in Chap. 3. The spontaneous emission itself is initiated by

$$\Omega^{\mathrm{SE}}_{\mathbf{k},\mathbf{q}_{3\mathrm{D}}} = \mathrm{i}\mathcal{F}_{\mathbf{q}_{3\mathrm{D}}}\left(f^{\mathrm{e}}_{\mathbf{k}+\mathbf{q}_{\mathrm{e}}}f^{\mathrm{h}}_{\mathbf{k}-\mathbf{q}_{\mathrm{h}}} + \sum_{\mathbf{k}'}c^{\mathbf{q},\mathbf{k},\mathbf{k}'}_{\mathrm{X}}\right) \tag{2.27}$$

that is non-vanishing as soon as electrons and holes are present or when the system contains exciton correlations $c_{\mathrm{X}}^{\mathbf{q},\mathbf{k},\mathbf{k}'} = \Delta\langle \hat{a}^{\dagger}_{c,\,\mathbf{k}'+\mathbf{q}_{\mathrm{e}}} \hat{a}^{\dagger}_{v,\,\mathbf{k}-\mathbf{q}_{\mathrm{h}}} \hat{a}_{c,\,\mathbf{k}+\mathbf{q}_{\mathrm{e}}} \hat{a}_{v,\,\mathbf{k}'-\mathbf{q}_{\mathrm{h}}} \rangle$. Typically, the carrier distributions reach their quasi-equilibrium form very rapidly via Coulomb and phonon scattering. In comparison, the spontaneous emission proceeds slowly on a nanosecond time scale such that both f^{λ} and c_{X} can be considered quasi-stationary when momentary PL spectra are analyzed. The investigations in Chaps. 3 and 4 will benefit from this feature. The spontaneous-emission source (2.27) discloses the fact that both electron–hole plasma and exciton correlations may initiate photon-assisted electron–hole recombination [51, 120, 121, 125–127]. As expected from the quantum nature of light, both sources are proportional to the vacuum-field amplitude within $\mathcal{F}_{\mathbf{q}_{3\mathrm{D}}}$, showing that spontaneous emission purely arises from the inherent quantum fluctuations of light. However, both sources exhibit substantial differences in particle selectivity: The momentum-conservation aspects of Eqs. (2.25) and (2.27) show that all electron–hole states whose momenta match the photon momentum, i.e., $\hbar(\mathbf{k}_{\mathrm{e}} - \mathbf{k}_{\mathrm{h}}) = \hbar\mathbf{q}$, may contribute to the emission. Moreover, the radiative recombination only leads to slow changes of carrier distributions on a nanosecond timescale. In contrast, only optically *bright excitons* with momenta within the radiative cone, $\hbar\mathbf{q} \simeq \mathbf{0}$, may contribute to the emission in comparison to (nonradiative) *dark excitons* where $\hbar|\mathbf{q}| > \hbar q_{\mathrm{opt}}$. Typically, $q_{\mathrm{opt}} \lesssim {}^{0.1}/_{a_0}$. This is based on the fact that photons in the vicinity of the band edge have only very small momenta. This momentum selectivity gives rise to spontaneous emission with high probability in direction perpendicular to the quantum-well plane and usually initiates hole burning leading to strongly non-thermal exciton distributions in the emission process [29, 66, 120]. The exciton correlations in Eq. (2.27) follow the dynamics [2, 24, 29, 67]

$$\begin{aligned} \mathrm{i}\hbar\frac{\partial}{\partial t} c_{\mathrm{X}}^{\mathbf{q},\mathbf{k},\mathbf{k}'} &= \left(\epsilon^{\mu}_{\mathbf{k}} - \epsilon^{\mu}_{\mathbf{k}'} - \Sigma_{\mathbf{k},\mathbf{q}} + \Sigma_{\mathbf{k}',\mathbf{q}}\right) c_{\mathrm{X}}^{\mathbf{q},\mathbf{k},\mathbf{k}'} + S_{\mathrm{X}}^{\mathbf{q},\mathbf{k},\mathbf{k}'} + D_{\mathrm{QED}}^{\mathbf{q},\mathbf{k},\mathbf{k}'} + c_{\mathrm{X,\,THz}}^{\mathbf{q},\mathbf{k},\mathbf{k}'} + c_{\mathrm{X,\,mag}}^{\mathbf{q},\mathbf{k},\mathbf{k}'} + D_{\mathrm{X,\,rest}}^{\mathbf{q},\mathbf{k},\mathbf{k}'} + T_{\mathrm{X}}^{\mathbf{q},\mathbf{k},\mathbf{k}'} \\ &\quad + \Big(1 - f^{\mathrm{e}}_{\mathbf{k}'+\mathbf{q}_{\mathrm{e}}} - f^{\mathrm{h}}_{\mathbf{k}'-\mathbf{q}_{\mathrm{h}}}\Big) \sum_{\mathbf{l}} V_{\mathbf{l}-\mathbf{k}'}\, c_{\mathrm{X}}^{\mathbf{q},\mathbf{k},\mathbf{l}} - \Big(1 - f^{\mathrm{e}}_{\mathbf{k}+\mathbf{q}_{\mathrm{e}}} - f^{\mathrm{h}}_{\mathbf{k}-\mathbf{q}_{\mathrm{h}}}\Big) \sum_{\mathbf{l}} V_{\mathbf{l}-\mathbf{k}}\, c_{\mathrm{X}}^{\mathbf{q},\mathbf{l},\mathbf{k}'} \end{aligned} \tag{2.28}$$

where $S_{\mathrm{X}}^{\mathbf{q},\mathbf{k},\mathbf{k}'} = V_{\mathbf{k}-\mathbf{k}'}\big[f^{\mathrm{e}}_{\mathbf{k}+\mathbf{q}_{\mathrm{e}}} f^{\mathrm{h}}_{\mathbf{k}-\mathbf{q}_{\mathrm{h}}} (1 - f^{\mathrm{e}}_{\mathbf{k}'+\mathbf{q}_{\mathrm{e}}})(1 - f^{\mathrm{h}}_{\mathbf{k}'-\mathbf{q}_{\mathrm{h}}}) - (1 - f^{\mathrm{e}}_{\mathbf{k}+\mathbf{q}_{\mathrm{e}}})(1 - f^{\mathrm{h}}_{\mathbf{k}-\mathbf{q}_{\mathrm{h}}}) f^{\mathrm{e}}_{\mathbf{k}'+\mathbf{q}_{\mathrm{e}}} f^{\mathrm{h}}_{\mathbf{k}'-\mathbf{q}_{\mathrm{h}}}\big] + S_{\mathrm{X}}^{\mathrm{coh}}$ describes Boltzmann-type in- and out-scattering of carriers and acts as a source term for the exciton-correlation dynamics enabling the creation of excitonic correlations as soon as carriers are present. The term $S_{\mathrm{X}}^{\mathrm{coh}}$ contains scattering among densities and the coherent polarizations. The explicit forms are given in Ref. [24]. For dilute densities, the *main-sum approximation* [29] may be applied to reduce the full structure [24] of the incoherent Coulomb-induced doublet correlations to the form presented by Eq. (2.28). The most important part is given by the second line which denotes the main-sum terms. These lead to the possibility of describing the formation of truly bound excitons. As a result of spontaneous recombination, the doublet contributions of the light–matter interaction lead to the source terms

$$D_{\mathrm{QED}}^{\mathbf{q},\mathbf{k},\mathbf{k}'} = -\mathrm{i}\Big(1 - f^{\mathrm{e}}_{\mathbf{k}'+\mathbf{q}_{\mathrm{e}}} - f^{\mathrm{h}}_{\mathbf{k}'-\mathbf{q}_{\mathrm{h}}}\Big) \sum_{q_{\perp}} \mathcal{F}^{\star}_{\mathbf{q}_{3\mathrm{D}}} \Pi_{\mathbf{k},\mathbf{q}_{3\mathrm{D}}} - \mathrm{i}\Big(1 - f^{\mathrm{e}}_{\mathbf{k}+\mathbf{q}_{\mathrm{e}}} - f^{\mathrm{h}}_{\mathbf{k}-\mathbf{q}_{\mathrm{h}}}\Big) \sum_{q_{\perp}} \mathcal{F}_{\mathbf{q}_{3\mathrm{D}}} \Pi^{\star}_{\mathbf{k}',\mathbf{q}_{3\mathrm{D}}} \tag{2.29}$$

showing again the conservation of the center-of-mass momentum $\hbar\mathbf{q}$ in the emission process. The terahertz interaction (2.12) adds a new term to the exciton correlations,

$$c_{\mathrm{X,\,THz}}^{\mathbf{q},\mathbf{k},\mathbf{k}'} = -\mathbf{j}_{\mathbf{k}-\mathbf{k}'} \cdot \mathbf{A}_{\mathrm{THz}}(t)\, c_{\mathrm{X}}^{\mathbf{q},\mathbf{k},\mathbf{k}'}\,, \tag{2.30}$$

where the current-matrix element $\mathbf{j}_{\mathbf{k}} \equiv \mathbf{j}_{\mathrm{e},\mathbf{k}} + \mathbf{j}_{\mathrm{h},\mathbf{k}} = -|e|\hbar\mathbf{k}/\mu$ defines coupling to the terahertz field $\mathbf{A}_{\mathrm{THz}}(t)$. Since it couples purely to four-point correlations, the terahertz response of incoherent excitations is suitable to directly detect correlations of electron–hole pairs in the semiconductor system [66–71, 120, 128–139]. The contribution $c_{\mathrm{X,\,mag}}^{\mathbf{q},\mathbf{k},\mathbf{k}'}$ includes possible magnetic-field effects which will be introduced in Secs. 5.1 and 5.1.2.

All remaining two-particle correlations are collected in $D_{\mathrm{X,\,rest}}^{\mathbf{q},\mathbf{k},\mathbf{k}'}$ and will be neglected because they describe microscopic scattering of a two-particle correlation with a singlet beyond the main-sum approximation. The exciton-correlation dynamics also show a hierarchical coupling to triplets $T_{\mathrm{X}}^{\mathbf{q},\mathbf{k},\mathbf{k}'}$. Within the scope of the investigation of phonon-assisted processes, the triplets are treated on the level of a dephasing approximation. In Chap. 5, however, this triplet scattering plays a major role for the scattering of exciton populations.

3

Enhancement of the phonon-sideband luminescence in semiconductor microcavities

The project presented in this chapter was the first project of my doctoral studies and represents an extension of what I have done as a diploma student. Preliminary investigations for this project are already presented in my diploma thesis [140] where I performed numerical studies on phonon absorption and emission of semiconductor quantum-well systems.

3.1 Phonon-assisted processes in the semiconductor luminescence

The semiconductor emission in the incoherent regime is essentially described by the semiconductor luminescence equations (SLEs) outlined in Sec. 2.3. Once the spontaneous-emission process is initiated, the Coulomb interaction couples photon-assisted polarizations (2.25) with different momenta, clearly demarcating the coupled many-body system from a two-level system. The resulting discrete states are typically labeled by the usual set of electronic states known from atomic physics starting with the most prominent, so-called $1s$*-exciton state*. As a result of Coulomb interaction, this state and the closest subsequent states are located below the band-gap energy of the respective sample [1, 124]. Owing to symmetry reasons, only s-like states lead to excitonic resonances in the photoluminescence (PL) spectrum. These may either stem from electron–hole plasma or genuine exciton populations [51, 121]. If the sample is embedded in a cavity [57, 90–92], the stimulated feedback of light (2.26) couples the photon modes and enables reabsorption of emitted light. The radiative environment drastically modifies the overall emission properties, e.g., yielding the Purcell effect [141], inhibited emission [142, 143], or the scenario of normal-mode coupling [52, 57, 144] where the eigenmode of a high-quality microcavity and the exciton resonance are strongly coupled. Fundamental principles of microcavities [92, 94] are introduced in Sec. 2.1.2 and applied to a special design in Sec. 3.3.

Beyond the singlet–doublet approximation generating the SLEs, the triplet contributions of the cluster-expansion approach not only involve Coulomb scattering but also induce coupling to phonon-induced correlations. These may lead to phonon-assisted luminescence where electrons and holes recombine under simultaneous emission or absorption of a phonon [47]. Thus, both Coulomb and phonon interactions contribute in optical experiments and significantly change the resulting spectra. In semiconductors featuring strong coupling of carriers and lattice vibrations, the participation of LO phonons gives rise to discrete, pronounced replicas, i.e., *phonon sidebands* (PSBs) [48, 49, 145], in the photoluminescence spectrum. Since LO-phonon energies are typically very large compared to $k_{\mathrm{B}}T$, only phonon emission [146] is possible while—even for increased temperatures—the amount of absorbable phonons plays a less significant role. Actually, pronounced phonon sidebands are mainly observed at the low-energy side of the $1s$-exciton resonance in most luminescence experiments [50]. Contrary to acoustic phonons, optical phonons show almost momentum-independent dispersion, thus leading to multiple replicas at distinct frequencies below the excitonic lines [48,49,147]. Then, a dominant $1s$-exciton peak, traditionally called the *zero-phonon line* (ZPL) [148–153], is accompanied by several PSBs at energies $E_{1s} - n\,\hbar\Omega$ where n is an integer denoting the order of the phonon sideband.

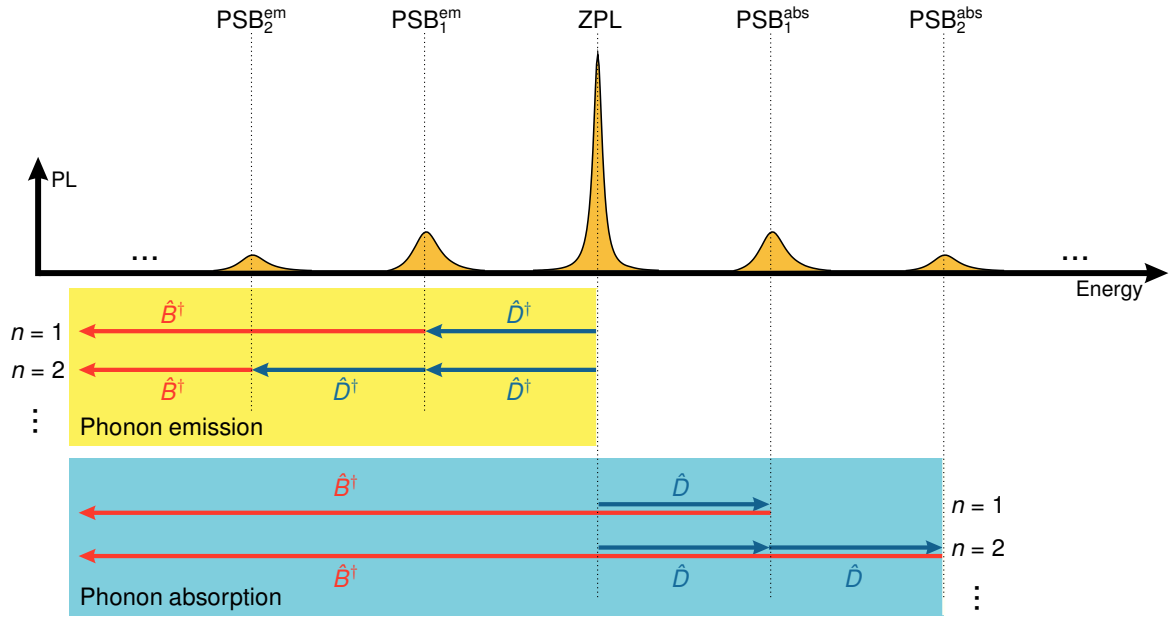

Figure 3.1 | Phonon sidebands in the semiconductor luminescence. Emission of a photon ($\hat{B}^\dagger$) under emission ($\hat{D}^\dagger$, yellow-shaded box) or absorption ($\hat{D}$, blue-shaded box) of phonons in the photoluminescence (PL). Phonon sideband n (PSB$_n$) is separated by n LO-phonon energies from the zero-phonon line (ZPL). Processes up to PSB$_2$ are shown. Owing to recombination of carriers with center-of-mass momenta $\hbar\mathbf{Q} > \mathbf{0}$, the PSBs show broad tails at the high-energy side. For clarity, only ZPL and PSBs but no continuum states are shown. Figure based on Refs. [47, 140].

Figure 3.1 presents a schematic PL spectrum featuring ZPL and equidistant-spaced PSBs up to the second phonon sideband. While phonon emission takes place on the low-energy side of the ZPL, sidebands resulting from phonon absorption are located at energies $E > E_{1s}$. For clarity, the presentation is restricted to the essential features and shows only ZPL and PSB contributions while neglecting higher excitonic and continuum states. The yellow- and blue-shaded boxes below the spectrum connect the operator dynamics to phonon emission (creation of a phonon via $\hat{D}^\dagger$) and phonon absorption (annihilation of a phonon via $\hat{D}$) processes. In the case of phonon emission, the energy of the n^{th} replica is lowered by $n\,\hbar\Omega$ with respect to the excitonic resonance, leading to the PSBs at the low-energy side of the ZPL. On the other hand, phonon absorption enhances the energy of the emitted photons which results in sidebands at the high-energy side of the ZPL. These sidebands, however, are located in the continuum of states and are very weak for the temperatures investigated here. As outlined before, this work concentrates on phonon emission exclusively, neglecting the influence of processes described by the blue-shaded box. Paper [I] and Refs. [47, 50] demonstrate that both the ZPL and the phonon replica do originate from different sources. Consequently, both electron–hole plasma and excitons contribute to the semiconductor response while the spectral shape does not depend on the emission source. Furthermore, the resulting sidebands may stem from free excitons or impurity-bound excitons. While free excitons show a pronounced center-of-mass (COM) dependence, impurity-bound excitons are uniformly distributed over all momenta [47, 48]. Owing to the momentum-conservation law, those excitons with center-of-mass momentum $\hbar|\mathbf{Q}| > \hbar Q_{\text{opt}}$ are not allowed to recombine radiatively. The interaction with LO phonons transfers the momentum to the phonon and allows the exciton to recombine. For elevated temperatures, the explicit center-of-mass dependence results in strongly asymmetric shapes of the sidebands accompanied with blue-shifted maxima. Since the photon momentum is vanishing with respect to typical electronic and vibrational momenta, the ZPL does not show this asymmetry. In the phonon-related projects of this thesis, we concentrate on thermally distributed free excitons following a Bose–Einstein distribution $\Delta N_{1s,\mathbf{Q}} = \Delta\langle \hat{X}^\dagger_{1s,\mathbf{Q}} \hat{X}_{1s,\mathbf{Q}} \rangle = f_{\text{BE}}(E^{\text{COM}}_{\mathbf{Q}})$ with respect to the center-of-mass energy $E^{\text{COM}}_{\mathbf{Q}} = \frac{\hbar^2\mathbf{Q}^2}{2M}$ with center-of-mass momentum $\hbar\mathbf{Q}$ and total mass $M = m_{\text{e}} + m_{\text{h}}$.

Zinc oxide (ZnO) is a direct II–VI semiconductor exhibiting a wide range of interesting properties. For example, its wide band gap allows optical transitions in the blue/ultraviolet range making this non-toxic compound semiconductor interesting for semiconductor-laser [154,155] and a myriad of industrial applications [156]. The large exciton binding energy of $E_\mathrm{b} = 60\,\mathrm{meV}$ [157–160] offers strong excitonic signatures in absorption and photoluminescence even at room temperature [161–163]. Furthermore, ZnO offers a relatively large LO-phonon energy of $E_\mathrm{LO} \equiv \hbar\Omega = 72\,\mathrm{meV}$ and energetically well-separated phonon-assisted resonances may be expected. While spatially large excitons are subject to the entire phonon background, spatially small excitons remain essentially unaffected by phonons. Owing to the fact that exciton binding energy and LO-phonon energy in ZnO are of similar orders of magnitude, an effective permittivity is needed for the correct numerical determination of the exciton binding energy [140, 164–167]. As a consequence of the high bond polarity, the formation of wurtzite structure is preferred to zincblende structure. This results in strong piezoelectric effects giving a distinct polar nature along the c-axis [0001] to ZnO [168]. This enables strong interaction between carriers and LO phonons and the observation of pronounced phonon sidebands in the spectrum [49, 147, 149, 152, 159, 163, 169–172]. ZnO shows the strongest polarity of all wurtzite-type semiconductors, besides the III–V compound GaN. However, the latter does not offer such an extraordinarily large exciton binding energy and contains toxic gallium. As a result of strong carrier–phonon coupling, it is interesting to study the effect of a microcavity which is tuned to be resonant with the PSB_1. The above-mentioned large LO-phonon energy and associated distinct separation of ZPL and PSB resonances makes ZnO an attractive candidate for such investigations.

As an extension of previous investigations on phonon-sideband luminescence of bare systems [47], the impact of a microcavity is investigated here. The following studies start with a fully dynamical solution by extending the SLEs by pertinent phonon-assisted contributions and numerically computing the steady-state luminescence. Since the inclusion of a cavity involves complex hierarchical coupling along the equations of motion, the analysis is restricted to the first replica of phonon emission, i.e., $\mathrm{PSB}_1^\mathrm{em}$ in Fig. 3.1. A nonperturbative steady-state solution in terms of an extended Elliott formula for arbitrary order of phonon sidebands has been presented earlier [48, 49]. However, this model does not include the possibility to describe the microcavity response. As a direct expansion to these previous works, a rigorous analytic model for phonon-assisted PL in a cavity is developed within the scope of the project presented here.

In this chapter, the basic features and the phonon-assisted contributions to the SLEs are introduced in Sec. 3.2. In Sec. 3.3, the impact of microcavities on PL spectra is explained and a possibility to tailor these cavities by freely tuning the resonance frequency is demonstrated. The numerical results are also presented here. Assuming enhanced cavity effects, the analytic model is developed in Sec. 3.4 and compared to the dynamical solutions.

3.2 Theory of phonon-sideband luminescence

The extension of the semiconductor luminescence equations (2.25) to describe phonon-assisted processes involves new operators $\hat{D}^\dagger_{\mathbf{p}_\mathrm{3D}}$ and $\hat{D}_{\mathbf{p}_\mathrm{3D}}$ which create or annihilate a phonon with momentum $\hbar\mathbf{p}_\mathrm{3D}$. The derivation follows analogous steps as before where the Heisenberg equation-of-motion method in combination with the cluster-expansion approach is utilized to derive and truncate the additional terms $\Pi^\mathrm{phon}_{\mathbf{k},\mathbf{q}_\mathrm{3D}}$ symbolically mentioned in Eq. (2.25). This procedure invokes the triplet level where three-operator quantities must be solved leading to phonon- and photon-assisted polarizations as well as phonon-assisted two-photon correlations. As specified by the structural nature of the cluster-expansion approach, these three-particle quantities couple to four-particle expectation values which need a special treatment. Before scrutinizing the dynamics responsible for the build-up of the PSB_1, the coupling of these new dynamics to the SLEs is examined. A straightforward derivation shows that the carrier–phonon interaction (2.15) introduces additional phonon-assisted contributions

$$\Pi^\mathrm{phon}_{\mathbf{k},\mathbf{q}_\mathrm{3D}} \equiv \hbar\Omega \sum_{\mathbf{p}_\mathrm{3D}} \left[g^c_{\mathbf{p}_\mathrm{3D}} \left(\Upsilon^\mathrm{em}_{\mathbf{k},\mathbf{q}_\mathrm{3D},\mathbf{p}_\mathrm{3D}} + \Upsilon^\mathrm{abs}_{\mathbf{k},\mathbf{q}_\mathrm{3D},\mathbf{p}_\mathrm{3D}} \right) - g^v_{\mathbf{p}_\mathrm{3D}} \left(\Upsilon^\mathrm{em}_{\mathbf{k}-\mathbf{p},\mathbf{q}_\mathrm{3D},\mathbf{p}_\mathrm{3D}} + \Upsilon^\mathrm{abs}_{\mathbf{k}-\mathbf{p},\mathbf{q}_\mathrm{3D},\mathbf{p}_\mathrm{3D}} \right) \right] \tag{3.1}$$

where the matrix element $g^\lambda_{\mathbf{p}_\mathrm{3D}}$ expresses the carrier–phonon coupling which may either be modeled via Fröhlich-type coupling [173–177], deformation potential scattering [176–180], or a mixture of both [47]. For

the investigations in this project, the coupling mechanism itself plays only a secondary role which is why the deformation potential is used. Here, owing to symmetry reasons [181], only $g^{v}_{\mathbf{p}_{3\mathrm{D}}}$ shows a (constant) finite value. The carrier–phonon coupling, however, is different for various materials and crucially affects the shape of the PL spectra, especially the ratio between higher-order sidebands. These effects are the central point of Chap. 4 which highlights the coupling mechanisms in more detail; see Sec. 4.1. Nevertheless, it may already be revealed that the choice of deformation-potential scattering at this point is correct and meaningful for ZnO.

For the description of phonon- and photon-assisted polarizations, the three-particle correlations $\Upsilon^{\mathrm{em}}_{\mathbf{k},\mathbf{q}_{3\mathrm{D}},\mathbf{p}_{3\mathrm{D}}} = \Delta\langle \hat{B}^{\dagger}_{\mathbf{q}_{3\mathrm{D}}} \hat{D}^{\dagger}_{\mathbf{p}_{3\mathrm{D}}} \hat{a}^{\dagger}_{v,\,\mathbf{k}-\mathbf{Q}_{\mathrm{h}}} \hat{a}_{c,\,\mathbf{k}+\mathbf{Q}_{\mathrm{e}}} \rangle$ for phonon emission and $\Upsilon^{\mathrm{abs}}_{\mathbf{k},\mathbf{q}_{3\mathrm{D}},\mathbf{p}_{3\mathrm{D}}} = \Delta\langle \hat{B}^{\dagger}_{\mathbf{q}_{3\mathrm{D}}} \hat{D}_{-\mathbf{p},\,p_{\perp}} \hat{a}^{\dagger}_{v,\,\mathbf{k}-\mathbf{Q}_{\mathrm{h}}} \hat{a}_{c,\,\mathbf{k}+\mathbf{Q}_{\mathrm{e}}} \rangle$ for phonon absorption must be solved. From these, only Υ^{em} generates photon emission that is below the excitonic states; in particular below the ZPL. The absorption dynamics Υ^{abs} follow analogously but are irrelevant for the PSBs studied here. Only if the role of phonon absorption, requiring $k_{\mathrm{B}}T \gg \hbar\Omega$, becomes important, these terms lead to a significant contribution. For the large LO-phonon energy provided by ZnO, the corresponding thermal energy is far beyond the temperatures investigated here. With these considerations, the analysis may confidently be restricted to Υ^{em} solely. The emission dynamics show a very similar form as Eq. (2.25) and read

$$\begin{aligned}
\mathrm{i}\hbar\frac{\partial}{\partial t}\,\Upsilon^{\mathrm{em}}_{\mathbf{k},\mathbf{q}_{3\mathrm{D}},\mathbf{p}_{3\mathrm{D}}} &= \left(\epsilon^{\mu}_{\mathbf{k}} + \epsilon^{M}_{\mathbf{Q}} - \Sigma_{\mathbf{k},\mathbf{Q}} - \hbar\omega_{\mathbf{q}_{3\mathrm{D}}} - \hbar\Omega\right)\Upsilon^{\mathrm{em}}_{\mathbf{k},\mathbf{q}_{3\mathrm{D}},\mathbf{p}_{3\mathrm{D}}} + Q[\Upsilon] \\
&\quad - \left(1 - f^{\mathrm{e}}_{\mathbf{k}+\mathbf{Q}_{\mathrm{e}}} - f^{\mathrm{h}}_{\mathbf{k}-\mathbf{Q}_{\mathrm{h}}}\right)\left[\sum_{\mathbf{k}'} V_{\mathbf{k}-\mathbf{k}'}\;\Upsilon^{\mathrm{em}}_{\mathbf{k}',\mathbf{q}_{3\mathrm{D}},\mathbf{p}_{3\mathrm{D}}} + \mathrm{i}\sum_{q'_{\perp}} \mathcal{F}_{\mathbf{q}+\mathbf{p},\,q'_{\perp}}\,\Delta\langle \hat{D}^{\dagger}_{\mathbf{p}_{3\mathrm{D}}} \hat{B}^{\dagger}_{\mathbf{q}_{3\mathrm{D}}} \hat{B}_{\mathbf{q}+\mathbf{p},\,q'_{\perp}} \rangle\right] \\
&\quad + \mathrm{i}\mathcal{F}_{\mathbf{q}_{3\mathrm{D}}}\left(f^{\mathrm{h}}_{\mathbf{k}-\mathbf{Q}_{\mathrm{h}}}\,\Xi^{cc}_{\mathbf{k},\mathbf{p}_{3\mathrm{D}},\mathbf{q}} - f^{\mathrm{e}}_{\mathbf{k}+\mathbf{Q}_{\mathrm{e}}}\,\Xi^{vv}_{\mathbf{k},\mathbf{p}_{3\mathrm{D}},\mathbf{0}} + \sum_{\mathbf{k}'} c^{\mathbf{p}_{3\mathrm{D}},\mathbf{q},\mathbf{k},\mathbf{k}'}_{\mathrm{X,\,ph}}\right)
\end{aligned} \tag{3.2}$$

where the center-of-mass momentum $\hbar\mathbf{Q} = \hbar(\mathbf{p}+\mathbf{q}) = \hbar(\mathbf{p}+\mathbf{q})_{\mathrm{e}} + \hbar(\mathbf{p}+\mathbf{q})_{\mathrm{h}}$ contains phonon momentum $\hbar\mathbf{p}$ and photon momentum $\hbar\mathbf{q}$. Equation (3.2) couples to two-photon correlations $\Delta\langle\hat{D}^{\dagger}\hat{B}^{\dagger}\hat{B}\rangle$ which are, at this stage, phonon-assisted quantities as well. The explicit form is given by Eq. (11) of Paper [IV]. The terms $\Xi^{cc}_{\mathbf{k},\mathbf{p}_{3\mathrm{D}},\mathbf{q}} = \Delta\left\langle \hat{D}^{\dagger}_{\mathbf{p}_{3\mathrm{D}}} \hat{a}^{\dagger}_{c,\,\mathbf{k}-\mathbf{Q}_{\mathrm{h}}+\mathbf{q}} \hat{a}_{c,\,\mathbf{k}+\mathbf{Q}_{\mathrm{e}}}\right\rangle$ and $\Xi^{vv}_{\mathbf{k},\mathbf{p}_{3\mathrm{D}},\mathbf{q}} = \Delta\left\langle \hat{D}^{\dagger}_{\mathbf{p}_{3\mathrm{D}}} \hat{a}^{\dagger}_{v,\,\mathbf{k}-\mathbf{Q}_{\mathrm{h}}} \hat{a}_{v,\,\mathbf{k}+\mathbf{Q}_{\mathrm{e}}-\mathbf{q}}\right\rangle$ represent phonon-assisted plasma-type scattering which initiate the emission correlations. In the steady state, they act as a static source; compare Eqs. (12)–(13) of Paper [IV]. For dilute densities, however, all nonlinear carrier-distribution contributions may be neglected. Besides these intraband sources, the remaining triplet source is the (quasi-stationary) phonon-assisted exciton correlation

$$\begin{aligned}
c^{\mathbf{p}_{3\mathrm{D}},\mathbf{q},\mathbf{k},\mathbf{k}'}_{\mathrm{X,\,ph}} &\equiv \Delta\langle \hat{D}^{\dagger}_{\mathbf{p}_{3\mathrm{D}}} \hat{a}^{\dagger}_{c,\,\mathbf{k}'-\mathbf{p}_{\mathrm{h}}} \hat{a}^{\dagger}_{v,\,\mathbf{k}-\mathbf{Q}_{\mathrm{h}}} \hat{a}_{c,\,\mathbf{k}+\mathbf{Q}_{\mathrm{e}}} \hat{a}_{v,\,\mathbf{k}'-\mathbf{p}_{\mathrm{h}}-\mathbf{q}} \rangle \\
&= \left[\phi^{\mathrm{R}}_{1s,\,\mathbf{q}}\left(\mathbf{r}=\mathbf{0}\right)\right]^{\star} \phi^{\mathrm{R}}_{1s,\,\mathbf{q}+\mathbf{p}}\left(\mathbf{k}\right) \frac{G^{1s,1s}_{\mathbf{q},\mathbf{p}_{3\mathrm{D}}}\,\Delta N_{1s,\mathbf{q}+\mathbf{p}}}{E_{1s,\mathbf{q}+\mathbf{p}} - E_{1s,\mathbf{q}} - \hbar\Omega - \mathrm{i}\eta_{\mathrm{X}}}
\end{aligned} \tag{3.3}$$

which is given in the exciton-basis representation with left- and right-handed exciton wavefunctions $\phi^{\mathrm{L/R}}_{\lambda,\,\mathbf{Q}}\left(\mathbf{k}\right)$ and exciton eigenenergies $E_{\lambda,\mathbf{Q}}$. Both follow from the Wannier equation which constitutes an excitonic eigenvalue problem; see App. A of Paper [IV]. The abbreviation $\phi^{\mathrm{R}}_{1s,\,\mathbf{q}}\left(\mathbf{r}=\mathbf{0}\right) = \sum_{\mathbf{k}} \phi^{\mathrm{R}}_{1s,\,\mathbf{q}}\left(\mathbf{k}\right)$ denotes the right-handed wavefunction at the real-space origin. These correlations contain the exciton–phonon-matrix element

$$\boldsymbol{G^{\nu,\nu'}_{\mathbf{q},\mathbf{p}_{3\mathrm{D}}}} = \hbar\boldsymbol{\Omega}\sum_{\mathbf{k}'} \boldsymbol{\phi^{\mathrm{L}}_{\nu,\,\mathbf{q}}}\left(\mathbf{k}'\right)\left[\boldsymbol{g^{c}_{\mathbf{p}_{3\mathrm{D}}}}\boldsymbol{\phi^{\mathrm{R}}_{\nu',\,\mathbf{q}+\mathbf{p}}}\left(\mathbf{k}'+\mathbf{p}_{\mathrm{h}}\right) - \boldsymbol{g^{v}_{\mathbf{p}_{3\mathrm{D}}}}\boldsymbol{\phi^{\mathrm{R}}_{\nu',\,\mathbf{q}+\mathbf{p}}}\left(\mathbf{k}'-\mathbf{p}_{\mathrm{e}}\right)\right]^{\star} \tag{3.4}$$

Generic exciton–phonon-matrix element

which weights the emission strength initialized by the exciton distribution $\Delta N_{1s,\mathbf{Q}}$. The $\Delta N_{1s,\mathbf{Q}}$ in turn directly follows from the c_{X} dynamics in the exciton basis. As already mentioned in Sec. 2.3, this distribution can show a significant hole burning around $\mathbf{q}=\mathbf{0}$. However, Eq. (3.1) reveals that the exciton distributions appear under

an integral resulting in an almost imperceptible change with respect to the low-momentum influence.

The remaining triplets $T[\Pi]$ in Eq. (2.25) and quadruplets $Q[\Upsilon]$ in Eq. (3.2) do not directly participate to phonon-assisted processes but provide excitation-induced broadening and shifts of the emission resonances. A related discussion is presented in Sec. 5.1.2 and App. B.2; the explicit forms are presented in, e.g., Refs. [2,24]. The ZPL, however, is almost dominated by the background decay constant and may be anticipated virtually robust under the influence of polarization–density scattering [124]. Excitation-induced dephasing (EID) mainly affects higher states leading to strong non-Lorentzian line shapes. Since the ZPL and resonances below the excitonic lines are of central importance here, these scattering contributions are treated at the level of a dephasing approximation by assuming phenomenological dephasing such that $T[\Pi] = -\mathrm{i}\gamma_0\Pi_{\mathbf{k},\mathbf{q}_{3\mathrm{D}}}$ and $Q[\Upsilon] = -\mathrm{i}\gamma_1\Upsilon^{\mathrm{em}}_{\mathbf{k},\mathbf{q}_{3\mathrm{D}},\mathbf{p}_{3\mathrm{D}}}$ where γ_0 and γ_1 are constants. Then, the phonon-assisted SLEs (2.23) and (2.25) with additional solutions provided by the dynamics (3.2) and the phonon-assisted two-photon correlations form a closed set of equations. These are solved fully dynamically by computing photoluminescence spectra until steady state is reached. In the simulations, typical material parameters of ZnO, listed in the last part of Sec. III of Paper [IV], are used. In complete analogy to the notation of Eqs. (2.25) and (2.28), the introduction of center-of-mass coordinates separates the energies in the first line of Eq. (3.2) to angle-independent quantities. Therefore, the only angle dependence stems from the carrier distributions $f^{\lambda}_{\mathbf{k}\pm\mathbf{Q}_\lambda}$. Noting that the photon momentum $\hbar\mathbf{q}$ is very small compared to the carrier momentum $\hbar\mathbf{k}$ or the phonon momentum $\hbar\mathbf{p}$, the assumption $\mathbf{Q} \simeq \mathbf{p}$ is justified. For conventional momentum ranges of phonon-assisted processes, the remaining full-vectorial dependence is very weak, and the dynamics may be solved assuming angle-independent momenta, without distorting the results. This dramatically reduces computation complexity, and thus consumption of time and memory.

3.3 Impact of tailored microcavities

To induce enhanced coupling between the light field and the semiconductor sample, the structure may be embedded into a microcavity. Such a dielectric environment crucially alters the reflection and transmission behavior, and thus gives rise to tremendous changes of the optical response. The focus of the following studies is the investigation of this influence for different cavity configurations.

Since a ZnO QW is investigated in this project, a dielectric environment of similar components is simulated. ZnO cavities have recently been worked out experimentally [182] and sample-growth techniques are developing into a direction [183–186] where one or multiple ZnO-type QWs can be placed between alternating $\mathrm{ZnO/Mg_{0.36}Zn_{0.64}O}$ layers. In the actual computations, such a cavity with one quantum well is simulated [81, 91] by assuming refractive indices $n_{\mathrm{ZnO}} = 2.2$ and $n_{\mathrm{MgZnO}} = 1.96$ [187–190] and assuming a spacer layer that has the same refractive index as the ZnO QW to avoid reflections inside the sample. The structural basic setup is presented in Fig. 1 of Paper [IV] and constitutes a typical microcavity used in confined semiconductor systems. It is well known that such a cavity consisting of layers with alternating refractive indices and thicknesses equal to a quarter wavelength in the corresponding medium [90, 91, 191] leads to the scenario of normal-mode coupling (NMC) when the sample is placed at an antinode of the intracavity field [54]. Here, the exciton peak splits into two peaks when the quality of the cavity increases, transferring the system into the nonperturbative regime where coupling between light and matter is strong [52, 57, 144]. Nevertheless, the resonance energy of the cavity can be adjusted by varying the thickness of the layers. Whereas it is resonant with the $1s$-exciton energy for $\lambda/4$ layers, it is possible to tune it to be resonant with, e.g., the PSB_1 located at $E_{1s} - \hbar\Omega$, for thicknesses deviating from this "standard" value. This leads to the central question of this investigation: *How is the PL influenced by a cavity tuned to be resonant with the first phonon sideband?* In the remainder of this chapter, the term "$1s$ cavity" denotes the cavity resonant with the $1s$-exciton energy, i.e., the ZPL, while "phonon cavity" names the detuned cavity which is resonant with the PSB_1. Figure 3.2 shows the computed photoluminescence spectra for the two cavity configurations. In both frames, the PL spectrum of the sample in a cavity (solid line) is compared with the bare QW in free space (light-shaded area). In the background, the dark-shaded area depicts the cavity reflection showing a sharp decline at the cavity resonance. The cavity in both cases consists of 34 DBR layers leading to a mirror reflection of 99.9%.

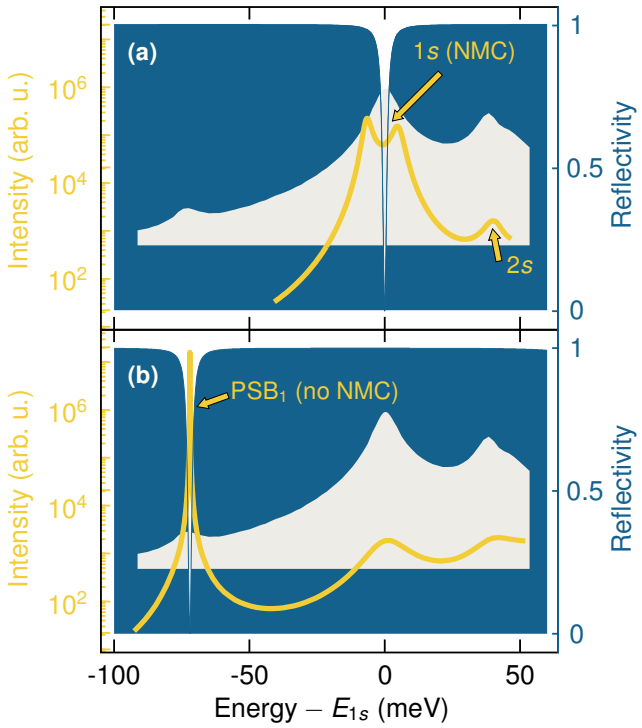

Figure 3.2 | Luminescence for 1*s* cavity versus phonon cavity. Microcavity luminescence including zero-phonon line (ZPL or 1*s*) and the first phonon sideband (PSB_1). The cavity is resonant with **(a)** the ZPL or **(b)** the PSB_1. The luminescence spectra with (solid line) and without (light area) cavity are shown with the reflectivity (dark area) of the bare cavity.

In Fig. 3.2 **(a)**, the cavity is obviously resonant with the $1s$-exciton energy leading to a clear splitting into two peaks (NMC) and decrease of the overall PL, as it is expected from the $1s$ cavity. The NMC is a direct consequence of the reversible emission and absorption of light at the excitonic resonance. It is the predominant mechanism when using the $1s$ cavity which is why the phonon peak is very tiny and not visible in the spectrum. Since the $1s$ cavity directly couples to the $1s$-exciton state, neither the PSB_1 nor the higher excitonic states are influenced and, especially, do not show any splitting. For the phonon cavity shown in Fig. 3.2 **(b)**, the cavity-PL spectrum differs fundamentally from the $1s$-cavity situation discussed before. Now, that the cavity coincides with the PSB_1, the PL is highly enhanced at the energetic position of the PSB_1. In stark contrast to the NMC observed before, the phonon cavity does not produce any splitting of resonances. Physically, the different situation can be explained by considering the different energies of emission and absorption: Owing to reversibility of emission–absorption cycles, the exciton peak with $1s$ cavity splits; in complete analogy to the coupled harmonic-oscillator situation [192]. On the other hand, the phonon peak with phonon cavity does not split since the cavity–PSB_1 coupling consists only of the photon-emission part at $E_{1s}-\hbar\Omega$. At low temperatures, no absorbable phonon population is present to close the emission–absorption cycle; compare the discussion in the previous section.

The results presented so far are computed for a certain number of DBR layers where a conspicuous coupling between light and matter is observed to produce NMC. To demonstrate that the computed PSB_1 results do not rely on the coupling strength, also DBR-dependent computations are performed where the number of DBR-mirror pairs is increased starting from the free-space configuration (0 DBR layers) to the regime where the $1s$ cavity produces a clear normal-mode splitting (34 DBR layers). Figure 3.3 shows the peak positions of the $1s$-exciton resonance and the PSB_1 as function of DBR-mirror pairs. In Fig. 3.3 **(a)**, the blue-solid line represents the peak positions when the $1s$ cavity is used while the yellow-dashed line shows the phonon-cavity results. When the stimulated emission overcomes the spontaneous processes, the $1s$-exciton resonance shows a clear bifurcation into NMC splitting. This happens around 8 DBR layers where the splitting sets in. The peak positions drift slightly away from the (unsplitted) $1s$ position until they remain unchanged in their energetic position since the coupling strength, compare Eq. (2.11), saturates in the strong-cavity limit. In contrast, the PSB_1 does not show any splitting indicating that the $1s$ cavity does not yield reversibility for this energy.

The phonon cavity (yellow-dashed line), however, shows a completely different behavior because it does not lead to NMC at the $1s$-exciton resonance since the propagating mode is off-resonant with respect to the ZPL. Besides this, the PSB_1 also remains a single-resonance peak. Figure 3.3 **(b)** represents the phonon-cavity results of the ZPL and PSB_1 together with the energy-resolved PL in logarithmic scale. The black-dashed lines correspond to the yellow-dashed lines of frame **(a)**. This graphic rendition in contour-plot format not only shows that no splitting occurs for both the ZPL and the PSB in phonon-cavity configuration, but also visualizes the peak heights and change of weighting induced by the phonon cavity: at the onset of strengthened stimulated emission (around 8–10 DBRs), the ZPL peak height decreases while the PSB_1 peak height grows accordingly. In agreement with the observations for the phonon cavity presented by the yellow-dashed lines in frame **(a)**, no splitting is observed at both resonances. Moreover, the ZPL is reduced for increasing number of DBR-mirror pairs while the PSB_1 increases and shows a pronounced narrowing in the strong-cavity limit. Thus, independent of the coupling strength and quality of the cavity, both the ZPL and the PSB_1 do not show any bifurcation, clearly underscoring the importance of the cavity resonance. These results clearly verify that, owing to the lack of phonon-assisted absorption discussed before, the phonon cavity does not provide the possibility of a closed photon-emission–absorption cycle.

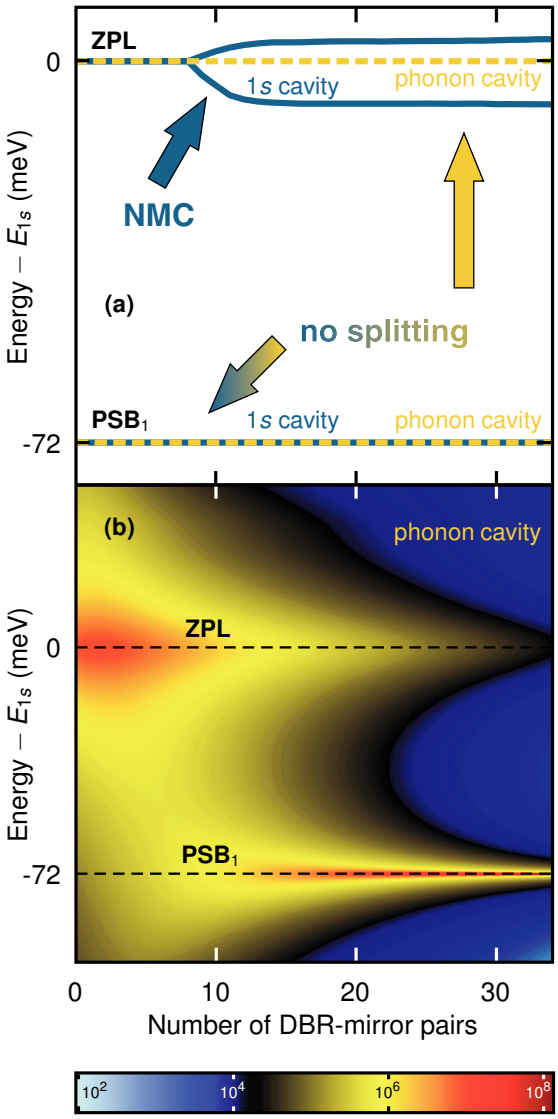

Figure 3.3 | Tailored-cavity peak positions. (a) Peak position of ZPL and PSB_1 versus number of DBR-mirror pairs. The blue-solid (yellow-dashed) line indicates the energies of the PL peaks for the 1*s* cavity (phonon cavity). **(b)** Peak evolutions for the phonon cavity: For increasing number of DBR-mirror pairs, the ZPL is reduced while the PSB_1 increases and narrows. Neither resonance shows any splitting.

The preceding fully dynamical studies reveal important findings. As an interim result, notably, the effects of tailored microcavities have distinct impact on the entire PL spectrum. This suggests that the intensities will experience changes as well when scanning the number of DBR layers. For better understanding, the integrated PL is plotted in Fig. 3.4 where the intensity of the exciton resonance for the $1s$ cavity is shown by the yellow-solid line. The intensity of the PSB_1 peak for the phonon cavity is indicated by the black-solid line and the total intensity for the phonon cavity by the gray-dashed line. Furthermore, also the maximum of the mode function at the quantum-well position (long-dashed blue) and the PSB_1 peak height (black-dotted line) are shown. As a result of the Purcell effect, the ZPL emission increases rapidly for low-reflection quality. Around the onset of reversibility, where the splitting in Fig. 3.3 sets in, the ZPL-emission intensity decreases when entering the NMC regime. Also the PSB_1-resonance intensity for the phonon cavity (black solid) shows an initial increase due to enhanced spontaneous emission, but then saturates to a constant value. For all coupling strengths, the phonon-peak emission and the mode-function maximum rise monotonously. The eventual saturation of the PSB_1-emission intensity is a result of dominant cavity–PSB_1 coupling, leading to narrowing of the phonon resonance while strong enhancement of the peak emission is observed. As a very intriguing observation, it is to mention that the total intensity in the phonon cavity approaches the phonon-peak intensity for strong coupling, clearly showing that the phonon cavity exclusively favors the PSB_1 emission over the ZPL contribution.

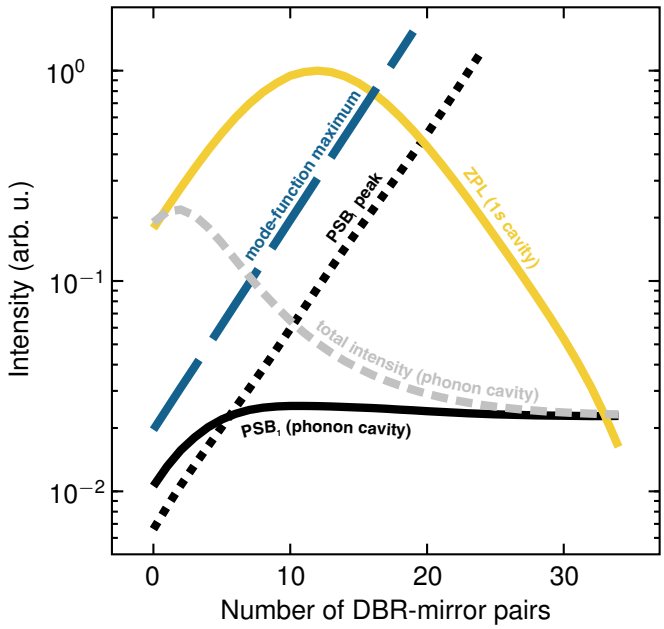

Figure 3.4 | Intensity of the photoluminescence spectrum (fully dynamical solution). The yellow-solid line shows the intensity of the exciton resonance (ZPL) for the 1*s* cavity while the black-solid line represents the intensity of first phonon sideband (PSB$_1$) for the phonon cavity. The total intensity for the phonon cavity is indicated by the gray short-dashed line. The mode-function maximum (long-dashed blue) and the peak height of PSB$_1$ (black-dotted) are also shown.

3.4 Analytic model

The numerical work put forward in the last section shows that the $1s$ cavity leads to the well-known effect of normal-mode coupling while the phonon cavity influences the photoluminescence in a completely different manner. To corroborate the results of the fully dynamical computation and to gain detailed understanding of the physical origin associated with the found effects, it is desirable to develop an analytic model to describe phonon-sideband luminescence in a microcavity. Another side benefit of an analytic formulation is the tremendous reduction of computational costs, and thus computing time and memory consumption. The general procedure to reach this goal is to set up the different operator dynamics in the exciton-picture representation and form a closed set of equations. This leads to a steady-state expression such that the photon flux of ZPL and PSB$_1$ contributions in normal direction may be expressed via

$$I_{\mathrm{PL}}\left(\omega_{\mathbf{0},q_\perp}\right) = \frac{2}{\hbar}\left|\mathcal{F}^{1s}_{\mathbf{0},\,q_\perp}\right|^2 \mathrm{Re}\left[\bar{\Pi}^{\mathrm{X,\,ZPL}}_{1s,\mathbf{0},q_\perp} + \bar{\Pi}^{\mathrm{X,\,PSB_1}}_{1s,\mathbf{0},q_\perp}\right] \tag{3.5}$$

with the scaled photon-assisted polarization $\bar{\Pi}^{\mathrm{X}}_{1s,\mathbf{q}_{3\mathrm{D}}} \equiv \Pi^{\mathrm{X}}_{1s,\mathbf{q}_{3\mathrm{D}}}/\mathcal{F}^{1s}_{\mathbf{q}_{3\mathrm{D}}}$. The quantity $\mathcal{F}^{1s}_{\mathbf{q}_{3\mathrm{D}}} \equiv \phi_{1s}(\mathbf{r}=\mathbf{0})\,\mathcal{F}_{\mathbf{q}_{3\mathrm{D}}}$ defines the strength of spontaneous emission and contains the $1s$-exciton wavefunction at the spatial origin. The analytic formulation of phonon-assisted photoluminescence including light–matter coupling effects involves sophisticated transformation steps. This section gives a brief review to present the general idea behind this procedure. A more detailed discussion is given in Sec. V of Paper [IV].

To capture the essence of the microcavity luminescence of the ZPL and PSB$_1$ emission via analytic expressions, the investigations are limited to the $1s$ contribution and the limits of dilute densities $f^{\mathrm{e}} \ll 1$ and $f^{\mathrm{h}} \ll 1$ are assumed. The singlet part of the total-source term $N_{1s} = N^{\mathrm{eh}}_{1s} + \Delta N_{1s}$ is proportional to $f^{\mathrm{e}} f^{\mathrm{h}}$ such that in this situation the main contribution to the PL stems from the correlated part, expressed by the exciton distribution $N_{1s,\mathbf{q}} = \Delta N_{1s,\mathbf{q}}$, if it exists [51]. In this situation, it is beneficial to switch from the electron–hole representation to the exciton picture [24] by projecting the full Eqs. (2.23), (2.25), (3.2), and the phonon-assisted two-photon correlations (Eq. (11) of Paper [IV]) via the excitonic wavefunctions; see App. A

of Paper [IV] which surveys the basic transformation steps and relations. The results of this transformation process are presented in Eqs. (18)–(23) of the same manuscript. For dilute densities, the excitonic eigenvalue problem is Hermitian and produces wavefunctions $\phi_\nu(\mathbf{k})$ which do not separate into left- and right-handed ones. For nonvanishing densities, however, it is rather essential to distinguish into left- and right-handed eigenfunctions $\phi^{\mathrm{L}}_{\nu,\mathbf{Q}}(\mathbf{k})$ and $\phi^{\mathrm{R}}_{\nu,\mathbf{Q}}(\mathbf{k})$ and assure correct normalization among the excitonic wavefunctions; compare a similar discussion in Sec. 5.1.2. Then, the wavefunctions parametrically depend on the COM momentum $\hbar\mathbf{Q}$.

3.4.1 Treatment of the stimulated parts

Even though the complexity of phonon-assisted SLEs is reduced considerably by introducing the exciton-basis representation and restricting the studies to the $1s$-exciton contribution, the non-trivial stimulated emission via $\sum\mathcal{F}\,\Delta\langle\hat{B}^\dagger\hat{B}\rangle$ and $\sum\mathcal{F}\,\Delta\langle\hat{D}^\dagger\hat{B}^\dagger\hat{B}\rangle$ remains and needs a special treatment. A solution without these stimulated parts is considerably easy and straightforward. The inclusion of these terms, however, entails an intricate interplay of different operator quantities. To control and simplify the cavity-induced coupling, the introduction of scaled, collective photon operators $\hat{\bar{B}}^\dagger_{\mathbf{q},\Sigma}\equiv\frac{1}{\mathcal{G}}\sum_{q'_\perp}[\mathcal{F}^{1s}_{\mathbf{q},q'_\perp}]^\star\hat{B}^\dagger_{\mathbf{q},q'_\perp}$ and $\hat{\bar{B}}_{\mathbf{q},\Sigma}\equiv\frac{1}{\mathcal{G}}\sum_{q'_\perp}\mathcal{F}^{1s}_{\mathbf{q},q'_\perp}\hat{B}_{\mathbf{q},q'_\perp}$ as well as the scaled, collective photon-assisted polarization $\bar{\Pi}^{\mathrm{X}}_{1s,\mathbf{q},\Sigma}\equiv\frac{1}{\mathcal{G}}\sum_{q'_\perp}|\mathcal{F}^{1s}_{\mathbf{q},q'_\perp}|^2\,\bar{\Pi}^{\mathrm{X}}_{1s,\mathbf{q},q'_\perp}$ proves useful. In the following, the theoretical description is formulated using these scaled (indicated by the bar, $\bar{}$, above the operator quantity) and collective (indicated by the capital-sigma index, $_\Sigma$) operators. Within the scope of this concept, a normalization $\mathcal{G}$ is introduced such that the scaled, collective operators $\hat{\bar{B}}^\dagger_{\mathbf{q},\Sigma}$ and $\hat{\bar{B}}_{\mathbf{q},\Sigma}$ satisfy Bosonic commutation relations. More specifically, this leads to the Bosonic commutation $[\hat{\bar{B}}_{\mathbf{q},\Sigma},\hat{\bar{B}}^\dagger_{\mathbf{q}',\Sigma}]_-=\delta_{\mathbf{q},\mathbf{q}'}$ and $[\hat{\bar{B}}_{\mathbf{q},\Sigma},\hat{\bar{B}}_{\mathbf{q}',\Sigma}]_-=[\hat{\bar{B}}^\dagger_{\mathbf{q},\Sigma},\hat{\bar{B}}^\dagger_{\mathbf{q}',\Sigma}]_-=0$ if $\mathcal{G}^2=\sum_{q_\perp}|\mathcal{F}^{1s}_{\mathbf{q},q_\perp}|^2$.

To investigate a situation where the stimulated effects are particularly strong, a planar semiconductor microcavity consisting of alternating DBR layers is assumed, as discussed in the previous section. In this situation, the normalization $\mathcal{G}$ has a direct physical interpretation since it contains the mode strength $|\mathcal{F}^{1s}_{\mathbf{q},q_\perp}|^2\propto|\mathbf{u}_{\mathbf{q},q_{\mathrm{cav}}}(z_{\mathrm{QW}})|^2$ corresponding to the cavity mode $|\mathbf{u}_{\mathbf{q},q_{\mathrm{cav}}}(z)|$ when the quantum well is positioned at one of the spatial-mode maxima, z_{QW}. For bare systems, the mode function is uniquely distributed over all momenta and shapes into a Lorentzian for intermediate coupling. For sufficiently strong coupling, the peak narrows around the cavity-mode energy $E_{\mathrm{cav}}=\hbar\omega_{\mathrm{cav}}$, whereas the area under $|\mathcal{F}^{1s}_{\mathbf{q},q_\perp}|^2$ remains unchanged for increased number of DBR-mirror pairs. In the limit of very strong coupling, the cavity mode approaches a δ-distributed shape allowing to introduce the *strong-cavity approximation* (SCA)

$$\sum_{q_\perp}|\boldsymbol{\mathcal{F}}^{\boldsymbol{1s}}_{\mathbf{q},q_\perp}|^{\mathbf{2}}\,(\boldsymbol{\omega}_{\mathbf{q},q_\perp}-\boldsymbol{\omega}_{\mathbf{cav}})\odot_{\mathbf{q},q_\perp}=\mathbf{0} \tag{3.6}$$

Strong-cavity approximation

whenever the mode function is strongly peaked around the cavity-resonance frequency ω_{cav} and the function $\odot_{\mathbf{q},q_\perp}$ is slowly varying around $\omega_{\mathbf{q},q_\perp}=\omega_{\mathrm{cav}}$. Applying the preceding definitions to the phonon-assisted SLEs and adopting the SCA leads to cancellation of energy differences in the homogeneous parts of Eqs. (2.23) and (2.25). Eventually, the effective-mode equations read

$$\mathrm{i}\hbar\frac{\partial}{\partial t}\Delta\langle\hat{\bar{B}}^\dagger_{\mathbf{q},\Sigma}\hat{\bar{B}}_{\mathbf{q},\Sigma}\rangle=2\mathrm{i}\mathcal{G}\,\mathrm{Re}\left[\bar{\Pi}^{\mathrm{X}}_{1s,\mathbf{q},\Sigma}\right], \tag{3.7}$$

$$\mathrm{i}\hbar\frac{\partial}{\partial t}\bar{\Pi}^{\mathrm{X}}_{1s,\mathbf{q},\Sigma}=[E_{1s,\mathbf{0}}-\hbar\omega_{\mathrm{cav}}-\mathrm{i}\gamma_0]\,\bar{\Pi}^{\mathrm{X}}_{1s,\mathbf{q},\Sigma}+\mathrm{i}\,\mathcal{G}\left(\Delta N_{1s,\mathbf{0}}-\Delta\langle\hat{\bar{B}}^\dagger_{\mathbf{0},\Sigma}\hat{\bar{B}}_{\mathbf{0},\Sigma}\rangle\right)+\sum_{\mathbf{p}}\Delta\langle\hat{\bar{D}}^\dagger_{\mathbf{p},\Sigma}\hat{\bar{B}}^\dagger_{\mathbf{0},\Sigma}\hat{X}_{\mathbf{p}}\rangle \tag{3.8}$$

with the collective phonon operator $\hat{\bar{D}}_{\mathbf{p},\Sigma}\equiv\sum_{p_\perp}\hbar\Omega\,g^{\nu,\nu'}_{\mathbf{p}_{3\mathrm{D}}}\hat{D}_{\mathbf{p}_{3\mathrm{D}}}$ where $g^{\nu,\nu'}_{\mathbf{p}_{3\mathrm{D}}}=G^{\nu,\nu'}_{\mathbf{p}_{3\mathrm{D}}}/(\hbar\Omega)$. A more detailed derivation and implementation of the SCA can be found in Eqs. (24)–(31) of Paper [IV]. In the following, the

emission in normal direction is studied such that $\mathbf{q} = \mathbf{0}$; compare Eq. (3.5). As a result of the SCA, Eq. (3.7) does not show any direct energy or cavity dependence anymore. This simplification lays the foundation of finding a steady-state expression of these investigations. Before going about the development of the steady-state solution, however, further reformatting is applied to the SLEs in exciton basis, see Eqs. (18)–(19) of Paper [IV], by introducing new quantities that signify the cavity and detuning effects better. For a neatly arranged structure of the equations, it thus proves beneficial to define new abbreviations $\Delta^{\mathrm{ZPL}}_{\omega,\mathbf{p}} \equiv E_{1s,\mathbf{p}} - \hbar\omega_{\mathbf{0},q_\perp}$ for the exciton–light detuning, $\Delta^{\mathrm{PSB},\pm}_{\omega,\mathbf{p}} \equiv E_{1s,\mathbf{p}} - \hbar\omega_{\mathbf{0},q_\perp} \pm \hbar\Omega$ defining the PSB–light detuning, as well as the cavity–light detuning $\Delta^{\mathrm{cav}}_{\omega} \equiv \hbar\omega_{\mathrm{cav}} - \hbar\omega_{\mathbf{0},q_\perp}$. This eventually produces the matrix representation

$$\mathrm{i}\hbar\frac{\partial}{\partial t}\begin{pmatrix} \bar{\Pi}^{\mathrm{X}}_{1s,\mathbf{0},q_\perp} \\ \Delta\langle \hat{\bar{B}}^{\dagger}_{\mathbf{0},\,q_\perp}\hat{\bar{B}}_{\mathbf{0},\Sigma}\rangle \end{pmatrix} = \mathbf{M}\begin{pmatrix} \bar{\Pi}^{\mathrm{X}}_{1s,\mathbf{0},q_\perp} \\ \Delta\langle \hat{\bar{B}}^{\dagger}_{\mathbf{0},\,q_\perp}\hat{\bar{B}}_{\mathbf{0},\Sigma}\rangle \end{pmatrix} + \begin{pmatrix} \mathrm{i}\,\Delta N_{1s,\mathbf{0}} + \sum_{\mathbf{p}}\Delta\langle \hat{\bar{D}}^{\dagger}_{\mathbf{p},\Sigma}\hat{\bar{B}}^{\dagger}_{\mathbf{0},\,q_\perp}\hat{X}_{\mathbf{p}}\rangle \\ \mathrm{i}\,[\bar{\Pi}^{\mathrm{X}}_{1s,\mathbf{0},\Sigma}]^{\star} \end{pmatrix} \tag{3.9}$$

$$\text{with } 2\times2 \text{ matrix } \mathbf{M} = \begin{pmatrix} \Delta^{\mathrm{ZPL}}_{\omega,\mathbf{0}} - \mathrm{i}\gamma_0 & -\mathrm{i}\,\mathcal{G} \\ \mathrm{i}\,\mathcal{G} & \Delta^{\mathrm{cav}}_{\omega} \end{pmatrix} \tag{3.10}$$

Photoluminescence dynamics in the exciton picture including stimulated contributions

describing the photoluminescence dynamics when microcavity effects are included. In the absence of phonon effects, i.e., $\Delta\langle \hat{\bar{D}}^{\dagger}_{\Sigma}\hat{\bar{B}}^{\dagger}\hat{X}\rangle \equiv 0$, the derived dynamics yield a closed set of equations without the need of additional contributions. By this means, at first a suitable solution algorithm is developed to seek the steady-state solution for the ZPL without phonon effects. To simplify and solve Eqs. (3.9), the derivation starts from the steady-state form of Eq. (3.8) where the left-hand side is set to zero. A close inspection of the term proportional to $\mathcal{G}$ in Eq. (3.8) then reveals that $\Delta\langle \hat{\bar{B}}^{\dagger}_{\mathbf{0},\Sigma}\hat{\bar{B}}_{\mathbf{0},\Sigma}\rangle$ is driven and a steady state is not reached unless $\mathrm{Re}[\bar{\Pi}^{\mathrm{X}}_{1s,\mathbf{q},\Sigma}]$ is demanded to vanish; compare Eq. (3.7). Then, the second term of the right-hand side of Eq. (3.8) discloses a constant collective photon-number correlation $\Delta\langle \hat{\bar{B}}^{\dagger}_{\mathbf{0},\Sigma}\hat{\bar{B}}_{\mathbf{0},\Sigma}\rangle = \Delta N_{1s,\mathbf{0}}$. These considerations simplify the matrix equation (3.9) further into a typical linear equation driven by a known constant source $\Delta N_{1s,\mathbf{0}}$. Since $\mathbf{M}$ includes dephasing, the set of equations eventually evolves toward a steady state which displays the determinant of matrix $\mathbf{M}$ in the denominator, resulting in a Lorentzian-type response; compare Eq. (40) in Paper [IV].

Here, it is convenient to rewrite the determinant via its roots such that $\det[\mathbf{M}] = (\Delta^{\mathrm{cav}}_{\omega} - \Delta_+)(\Delta^{\mathrm{cav}}_{\omega} - \Delta_-)$ where $\Delta_\pm = \frac{1}{2}\left(\Delta^{\mathrm{cav}}_{1s} + \mathrm{i}\gamma_0 \pm \Omega^{\mathrm{cav}}_{1s}\right)$ and $\Omega^{\mathrm{cav}}_{1s} = \sqrt{4\mathcal{G}^2 + (\Delta^{\mathrm{cav}}_{1s} + \mathrm{i}\gamma_0)^2}$. By doing so and performing a partial-fraction decomposition, the steady-state photon flux of the ZPL is proportional to the real part of

$$\bar{\Pi}^{\mathrm{X}}_{1s,\mathbf{0},q_\perp} = \frac{\mathrm{i}\,\Delta N_{1s,\mathbf{0}}}{\Delta_+ - \Delta_-}\left(\frac{\Delta_-}{\Delta^{\mathrm{cav}}_{\omega} - \Delta_-} - \frac{\Delta_+}{\Delta^{\mathrm{cav}}_{\omega} - \Delta_+}\right) \tag{3.11}$$

Analytic result of ZPL contribution to the photoluminescence

defining $\bar{\Pi}^{\mathrm{X,\,ZPL}}_{1s,\mathbf{0},q_\perp}$ in Eq. (3.5). This result evidently shows that the presence of a cavity leads to splitting of the $1s$-exciton resonance into two normal-mode peaks centered at $\mathrm{Re}[\hbar\omega_{\mathrm{cav}} - \Delta_\pm]$. The corresponding width of the Lorentzians is given by $\gamma_{0,\pm} = \mathrm{Im}[\Delta_\pm]$. As can be seen, Eq. (3.11) correctly describes the scenario of NMC found by the numerical investigations of Secs. 3.2 and 3.3, and thus provides a consistent and reliable model to describe photoluminescence including cavity effects. By using the same operator definitions and assumptions for the phonon-related quantities, a closed set of equations for this extension may likewise be formulated. Including dephasing, these equations eventually evolve toward a steady state as well. However, the phonon-related contributions involve sophisticated transformation and reformatting steps. The derivation and explicit

equations are quite lengthy and therefore just presented in Sec. V and App. B of Paper [IV]. For the sake of readability, the formalism presented in this thesis utilizes the same notation as the equations in the papers. Thus, the analytic model with phonon-assisted contributions follows the identical scheme.

Instead of presenting the detailed derivation of the steady-state PSB_1 emission, rather the complex interplay of the equation-of-motion structure of all quantities and expectation values is schematically visualized when the PSB_1 and microcavity effects are included. Figure 3.5 shows all quantities of the related equations-of-motion structure. In general, scaled quantities are used which is indicated by the bar on the phonon ($\hat{\bar{D}}^\dagger$) and photon ($\hat{\bar{B}}^\dagger$, $\hat{\bar{B}}$) operators; compare the prior definitions. The collective phonon operator $\hat{\bar{D}}^\dagger_\Sigma$, labeled by the capital sigma, is introduced in connection with Eq. (3.8). The explicit forms of the phonon-assisted equations of motion are given in App. B of Paper [IV]. In the present schematic illustration, each participating quantity is shown in a separate drop-shadow box. An arrow from a specific quantity to another indicates that its equation of motion involves contributions of the second one. The upper part of the figure contains all PL contributions *without* the participation of phonons (yellow-shaded ellipse and gray-shaded box) whereas the lower part represents the phonon contributions (blue-shaded box). As a general rule, all phonon-related quantities contain a scaled, collective phonon-creation operator $\hat{\bar{D}}^\dagger_\Sigma$.

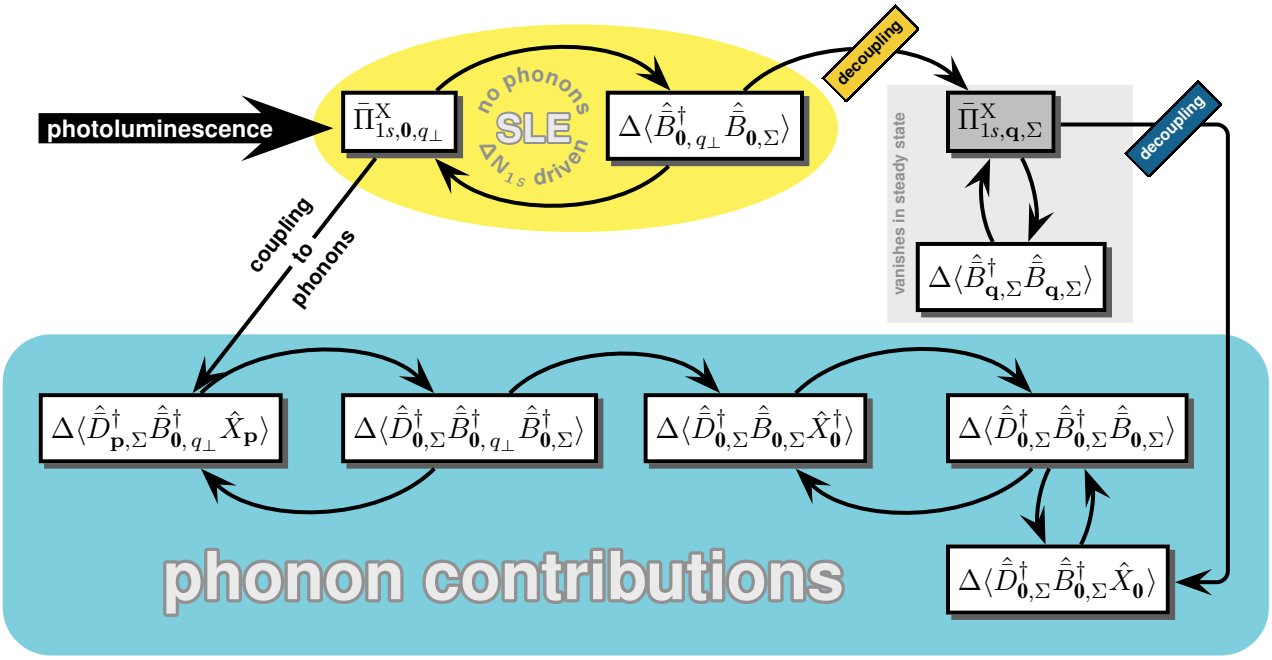

Figure 3.5 | Coupling of ZPL- and PSB_1-operator dynamics. An arrow from a specific quantity to another indicates that the first one couples to the second, i.e., its equation of motion contains contributions of the second quantity. In the upper part, all contributions without phonons are shown. They couple to the phonon-assisted quantities (blue-shaded box). The collective contributions (gray-shaded box) eventually vanish due to the steady-state requirement of the collective photon-number correlation, leading to decoupling from linked dependencies. The PL spectrum (black arrow) is eventually obtained by the real part of the photon-assisted polarization. Without phonons, the ZPL-photon flux is given by the two quantities in the yellow-shaded ellipse and driven by a constant source.

The photon flux or PL is related to the real part of the photon-assisted polarization, see Eqs. (2.24) and (3.5), indicated here by the black arrow. This quantity couples to two-photon correlations, i.e., the second quantity in the first line, which then couples to the collective photon-assisted polarization (3.8). Owing to the steady-state argument introduced with the correlated collective photon-number (3.7) and the collective photon-assisted polarization (3.8), $\bar{\Pi}^{\mathrm{X}}_\Sigma$ vanishes and is therefore shown dark-gray shaded. Then, both collective quantities are decoupled from linked dependencies, indicated by the orange and blue "decoupling" markers. This provides a constant driving source $\Delta N_{1s,\mathbf{0}}$ for the SLEs in the yellow-shaded ellipse and forms a closed set of equations when phonon effects are omitted. Despite the decoupling resulting from the steady-state criterion, phonons

are still coupled to the system via $\Delta\langle\hat{\bar{D}}^\dagger_\Sigma\hat{\bar{B}}^\dagger\hat{X}\rangle$, compare Eqs. (2.25) and (3.1), and enter the PL directly as additional terms to the photon-assisted polarization. Apparent from the exciton operator $\hat{X}$, this extension, located at the very left of the blue-shaded box, is the exciton-picture representation of Eq. (3.2). This coupling to the pure ZPL contribution is indicated by the arrow marked with "coupling to phonons" in the left figure part. The phonon contributions themselves then alternately involve collective two-photon correlations and photon-assisted polarizations, which naturally contain one phonon-creation operator each.

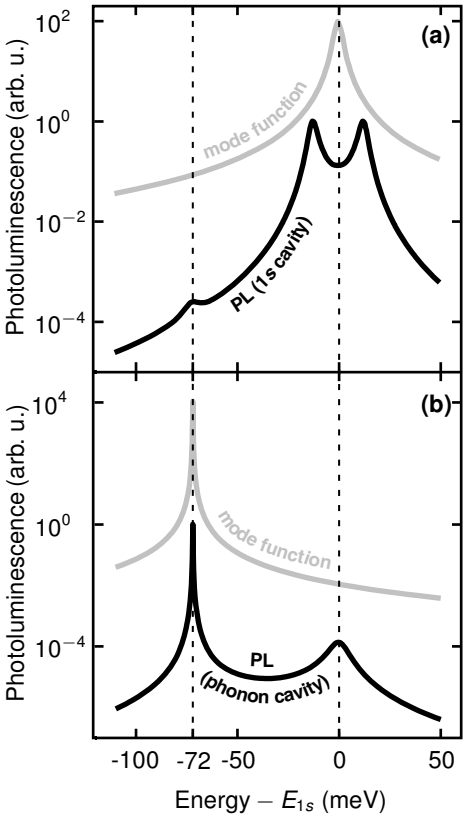

Figure 3.6 | Microcavity luminescence computed via the analytic model. The black-solid line shows the computed PL including the zero-phonon line (ZPL) and the first phonon sideband (PSB_1). The gray-solid line shows the mode function and the vertical-dashed lines indicate the positions of ZPL and PSB_1, respectively. The cavity is resonant with **(a)** the ZPL ($1s$ cavity) or **(b)** the PSB_1 (phonon cavity).

The overall steady-state PL arises out of the following procedure. The central quantity is always the photon-assisted polarization $\bar{\Pi}^{\mathrm{X}}$, shown on the left in the yellow-shaded ellipse. Assuming the steady-state criterion for the collective terms and omitting phonons (gray-shaded and blue-shaded box vanish), just the steady-state solution of the $\Delta\langle\hat{\bar{B}}^\dagger\hat{\bar{B}}_\Sigma\rangle$ dynamics must be derived by setting the left-hand side of the equation of motion to zero, rearranging the resulting equation, and then insert it to $\bar{\Pi}^{\mathrm{X}}$. With phonons, the procedure is similar but involves much more equations of motion, collected in the blue-shaded box. Starting from the farthermost node, $\Delta\langle\hat{\bar{D}}^\dagger_\Sigma\hat{\bar{B}}^\dagger_\Sigma\hat{X}\rangle$, its steady-state form is generated and inserted to the dynamics prior to that node. Then, the procedure repeats with the remaining equations. Performing rearrangements of the final resulting equation, the eventual analytic expression can be separated into a ZPL and a PSB_1 part; compare Eq. (3.5). The corresponding PSB contributions are presented in Eqs. (45)–(51) of Paper [IV].

In case of the phonon cavity, the cavity resonance $\hbar\omega_{\mathrm{cav}}$ corresponds to the PSB_1 energy $E_{1s,\mathbf{0}} - \hbar\Omega$. In a configuration close to the cavity resonance, the detunings introduced in connection with Eq. (3.9) reduce to $\Delta^{\mathrm{PSB},+}_{\omega,0} = 2\hbar\Omega + \Delta^{\mathrm{cav}}_\omega \to 2\hbar\Omega$ and $\Delta^{\mathrm{PSB},-}_{\omega,0} \to \Delta^{\mathrm{cav}}_\omega$. Owing to the large LO-phonon energy provided by ZnO, additionally $\hbar\Omega \gg \mathcal{G}$, $\hbar\Omega \gg \Delta^{\mathrm{cav}}_\omega$, and $\hbar\Omega \gg \gamma_{\{0,1\}}$ may be assumed. In these limits, the analytic expression for the PSB luminescence takes the simple form

$$\mathrm{Re}\left[\bar{\Pi}^{X,\,\mathrm{PSB}}_{1s,\mathbf{0},q_\perp}\right] \to \frac{\gamma_1\left[\chi_{\mathbf{0}} + \sum_{\mathbf{p}}\chi_{\mathbf{p}}\right]}{\left(\Delta^{\mathrm{cav}}_\omega\right)^2 + \gamma_1^2} \tag{3.12}$$

where $\chi_{\mathbf{p}}$ denotes the oscillator strength explicitly defined in Eq. (47) of Paper [IV]. The interesting aspect here is the denominator of the expression since it unambiguously substantiates that *the phonon cavity does not produce any splitting of the PSB$_1$ resonance*. Instead, it enhances the PSB_1 luminescence, which can be applied to increase the visibility of the PSB emission. Close to the cavity resonance, the expression (3.12) simplifies further since $\Delta^{\mathrm{cav}}_\omega$ then vanishes.

To prove the correctness of the derived analytic model graphically as well, Fig. 3.6 illustrates the resulting PL spectra for the $1s$ cavity and the phonon cavity. In both frames, the black-solid line shows the respective PL spectrum including the ZPL and PSB_1 contributions and the corresponding mode function, illustrated by the gray-solid line. The vertical black-dashed lines indicate the energetic positions of the ZPL and the PSB_1. The latter is located 72 meV below the ZPL. The cavity is chosen to be resonant with the ZPL using the $1s$ cavity, see frame **(a)**, or the PSB_1 with the phonon cavity shown in frame **(b)**. The cavity resonances are clearly visible by the peak position of the corresponding mode function in each frame. This shows that the analytic model is capable of reproducing the features of the fully numerical analysis presented in Fig. 3.2. In particular, the $1s$ cavity produces a pronounced splitting of the ZPL whereas the phonon cavity considerably enhances the PL at the PSB_1, while no splitting is observed.

3.4.2 Intensity behavior of the photoluminescence

After the steady-state photon flux and cavity effects for different resonance energies are computed and reproduced correctly, the investigation of the intensity dependence on the cavity configuration and quality remains to be verified. Indeed, the analytic model can be directly applied to derive the integrated photoluminescence shown in Fig. 3.4 and to investigate it in dependence of the cavity-mode strength. In order to characterize the overall ZPL and PSB_1 luminescence, the ZPL and PSB_1 part are integrated separately, i.e.,

$$\mathscr{I}^{\{\mathrm{ZPL},\,\mathrm{PSB}\}}_{\{1s,\,\mathrm{ph}\}}(\eta) = \int_{-\infty}^{\infty} I_{\mathrm{PL}}^{\{\mathrm{ZPL},\,\mathrm{PSB}\}}(\omega)\,\mathrm{d}\omega \tag{3.13}$$

where the upper indices indicate the respective contribution to the luminescence (ZPL or PSB). It is customary to assume a unitless Lorentzian

$$|u(\omega)|^2 = \frac{\mathcal{E}_0}{\pi}\frac{\eta}{(\hbar\omega - \hbar\omega_{\mathrm{cav}})^2 + \eta^2} \tag{3.14}$$

for the mode function with energy amplitude $\mathcal{E}_0$ and the half width at half maximum (HWHM) defined by η. In the present analysis, the resonance $\hbar\omega_{\mathrm{cav}}$ coincides with the $1s$ cavity (subindex "$1s$") or phonon cavity (subindex "ph"). Assuming enhanced cavity influence, the integrated luminescence eventually yields

$$\mathscr{I}^{\mathbf{ZPL}}_{\boldsymbol{1s}}(\boldsymbol{\eta}) \to \frac{\boldsymbol{\mathcal{E}_0\eta}}{\boldsymbol{\mathcal{G}^2}}\boldsymbol{\Delta N_{1s,0}} \tag{3.15}$$

$$\mathscr{I}^{\mathbf{PSB}}_{\mathbf{ph}}(\boldsymbol{\eta}) \to \sum_{\mathbf{p}} \frac{\boldsymbol{\mathcal{E}_0\chi_{\mathrm{p}}}\left[\boldsymbol{\Delta E_{\mathrm{p}}}\,\boldsymbol{\gamma_0} + \boldsymbol{\gamma_1\hbar\Omega}\right]}{\left[\boldsymbol{(\Delta E_{\mathrm{p}})^2} + \boldsymbol{\gamma_1^2}\right](\boldsymbol{\hbar\Omega})^2} \tag{3.16}$$

Integrated photoluminescence intensities of ZPL and PSB in the strong-cavity limit

where $\Delta E_{\mathbf{p}} = E_{1s,\mathbf{p}} - E_{1s,\mathbf{0}}$. Equation (3.15) denotes the intensity of the ZPL with $1s$ cavity while for the phonon cavity, the first-phonon-sideband PL is given by Eq. (3.16). As the cavity η is the HWHM of the mode function which narrows for increasing number of DBR layers, and thus the quality of the cavity, η decreases for enhanced reflectivity. Then, the linear proportionality of the ZPL intensity to the cavity η shows that the overall NMC PL decreases for enhanced cavity in the $1s$-cavity case. The situation is different for the PSB_1 intensity (3.16) with the phonon cavity where a saturation to a constant level sets in, unlike Eq. (3.15).

These mathematical findings already reveal that the results of Fig. 3.4 are—at least qualitatively—reproduced and confirm that the cavity changes exciton and phonon resonance differently when tuned to coincide with the respective frequencies. For a quantitative analysis, the integrated luminescence spectra is plotted in Fig. 3.7 in the same way as the fully numerical results presented in Fig. 3.4. The yellow-solid line shows the intensity of the ZPL photoluminescence using the $1s$ cavity and the black-solid line represents the PSB_1 intensity for the phonon cavity. Also the total intensity is shown where the ZPL and the PSB_1 luminescence are integrated using the phonon cavity (gray-dashed line). The mode-function maximum is indicated by the blue-dashed line. Looking at the yellow-solid line, the ZPL intensity first increases but then starts decreasing at the point when the exciton resonance splits due to the transition into the nonperturbative regime. While the mode-function maximum increases exponentially, the PSB_1 shows a clear saturation, as expected from the fully numerical computations. The complete PL intensity for the phonon cavity depicted by the gray-dashed line shows again that for a high reflectivity, the PSB_1 emission obviously dominates the system. The x-axis on the bottom shows the reciprocal of the mode function's line width η while the corresponding number of DBR-mirror pairs from the fully numerical computation is shown at the top x-axis.

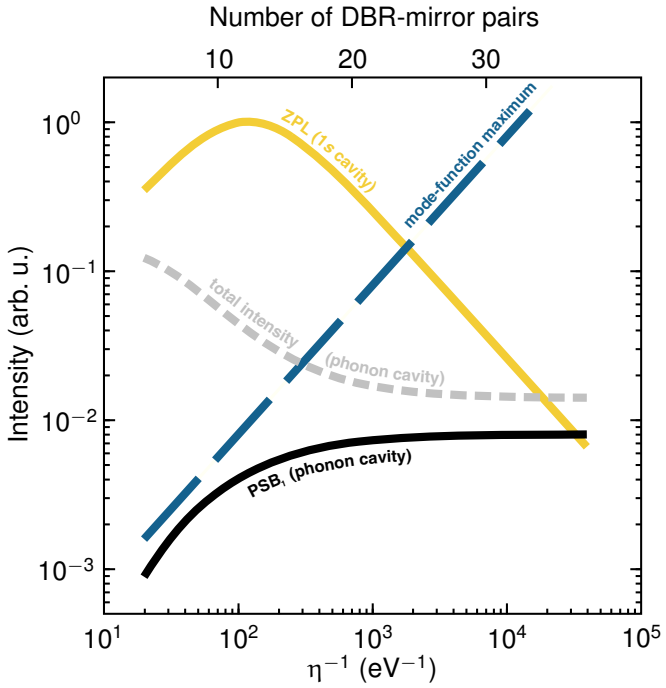

Figure 3.7 | Intensity of the photoluminescence spectrum (analytic model). Similar to Fig. 3.4, the yellow-solid line represents the intensity of the exciton resonance (ZPL) when using the 1*s* cavity and the black-solid line shows the intensity of first phonon sideband (PSB_1) with phonon cavity. The gray short-dashed line shows the total intensity for the phonon cavity and the long-dashed blue line represents the mode-function maximum. The top *x*-axis indicates the number of DBR-mirror pairs that correspond to the mode-function HWHM at the bottom *x*-axis.

4

Phonon-assisted luminescence of polar semiconductors: Fröhlich coupling versus deformation-potential scattering

In the previous chapter, the theoretical framework introduced in Chap. 2 has been applied to explore phonon-assisted emission in the semiconductor luminescence spectrum where the exciton resonance or zero-phonon line (ZPL) is accompanied by the first phonon sideband (PSB_1) arising at one LO-phonon energy below the ZPL. The computed spectra of this theoretical study have been subjected to the concept of a microcavity giving rise to considerable changes of the overall photoluminescence (PL) spectrum.

In the present chapter, the impact of a microcavity is not pursued further. Instead, the particular emphasis is put on the origin of exciton–phonon interaction in polar semiconductors. Phonon sidebands provide an appropriate measure to probe, e.g., the carrier–phonon interaction [168, 184, 193, 194] in semiconductors. The intensity ratios of ZPL and PSBs strongly depend on the exciton–phonon coupling. On the basis of the Franck–Condon principle [195–198], the coupling is expressed via the Huang–Rhys factor [176, 199]. In the presence of carrier–carrier Coulomb scattering it is indispensable to also incorporate the phonon-conditioned coupling in the description of an interacting many-body system as it plays a central role in the formation [29] of truly bound electron–hole pairs, i.e., excitons. Against this background, phonon-assisted PL measurements are performed. The spectra are investigated with respect to the temperature dependence of the relative sideband ratios of the first (PSB_1) and the second (PSB_2) phonon sideband. Additional studies of the pump-power dependence corroborate the results. For the investigation, the binary compounds zinc oxide (ZnO), cadmium sulfide (CdS), and zinc sulfide (ZnS) are used. All three are typical representatives for polar wide-gap semiconductors exhibiting strong electron–phonon- and Coulomb-interaction effects [158, 200–202]. The measurements are analyzed and validated by a rigorous many-body approach.

The results presented in this chapter are published in Paper [III]. The experiments have been performed by Dr. Alexey A. Chernikov[1,2] and Verena Bornwasser[1] from the groups of Professor Martin Koch[1] and Priv.-Doz. Sangam Chatterjee, PhD.[1] The samples have been provided by Dr. Thomas Wassner[3] and the groups of Professors Martin Eickhoff[4] and Bruno K. Meyer.[4]

4.1 Interaction mechanisms of LO phonons in semiconductors

Inelastic scattering between charge carriers and lattice vibrations in semiconductors may be described by various types of electron–phonon interaction, namely the *Fröhlich interaction* [173–177] for longitudinal-optical phonons, the *piezoelectric effect* for acoustic phonons [176], and the *deformation-potential scattering* [176–180] for both acoustic and optical phonons. From a theoretical point of view, the corresponding matrix elements enter at the early stage of the corresponding carrier–phonon-coupling Hamiltonian (2.15). In this section, both mechanisms are briefly introduced and presented within the physical framework.

[1] Philipps-Universität Marburg (Germany).
[2] (present address:) Columbia University in the City of New York, NY (USA).
[3] Walter Schottky Institut, Technische Universität München, Garching (Germany).
[4] Justus-Liebig-Universität Gießen (Germany).

If the unit cell consists of more than one atom, optical phonons are present in the system as well. Since this work concentrates on the investigation of two-element compounds, the analysis is restricted to the diatomic case. A close inspection of the generic phonon-matrix element shows that in the long-wavelength limit, electrons are solely scattered by longitudinal phonons [47]. The long-wavelength LO phonons involve uniform displacements of oppositely charged ions within a unit cell causing the ions to oscillate against each other. This eventually generates a macroscopic electric field in the structure. The interaction of this longitudinal electric field with the electrons can then be modeled in a very similar way as for the piezoelectric field of acoustic phonons caused by strain in non-centrosymmetric structures [176]. The relative displacement $\Delta\boldsymbol{\kappa}(\mathbf{R}) = \boldsymbol{\kappa}_1(\mathbf{R}) - \boldsymbol{\kappa}_2(\mathbf{R})$ results in a macroscopic polarization $\Delta\mathbf{P}$ oriented parallel with respect to the relative displacement. This polarization creates a Coulomb-mediated macroscopic field in the unit cell (shaded square) at $\mathbf{R}$, compare Fig. 4.1 **(a)** where the described lattice perturbation among anions (large spheres) and cations (small spheres) in a polar crystal is schematically illustrated. Since the potential energy of a particle in an electric field depends on its charge but not on other inherent properties like, e.g., its effective mass, band-independent matrix elements are observed in this case. Optical phonons displace the ions in opposite directions to each other, thus leading to a typical $1/|\mathbf{p}_{3\mathrm{D}}|$ dependence of the matrix element which conditions the electron–phonon interaction. As a result, the effective interaction displays a characteristic Coulombic behavior leading to the so-called *Fröhlich model* for lattice vibrations. Within the scope of the polaron transformation [47, 49], the related electron–phonon-coupling element [174] can readily be formulated as

$$\left|g_{\mathbf{p}_{3\mathrm{D}}}^{\lambda,\,\mathrm{Fröhlich}}\right|^2 = \frac{e^2}{2\varepsilon_0\,\hbar\Omega\,\mathcal{L}^3}\frac{1}{|\mathbf{p}_{3\mathrm{D}}|^2}\left[\frac{1}{\varepsilon(\infty)} - \frac{1}{\varepsilon(0)}\right],\ \lambda = \{c,\,v\} \tag{4.1}$$

Fröhlich-coupling matrix element for the electron–phonon interaction

where c and v represent conduction and valence bands, respectively. The matrix element (4.1) contains the LO-phonon energy $\hbar\Omega$, the electron charge $-|e|$, vacuum permittivity ε_0, normalization volume $\mathcal{L}^3$, and the transferred momentum $\hbar\mathbf{p}_{3\mathrm{D}}$ between charge carrier and LO phonon. Here, the matrix element is given as a unitless quantity and thus multiplied by $\hbar\Omega$ in the Hamiltonian (2.15). The square of the absolute value of the Fröhlich-interaction-matrix element is proportional to the vacuum matrix element $V_{\mathbf{p}_{3\mathrm{D}}} = \frac{e^2}{\varepsilon_0\mathcal{L}^3}\frac{1}{|\mathbf{p}_{3\mathrm{D}}|^2}$ of the Coulomb interaction, showing a strong dependence on the wavevector $\mathbf{p}_{3\mathrm{D}}$ [176]. Owing to the characteristic momentum dependence, the effective coupling strength can be considered *short-ranged* in momentum space and thus long-ranged in real space. Thus, this scattering mechanism is most efficient for the transfer of small momenta among electrons and phonons and decays for large momenta. The shaded area in Fig. 4.1 **(c)** illustrates this behavior by showing the relative coupling strength in dependence of the phonon momentum. As can be seen, the Fröhlich-coupling matrix element (4.1) is proportional to the difference of the inverse relative permittivities of low, $\varepsilon(0)$, and high, $\varepsilon(\infty)$, frequencies. In the low-frequency regime, the effective interaction is caused due to all charges including ions in the crystal structure. For high frequencies, the ions cannot follow the fast oscillations of the electric field anymore such that basically only the electronic contribution to the screening remains. Therefore, the relative permittivity for high frequencies describes the screening contribution of all charges except the vibratory ions.

In general, the Fröhlich interaction is presumably the most prominent carrier–phonon scattering mechanism [173–175, 203] and commonly used also for the description of exciton–phonon coupling in semiconductors [204–207]. The Fröhlich model is typically applied to describe surface-related phonon scattering [208], vibrational properties of low-dimensional systems [209], and coupling to polaritons [171, 210]. Owing to the attractive interaction of electrons and holes, however, it can be considered strong for a single carrier but may be much less efficient for a correlated electron–hole pair. This partial cancellation is a result of the opposite charges of electrons and holes within excitons [130, 211–213] since a correlated electron–hole pair in its entirety is an electrically neutral compound, rendering interaction with polar LO modes weak. Indications for this behavior have already been reported, e.g., on exciton–phonon scattering in confined quantum-dot systems [214–216].

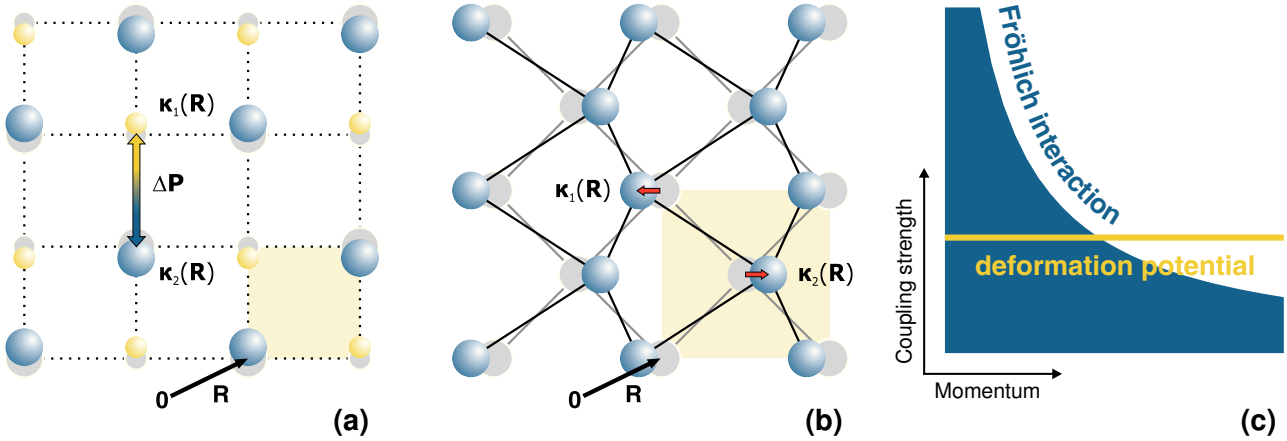

Figure 4.1 | Fröhlich interaction and deformation potential. (a) In polar crystals, LO phonons generate macroscopic polarization fields between anions (large spheres) and cations (small spheres), leading to Fröhlich-type phonon interaction. The induced polarization $\Delta\mathbf{P}$ in the unit cell (shaded square) at $\mathbf{R}$ is then parallel to the relative displacement. **(b)** In nonpolar crystals, optical phonons alter the electronic band energies by changing bond lengths and angles which can be described by deformation potential. In both figures, the equilibrium positions of the atoms are indicated by the gray-shaded circles. **(c)** Momentum dependency of Fröhlich interaction and deformation potential.

Owing to the polarization buildup when the oppositely charged ions are displaced against each other, electron–phonon coupling induced by Fröhlich interaction can only be present in polar semiconductors such as gallium arsenide (GaAs) and gallium phosphide (GaP) [180, 181]. Additionally, it is particularly strong in wide-gap materials like CdS, ZnO, and gallium nitride (GaN) [151]. Nevertheless, in non-polar semiconductors, LO phonons can still distort the lattice. This changes the electronic energies leading to an effective electron–phonon interaction. In the case of non-polar semiconductors such as germanium (Ge) and silicon (Si) [217], the coupling mechanism can be modeled via the so-called *deformation-potential scattering*. Contrary to acoustic phonons which stretch or compress the crystal due to a macroscopic distortion of the lattice, optical phonons vary the bond lengths and bond angles. This is depicted in Fig. 4.1 **(b)** where the unit cell at $\mathbf{R}$ is again indicated by the shaded area. For small distortions, the relative displacement is linear in $\Delta\boldsymbol{\kappa}(\mathbf{R})$. Theoretically, the optical deformation potential can be described via the difference between the crystal potential in the distorted lattice and that in the undeformed lattice [178], weighted by the explicitly *band-dependent* optical deformation-potential constants $d^{\lambda}_{\mathrm{opt}}$. In practice, it is customary to neglect the arising angle dependence associated with the optical deformation potential and use the angle-averaged quantity

$$\left|g^{\lambda,\text{opt. def.}}\right|^2 = \frac{1}{2\rho\mathcal{L}^3\,\hbar\Omega^3}\,\frac{(M_1+M_2)^2}{2M_1M_2}\,\frac{|d^{\lambda}_{\mathrm{opt}}|^2}{a_{\mathrm{L}}^2} \tag{4.2}$$

Optical-deformation potential for the electron–phonon interaction

which is given here as the (physical) quantity with the square of the absolute value. Beside the deformation-potential constant $d^{\lambda}_{\mathrm{opt}}$, normalization volume $\mathcal{L}^3$, and LO-phonon energy $\hbar\Omega$, the matrix element contains the lattice constant a_{L}, the density of the material ρ as well as masses M_1 and M_2 of the constituent atoms. Notably, the deformation-potential coupling-matrix element (4.2) exists only for the valence band. Owing to symmetry reasons in direct semiconductors, there is no deformation potential among electrons in the lowest conduction band and optical phonons [181,218]. Thus, d^{c}_{opt} vanishes while d^{v}_{opt} has a finite value in the range of some 10 eV and is also often denoted as $d_0 \equiv d^{v}_{\mathrm{opt}}$ in the literature.

The authors of Ref. [219] apply a tight-binding approach to calculate the optical deformation potentials for several tetrahedral semiconductors in diamond and zincblende structure and obtain a value of $d^{v} = 39.8\,\mathrm{eV}$

for ZnO and $d^v = 23.7\,\mathrm{eV}$ for CdS. In the experiments, wurtzite-structure materials are used such that these values must be converted. The authors of Ref. [220] present a general derivation of the deformation potential in wurtzite- and zincblende-type semiconductors and suggest a conversion rule connecting both systems. With this procedure, it is possible to calculate the wurtzite-structure deformation-potential coupling constants $d^v_{\mathrm{ZnO}} = 49.7\,\mathrm{eV}$ and $d^v_{\mathrm{CdS}} = 29.6\,\mathrm{eV}$ which are used in our theoretical approach. The value of ZnS in zincblende structure is $d^v = 30.4\,\mathrm{eV}$ which results in $d^v_{\mathrm{ZnS}} = 38.0\,\mathrm{eV}$ for wurtzite-type ZnS.

The deformation of the lattice is a local effect in real space rendering the deformation-potential scattering almost constant in momentum space. As can be seen in Fig. 4.1 **(c)**, the deformation potential offers a smaller coupling strength for small momenta but can overtake the Fröhlich interaction for large momenta. While the Fröhlich interaction shows a pronounced momentum dependence, the deformation potential is uniformly distributed over all momenta. Therefore, deformation potential is *long-ranged* in momentum space [181] and almost independent of the system configuration, thus leading to only slight changes when comparing the effects on a single carrier or a correlated many-body system. In comparison to the Fröhlich interaction, the deformation potential is supposed to display a rather weak interaction strength in polar semiconductors and is thus mostly ignored in such materials. As can be shown [47], the Fröhlich-interaction-matrix element is real-valued whereas the deformation potential is intrinsically a purely imaginary quantity. This fact leads to the simple generalized form for the combined matrix element

$$\left|g^{\lambda,\,\mathrm{LO}}_{\mathbf{P}_{3\mathrm{D}}}\right|^2 = \left|g^{\lambda,\,\mathrm{Fröhlich}}_{\mathbf{P}_{3\mathrm{D}}}\right|^2 + \left|g^{\lambda,\,\mathrm{opt.\,def.}}_{\mathbf{P}_{3\mathrm{D}}}\right|^2 \tag{4.3}$$

showing that the contributions of the different coupling mechanisms can be evaluated separately and finally added up to form the resulting electron–phonon interaction.

These considerations lead to the question of which scattering mechanism is dominating in which material and how it can be modified by the interacting many-body system. Especially for the momentum-dependent Fröhlich interaction, partial or complete suppression may be anticipated. Under these circumstances, deformation potential would remain as the predominant carrier–phonon-interaction mechanism; in striking contrast to common opinion. In the next section, the microscopic aspects of these questions are scrutinized. In Sec. 4.3, the material systems and related experiments are elucidated and compared to the theoretical findings.

4.2 Theoretical description of exciton–phonon scattering

The derivation and theory behind the appearance of phonon-sideband emission in the semiconductor luminescence is introduced in the previous chapter and has been thoroughly discussed in the literature [47–49, 221]. In this section, the constituents of phonon-assisted luminescence including contributions up to the second phonon sideband are briefly recapitulated. Altering the carrier distribution in reciprocal space provides information about the dependence of the carrier–phonon-interaction strength on the transferred momentum. Temperature-dependent studies of the relative PSB ratios thus allow for the identification of the predominant exciton–phonon-coupling mechanism. Regarding studies of the temperature dependence of phonon sidebands appearing in the luminescence spectrum, it is sufficient to determine the first two emission replica. More details are given in Paper [III] and appendices therein. The resulting steady-state luminescence spectrum in free space follows from the summed photon flux that is proportional to

$$I_{\mathrm{PL}} = I_{\mathrm{ZPL}}(\omega) + I_{\mathrm{PSB}_1}(\omega) + I_{\mathrm{PSB}_2}(\omega) \tag{4.4}$$

with separate contributions for ZPL, PSB_1, and PSB_2. When the $1s$-exciton population dominates over electron–hole plasma sources [I, 50], the ZPL spectrum follows from the Elliott formula

$$I_{\mathrm{ZPL}}(\omega) = \mathrm{Im}\left[\frac{N_{\mathrm{ZPL}} - \delta N^{(1)}_{\mathrm{ZPL}} - \delta N^{(2)}_{\mathrm{ZPL}}}{E_{1s,\mathbf{0}} - \hbar\omega - \mathrm{i}\gamma_0}\right] \tag{4.5}$$

where a phenomenological dephasing γ_0 for the ZPL is used. The strength of $1s$ emission is defined by the exciton population $N_{\mathrm{ZPL}} = \Delta N_{1s,\mathbf{0}}$ at the vanishing momentum. In general, $\Delta N_{1s,\mathbf{Q}}$ defines the center-of-mass distribution of $1s$ excitons and is assumed to follow a Bose–Einstein distribution. In analogy to the previous chapter, the corresponding exciton energy $E_{\nu,\mathbf{Q}} = \mathcal{E}_\nu + E_{\mathbf{Q}}^{\mathrm{COM}}$ is defined as the sum of the exciton eigenenergy $\mathcal{E}_\nu$ and the center-of-mass energy $E_{\mathbf{Q}}^{\mathrm{COM}} = \frac{\hbar^2\mathbf{Q}^2}{2M}$ with COM momentum $\hbar\mathbf{Q}$ and total mass $M = m_\mathrm{e} + m_\mathrm{h}$. Additionally, the numerator of Eq. (4.5) features two corrections to the ZPL resulting from single-phonon-, $\delta N_{\mathrm{ZPL}}^{(1)}$, and two-phonon-, $\delta N_{\mathrm{ZPL}}^{(2)}$, assisted processes. The explicit forms are given by Eqs. (8) and (9) in Paper [III]. These corrections, however, influence the spectra only very slightly since the ZPL is several orders of magnitude larger than the phonon sidebands. Furthermore, the large LO-phonon energy largely attenuates the momentum dependence of the PSB corrections. Since only effects up to the second phonon sideband are included, no higher-order corrections alter the ZPL. Introducing phenomenological dephasings γ_1 and γ_2, the phonon-sideband contributions for PSB_1 and PSB_2 follow a similar form as Eq. (4.5) and read

$$I_{\mathrm{PSB}_1}(\omega) = \mathrm{Im}\left[\sum_{\mathbf{Q}} \frac{N_{\mathrm{PSB}_1,\mathbf{Q}} - \delta N^{(2)}_{\mathrm{PSB}_1,\mathbf{Q}}}{E_{1s,\mathbf{Q}} - \hbar\Omega - \hbar\omega - \mathrm{i}\gamma_1}\right], \tag{4.6}$$

$$I_{\mathrm{PSB}_2}(\omega) = \mathrm{Im}\left[\sum_{\mathbf{Q}} \frac{N_{\mathrm{PSB}_2,\mathbf{Q}}}{E_{1s,\mathbf{Q}} - 2\hbar\Omega - \hbar\omega - \mathrm{i}\gamma_2}\right]. \tag{4.7}$$

The magnitude of the PSB resonances is defined by $N_{\mathrm{PSB}_1,\mathbf{Q}}$ and $N_{\mathrm{PSB}_2,\mathbf{Q}}$ for the first and second PSB, and the correction $\delta N^{(2)}_{\mathrm{PSB}_1,\mathbf{Q}}$ to PSB_1 originating from PSB_2; consult Eqs. (15)–(17) of Paper [III] for explicit forms. The $\mathbf{Q}$ sum in Eqs. (4.6) and (4.7) discloses the discrete momentum transfer of each transition event, leading to the characteristic broadening of the high-energy tails in the PSB spectra [222]. Besides this momentum dependence, the system temperature, available phase-space for scattering processes, and phenomenological dephasings are also reflected by the high-energy flank of the PSB_1. These features mix nontrivially such that the slope is, in general, different for various PSBs. Thus, a direct extraction of the carrier temperature from the PSB-line shape is not feasible by, e.g., fitting a Boltzmann distribution to the high-energy flank of a PSB.

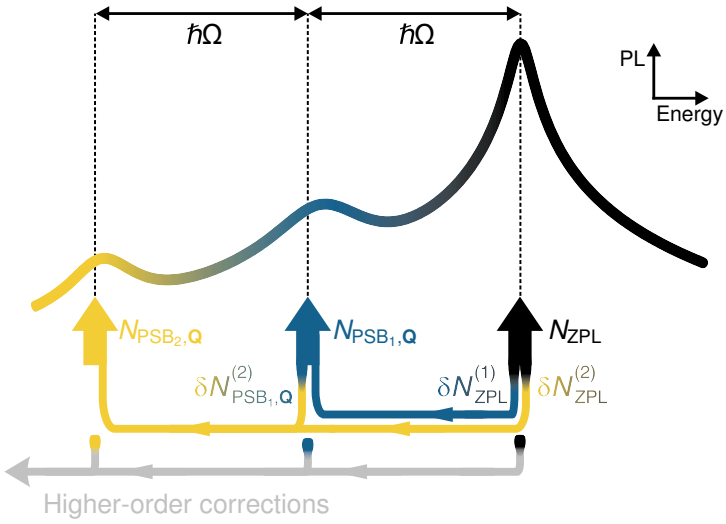

Figure 4.2 | Emission dynamics of phonon sidebands. Schematic representation of zero-phonon line (ZPL, black), first phonon sideband (PSB_1, blue), and second phonon sideband (PSB_2, yellow) emission dynamics. All sidebands are separated by the optical phonon energy $\hbar\Omega$. The respective emission strengths N are indicated by the upright arrows. The color-gradiented funnels refer to corrections δN of a sideband with respect to sidebands of lower order. Corrections resulting from higher-order sidebands are indicated in gray.

With the same reasoning as mentioned above, the photon flux of the PSB_1 is modified *only* by a correction stemming from the second PSB emission whereas the PSB_2 emission is not modified further. If higher-order PSBs are considered as well, all emission contributions $I_{\mathrm{PSB}_n}(\omega)$—including $n = 0$, i.e., the ZPL—will experience corrections from all other sidebands of order $n' > n$. However, the magnitude of correction decreases rapidly with increasing sideband order. As a general feature, the phonon-assisted corrections merely redistribute the emission among ZPL and the PSBs and it is straightforward to demonstrate that the total-PL intensity, $\int I_{\mathrm{PL}}\,\mathrm{d}\omega$, remains unchanged under phonon-assisted processes [223]. The interplay and connections among the different sideband contributions $N_{\mathrm{ZPL},\mathbf{Q}}$, $N_{\mathrm{PSB}_1,\mathbf{Q}}$, and $N_{\mathrm{PSB}_2,\mathbf{Q}}$ as well as associated corrections $\delta N^{(1)}_{\mathrm{ZPL}}$, $\delta N^{(2)}_{\mathrm{ZPL}}$, and $\delta N^{(2)}_{\mathrm{PSB}_1,\mathbf{Q}}$ are depicted in

Fig 4.2 where the PL is shown in dependence of the photon energy. Starting with the ZPL (black), corrections resulting from PSB_1 (blue/black colored) and PSB_2 (yellow/black colored) emerge. The first replica (blue) is then constructed via $N_{\mathrm{PSB}_1,\mathbf{Q}}$ and modified by corrections (yellow/blue colored) that eventually participate in the buildup of the PSB_2 (yellow). Possible higher-order corrections are indicated by the gray line whereas the corresponding modifications to ZPL, PSB_1, and PSB_2 are indicated by their respective colors. The included sidebands appear one and two phonon energies below the ZPL, respectively.

The phonon-related populations as well as the PSB corrections to the ZPL in Eq. (4.5) contain the exciton–phonon-coupling element $G^{\nu,\nu'}_{\mathbf{p}_{3\mathrm{D}}}$ providing the strength of coupling among excitons and phonons. Previous studies on the exciton–phonon scattering showed that the scattering probability $|G^{\nu,\nu'}_{\mathbf{p}_{3\mathrm{D}}}|^2$ exhibits significant coupling for combinations $(1s,1s)$ and $(1s,2p)$ [47]. Thus, G plays a central role in this approach. The many-body correlations induce significant modifications in the relative coupling strength of the carrier–phonon interaction when an intrinsic Coulomb-mediated dependence is present. Within the scope of the investigations presented in the previous chapter, G has already been introduced; compare Eq. (3.4). In the low-density regime, it is justified to replace the excitonic wavefunctions $\phi^{\{\mathrm{L,R}\}}_{\nu,\mathbf{Q}}(\mathbf{k})$ by $\phi_\nu(\mathbf{k})$. In case of the Fröhlich interaction, the matrix elements for conduction and valence band are equal. By setting $g^c_{\mathbf{p}_{3\mathrm{D}}} = g^v_{\mathbf{p}_{3\mathrm{D}}} \equiv g^{\text{Fröhlich}}_{\mathbf{p}_{3\mathrm{D}}}$ in Eq. (3.4), the exciton–phonon-matrix element for the Fröhlich coupling between excitons and phonons reads

$$G^{\nu,\nu',\,\text{Fröhlich}}_{\mathbf{p}_{3\mathrm{D}}} = \hbar\Omega\, g^{\text{Fröhlich}}_{\mathbf{p}_{3\mathrm{D}}} \sum_{\mathbf{k}'} \phi_\nu(\mathbf{k}') \left[\phi_{\nu'}(\mathbf{k}'+\mathbf{p}_\mathrm{h}) - \phi_{\nu'}(\mathbf{k}'-\mathbf{p}_\mathrm{e})\right]^\star . \tag{4.8}$$

where $\mathbf{p} = \mathbf{p}_\mathrm{e} + \mathbf{p}_\mathrm{h}$ with $\mathbf{p}_\mathrm{e} = \frac{m_\mathrm{e}}{m_\mathrm{e}+m_\mathrm{h}}\mathbf{p}$ and $\mathbf{p}_\mathrm{h} = \frac{m_\mathrm{h}}{m_\mathrm{e}+m_\mathrm{h}}\mathbf{p}$. Since $\phi_{\nu'}(\mathbf{k}' \pm \mathbf{p}_{\{\mathrm{h,e}\}}) \simeq \phi_{\nu'}(\mathbf{k}')$ for small phonon momenta $\hbar\mathbf{p}$, the wavefunctions in the bracketed term largely cancel each other in this momentum range. This leads to a very weak Fröhlich contribution for small phonon momenta $\hbar\mathbf{p}$. More precisely, this particularly affects the momentum range where Fröhlich is supposed to contribute most; see Fig. 4.1 **(c)**. As the deformation potential vanishes for the conduction band but not for the valence band, the partial cancellation does not apply for this scattering mechanism; compare Eq. (3.4) by setting $g^c_{\mathbf{p}_{3\mathrm{D}}}$ to zero. This means that only the Coulomb-mediated Fröhlich interaction experiences an appreciable reduction in coupling strength while the deformation potential remains unaffected by the many-body dynamics. *Notably, the Fröhlich interaction couples excitons with phonons less efficiently than the deformation potential does.* In other words, the Fröhlich interaction shows a strong coupling among carriers and LO phonons for an uncorrelated system but, however, becomes inefficient for a correlated many-body system. Figure 4.3 schematically illustrates this fact where uncorrelated, i.e., free, carriers (left figure) are compared with truly bound excitons (right figure). While the electric field of LO phonons may couple strongly to uncorrelated carriers, exciton–phonon coupling becomes ineffective and free movement of the single charge carriers is not possible anymore. For materials with large exciton binding energy and thus small Bohr radius as it is for, e.g., ZnO, this may lead to a quasi-neutral exciton and with this an even stronger suppression of the Fröhlich interaction. In this situation, this scattering channel couples excitons less efficiently with phonons and deformation potential may be the dominating scattering mechanism describing lattice vibrations in the system.

In addition to the individual analysis of the exciton–phonon-matrix element (3.4), the interplay with all remaining momentum- and temperature-dependent quantities leading to the buildup of the phonon sidebands needs a closer inspection. Equations (15) and (17) of Paper [III] reveal a dependence of the PSB-resonance magnitudes $N_{\mathrm{PSB}_n,\mathbf{Q}}$ scaling with $|G^{\nu,\nu'}_{\mathbf{p}}|^{2n}$ where n is the phonon-sideband order. This entails a squared behavior for the PSB_1 while the PSB_2 scales with the fourth power in the exciton–phonon-matrix element. In general, the strength of each involved interaction mechanism may be distinguished by the characteristic temperature dependence of the $\mathrm{PSB}_2/\mathrm{PSB}_1$-intensity ratio [47]. This ratio is influenced, firstly, by the distribution of carriers in momentum space, given by the temperature entering in the exciton population $\Delta N_{1s,\mathbf{Q}}$ and, secondly, by the dependence of the exciton–phonon-matrix element G on the transferred momentum. Naturally, increasing the temperature leads to population of excitons also favoring higher momenta (dark excitons). In turn, the phonon-matrix element (4.1) decreases for increasing momenta. These opposed behaviors—increasing high-momenta exciton populations for rising temperature versus weakened exciton–phonon scattering for larger momenta—

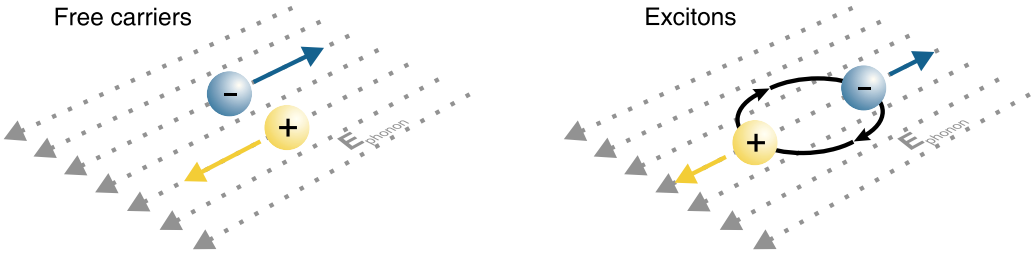

Figure 4.3 | Free carriers versus excitons in the presence of phonons. In the case of uncorrelated (free) carriers, electrons and holes move separately in the phonon-induced electric field (left figure). The exciton constituents, however, show Coulomb attraction and repulsion, respectively. The center-of-mass scattering is then strongly suppressed which results in a less efficient Fröhlich interaction for excitons and phonons (right figure). The picture is based on the illustration presented in Ref. [224].

are expected to lead to a PSB_2/PSB_1-intensity ratio which decreases with increasing temperature when the momentum-dependent Fröhlich interaction dominates. In case of the momentum-independent deformation-potential scattering, the phonon-matrix element (4.2) is constant and thus independent of the $\mathbf{p}$ and $\mathbf{Q}$ sums in Eqs. (4.6)–(4.7) and Eqs. (16)–(17) of Paper [III]. Hence, it does not impinge upon the temperature distribution of the carriers, leaving this parameter completely unaffected, which results in a temperature-independent PSB_2/PSB_1-intensity ratio.

As a core statement, it can be concluded that a strongly temperature-dependent second-to-first phonon-sideband dependence is expected for the polar exciton–phonon coupling while theory predicts a ratio that remains completely unaffected by a temperature sweep for materials where the deformation-potential scattering dominates. Consequently, the PSB_2/PSB_1-intensity ratio offers an experimentally accessible method to determine the dominating coupling mechanism in a material and identify the nature of exciton–phonon interaction in semiconductors. In an experiment, the temperature may be controlled and adjusted via the lattice temperature and/or excitation conditions.

4.3 Experiments and results

To prove the theoretical predictions, three typical polar, wide-gap bulk materials, namely ZnO, ZnS, and CdS, are used for the experimental investigations. All exhibit large exciton binding energies [225] thus favoring the formation of excitons before phase-space-filling effects lead to ionization and elimination of these states. This allows excitonic-emission measurements below the Mott transition [2,180,226]. The chosen samples have thicknesses 0.3 µm (ZnO), 0.1 µm (ZnS), and 10 µm (CdS); see Sec. III of Paper [III] for further details. Following the theoretical insights of the previous section, time-resolved PL is measured by applying a short-pulse interband excitation and evaluating the spectrally and temporally integrated PSB intensities. In the measurements, an excitation density of $n_0 = 10^{11}\,\mathrm{cm}^{-2}$ photons per pulse is used corresponding to an injected carrier density well below the estimated Mott densities [180, 226] for these materials; an essential criterion for the formation of correlated electron–hole pairs, i.e., excitons. Preliminary studies on the samples reveal signatures of free and donor-bound excitons in the PL spectra of our samples [224]. However, owing to ionization of donor-bound excitons with rising temperature, these resonances are only visible for low temperatures. Relating to the spectral spacing of the PSBs by multiples of the LO-phonon energy, the observed phonon replica are clearly attributed to the free-exciton transition. The weak participation of donor-bound excitons as well as the broad temperature range of PSB-emission signatures render the samples as ideal candidates for the intended investigations.

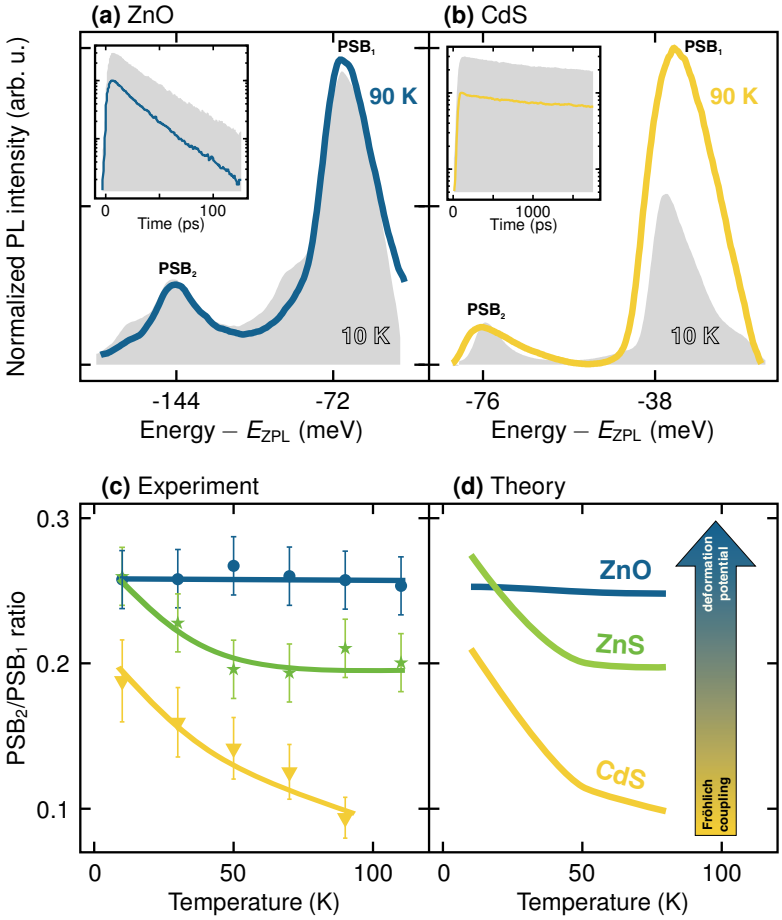

Figure 4.4 | Temperature dependence of PL spectra and phonon-sideband ratios. *Top*: time-integrated PL spectra of first and second PSB at lattice temperatures of $T = 10\,\mathrm{K}$ (shaded) and $T = 90\,\mathrm{K}$ (solid) for **(a)** ZnO and **(b)** CdS. Insets show the emission dynamics of PSB_2 for both temperatures. The excitation density is $n_0 = 10^{11}$ photons/cm^2 per pulse. *Bottom*: **(c)** experimental PSB_2/PSB_1 ratios versus lattice temperature for ZnO (blue circles), ZnS (green stars), and CdS (yellow triangles) for the same excitation density as in **(a)** and **(b)**. Solid lines are guides to the eye. Frame **(d)** shows the ratios computed via the many-body approach. The vertical arrow indicates the development of exciton–phonon scattering.

The top row of Fig. 4.4 shows time-integrated PL spectra of the phonon resonances for **(a)** ZnO and **(b)** CdS assuming two different lattice temperatures of $T = 10\,\mathrm{K}$ (shaded) and $T = 90\,\mathrm{K}$ (solid line). For better comparability, the spectra are normalized with respect to the PSB_2 peak and energetically shifted with respect to the corresponding ZPL. The ZnO spectrum measured at $T = 10\,\mathrm{K}$, shown by the shaded area in Fig. 4.4 **(a)**, additionally shows weak signatures at the low-energy flanks of the (free-exciton related) phonon replica, which can be attributed to donor-bound excitons. As mentioned above, these signatures vanish rapidly with rising temperature. As a result of momentum conservation [21, 227–231], mixed exciton–photon states known as *polaritons* [21, 114, 231, 232] build up in bulk semiconductors. These are predominantly reflected at the surface and may propagate through the crystal. Under suitable conditions, however, photon emission can occur rendering the near-band-edge PL strongly dependent on surface properties [180]. Since the PSB replica, but not the ZPL, are of sole importance for the studies performed here, the ZPL is neglected in the analysis by consistently fitting the bound-exciton resonances with Lorentzians and subsequently subtracting them from the measured spectra [224]. This eventually reveals the genuine spectral shape of the phonon sidebands. An obvious distinction may be seized when comparing the relative ratio of second and first phonon sideband in both spectra. This ratio remains constant for both temperatures in case of ZnO shown in frame **(a)** but exhibits a clear reduction in case of CdS presented in frame **(b)**. The insets of Figs. 4.4 **(a)** and **(b)** show the time-resolved transients of the PSB_2 emission clearly demonstrating a single-exponential decay and thus confirming exciton-related PL [I, 51] without additional thermal activation of further recombination channels.

To quantify the observations, the lower frames of Fig. 4.4 present temperature-dependent PSB_2/PSB_1 ratios of ZnO, ZnS, and CdS. The experimental data in frame **(c)** is compared with the many-body computations in frame **(d)**. Without applying any fitting procedures, the experimentally obtained results are in perfect match with the theoretical predictions and clearly show that the ratio remains constant for ZnO but strongly decreases for CdS. ZnS shows an intermediate behavior. The theoretical results are computed by calculating the relative contributions of Fröhlich and deformation-potential coupling using typical material parameters from the literature [219, 220, 233, 234]. At the basis of these well-known and well-proven parameters, the computed effects may be considered as fundamental and inherent features of the investigated material systems. According to the considerations presented in the previous section, the temperature-independent behavior of ZnO stems from deformation-potential scattering while CdS is dominated by the polar exciton–phonon coupling via Fröhlich interaction. Besides this, ZnS is governed by a mixture of both mechanisms. The vertical arrow in Fig. 4.4 **(d)** indicates the development of exciton–phonon scattering in the three investigated materials.

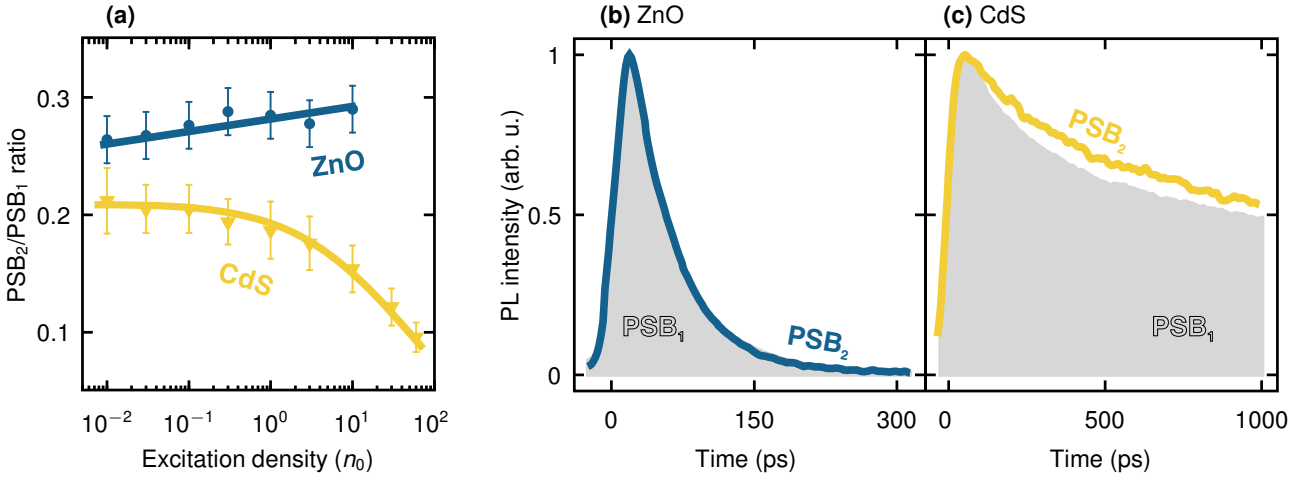

Figure 4.5 | Second-to-first sideband ratio versus excitation density. (a) PSB_2/PSB_1 ratios for ZnO (blue circles) and CdS (yellow triangles) at $T = 10$ K. n_0 corresponds to a photon flux of 10^{11} photons/cm^2 per pulse. Solid lines are guides to the eye. Normalized PL dynamics of PSB_1 (shaded area) and PSB_2 (solid line) for **(b)** ZnO and **(c)** CdS.

As a last evidence of these striking findings, the pump-power dependence of the PSB emission is investigated. Increasing the excitation density may lead to generation of a considerable non-equilibrium phonon population, known as the *hot-phonon effect* [43]. As a result of reabsorption of phonons by carriers, this leads to an increasing carrier temperature and thus to a population of high-momentum exciton states. According to this argumentation, the excitation-density dependence constitutes another way to detect the exciton–phonon scattering mechanism when comparing second-to-first phonon-sideband ratios. The results are shown in Fig. 4.5 **(a)** at 10 K as function of excitation density in units of n_0 as defined before. While ZnO shows only a slight increase for higher carrier densities, the ratio of CdS decreases almost by a factor of two, corroborating the previous results. Frames **(b)** and **(c)** additionally confirm these different behaviors. Here, the relative PL dynamics of PSB_1 (shaded) and PSB_2 (solid line) are compared for both materials. In case of ZnO, the time-dependent traces are equal while they differ from each other for CdS. Thus, *Fröhlich interaction prevails in CdS while exciton–phonon scattering in ZnO is dominated by deformation-potential scattering*.

Yet, since all three materials show pronounced polar features, it is needed to be mentioned that scattering among *single electrons* and optical phonons is still dominated by Fröhlich coupling in all investigated cases. Only the strong Coulomb coupling of electrons and holes renders deformation potential the dominant mechanism in ZnO.

The Inner Horizon V

See page XLIV for reference.

5

Magnetic-field control of terahertz and Coulomb interactions among excitons

Exciting a semiconductor with an optical pulse whose frequency is energetically close to the fundamental absorption edge generates a coherent polarization. As a result of light–matter and many-body interaction, this polarization decays radiatively or is converted into quasi-particle excitations such as bound pairs, i.e., excitons, as plasma, or a mixture of both. Interband spectroscopy, though, cannot monitor the existence of incoherent populations directly [71], as these quasi-particles do not directly couple to the light field. The exciton binding energies and transition energies between exciton states fall in the frequency range of terahertz (THz). Thus, THz fields may efficiently probe these systems [66] and induce controlled transitions between exciton states [69,135, 137–139]. Besides this, the Coulomb interaction plays a crucial role in interacting many-body systems. Recent works [59] reveal that an effective $1s$-to-$2p$ exciton-population transfer is accompanied by the emergence of a (initially unexcited) $2s$ population. As a direct $1s$-to-$2s$ transition is dipole-forbidden with respect to THz fields, this population transfer could unambiguously be attributed to diffusive Coulomb scattering.

The binding energy of an exciton provides information about the strength of the Coulomb interaction. On the other hand, its response to internal and external fields reveals facts about polarizability. Applying a two-color excitation using near-infrared and THz pulses, it is thus an interesting challenge to investigate how a magnetic field affects excitons and the Coulomb-mediated, THz-induced intra-exciton transitions. Applying a strong magnetic field gives rise to notably confined electronic states [235,236]. This allows to trace the transition from systems without magnetic field to substantial confinement effects: For vanishing magnetic field, the Coulomb interaction leads to the usual quantum-confined hydrogen eigenstates. At the limit of strong magnetic field, the eigenenergies are energetically equally spaced Landau orbitals. Bringing both the Coulomb interaction and a magnetic field into effect, however, leads to the generation of so-called *magnetoexcitons* [235–238]. Besides substantial changes to the wavefunctions and overlap among these, the eigenenergies show a typical splitting in close analogy to the Zeeman splitting [239] known from atomic physics.

The experiments have been performed by Dr. Jayeeta Bhattacharyya,[1] Sabine Zybell,[1,2] and Faina Lomakina[1,2] from the groups of Priv.-Doz. Dr. Harald Schneider[1] and Professor Manfred Helm.[1,2] The samples have been provided by A. M. Andrews, PhD[3] and Professor Gottfried Strasser.[3] The theory part is a collaboration between Dr. Lukas Schneebeli, Benjamin Breddermann, and me. The work is divided as follows: While I have set up the total Hamiltonian by expanding Hamiltonian (2.10) by magnetic-field effects and derived the generalized Wannier equation, Benjamin Breddermann has included excitation-induced dephasing (EID) contributions to the eigenvalue problem. This part is mainly presented in Sec. 5.1 and reflected in Figs. 5.1, 5.4, and 5.7. Based on the exciton wavefunction- and eigenvalue-related quantities, Dr. Lukas Schneebeli has solved the exciton dynamics (5.10) and derived the resulting photoluminescence spectra (5.12), pictured in Fig. 5.6.

This project had not been finished completely until the submission of this thesis. The corresponding manuscript for Paper [VII] has just been submitted and reveals more intriguing details and figures.

[1]Institute of Ion Beam Physics and Materials Research, Helmholtz-Zentrum Dresden–Rossendorf (HZDR), Dresden (Germany).
[2]Technische Universität Dresden (Germany).
[3]Institute of Solid State Electronics, Technische Universität Wien (Austria).

5.1 Excitons in magnetic field

The proper description of an interacting many-body system subjected to a magnetic field follows from the quantum-electrodynamical Hamiltonian (2.10), rigorously expanded to fully include linear and nonlinear magnetic-field contributions. Additionally, also terahertz effects are included to describe both constant magnetic field $\mathbf{B}$ and THz field $\mathbf{E}_{\mathrm{THz}}$ by a common vector potential $\mathbf{A} = \mathbf{A}_0 + \mathbf{A}_{\mathrm{THz}}$. If all excitations exist close to the Γ point, the magnetic-field effects follow from the effective-mass approximation [240]. The justification of this approach becomes clear when considering the magnetic length $l_{\mathrm{mag}} = \sqrt{\hbar/(eB)}$ which is the radius of the classical cyclotron orbit. Via $2\pi l_{\mathrm{mag}}^2$, it defines the area that contains one quantum of magnetic flux. Even for large magnetic fields, l_{mag} is in the range of 10–100 nm, i.e., much larger than the lattice constant [241]. Hence, the effective-mass approximation with parabolic bands in the vicinity of the Γ point is a reasonable choice in this situation. For the description of excitonic effects, basically, the exciton eigenvalues E_λ and eigenfunctions $\phi_\lambda(\mathbf{r})$ of eigenstate λ are needed. These follow from a generalized Wannier equation [2,113] which is discussed in Sec. 5.1.2. Before solving the excitonic eigensystem, the total-system Hamiltonian is developed.

5.1.1 Two-body problem subjected to magnetic field

To have a well-defined situation, the derivation starts from Hamiltonian (2.10) with minimal substitution and Coulomb gauge. Separating real-space coordinates of electron and hole, it takes the expanded form

$$\hat{H} = \frac{\mathbf{p}_{\mathrm{e}}^2}{2m_{\mathrm{e}}} + \frac{\mathbf{p}_{\mathrm{h}}^2}{2m_{\mathrm{h}}} + |e|\left[\frac{\mathbf{A}(\mathbf{r}_{\mathrm{e}})\cdot\mathbf{p}_{\mathrm{e}}}{m_{\mathrm{e}}} - \frac{\mathbf{A}(\mathbf{r}_{\mathrm{h}})\cdot\mathbf{p}_{\mathrm{h}}}{m_{\mathrm{h}}}\right] + \frac{e^2\mathbf{A}^2(\mathbf{r}_{\mathrm{e}})}{2m_{\mathrm{e}}} + \frac{e^2\mathbf{A}^2(\mathbf{r}_{\mathrm{h}})}{2m_{\mathrm{h}}} - V(\mathbf{r}_{\mathrm{e}} - \mathbf{r}_{\mathrm{h}}) \tag{5.1}$$

where the free-light-field Hamiltonian (2.8) is neglected for now. Equation (5.1) defines a two-body problem that is presented here in the real space. The Coulomb interaction is then $V(\mathbf{r}) = \frac{e^2}{4\pi\epsilon_{\mathrm{r}}\varepsilon_0|\mathbf{r}|}$. Since both electron and hole can move, Eq. (5.1) must be solved as a genuine two-body problem. To properly account for this configuration, it is reasonable to introduce relative ($\mathbf{r}$) and center-of-mass ($\mathbf{R}$) coordinates

$$\begin{aligned}
&\mathbf{R} = \frac{m_{\mathrm{e}}}{M}\mathbf{r}_{\mathrm{e}} + \frac{m_{\mathrm{h}}}{M}\mathbf{r}_{\mathrm{h}}\,, \quad \mathbf{r}_{\mathrm{e}} = \mathbf{R} + \frac{m_{\mathrm{h}}}{M}\mathbf{r}\,, \quad \nabla_{\mathrm{e}} \equiv \nabla_{\mathbf{r}_{\mathrm{e}}} = \frac{\partial\mathbf{R}}{\partial\mathbf{r}_{\mathrm{e}}}\nabla_{\mathbf{R}} + \frac{\partial\mathbf{r}}{\partial\mathbf{r}_{\mathrm{e}}}\nabla_{\mathbf{r}} = \frac{m_{\mathrm{e}}}{M}\nabla_{\mathbf{R}} + \nabla_{\mathbf{r}}\,,\\
&\mathbf{r} = \mathbf{r}_{\mathrm{e}} - \mathbf{r}_{\mathrm{h}}\,, \qquad\qquad \mathbf{r}_{\mathrm{h}} = \mathbf{R} - \frac{m_{\mathrm{e}}}{M}\mathbf{r}\,, \quad \nabla_{\mathrm{h}} \equiv \nabla_{\mathbf{r}_{\mathrm{h}}} = \frac{\partial\mathbf{R}}{\partial\mathbf{r}_{\mathrm{h}}}\nabla_{\mathbf{R}} + \frac{\partial\mathbf{r}}{\partial\mathbf{r}_{\mathrm{h}}}\nabla_{\mathbf{r}} = \frac{m_{\mathrm{h}}}{M}\nabla_{\mathbf{R}} - \nabla_{\mathbf{r}}\,.
\end{aligned} \tag{5.2}$$

In the studies presented here, the magnetic field is aligned in growth direction, i.e., perpendicular to the quantum-well sample that is in the x–y plane, such that $\mathbf{B} = B\mathbf{e}_z$ (Faraday geometry). Together with Maxwell's equations, this defines the vector potential in the symmetric gauge [1] $\mathbf{A}_0 = \frac{1}{2}\mathbf{B}\times\mathbf{r}$. The separation (5.2) casts Hamiltonian (5.1) into

$$\begin{aligned}
\hat{H} =& -\frac{\hbar^2}{2M}\nabla_{\mathbf{R}}^2 - \frac{\hbar^2}{2\mu}\nabla_{\mathbf{r}}^2 - V(\mathbf{r}) - \mathrm{i}\hbar\Big(\bar{\boldsymbol{\omega}}_\mu\cdot[\,\mathbf{R}\times\nabla_{\mathbf{r}}] + \bar{\boldsymbol{\omega}}_M\cdot[\,\mathbf{r}\times\nabla_{\mathbf{R}}]\Big)\\
&- \mathrm{i}\hbar\frac{\bar{\boldsymbol{\omega}}_{\mathrm{e}} - \bar{\boldsymbol{\omega}}_{\mathrm{h}}}{2}\cdot[\,\mathbf{r}\times\nabla_{\mathbf{r}}] + \frac{1}{2}\mu\bar{\omega}_\mu^2(\mathbf{R}_\parallel + \mathbf{r}_\parallel)^2 - \frac{3}{2}\mu\bar{\omega}_\mu^2\frac{\mu}{M}\mathbf{r}_\parallel^2 - \frac{m_{\mathrm{h}}}{2}\,(\bar{\boldsymbol{\omega}}_{\mathrm{e}}\cdot\bar{\boldsymbol{\omega}}_{\mathrm{h}})(\mathbf{R}_\parallel\cdot\mathbf{r}_\parallel)
\end{aligned} \tag{5.3}$$

where effective cyclotron frequencies are introduced, namely $\bar{\boldsymbol{\omega}}_\mu \equiv \frac{|e|\mathbf{B}}{2\mu}$ with reduced mass μ and $\bar{\boldsymbol{\omega}}_M \equiv \frac{|e|\mathbf{B}}{2M}$ with total mass $M = m_{\mathrm{e}} + m_{\mathrm{h}}$, as well as $\bar{\boldsymbol{\omega}}_{\mathrm{e}} = \frac{|e|\mathbf{B}}{m_{\mathrm{e}}}$ for electrons and $\bar{\boldsymbol{\omega}}_{\mathrm{h}} = \frac{|e|\mathbf{B}}{m_{\mathrm{h}}}$ for holes. The form (5.3) corresponds to the Hamiltonian used by Schmitt-Rink *et al.* [237] and directly shows that the eigenvalue problem of Hamiltonian (5.3) cannot be solved with a simple separation of $\mathbf{r}$ and $\mathbf{R}$. To solve this problem, $\hat{H}' = \hat{U}\,\hat{H}\,\hat{U}^\dagger$ may be applied to Hamiltonian (5.3) with the generalized Göppert-Mayer transformation [2,97] $\hat{U} = \exp\left[\frac{\mathrm{i}}{\hbar}|e|\,\mathbf{r}\cdot\mathbf{A}_0(\mathbf{R})\right]$; compare Sec. 2.1.2.

A straightforward derivation yields

$$\hat{\boldsymbol{H}}' = \frac{\hat{\mathbf{p}}^2}{2\boldsymbol{\mu}} + \frac{\hat{\mathbf{P}}^2}{2\boldsymbol{M}} - \boldsymbol{V}(\mathbf{r}) + \frac{\boldsymbol{\mu}}{\mathbf{2}}\bar{\boldsymbol{\omega}}_{\boldsymbol{\mu}}^{\mathbf{2}}\,\mathbf{r}_{\parallel}^{\mathbf{2}} + \frac{|\bar{\boldsymbol{\omega}}_{\mathrm{e}}| - |\bar{\boldsymbol{\omega}}_{\mathrm{h}}|}{\mathbf{2}}\,\hat{\boldsymbol{L}}_z + \bar{\boldsymbol{\omega}}_M \cdot (\mathbf{r} \times \hat{\mathbf{P}}) \tag{5.4}$$

Total-system Hamiltonian with constant magnetic field

where $\mathbf{r}_{\parallel}$ is the in-plane component of $\mathbf{r}$ and $\hat{L}_z \equiv \mathbf{e}_z \cdot [\mathbf{r} \times \hat{\mathbf{p}}] = -\mathrm{i}\hbar\,\frac{\partial}{\partial\varphi}$ is the z-component of the angular momentum defined with respect to the relative motion. The transformed Hamiltonian (5.4) corresponds to the model presented by Nickel *et al.* [238]. Compared to Eq. (5.3), the transformation procedure decouples relative and center-of-mass (COM) coordinates since no mixed terms between $\mathbf{r}$ and $\mathbf{R}$ appear anymore. It is important to mention that the $\hat{L}_z$ part contains the *difference* of the cyclotron frequencies of electron and hole, and hence a modified reduced-mass cyclotron frequency because $\frac{|\bar{\omega}_{\mathrm{e}}|-|\bar{\omega}_{\mathrm{h}}|}{2} = |\bar{\boldsymbol{\omega}}_{\mu}|\sqrt{1-4\frac{\mu}{M}}$.

In analogy to the hydrogen problem [1], $\hat{L}_z$ commutes with the transformed Hamiltonian $\hat{H}'$ so that it is favorable to represent the eigenstate λ with the usual set of electronic states known from atomic physics. This generates a joint set of eigenfunctions corresponding to the eigenvalue $\hbar m$ where $|m| \leq l$ is the magnetic quantum number within the subshell defined by the common azimuthal quantum number $l < n$ to the principal quantum number n. In general, the quantum numbers form a discrete set of integers where $n = 1, 2, \ldots,$ $l = 0, 1, 2, \ldots, (n-1)$, and $m = -l, \ldots, 0, \ldots, l$. Compared to the Schrödinger equation for the relative motion of the hydrogen atom, however, a center-of-mass dependency arises, accompanied by a lifting of the degeneracy between different m-quantum-number states for fixed principal quantum number n, when the system is subjected to a magnetic-field. Especially, the $2s$ and $2p$ states are important candidates for this lifting. Before seeking the solutions of Hamiltonian (5.4), the new terms of Eq. (5.4) and their physical impact are scrutinized in more detail.

The Hamiltonian (5.4) shows contributions linear in the magnetic field but also a harmonic potential which is quadratic in $\mathbf{r}_{\parallel}$. To get a better understanding of the interplay of Coulombic and magnetic-field effects on excitons, it is beneficial to combine the Coulomb-potential and the harmonic-potential terms into an effective potential

$$V_{\mathrm{eff}}(\mathbf{r}) = -V(\mathbf{r}) + \frac{\mu}{2}\bar{\boldsymbol{\omega}}_{\mu}^{2}\,\mathbf{r}_{\parallel}^{2}\,. \tag{5.5}$$

For vanishing magnetic field, i.e., $\bar{\boldsymbol{\omega}}_{\mu} \to \mathbf{0}$, $V_{\mathrm{eff}}(\mathbf{r})$ corresponds to the bare Coulomb attraction such that the eigenstates are the usual quantum-confined hydrogen states [118]. In this situation, the ground state is defined by the $1s$ solution with $n = 1$ and $m = 0$. The nearest excited states are defined by $2s$ ($n = 2$, $m = 0$) and $2p$ ($n = 1$, $m = \pm 1$). For finite quantum-well thickness, the $2s$ and $2p$ states are nearly degenerate. For the artificial case of vanishing quantum-well thickness, the eigenstates pass over into the bare two-dimensional hydrogen spectrum where $2s$ and $2p$ are degenerate. The corresponding eigenstates are analytically known [2] and expressible via the sequence of associated Laguerre polynomials [242] and the Hermite polynomials [243]. The other limiting case is where the magnetic field dominates producing the harmonic-oscillator solutions [244]. As a typical behavior of hydrogenic eigenfunctions, the spectrum consists of discrete (bound-state) and continuous (scattering-state) parts, while for $B \neq 0$ the spectrum is always discrete [237]. In the full problem, Coulomb and magnetic-field effects both contribute with commensurable influence to the total solution. In a realistic situation, the mixed Coulomb-potential and magnetic-field contributions thus change the behavior of the excitonic eigensystem while the terms linear in the magnetic field alter further the solutions. The $\hat{L}_z$ contribution within Hamiltonian (5.4) only contributes for $m \neq 0$ and hence shifts the $2p$-state energy by $\pm\hbar\frac{|\bar{\omega}_{\mathrm{e}}|-|\bar{\omega}_{\mathrm{h}}|}{2}$ for $m = \pm 1$. As previously mentioned, this leads to lifting of the degeneracy between the $2p_-$ ($m = -1$) and the $2p_+$ ($m = +1$) states. The center-of-mass momentum in the last term of Eq. (5.4) produces an additional linear potential $\bar{\boldsymbol{\omega}}_M \cdot (\mathbf{r} \times \hat{\mathbf{P}})$ that essentially moves the center of the harmonic potential within $V_{\mathrm{eff}}(\mathbf{r})$.

5.1.2 Generalized Wannier equation

On the basis of the derivations of Sec. 5.1.1, the solution of the exciton problem $\hat{H}'\phi_\lambda(\mathbf{r},\,\mathbf{R}) = E_\lambda\,\phi_\lambda(\mathbf{r},\,\mathbf{R})$ follows with an ansatz $\phi_\lambda(\mathbf{r},\,\mathbf{R}) = \phi_{\lambda,\mathbf{Q}}(\mathbf{r})\,\mathrm{e}^{\mathrm{i}\mathbf{Q}\cdot\mathbf{R}}$ where the plane-wave part corresponds to the center-of-mass motion of the exciton. Contrary to the usual hydrogen problem, the eigenfunction $\phi_{\lambda,\mathbf{Q}}$ depends parametrically on the COM momentum $\mathbf{P} = \hbar\mathbf{Q}$. Inserting Hamiltonian (5.4) into this ansatz results in

$$\left[\tfrac{\hat{\mathbf{p}}^2}{2\mu} + \tfrac{\hat{\mathbf{P}}^2}{2M} - \boldsymbol{V}(\mathbf{r}) + \tfrac{\mu}{2}\bar{\omega}_\mu^2\,\mathbf{r}_\parallel^2 + \tfrac{|\bar{\omega}_\mathrm{e}|-|\bar{\omega}_\mathrm{h}|}{2}\,\hat{\boldsymbol{L}}_z + \bar{\boldsymbol{\omega}}_M\cdot(\mathbf{r}\times\hat{\mathbf{P}})\right]\boldsymbol{\phi_\lambda}(\mathbf{r},\,\mathbf{R}) = \boldsymbol{E_\lambda}\,\boldsymbol{\phi_\lambda}(\mathbf{r},\,\mathbf{R})\,. \tag{5.6}$$

Wannier equation including magnetic-field effects

As outlined in Paper [V] and in App. A of Paper [IV], this corresponds to a Wannier equation. Fourier-transforming Eq. (5.6) into the $\mathbf{k}$-space shows that it constitutes a Hermitian eigenvalue problem in the low-density regime. Under these circumstances, the eigenfunctions form a complete set of orthogonalized functions which embody the solution for the homogeneous part of the semiconductor Bloch equations [1, 110]. For finite densities, the problem becomes non-Hermitian and it is beneficial to expand the exciton basis to introduce left- and right-handed eigenfunctions that solve the *generalized eigenvalue equations*

$$\begin{aligned}\boldsymbol{E}_{\lambda,\mathbf{Q}}\,\boldsymbol{\phi}^{\mathbf{R}}_{\lambda,\,\mathbf{Q}}(\mathbf{k}) = \Big(\boldsymbol{\epsilon}^{\mu}_{\mathbf{k}} + \boldsymbol{\epsilon}^{M}_{\mathbf{Q}} - \boldsymbol{\Sigma}_{\mathbf{k},\mathbf{Q}} - \tfrac{\mu}{2}\bar{\omega}_\mu^2\,\triangle_{\mathbf{k}} + \left[\tfrac{|\bar{\omega}_\mathrm{e}|-|\bar{\omega}_\mathrm{h}|}{2} + |\bar{\omega}_M|\,\tfrac{|\mathbf{Q}|}{|\mathbf{k}|}\right]\hat{\boldsymbol{L}}_z\Big)\,\boldsymbol{\phi}^{\mathbf{R}}_{\boldsymbol{\lambda},\,\mathbf{Q}}(\mathbf{k}) \\ -(\mathbf{1} - \boldsymbol{f}^{\mathrm{e}}_{\mathbf{k}+\mathbf{Q}_\mathrm{e}} - \boldsymbol{f}^{\mathrm{h}}_{\mathbf{k}-\mathbf{Q}_\mathrm{h}})\sum_{\mathbf{k}'}\boldsymbol{V}_{\mathbf{k}-\mathbf{k}'}\,\boldsymbol{\phi}^{\mathbf{R}}_{\boldsymbol{\lambda},\,\mathbf{Q}}(\mathbf{k}') + \sum_{\mathbf{k}'}\boldsymbol{\gamma}^{\mathbf{k},\mathbf{k}'}_{\mathbf{X}}\,\boldsymbol{\phi}^{\mathbf{R}}_{\boldsymbol{\lambda},\,\mathbf{Q}}(\mathbf{k}')\,,\end{aligned} \tag{5.7}$$

$$\begin{aligned}\left[\boldsymbol{\phi}^{\mathbf{L}}_{\lambda,\,\mathbf{Q}}(\mathbf{k})\right]^\star\boldsymbol{E}_{\lambda,\mathbf{Q}} = \left[\boldsymbol{\phi}^{\mathbf{L}}_{\lambda,\,\mathbf{Q}}(\mathbf{k})\right]^\star\Big(\boldsymbol{\epsilon}^{\mu}_{\mathbf{k}} + \boldsymbol{\epsilon}^{M}_{\mathbf{Q}} - \boldsymbol{\Sigma}_{\mathbf{k},\mathbf{Q}} - \tfrac{\mu}{2}\bar{\omega}_\mu^2\,\triangle_{\mathbf{k}} + \left[\tfrac{|\bar{\omega}_\mathrm{e}|-|\bar{\omega}_\mathrm{h}|}{2} + |\bar{\omega}_M|\,\tfrac{|\mathbf{Q}|}{|\mathbf{k}|}\right]\hat{\boldsymbol{L}}_z\Big) \\ -\sum_{\mathbf{k}'}\left[\boldsymbol{\phi}^{\mathbf{L}}_{\lambda,\,\mathbf{Q}}(\mathbf{k}')\right]^\star(\mathbf{1} - \boldsymbol{f}^{\mathrm{e}}_{\mathbf{k}'+\mathbf{Q}_\mathrm{e}} - \boldsymbol{f}^{\mathrm{h}}_{\mathbf{k}'-\mathbf{Q}_\mathrm{h}})\boldsymbol{V}_{\mathbf{k}-\mathbf{k}'} + \sum_{\mathbf{k}'}\left[\boldsymbol{\phi}^{\mathbf{L}}_{\lambda,\,\mathbf{Q}}(\mathbf{k}')\right]^\star\boldsymbol{\gamma}^{\mathbf{k},\mathbf{k}'}_{\mathbf{X}}\end{aligned} \tag{5.8}$$

Generalized Wannier equation including magnetic-field effects

which follow from the homogeneous part of the exciton-correlation dynamics (2.28). In these eigenvalue equations, the Coulomb renormalization $\Sigma_{\mathbf{k},\mathbf{Q}} \equiv \sum_{\mathbf{k}'} V_{\mathbf{k}-\mathbf{k}'}(f^{\mathrm{e}}_{\mathbf{k}'+\mathbf{Q}_\mathrm{e}} + f^{\mathrm{h}}_{\mathbf{k}'-\mathbf{Q}_\mathrm{h}})$, as well as the same relative- and COM decomposition as used in Eq. (2.25) are introduced.[4] If the $\mathbf{Q}$-dependence of energy renormalizations and phase-space filling are small, the exciton energy $E_{\lambda,\mathbf{Q}} = \mathcal{E}_\lambda + \frac{\hbar^2\mathbf{Q}^2}{2M}$ decomposes into the exciton eigenenergy $\mathcal{E}_\lambda$ and COM energy of the electron–hole pair; however, only for s-like states. Under these circumstances, the latter is then removed for the energy differences observed by THz transitions, as expected from Eqs. (5.6)–(5.8). However, this does not apply for p-like states where $\hat{L}_z$ introduces an additional linear COM potential.

In addition to the insights of the real-space representation presented in the last section, the form of Eqs. (5.7) and (5.8) allows to explore the physical and mathematical structure of the system configuration in more detail. The kinetic and Coulomb terms follow from the discussion of Sec. 2.1.1. Thus, the attention is focused on the magnetic-field dependent parts here. The spatial dependence of the harmonic potential $\frac{\mu}{2}\bar{\omega}_\mu^2\,\mathbf{r}_\parallel^2$ in Hamiltonian (5.4) casts into a Laplace operator via $\mathbf{r}_\parallel^2 \to -\triangle_{\mathbf{k}}$ in momentum-space representation. This harmonic potential contributes for all exciton states, independent of the magnetic quantum number. However, App. A shows that the angular part of the Laplacian vanishes for s-like states; compare Eq. (A.17). Proceeding similarly, the relative-motion part in Eq. (5.4) becomes the first term in the squared bracket where the

[4] To emphasize the center-of-mass dependence of excitons, the COM momentum in the exciton-basis representation is denoted by capitalized $\hbar\mathbf{Q}$ instead of $\hbar\mathbf{q}$ as used in Eq. (2.28). However, the (capitalized) COM momentum used here is not to be confused with the definitions given in Chap. 3 where the phonon momentum has also been included in $\hbar\mathbf{Q}$.

z-component of the angular momentum eventually leads to the eigenvalue $\hbar m$; compare a similar discussion in App. A.2. The last term of Eq. (5.4) contains the center-of-mass momentum $\mathbf{P} = \hbar\mathbf{Q}$. For isotropic systems, the electron movement does not depend on the direction in the plane. Without loss of generality, the exciton may be chosen to move in a specific direction, i.e., $\mathbf{Q} = Q\mathbf{e}_x$ or $\mathbf{Q} = Q\mathbf{e}_y$. Applying the very same procedure as before, the center-of-mass part shapes up to the second term in the squared bracket, i.e., $|\bar{\boldsymbol{\omega}}_M| \frac{|\mathbf{Q}|}{|\mathbf{k}|}\hat{L}_z$ in Eqs. (5.7) and (5.8). This format directly shows that the COM contribution of the magnetic field only applies for p-like states. This leads to an additional shift which wins on strength once the center-of-mass momentum becomes larger or the magnetic field increases. Isotropy claims a direction-independent movement which is why only the absolute value of $\mathbf{Q}$ enters the COM contribution. While no angular dependency is observed for radially symmetric (s-like) states, the $\hat{L}_z$ contribution unambiguously displays a lift of the degeneracy for p-like states once a magnetic field is applied. Due to the influence of an external magnetic field, the Coulomb-matrix element undergoes some substantial change as well. The explicit derivation is done in App. C.

In Eqs. (5.7) and (5.8), a momentum-dependent scattering $\gamma_{\mathrm{X}}^{\mathbf{k},\mathbf{k}'}$ is added, originating from the fact that the coherent polarization, compare Eq. (1) in Paper [VI], vanishes either via radiative decay or nonradiatively via microscopic scattering processes [2]. The microscopic origin of nonradiative decay stems from the singlet source that initially generates the coherent exciton-correlation dynamics, compare Eq. (B.14), once polarization is present in the system. It describes scattering between particles where the Coulomb interaction accounts for correct momentum exchange among participating singlets and eventually leads to dephasing of the polarization [144,245]. Since this process is the result of the electron–hole excitation in the system, it is often referred to as *excitation-induced dephasing* (EID) [24,30,31,246–248]. The effects of EID profoundly alter the many-body system and lead to state-dependent broadening of excitonic resonances for elevated densities. The most accurate description is achieved via the *second-Born–Markov approximation* [1, 241] where scattering among densities and polarizations is described in terms of correlations [2] by expressing the doublets at the scattering level and using a steady-state solution of the coherent-carrier correlations within the Markov limit [82, 249]. Albeit this approach is computationally feasible, it is very sophisticated and numerically still challenging. Therefore, it seems meaningful to elaborate an analytic model that includes the important symmetries and the diffusive character of Coulomb-induced scattering. For further details consult Refs. [24, 124]. The derivation of the diffusive scattering model for s- and p-like symmetry is sketched in App. B.2 of this thesis.

After numerically computing the excitonic eigensystem constituted by Eqs. (5.7) and (5.8), the resulting eigenfunctions have to be normalized using the generalized orthogonality and completeness relations; see Eqs. (A5) of Paper [IV]. Additionally, it is important to conserve the physical character of the pair-correlation function $\Delta g_{\mathrm{eh}}(\mathbf{r}_\parallel) = \sum_\beta \Delta n_\beta |\phi_\beta^{\mathrm{R}}(\mathbf{r}_\parallel)|^2$ with density Δn_β of β-excitons, compare Eqs. (234)–(235) of Ref. [24], and thus normalize the right-handed eigenfunctions also among each other.

5.1.3 Results and discussion

The derivations of Secs. 5.1.1 and 5.1.2 show that the magnetic field significantly influences the electron–hole relative motion. New contributions in the Hamiltonian (5.4) modify the bare Coulomb potential, giving rise to an interesting interplay of carrier–carrier and carrier–magnetic-field coupling. This leads to the generation of magnetoexcitons. Additionally, the exciton eigenenergies and eigenfunctions depend parametrically on the center-of-mass momentum. As the main effect, the degeneracy of the $2p_+$ and $2p_-$ states is removed once the magnetic field attains a finite value.

The results of the preceding theoretical model and associated computations are summarized in Fig. 5.1 where a carrier density of $n = 5 \cdot 10^9\,\mathrm{cm}^{-2}$ at electron and hole temperatures of $T_{\mathrm{e}} = 39.87\,\mathrm{K}$ and $T_{\mathrm{h}} = 11.28\,\mathrm{K}$ is assumed. In frame **(a)**, the eigenenergies for $E_{1s,\mathbf{Q}}$ (black-solid line), $E_{2s,\mathbf{Q}}$ (blue-solid line), $E_{2p_+,\mathbf{Q}}$ (thin-yellow line), and $E_{2p_-,\mathbf{Q}}$ (thick-yellow line) are plotted versus magnetic field. The vertical arrows indicate the possible THz transitions between $1s$ and $2p_\pm$, respectively. In this representation, the trivial $\frac{\hbar^2\mathbf{Q}^2}{2M}$ dependence is removed from the energies because it does not affect the energy differences observed by the THz transitions. This leads to complete removal of the COM-$\mathbf{Q}$ dependence of s-like states. A comparison of the $\mathbf{Q} = \mathbf{0} \equiv \mathbf{Q}_0$ (solid lines) and $|\mathbf{Q}| = 2/a_0 \equiv \mathbf{Q}_2$ (dashed lines) where a_0 is the exciton Bohr radius, however, shows that

the $2p_\pm$ states strongly depend on the center-of-mass momentum. In addition, the $E_{2p_+,\mathbf{Q}}$ and $E_{2p_-,\mathbf{Q}}$ exhibit a clear splitting which becomes even stronger for finite values of the center-of-mass momentum. In all cases, the splitting between $2p_+$ and $2p_-$ branches is asymmetric. More specifically, the $2p_+$ energy shifts much more from its zero-field value than the $2p_-$ state does [238, 250–254]. This follows from the interplay of the angular part of the Laplacian, compare App. A.2, and the $\hat{L}_z$ contribution within Eqs. (5.7) and (5.8) where $\triangle_{\varphi_\mathbf{k}}$ contains a sign-independent m^2 part while the $\hat{L}_z$ term yields a sign-dependent $\pm\hbar m$ contribution. The solutions show an obvious asymmetry between the $+|m|$ and $-|m|$ solutions when these two contributions are combined. The Coulomb scattering between the $2p_\pm$ and $2s$ states is indicated by the red-dashed arrows. This mechanism is discussed in more detail in the next section.

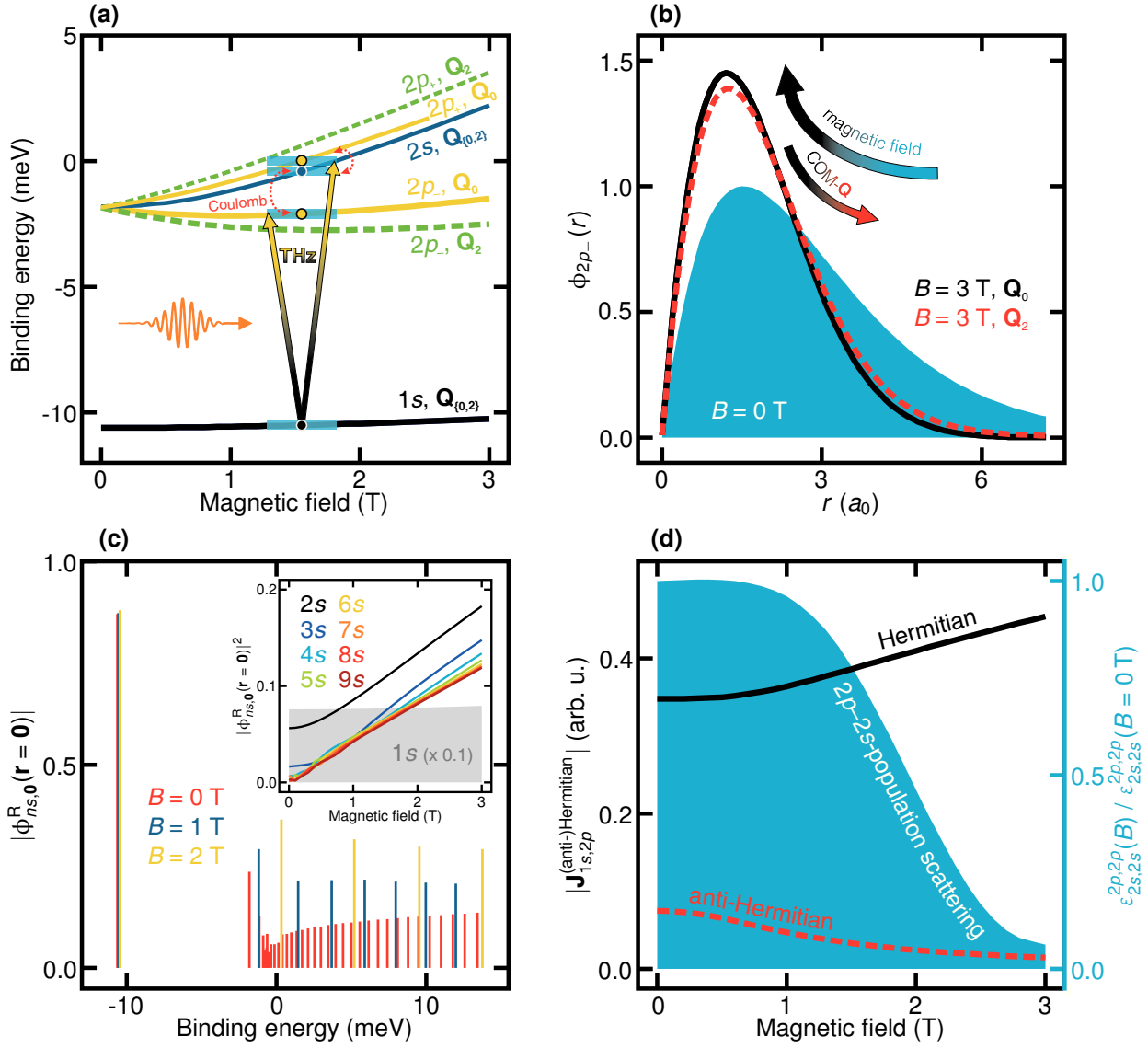

Figure 5.1 | Exciton eigenenergies and eigenfunctions, oscillator strengths, and matrix elements. (a) Shifts of the 1*s* (black), 2*s* (blue), $2p_+$ (thin), and $2p_-$ (thick) eigenenergies versus magnetic field for $\mathbf{Q} = \mathbf{0}$ ($\mathbf{Q}_0$, solid) and $|\mathbf{Q}| = {}^2/_{a_0}$ ($\mathbf{Q}_2$, dashed). The THz pulse (orange) couples the 1*s* to the $2p_\pm$ states (gradient-colored arrows, shown here for $\mathbf{Q}_0$). **(b)** Change of the $2p_-$ wavefunction with magnetic field and COM momentum. Zero field (shaded) is compared to $B = 3\,\mathrm{T}$ for $\mathbf{Q}_0$ (solid) and $\mathbf{Q}_2$ (dashed). **(c)** Square root of oscillator strengths versus real parts of the excitonic eigenenergies for different B fields. The inset shows oscillator strengths for *ns* states in dependence of the magnetic field. **(d)** $2p$-to-$2s$-exciton population scattering (shaded, right y-axis) and (anti-)Hermitian parts of the 1*s*-to-2*p* THz-transition-matrix element (dashed and solid, left y-axis).

The influence of a magnetic field on the exciton eigenfunctions is presented in Fig. 5.1 **(b)** where the $2p_-$ wavefunction in real space is shown for different magnetic-field and COM configurations. Comparing the $2p_-$ wavefunction for $B = 0\,\mathrm{T}$ (shaded) and $B = 3\,\mathrm{T}$ (solid and dashed lines) shows that the magnetic field obviously concentrates the wavefunctions toward the origin. This effect is slightly diminished by the center-of-mass motion because a finite $\mathbf{Q}$ (dashed line) leads to an additional linear potential, increasing the probability of finding the exciton at positions $\mathbf{r_Q} > \mathbf{r_0}$. In contrast, the $1s$ wavefunction is only slightly changed by the magnetic field, indicating that the Coulomb effects outweigh the magnetic-field influence. The $1s$-exciton wavefunction is presented in Fig. 2 **(a)** of Paper [V] and shows a very stable behavior for increased magnetic field.

In general, the exciton wavefunctions in real space become broader and more nodes appear as the principal quantum number n is increased. An external magnetic field will "enclose" the electron–hole pair in a harmonic potential forcing the magnetic-field-dependent wavefunctions to be more strongly attracted toward the origin compared to the zero-field wavefunctions. This in-plane confinement eventually tends to increase the oscillator strengths [237, 255, 256] of the PL emission, especially for the $2s$ and higher states: The attraction is enhanced as n is increased, i.e., the further the wavefunctions are situated from the origin, the stronger the impact of a magnetic field will be. As a result, the magnetic field introduces more attraction for the higher states than for the $1s$ state which behaves relatively robust under the influence of a magnetic field. These findings are summarized in Fig. 5.1 **(c)** where the oscillator strengths of s-like states are plotted versus the respective exciton binding energy of the states, i.e., the real parts of the exciton eigenenergies resulting from the Wannier equations (5.7) and (5.8). Since the $1s$-oscillator strength is very dominant compared to higher-order states, the square root of the oscillator strength $|\phi^{\mathrm{R}}_{ns,\mathbf{0}}(\mathbf{r} = \mathbf{0})|^2$ is plotted here. This representation equally expresses all important effects but emphasizes the behavior of ns states with $n > 1$. The red lines show the zero-field results while blue shows the states for $B = 1\,\mathrm{T}$ and yellow for $B = 2\,\mathrm{T}$. As a result of EID, a clear $2s$ resonance cannot be distinguished anymore since it is composed of a whole cluster of resonances [124] for $B = 0\,\mathrm{T}$ (red lines). This clustering is an important component for the computation of the overall PL spectrum of the exciton-population dynamics presented in Sec. 5.2, as it leads to more weight and thus a stronger $2s$ signal in the zero-field case. Different case studies show that the clustering effect is more prominent for a carrier density around $n = 5 \cdot 10^9\,\mathrm{cm}^{-2}$ as chosen here. The consequences of EID effects will be discussed in the following section. Once the magnetic field is set to finite values, the carrier motion is quantized to Landau orbitals due to the Lorentz force. This effect becomes clearly manifest in the equally spaced energetic splitting of eigenstates when the magnetic field increases in strength (blue and yellow lines). The inset of Fig. 5.1 **(c)** shows the s-like oscillator strengths as a function of magnetic field whereas the $1s$-oscillator strength (shaded) is scaled down by a factor of 0.1. As previously mentioned, the $1s$ state behaves rather robust for different magnetic-field strengths while higher-order states show distinct modifications. Figure 5.1 **(d)** displays the exciton-scattering elements among $2p$ and $2s$ populations together with the THz-transition elements for the $1s$-to-$2p$ transition. Both quantities are computed using the eigenfunctions resulting from Eqs. (5.7) and (5.8). Their explicit form, role, and physical interpretation in the studies of this project are discussed in the next section.

5.2 Influence of a magnetic field on Coulomb scattering, THz transitions, and exciton dynamics

The studies presented in this section and related Paper [VII] are a direct continuation of the investigations recently presented in Ref. [59] and Supplemental Material (SM). To introduce the basic framework, these preceding works are briefly summarized here.

Terahertz excitations resonant with the $1s$-to-$2p$ exciton-transition energy in semiconductor QWs have recently been shown to lead to pronounced population transfer into the $2s$ state [59]. The THz pulse causes a partial depletion of the $1s$ state by transferring exciton populations from the $1s$ to the $2p$ state. This *quenching* of the $1s$ PL has previously been discussed in the literature [69, 254]. Although the excitonic resonances in the optical absorption or the PL spectrum result exclusively from bright excitons, i.e., excitons with COM momentum within the optical cone $|\mathbf{Q}\,a_0| \lesssim 0.1$, this is not the case for THz-induced transitions since they involve excitons with *all* COM momenta. Consequently, the THz pulse causes the exciton populations to temporarily

occupy optically dark states that may not recombine radiatively. As a result of scattering among dark and bright exciton populations, this *exciton shelving* [59, 257] eventually leads to the observation of more luminescing $1s$ excitons after a THz pulse has been applied to the system compared to a situation where the sample is not subjected to a THz pulse. Apart from this quenching behavior of the $1s$ PL, a clear transient increase of the $2s$ PL is observed. As aforementioned, the $2p$ state is optically dark and thus may not contribute radiatively to the PL.

Owing to parity-conservation rules, direct $1s$-to-$2s$ THz excitation, however, is dipole-forbidden such that the THz cannot induce transitions from the $1s$ to the $2s$ state. Additionally, a THz pulse is far off-resonant with respect to the energy separation of the nearly degenerate $2p$ and $2s$ states; compare Fig. 5.1 **(a)** for $B = 0\,\mathrm{T}$. In other words, the unexpected increase of the $2s$ PL cannot be attributed to the THz pulse. Instead, this effective $1s$-to-$2s$ transition is explained by diffusive Coulomb scattering which breaks the symmetry of THz-transition selection rules and generates a mixing of $2s$ and $2p$ populations; see App. B.1 of this thesis and SM of Ref. [59] for a detailed explanation. In combination with a THz-induced $1s$-to-$2p$ transition, the Coulomb interaction gives rise for the direct generation of an effective $1s$-to-$2s$ transition such that the symmetry-forbidden $2s$ populations are created via many-body scattering. This direct $1s$-to-$2s$ coupling has no atomic analogue, revealing crucial differences between atoms and interacting many-body systems. Figure 5.2 diagrams the energy levels of the three lowest heavy-hole (hh) states $1s$, $2p$, and $2s$ together with THz transition and Coulomb-scattering channel. The experimental and theoretical details are described in Ref. [59] and related SM.

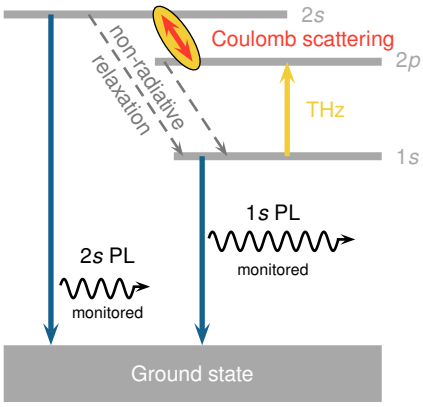

Figure 5.2 | Three lowest hh-states and involved carrier-relaxation paths. The system is excited by a THz pulse (yellow) resonant with the 1*s*–2*p* intra-exciton transition. The directly measured 2*s* PL emerges due to Coulomb scattering (red) between the 2*p* and the 2*s* state. After THz excitation, the 1*s* PL recovers due to backscattering from 2*s* and 2*p* (dashed).

As a direct extension to this previous work, the Coulomb-assisted, THz-induced coupling between the $1s$ and the $2s$ states may systematically be controlled by applying an external magnetic field. The magnetic field modifies both the THz transitions and the Coulomb scattering by introducing substantial changes to the exciton energies and wavefunction overlap between the $1s$-, $2p$-, and $2s$-exciton states. After the derivations of a stationary system subjected to a magnetic field presented in the last section, these results are now applied to compute the influence and modifications of a magnetic field on the exciton-correlation dynamics and resulting PL spectra.

5.2.1 Experiment

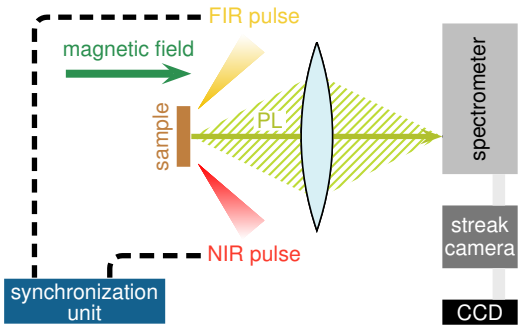

Figure 5.3 | Sketch of experimental setup. The electronically-synced FIR and NIR pulses are both focused onto the sample. After passing a spectrometer, the PL is detected by a synchroscan streak camera.

In the experiment which studies the influence of a magnetic field, a high-quality multiple quantum-well structure is investigated, consisting of 60 periods of GaAs QWs of 8.2 nm width which are separated by 19.6 nm-wide AlGaAs barriers. The $1s$-to-$2p$ exciton transition is excited by 25-ps long far-infrared (FIR) pulses produced by the free-electron laser (FEL) at the Helmholtz-Zentrum Dresden–Rossendorf (HZDR), Dresden (Germany). In all measurements, the FEL energy is kept fixed while the magnetic field is increased. Two different configurations of FEL energies are investigated: First, the energy is tuned to be resonant with the $1s$-to-$2p$-energy separation at vanishing magnetic field, corresponding to $\hbar\omega_{\mathrm{THz}} = 8.7\,\mathrm{meV}$, and second to be resonant with the $1s$-to-$2p_+$ transition at $B = 1.6\,\mathrm{T}$ where $\hbar\omega_{\mathrm{THz}} = 10.6\,\mathrm{meV}$. Keeping the FEL energy fixed, the magnetic field is swept between 0 T and 3 T. The excitons are generated by a near-infrared (NIR) excitation using a Ti:Sapphire laser emitting 4 ps (FWHM) pulses at 1.615 eV with a repetition rate of 78 MHz. The NIR excita-

tion is slightly above the $1s$-hh energy which is at 1.566 eV, as inferred from absorption measurements at 10 K. Using a pulse picker, every sixth pulse is selected to fit the 13-MHz clock pulse of the FEL [258]. The electronically synchronized pulses are focused onto the sample. About 600 ps after the NIR excitation, the mechanically time-delayed THz pulse arrives. This guarantees enough time for exciton formation and cooling [29, 51, 257], thus producing a situation where virtually 100% of the electron–hole pairs are bound to excitons such that plasma contributions are negligible. After passing a spectrometer, the PL is detected by a synchroscan streak camera. The experimental setup is sketched in Fig. 5.3.

The experimental techniques are similar to the experiments performed in Ref. [59]. However, in this present study the impact of an external magnetic field on the interacting many-body system is investigated by exciting the magnetic-field-dependent $1s$-to-$2p$ intra-exciton transition with a narrow-band THz pulse.

5.2.2 Exciton-correlation dynamics

The description of exciton-population and transition-amplitude dynamics starts from the quantum kinetics of two-particle correlations (2.28). To analyze how exciton populations evolve in time, it is convenient to convert the COM representation of the exciton correlations to the exciton basis using relations (A6)–(A7) of Paper [IV]. Including the THz part $c^{\mathbf{q},\mathbf{k},\mathbf{k}'}_{\mathrm{X},\,\mathrm{THz}}$ in Eq. (2.28) allows for the description of the influence of THz fields on the interacting many-body system. The Coulomb scattering among excitons results from the three-particle scattering $T^{\mathbf{q},\mathbf{k},\mathbf{k}'}_{\mathrm{X}}$. Its full form shows a very complicated structure and is presented in, e.g., Refs. [2, 24, 59]. One of the key properties related to the three-particle scattering is the conservation law of exciton populations, $\sum_{\mathbf{q},\mathbf{k},\mathbf{k}'} T^{\mathbf{q},\mathbf{k},\mathbf{k}'}_{\mathrm{X}} = 0$, such that Coulomb scattering always satisfies a diffusive redistribution of exciton correlations in momentum space. The notion of diffusive triplet scattering very closely follows the argumentation presented in App. B.2 needed for the momentum-dependent scattering in the generalized Wannier equation. Similar to the simplifications presented in Sec. 5.1.2 with respect to the scattering matrix of EID, it is also desirable to introduce assumptions for the triplet scattering. Nevertheless, all approaches must necessarily satisfy the essential symmetries and conservation laws such that a simple phenomenological dephasing model is not sufficient for a consistent description of the diffusive character of Coulomb scattering. The basic principles and fundamental ideas are properly rendered by a diffusive scattering model [24, 59]

$$T^{\mathbf{q},\mathbf{k},\mathbf{k}'}_{\mathrm{diff}} = -\mathrm{i}\hbar\gamma\left[c^{\mathbf{q},\mathbf{k},\mathbf{k}'}_{\mathrm{X}} - \frac{1}{2\pi}\int \mathrm{d}\varphi_{\mathbf{K}}\; c^{\mathbf{q},\mathbf{k}+\mathbf{K},\mathbf{k}'+\mathbf{K}}_{\mathrm{X}}\right] \tag{5.9}$$

with overall scattering strength γ and momentum exchange $\hbar\mathbf{K}$ in the Coulomb-scattering process. Typical values for $\mathbf{K}$ are in the range of $1/a_0$. As shown in App. B.1 of this thesis and SM of Ref. [59], the diffusive Coulomb scattering not only efficiently converts exciton populations but also yields relaxation among the exciton states. More technical details on diffusive scattering in general are given in Ref. [2]. The scattering model, as it is also used in the computations of this present project, is introduced in the SM of Ref. [59]. After projecting Eq. (5.9) to the exciton basis, the diffusive scattering may eventually be expressed by the diffusive Coulomb matrix $\varepsilon^{\lambda,\nu}_{\alpha,\beta} \equiv \varepsilon^{\lambda,\nu}_{\alpha,\beta}(|\mathbf{K}|)$. Its explicit form and a generic, analytical representation for s- and p-like states is presented in App. B.1 of this thesis. The matrix elements of Coulomb scattering are computed using the exciton wavefunctions. These, in turn, are modified by an external magnetic field; see the discussion in Sec. 5.1.

To demonstrate the effect of a magnetic field on the exciton wavefunctions and Coulomb-mediated scattering, Fig. 5.4 presents the spatially resolved real parts of the exciton wavefunctions $\phi_\lambda(\mathbf{r})$ of $\lambda = 1s$ (bottom), $2p$ (middle), and $2s$ (top) states as contour plots. The left column shows the $B = 0\,\mathrm{T}$ results and the right column the wavefunctions for $B = 3\,\mathrm{T}$. The THz field connects the $1s$ and $2p$ states via dipole coupling. In the illustration, the strength of dipole-allowed THz transitions ($1s$-to-$2p$) is indicated by the thickness of the vertical arrows. The Coulomb-scattering strength between $2s$ and $2p$ states is represented via the thickness of the slanted arrows. As shown by Eq. (B.3), the Coulomb scattering contains the scattering momentum $\hbar\mathbf{K}$ which is exchanged in the scattering process. The $2s$ wavefunctions are presented without Coulomb-induced modulations

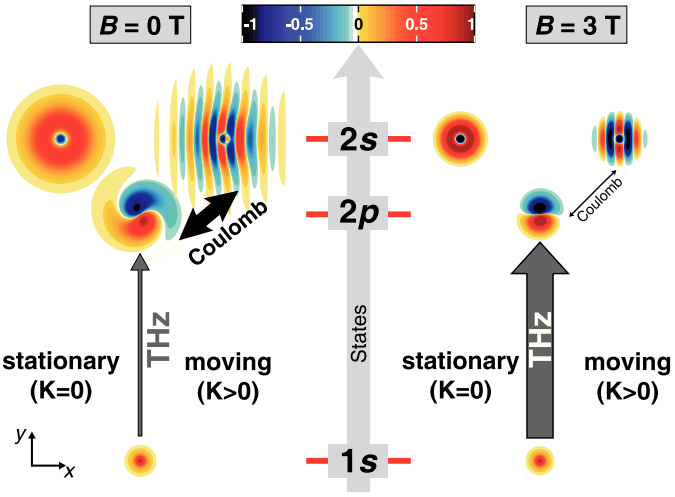

Figure 5.4 | Magnetic-field effects on exciton wavefunctions and Coulomb scattering. The *B*-field (left column: vanishing field; right column: $B = 3\,\mathrm{T}$) constrains the 1*s*, 2*s*, and 2*p* wavefunctions while Coulomb scattering leads to modulations and spreading ("moving") of the unscattered wavefunctions ("stationary"). For better visibility, the 2*s* and 2*p* wavefunctions are shown spatially separated. Thickness of the slanted arrows indicates the scattering strength. Possible THz transitions with strengths are shown by the vertical arrows.

where the scattering momentum vanishes ($\hbar\mathbf{K} = \mathbf{0}$, "stationary") and with finite scattering momentum ($\hbar\mathbf{K} > \mathbf{0}$, "moving"). In particular, the Fourier transform of $\phi_{2s}(\mathbf{k})$ ("stationary", top) and $\phi_{2s}(\mathbf{k}+\mathbf{K})$ ("moving", top), as well as $\phi_{2p}(\mathbf{k})$ (middle) are shown. Obviously, the scattering momentum $\hbar\mathbf{K}$ modulates the stationary wavefunction of $2s$ (top) such that the moving $2s$ wavefunction reveals oscillating patterns. As known from the hydrogen problem, the $2p$ state (middle) resembles the typical ellipsoid shape with two lobes and a node at $\mathbf{r} = \mathbf{0}$. Additionally, the momentum dependence of EID leads to a twisting effect in the wavefunctions that becomes obvious especially for p-like states. For vanishing magnetic field (left column), a pronounced Coulomb-scattering strength is obtained, as indicated by the thick, slanted arrow. This shows that combined THz field and diffusive Coulomb scattering lead to an effective $1s$-to-$2s$ transition, as observed in Ref. [59]. In contrast, a finite magnetic field (right column) spatially attenuates and constrains the wavefunctions and thus concentrates them toward the spatial origin; compare also Fig. 5.1 **(b)**. As a result of the less-spread wavefunction and increased energetic $2s$-to-$2p_\pm$ difference compared to the $B = 0\,\mathrm{T}$ case, see Fig. 5.1 **(a)**, the Coulomb-scattering strength decreases for increasing magnetic field; compare Fig. 5.1 **(d)**. Due to enhanced confinement near $\mathbf{r} = \mathbf{0}$, the THz-transition probability increases for increasing magnetic field; compare Fig. 5.1 **(d)**. The increasing off-resonance between THz energy and $1s$-to-$2p_\pm$ transition energies for growing magnetic-field strength, however, counteracts this effect. Thus, major modifications due to combined effects of THz and magnetic field are expected.

In order to compute the exciton-correlation dynamics, we determine the c_X dynamics (2.28) with THz contributions and diffusive Coulomb scattering. In the exciton basis, these take the form

$$\mathrm{i}\hbar\frac{\partial}{\partial t}\Delta N_{\lambda,\nu,\mathbf{Q}}(t) = \left[E_{\nu,\mathbf{Q}} - E_{\lambda,\mathbf{Q}} - \mathrm{i}\gamma_{\lambda,\nu}(1-\delta_{\lambda,\nu})\right]\Delta N_{\lambda,\nu,\mathbf{Q}}(t) - \mathrm{i}\sum_{\alpha,\beta}\varepsilon^{\lambda,\nu}_{\alpha,\beta}\,\Delta N_{\alpha,\beta,\mathbf{Q}}(t) + \sum_\beta\left[\mathbf{J}_{\lambda,\beta,\mathbf{Q}}\,\Delta N_{\beta,\nu,\mathbf{Q}}(t) - \mathbf{J}^\star_{\nu,\beta,\mathbf{Q}}\,\Delta N_{\lambda,\beta,\mathbf{Q}}(t)\right]\cdot\mathbf{A}_\mathrm{THz}(t) \tag{5.10}$$

Exciton-correlation dynamics with Coulomb-scattering and THz contributions

where the exciton populations are described by the diagonal elements $\Delta N_{\lambda,\lambda,\mathbf{Q}} \equiv \Delta N_{\lambda,\mathbf{Q}}$ while the off-diagonal elements $\Delta N_{\lambda,\nu\neq\lambda,\mathbf{Q}}$ describe exciton-transition amplitudes and correlated electron–hole plasma. In the experiment, the THz pulse enters about 600 ps after the NIR excitation, allowing for exciton formation and cooling such that practically all electron–hole pairs are bound to excitons, producing a situation of pure occupation of the $1s$-exciton state $\Delta N_{1s,\mathbf{Q}}$. In other words, in the calculations it may be assumed that the exciton-formation process has already taken place such that the correlated electron–hole-plasma contribution may be omitted. Equation (5.10) includes the computed eigenenergies of states λ and ν following from Eqs. (5.7) and (5.8). Since the center-of-mass energy does not depend on the states, it cancels and does not contribute to the energy differences observed by THz transitions. The state-dependent dephasing $\gamma_{\lambda,\nu}$ is chosen such that only exciton-transition amplitudes are affected while exciton populations ($\lambda = \nu$) are conserved.

The THz coupling follows from the transition-matrix element

$$\mathbf{J}_{\lambda,\nu,\mathbf{Q}} \equiv \sum_{\mathbf{k}} \phi^{\mathrm{L}}_{\lambda,\,\mathbf{Q}}\,(\mathbf{k})\;\mathbf{j}_{\mathbf{k}}\;\left[\phi^{\mathrm{R}}_{\nu,\,\mathbf{Q}}\,(\mathbf{k})\right]^{\star} \tag{5.11}$$

containing the current-matrix element $\mathbf{j}_{\mathbf{k}} = -|e|\hbar\mathbf{k}/\mu$ with reduced mass μ. Every quadratic matrix can be represented as the sum of a Hermitian (H) and an anti-Hermitian (AH) matrix. Against this background, the THz-transition matrix (5.11) may be separated into $\mathbf{J}^{\mathrm{H}}_{\lambda,\nu,\mathbf{Q}} = \frac{1}{2}\big(\mathbf{J}_{\lambda,\nu,\mathbf{Q}} + \mathbf{J}^{\star}_{\nu,\lambda,\mathbf{Q}}\big)$ and $\mathbf{J}^{\mathrm{AH}}_{\lambda,\nu,\mathbf{Q}} = \frac{1}{2}\big(\mathbf{J}_{\lambda,\nu,\mathbf{Q}} - \mathbf{J}^{\star}_{\nu,\lambda,\mathbf{Q}}\big)$ such that $\mathbf{J}_{\lambda,\nu,\mathbf{Q}} = \mathbf{J}^{\mathrm{H}}_{\lambda,\nu,\mathbf{Q}} + \mathbf{J}^{\mathrm{AH}}_{\lambda,\nu,\mathbf{Q}}$. As a consequence of particle conservation, the THz-transition matrix must be Hermitian. This can be shown by summing the THz contributions of Eq. (5.10) over all populations, i.e., $\lambda = \nu$, leading to $\mathrm{i}\hbar\partial_t \sum_\lambda \Delta N_{\lambda,\mathbf{Q}}(t)|_{\mathrm{THz}} = 0$. Interestingly, both bright and dark populations are conserved separately such that the THz coupling merely redistributes the populations with respect to their center-of-mass momenta while conserving the total amount of carrier populations. For vanishing EID effects in Eqs. (5.7) and (5.8), the resulting eigenfunctions are purely real-valued such that $\mathbf{J}^{\mathrm{AH}}_{\lambda,\nu,\mathbf{Q}} = \mathbf{0}$. For low to intermediate diffusive scattering, the anti-Hermitian part has a finite value but, however, is small compared to the Hermitian part. The Hermitian and anti-Hermitian parts of $\mathbf{J}_{\lambda,\nu,\mathbf{Q}}$ thus also give a measure for the strength of EID. This is shown by the left y-axis of Fig. 5.1 **(d)** where the Hermitian and anti-Hermitian parts of the $1s$-to-$2p$-transition-matrix element are plotted versus magnetic-field strength. As can be seen, the anti-Hermitian part is well below the Hermitian part and even decreases with increasing magnetic field. In contrast, the strength of the Hermitian part grows with magnetic field, thus showing an increase of the probability of THz-transitions with stronger magnetic field. The remaining THz-matrix elements (not shown) for $1s$-to-np, $n > 2$, transitions exhibit a similar behavior but, however, are clearly weaker than the $1s$-to-$2p$ THz transition.

The exciton configurations before the THz pulse excites the sample are initialized by Boltzmann distributions for dark- as well as bright-exciton populations. Additionally, a hole burning as shown in Fig. 5.5 for $|\mathbf{Q}\,a_0| \lesssim 0.1$ is implemented for the bright exciton populations, which amounts to 0.08 for the initial distribution of bright $1s$ excitons. After the THz pulse has quenched the $1s$ state, the $1s$ population recovers via scattering with, e.g., acoustic phonons. This recovery is implemented by a relaxation model to describe how dark and bright excitons relax toward a Boltzmann distribution in the steady state while conserving the total particle number. As THz fields act on excitons with all COM momenta, a dark-to-bright coupling accounts for redistribution of momenta among excitons.

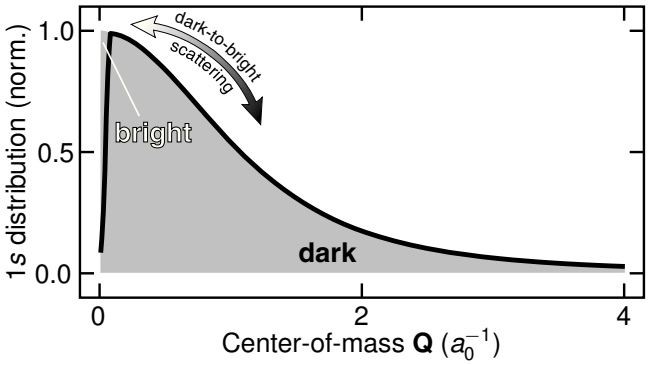

Figure 5.5 | Hole burning of the 1*s*-exciton distribution. Bright-exciton populations contribute to the luminescence leading to rapid depletion of excitons with small COM-**Q** (solid line). This leads to hole burning in the 1*s*-exciton distributions (shaded area). Scattering between dark and bright excitons redistributes high- and low-momentum states.

The full time dynamics of the exciton correlations (5.10) are computed by combining these (self-contained) models with the diffusive Coulomb scattering and THz-pulse excitation. The time-resolved PL (TRPL) spectra follow from the time-resolved populations of bright excitons, implemented in an Elliott formula [24]

$$\mathbf{PL}(\boldsymbol{\omega}, \boldsymbol{t}) = \mathbf{Im}\left[\frac{\left|\boldsymbol{\phi}^{\mathbf{R}}_{\mathbf{1}s,\mathbf{0}}\,(\mathbf{r}=\mathbf{0})\right|^{\mathbf{2}}\,\boldsymbol{\Delta N}_{1s,\mathbf{0}}(\boldsymbol{t})}{\boldsymbol{E}_{1s,\mathbf{0}} - \hbar\boldsymbol{\omega} - \mathbf{i}\tilde{\boldsymbol{\gamma}}_{1s}} + \sum_{\boldsymbol{j}=\mathbf{2}}^{\boldsymbol{n}_{\max}} \frac{\left|\boldsymbol{\phi}^{\mathbf{R}}_{\boldsymbol{js},\mathbf{0}}\,(\mathbf{r}=\mathbf{0})\right|^{\mathbf{2}}\,\boldsymbol{\Delta N}_{\boldsymbol{js},\mathbf{0}}(\boldsymbol{t})}{\boldsymbol{E}_{\boldsymbol{js},\mathbf{0}} - \hbar\boldsymbol{\omega} - \mathbf{i}\boldsymbol{\gamma}_{\boldsymbol{js}}}\right] \tag{5.12}$$

Frequency- and time-resolved photoluminescence

with oscillator strengths $|\phi^{\mathrm{R}}_{js,\mathbf{0}}\,(\mathbf{r}=\mathbf{0})\,|^2$ of js excitons; see inset of Fig. 5.1 **(c)**. The exciton energies $E_{js,\mathbf{0}}$ correspond to the real parts of the eigenenergies resulting from Eqs. (5.7) and (5.8) while the imaginary parts

enter the state-dependent dephasings γ_{js}. In the experiment, a neutral-density filter is used at the high-energy flank of the $1s$ peak to enhance the $2s$ signal by attenuating the low-energy parts of the spectrum. In the computation, this is modeled via a Fermi–Dirac-like cutoff function $\tilde{\gamma}_{1s} \equiv \gamma_{1s} \left[\exp\left(\frac{\hbar\omega - E_{\text{cut}}}{\Delta E_{\text{filter}}}\right) + 1\right]^{-1}$ where E_{cut} is chosen roughly 4 meV above the $1s$ resonance and ΔE_{filter} is in the range of 0.5–1 meV. Additionally, the PL spectrum is inhomogeneously broadened to account for disorder-related effects.

The magnetic-field effects enter the PL via all stationary quantities such as the exciton eigenenergies and wavefunctions. The exciton populations are computed using Eq. (5.10) where all state combinations of populations ($\lambda = \nu$) and transition amplitudes ($\lambda \neq \nu$) of bright and dark excitons dynamically interact. The magnetic field influences the dynamics directly via the wavefunctions which enter the Coulomb-scattering and THz-transition elements, and via the exciton energies entering the kinetic part of the equations of motion. To account for ionization of excitons and multi-photon transitions, the four-level system including the $1s$, $2s$, $2p_+$, and $2p_-$ states is expanded to include also excited states ($3s$, $4s$, …, $n_{\max}s$; $3p_\pm$, $4p_\pm$, …, $n_{\max}p_\pm$) up to $n_{\max} = 20$.

5.2.3 Results, discussion, and further prospects

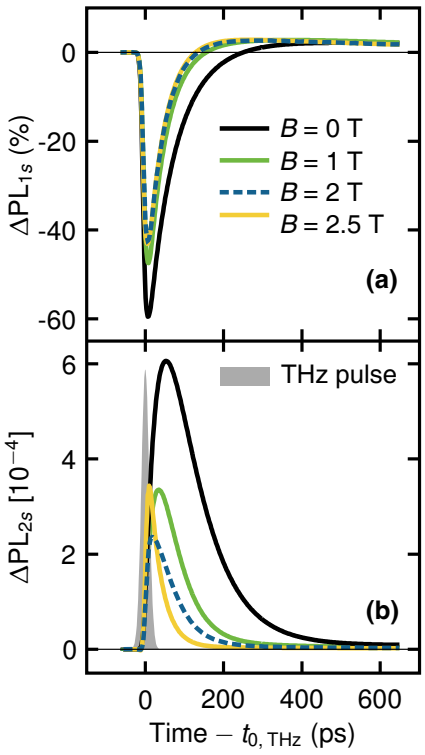

Figure 5.6 | Effect of a *B*-field on THz-induced population transfer. The ΔPL_λ for **(a)** λ = 1*s* and **(b)** λ = 2*s* is shown for *B* = 0, 1, 2, and 2.5 T versus time. The 1*s* hole burning is 0.98. The time axis is normalized with respect to the center of the THz pulse (shaded). The thin, horizontal lines indicate the zero levels of 1*s* quench and 2*s* excess.

To quantify the THz-induced effects and monitor the magnetic-field-influenced changes, Fig. 5.6 shows the computed, differential photoluminescence $\Delta\text{PL}(t) = \text{PL}_{\text{THz}}(t) - \text{PL}_{\text{ref}}(t)$ between the PL with, $\text{PL}_{\text{THz}}(t)$, and without, $\text{PL}_{\text{ref}}(t)$, terahertz excitation. Four different magnetic-field configurations are shown, i.e., vanishing field (black) as well as $B = 1\,\text{T}$ (green), 2 T (blue dashed), and 2.5 T (yellow). The time-resolved ΔPL are energy-integrated around the corresponding $1s$ and $2s$ energies. Frame **(a)** shows ΔPL_{1s} and frame **(b)** presents ΔPL_{2s}. The THz pulse is chosen to be resonant with the $1s$-to-$2p$ transition at vanishing field for all time traces, i.e., the THz wavelength is kept constant at $\lambda = 142\,\mu\text{m}$ corresponding to $\hbar\omega_{\text{THz}} = 8.7\,\text{meV}$.

The time scale is normalized with respect to the center of the THz pulse (shaded in frame **(b)**). At the arrival of the THz pulse, the ΔPL_{1s} in Fig. 5.6 **(a)** shows a sharp decline due to significant quenching [69, 254] of the $1s$-exciton population. For long times, the differential $1s$ PL overshoots to positive values as a result of exciton shelving [59]. While the results for vanishing field (black curve) essentially reflect the results presented in Ref. [59], the extension with an external magnetic field applied to the sample shows distinct modifications of the quenching behavior. The ΔPL_{1s} shows a maximum quench of about 60% which slightly decreases to roughly 42% when increasing the magnetic field from $B = 0\,\text{T}$ to $B = 2.5\,\text{T}$. This is a direct result of the lifted $2p_-$–$2p_+$ degeneracy with increasing magnetic field: While for vanishing field, $2p_-$ and $2p_+$ are degenerate and the $1s$-exciton population is equally transferred to both the $2p_-$ and the $2p_+$ branches, the magnetic field modifies the system such that only $2p_-$ contributes for high magnetic fields. This effect is discussed in more detail later. In contrast to increasing off-resonance of the THz pulse with respect to the lifted energy branches, the THz-transition-matrix elements increase with increasing magnetic field; see Fig. 5.1 **(d)**. This results in a complicated interplay of two competing processes that influence the quenching behavior.

The time evolution of ΔPL_{2s}, on the other hand, shows a strictly positive-valued behavior where a clear spike arises. This reveals that the diffusive Coulomb scattering in combination with a $1s$-to-$2p$-resonant THz excitation is capable to induce a *direct* $1s$-to-$2s$-state transfer; see App. B.1 of this thesis and SM of Ref. [59].

Eventually, the decay of $\Delta\mathrm{PL}_{2s}$ clearly takes place with two different time scales where fast Coulomb-mediated scattering is followed by slow relaxation due to acoustic phonons. With increasing magnetic field, the $\Delta\mathrm{PL}_{2s}$ is gradually reduced. However, compared to the moderate reduction of the $1s$ quench with increasing magnetic-field strength shown in frame **(a)**, the $2s$-excess PL decreases much more rapidly by a factor of 2.6, showing that the magnetic field can substantially control the intra-exciton Coulomb-scattering strength into the $2s$ state. Besides this, the maximum of the $\Delta\mathrm{PL}_{2s}$ gradually shifts in time toward smaller time values while showing a faster decay. This time shift is a direct result of the fact that the magnetic field renders the system more few-level-like. For $B = 0\,\mathrm{T}$, the $2s$ PL is also influenced by a comparably slow relaxation from higher ns states to the $2s$ state, while for finite magnetic-field strengths the $2s$ PL mainly arises from an interplay of states up to only $n = 3$. On the other side, the faster decay is a result of reduced Coulomb-scattering strength; compare Fig. 5.1 **(d)**. While for $B = 0\,\mathrm{T}$, the processes of radiative decay, dark-to-bright coupling, relaxation, and Coulomb scattering influence the decay behavior of the $2s$ PL, the influence of the Coulomb scattering is largely reduced for finite magnetic fields such that the decay is dominated by the time scales of the other processes. In addition to this, the $\Delta\mathrm{PL}_{2s}$ decreases for increasing magnetic-field strength, which is also a result of reduced influence of Coulomb scattering. However, the $\Delta\mathrm{PL}_{2s}$ rises again for the case where a magnetic field of $B = 2.5\,\mathrm{T}$ is assumed. This increase for $B = 2.5\,\mathrm{T}$ is explained by additional THz transitions which in this case result from the dipole-allowed $2p_-$-to-$3s$ transition. This effect will be discussed below in the context of Fig. 5.7 **(b)**. Suppressing the diffusive Coulomb scattering confirms that the pronounced $2s$ peak exclusively originates from the diffusive Coulomb scattering and subsequent equilibration [59]. This behavior is also confirmed for computations with finite magnetic-field strengths (not shown).

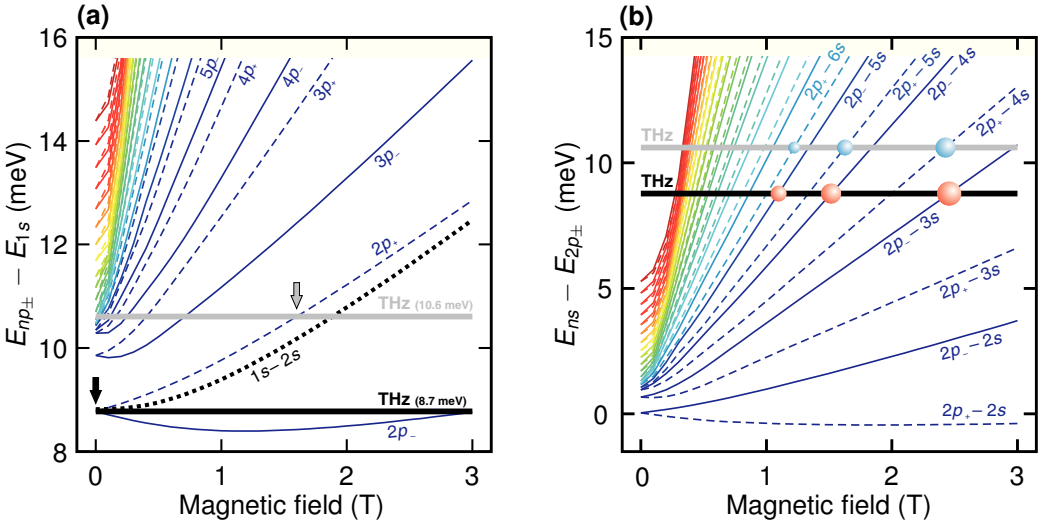

Figure 5.7 | Exciton-transition energies as function of magnetic field. Transition energies from **(a)** 1*s*-to-$np_\pm$ and **(b)** $2p_\pm$-to-*ns* exciton states. The black-solid line indicates the THz central energy of $\hbar\omega_{\mathrm{THz}}$= 8.7 meV (resonant with the 1*s*-to-2*p* transition at B = 0 T, marked with the black arrow) and the gray-solid line shows the THz central energy of $\hbar\omega_{\mathrm{THz}}$= 10.6 meV (resonant with the 1*s*-to-2p_+ transition at B = 1.6 T, marked with the gray arrow). The thick-dashed line in **(a)** presents the 1*s*-to-2*s*-energy difference. The red and blue spheres in **(b)** highlight important THz transitions from $2p_\pm$ to higher *s*-like states, which are discussed in the text. The size of the spheres indicates the respective THz-coupling strength. In both frames, the p_- (p_+)-related branches are presented by solid (dashed) lines.

The preceding discussion shows that applying a magnetic field remarkably influences the THz-transition probabilities and Coulomb-scattering strengths. For a closer inspection of the $2p_-$–$2p_+$-degeneracy lifting and possible additional THz transitions, Fig. 5.7 **(a)** shows the energy difference $E_{np_\pm} - E_{1s}$ for dipole-allowed THz transitions between the $1s$ and $np_\pm$-exciton states as function of magnetic field. The p_- (p_+)-related branches are presented by solid (dashed) lines. The two THz energies applied in the studies are indicated by the solid, horizontal lines where the black line corresponds to $\hbar\omega_{\mathrm{THz}} = 8.7\,\mathrm{meV}$, resonant with the $1s$-to-$2p$-transition at $B = 0\,\mathrm{T}$, and the gray line represents $\hbar\omega_{\mathrm{THz}} = 10.6\,\mathrm{meV}$, resonant with the $1s$-to-$2p_+$-transition at $B = 1.6\,\mathrm{T}$.

For clarification, the resonance positions are indicated by the gray and black arrows. Additionally, the $1s$-to-$2s$-energy difference is shown as black-dotted line. Obviously, the np_- and np_+ branches become non-degenerate for increasing magnetic-field values, leading to a fan chart of magnetoexcitons. In case of the THz excitation at $\hbar\omega_{\mathrm{THz}} = 8.7\,\mathrm{meV}$, the lower $2p$ branch, i.e., $2p_-$, clearly contributes much more throughout the complete B range in comparison to the upper branch, i.e., $2p_+$. While the $2p_+$ branch shows a continuous blue shift with increasing magnetic field, the $2p_-$ branch first shows a red shift [251, 252] which is followed by a successive blue shift [238, 251–253]. The origin of this effect has already been discussed in Sec. 5.1.3. The stronger blue shift of the $2p_+$ branch reveals that for increasing magnetic field, the upper branch becomes off-resonant more rapidly with respect to the THz field. Thus, for the THz excitation at $\hbar\omega_{\mathrm{THz}} = 8.7\,\mathrm{meV}$, the $2p_-$ branch offers the dominant contribution for non-vanishing magnetic field while $2p_+$ only plays a minor role. Additionally, this THz energy is far away from higher branches beyond $2p_\pm$, thus eliminating any possibility for THz transitions from the $1s$ state to states beyond $2p_\pm$. This situation suddenly changes when the THz field is tuned to be resonant with the $1s$-to-$2p_+$ transition at $B = 1.6\,\mathrm{T}$, i.e., $\hbar\omega_{\mathrm{THz}} = 10.6\,\mathrm{meV}$, indicated by the horizontal, gray-colored line and the gray arrow. Again, the THz energy is kept constant at this value for all magnetic-field sweeps within this data set. As can be seen from Fig. 5.7 **(a)**, the THz field is also resonant with transitions from the $1s$ state to higher states beyond $2p_\pm$. This resonance occurs for magnetic fields below $B = 1\,\mathrm{T}$. The $\Delta\mathrm{PL}_{1s}$ is thus expected to peak at $B = 1.6\,\mathrm{T}$ whereas lower magnetic-field values also contribute appreciably when the $1s$ quench is scanned in dependence of the magnetic field. Owing to reduced THz-transition probabilities for increasing principal quantum number n, i.e, $1s$-to-$np_\pm$, however, the most prominent transition is expected to arise at $B = 1.6\,\mathrm{T}$. Besides this observation, the $2p_+$ branch now yields the dominant contribution while the $2p_-$ is strongly off-resonant with respect to the THz field for the magnetic fields investigated here. With respect to higher exciton states and the ionization continuum, *the magnetic field renders the system rather few-level-like compared to a system which is not subjected to a magnetic field.*

So far, only THz-induced transitions from the $1s$ to $2p_\pm$ or higher p-like states have been scrutinized. After the THz pulse has already transferred $1s$-exciton populations to the $2p_\pm$ states, additional dipole-allowed transitions may occur [259]. To also scan for additional resonances, Fig. 5.7 **(b)** presents the energy difference between the $2p_\pm$ to higher s-like states. The black and gray horizontal lines again indicate the THz energies at $\hbar\omega_{\mathrm{THz}} = 8.7\,\mathrm{meV}$ and $\hbar\omega_{\mathrm{THz}} = 10.6\,\mathrm{meV}$, respectively. The colored, solid (dashed) lines represent the p_- (p_+)-related branches. Evidently, no channel to $2s$ is observed in this range of magnetic-field strength such that the $2s$ excess cannot stem from possible THz transitions but may clearly be attributed to the diffusive Coulomb scattering. Only for large magnetic fields (not shown), transitions from $2p_-$ to $2s$ become possible as well, i.e., when the lowest solid line intersects the horizontal lines. However, the red and blue spheres show that there are channels from, e.g., $2p_-$ to $3s$ at $B = 2.5\,\mathrm{T}$, from $2p_-$ to $4s$ at $B = 1.5\,\mathrm{T}$, from $2p_+$ to $4s$ at $B = 2.4\,\mathrm{T}$, and so on. The size of the spheres schematically indicates the strength of the respective THz transition. Since the THz-current-matrix element $|\mathbf{J}_{2p,ns}|$ decreases with increasing n, the $2p_-$-to-$3s$ is the strongest one among all these higher-order transitions. These populations of higher s-like states relax to the $2s$ state, giving rise to pronounced signatures in the magnetic-field-dependent $2s$-exciton populations and corresponding PL spectra. The differential $2s$ PL shown in Fig. 5.6 **(b)** demonstrates this scenario. Here, the $\Delta\mathrm{PL}_{2s}$ gradually decreases for increasing magnetic field from $B = 0\,\mathrm{T}$ to $B = 2\,\mathrm{T}$. Increasing the magnetic-field strength further beyond $B = 2\,\mathrm{T}$ shows that the maximum is rising again (here only $B = 2.5\,\mathrm{T}$ is shown). This is a direct result from the above-mentioned $2p_-$-to-$3s$ transition at $B = 2.5\,\mathrm{T}$ where populations are transferred from $2p_-$ to $3s$, followed by a subsequent relaxation to $2s$. If higher states are not taken into account in the theory, this effect does not show up.

The presented results reveal that the exciton-correlation dynamics and with these the resulting PL spectra are clearly modified and influenced by an external magnetic field. A magnetic field is capable of controlling the intra-exciton Coulomb scattering among exciton populations and renders the system more few-level-like. Furthermore, the THz field may also induce transitions to higher states giving rise to additional resonances in the population dynamics. More details and figures of this project, illustrating the effects of Coulomb scattering and THz excitations in the presence of an external magnetic field, are presented in the upcoming Paper [VII].

6 Conclusions and Outlook

In this thesis, a microscopic theory has been applied and extended to describe phonon-assisted processes and terahertz excitations in semiconductors. All investigations have been performed in the incoherent regime where all coherent quantities vanish and the quantum nature of light becomes important. Based on the Heisenberg equation-of-motion approach, the cluster-expansion scheme has been adopted to truncate the infinite hierarchy of coupled equations. In this context, the arising expectation values are classified by recursively identifying correlated clusters. By this means, the many-body hierarchy is systematically factorized into lower- and higher-order expectation values. As a result of the sequential buildup of correlated clusters, the procedure leads to a physical and intuitive interpretation of the clusters and the truncation scheme. In the presented microscopic theory, the generic structure of the cluster-expansion approach appeared to be very beneficial as it can be straightforwardly generalized to include new coupling effects without the necessity to reformulate the existing theory from scratch.

In the first project, the semiconductor luminescence equations (SLEs) have been extended to include LO-phonon-assisted processes involving the first phonon sideband (PSB) arising at the low-energy side of the $1s$-exciton resonance which is often referred to as the zero-phonon line (ZPL). For the description of photon-assisted polarizations in the incoherent regime where the calculation involves a completely quantized light field described by photon-creation and -annihilation operators, it is sufficient to truncate the hierarchy of coupled equations at the singlet–doublet level of the cluster-expansion scheme. However, extending this theory to describe also PSBs arising at the low-energy side of the ZPL leads to additional phonon-creation operators. In this context, the n^{th} PSB is described by $(n+2)$-particle correlations such that the first PSB already invokes the triplet level of the cluster-expansion scheme. Consistently including stimulated-emission effects, a microscopic theory has been presented to describe phonon-assisted luminescence in a microcavity. Besides a full numerical evaluation of the phonon-assisted SLEs, a rigorous analytic model has also been developed. The obstacles that arise from the stimulated parts in the SLEs could systematically be handled by introducing the *strong-cavity approximation*. This opened up the possibility of formulating a closed analytical formula to describe phonon-assisted luminescence in a cavity. In both the numerical and the analytical computations, the standard scenario where the cavity resonance coincides with the $1s$-exciton resonance, i.e., the ZPL, has been expanded by the option of freely tuning the cavity resonance to any arbitrary frequency. This rendered investigations of different cavity configurations possible. On the one hand, normal-mode coupling for a cavity resonant with the ZPL was observed but, on the other hand, a new effect could also be identified where the PSB is highly enhanced if the cavity resonance is shifted to coincide with the first phonon-sideband resonance. Intensity studies in dependence of the quality of the cavity indicate an initial increase of the luminescence intensity due to the Purcell effect, followed by a subsequent decrease as the system transitions into the nonperturbative regime, if the cavity is resonant with the ZPL. For a cavity resonant with the first PSB, the integrated luminescence saturates which reveals qualitative changes in the cavity effects and the impact of a detuned microcavity on the system properties.

As already investigated in the first project, the interaction between electrons and longitudinal-optical (LO) phonons gives rise to pronounced PSBs in the luminescence spectrum. This interaction may be modeled by either the short-ranged optical deformation-potential scattering or the long-ranged Fröhlich interaction which

exists in polar media. In order to identify the origin of exciton–phonon interaction in polar semiconductors, time-resolved photoluminescence spectroscopy has been used to investigate the PSBs of three polar, wide-gap materials, namely ZnO, ZnS, and CdS, as a function of temperature and excitation density. The experimental results have been confirmed by a theoretical many-body approach where the relative contributions of Fröhlich interaction and optical deformation-potential scattering were identified. Here, a steady-state luminescence formula has been developed to investigate exciton-population-dominated first (PSB_1) and second (PSB_2) phonon-sideband luminescence. For low densities where correlated emission sources prevail, the exciton picture constitutes a suitable formulation for the description of PSBs, as the hierarchy problem that arises from the Coulomb interaction is eliminated in this representation. The experiment–theory comparison has demonstrated that many-body interactions significantly influence the phonon-interaction mechanisms. While Fröhlich interaction governs the scattering in CdS, deformation-potential scattering prevails in ZnO. In ZnS, both processes contribute equally. As an important fact, the theoretical studies have shown that scattering between *single electrons* and an optical phonon is dominated by the Fröhlich interaction in all three investigated materials. However, the strong Coulomb coupling between electrons and holes leads to strong suppression of the Fröhlich interaction, particularly in ZnO, such that optical deformation potential is here the overall dominant mechanism that is responsible for the sideband emission.

The studies on the exciton–phonon interaction have demonstrated that Coulombically bound electron–hole pairs, i.e., excitons, have pronounced effects on the optical properties of semiconductors. After creation of polarizations, carriers, and correlations in the semiconductor via an optical interband excitation using visible or near-infrared (NIR) light, some fraction of the excited carriers may bind into excitons. As the energy spacing between intra-exciton transitions is in the terahertz (THz) range, THz spectroscopy is ideally suited to probe correlated semiconductor many-body states and to induce controlled transitions between the different states. In contrast to interband processes, intraband transitions do not alter the number of total excited carriers. Recently, the THz-induced, dipole-forbidden $1s$-to-$2s$ transition has been reported, which could be traced back to the diffusive Coulomb scattering among $1s$, $2p$, and $2s$ states. Based on these studies, the influence of an external magnetic field on THz transitions and Coulomb scattering has been investigated in the third project. A magnetic field significantly alters the properties of excitons such as the eigenenergies and wavefunctions. However, the internal energy spacing between different exciton states remains in the THz regime such that THz spectroscopy is still in demand when a magnetic field is applied. As the Coulomb scattering induces intra-exciton transitions, the variations of the exciton properties induced by a magnetic field enable major control of the scattering among exciton states. Using time-resolved photoluminescence measurements of GaAs/AlGaAs multiple quantum wells, the dynamics of excitons have been probed via excitation using narrow-band THz pulses resonant with the dipole-allowed $1s$-to-$2p$ intra-exciton transition. The experimental findings have been corroborated by a theoretical model by fully including linear and nonlinear magnetic-field contributions to the total-system Hamiltonian. The magnetic field varies the exciton eigenvalues and eigenfunctions, and with this the THz-induced, Coulomb-mediated intra-exciton transitions and exciton-population dynamics. Besides significant changes in the co-operative interaction of Coulomb scattering and THz field, both experiment and theory could reveal additional THz-induced transitions to higher exciton states which would not be observable without a magnetic field. As a very intriguing result, it could be shown that the system becomes few-level-like when a magnetic field is applied. This project had not been finished completely when submitting this thesis. More details and results are presented in the upcoming manuscript [VII].

The combination of THz pulses with a magnetic field opens up new prospects in scientific research. For example, it is well studied that resonant excitation of an optically pre-excited system with a THz pulse that is close to resonant with the intra-exciton $1s$-to-$2p$ transition may lead to pronounced Rabi-flopping effects. Using strong THz pulses, recent studies have shown that the $1s$-exciton resonance bleaches and a significant splitting evolves as the THz intensity is increased [138]. The authors could furthermore show that the ionization continuum of excitonic states plays a significant role resulting in pronounced spectral wings. Since a magnetic field modifies the excitonic system to exhibit a rather few-level-like character, the multi-THz-photon ionization might be controlled systematically and it would be interesting to investigate how such a system can be reduced to a two-level system by applying an external magnetic field.

A

Numerical discretization of the Laplace operator

In second quantization, the Hamiltonian arising from the contribution proportional to $\mathbf{B}^2$ displays a second-order derivative with respect to $\mathbf{k}$; compare Eqs. (5.6)–(5.8). Thus, for numerical computations, the generic Laplace operator must be discretized [260, 261] and applicable boundary conditions have to be identified. In polar coordinates, the Laplace operator can be written as

$$\triangle = \frac{1}{k}\frac{\partial}{\partial k}k\frac{\partial}{\partial k} + \frac{1}{k^2}\frac{\partial^2}{\partial \varphi_{\mathbf{k}}^2} = \underbrace{\frac{1}{k}\frac{\partial}{\partial k}}_{\mathbf{M}_{\triangle_k}^{(1)}} + \underbrace{\frac{\partial^2}{\partial k^2}}_{\mathbf{M}_{\triangle_k}^{(2)}} + \underbrace{\frac{1}{k^2}\frac{\partial^2}{\partial \varphi_{\mathbf{k}}^2}}_{\mathbf{M}_{\triangle_{\varphi_{\mathbf{k}}}}} \tag{A.1}$$

where the first- and second-order derivatives with respect to k and the derivative with respect to φ are labeled with matrices $\mathbf{M}_{\triangle_k}^{(1)}$, $\mathbf{M}_{\triangle_k}^{(2)}$, and $\mathbf{M}_{\triangle_{\varphi_{\mathbf{k}}}}$, respectively. In the following, these derivatives shall be discretized and written in matrix form. To find an approximation for the first- and second-order derivatives $\frac{\partial}{\partial k}$ and $\frac{\partial^2}{\partial k^2}$, it is customary to start with a Taylor expansion of an arbitrary function $u(k)$ around a grid point k_i [260]:

$$u(k_i + \delta k) = u(k_i) + u'(k_i)\,\delta k + \frac{1}{2}u''(k_i)\,(\delta k)^2 + \frac{1}{6}u'''(k_i)\,(\delta k)^3 + \mathcal{O}\Big((\delta k)^4\Big)\,, \tag{A.2}$$

$$u(k_i - \delta k) = u(k_i) - u'(k_i)\,\delta k + \frac{1}{2}u''(k_i)\,(\delta k)^2 - \frac{1}{6}u'''(k_i)\,(\delta k)^3 + \mathcal{O}\Big((\delta k)^4\Big)\,, \tag{A.3}$$

where $u^{(n)}(k_i)$ denotes the n^{th} derivative of u evaluated at point k_i. Summing Eqs. (A.2) and (A.3) results in

$$u(k_i + \delta k) + u(k_i - \delta k) = 2u(k_i) + u''(k_i)\,(\delta k)^2 + \mathcal{O}\Big((\delta k)^4\Big) \tag{A.4}$$

which yields the second-order central difference

$$\left(\frac{\partial^2 u}{\partial k^2}\right)_i = \frac{u_{i+1} - 2u_i + u_{i-1}}{(\delta k)^2} + \mathcal{O}\Big((\delta k)^2\Big)\,. \tag{A.5}$$

An analogous derivation where Eqs. (A.2) and (A.3) are subtracted from each other yields the discretization for the first-order derivative

$$\left(\frac{\partial u}{\partial k}\right)_i = \frac{u_{i+1} - u_{i-1}}{2\,\delta k} + \mathcal{O}\Big((\delta k)^2\Big)\,. \tag{A.6}$$

To solve the general eigenvalue problem

$$\mathbf{M}\cdot\mathbf{v} = \lambda\mathbf{v} \tag{A.7}$$

with eigenvector $\mathbf{v}$ and eigenvalue λ, the general discretization scheme for the derivatives with respect to k can be written in matrix form as

$$\left(\frac{\partial u}{\partial k}\right)_i = \frac{1}{2\,\delta k} \begin{pmatrix} & & & & & & & & 0 \\ -1 & 0 & 1 & & & & & & \\ & -1 & 0 & 1 & & & & & \\ & & -1 & 0 & 1 & & & & \\ & & & \ddots & \ddots & \ddots & & & \\ & & & & \ddots & \ddots & \ddots & & \\ & & & & & -1 & 0 & 1 & \\ & & & & & & -1 & 0 & 1 \\ & & & & & & & & \\ 0 & & & & & & & & \end{pmatrix} \in \mathbb{R}^{(N+2)\times(N+2)} \tag{A.8}$$

and

$$\left(\frac{\partial^2 u}{\partial k^2}\right)_i = \frac{1}{(\delta k)^2} \begin{pmatrix} & & & & & & & & 0 \\ 1 & -2 & 1 & & & & & & \\ & 1 & -2 & 1 & & & & & \\ & & 1 & -2 & 1 & & & & \\ & & & \ddots & \ddots & \ddots & & & \\ & & & & \ddots & \ddots & \ddots & & \\ & & & & & 1 & -2 & 1 & \\ & & & & & & 1 & -2 & 1 \\ & & & & & & & & \\ 0 & & & & & & & & \end{pmatrix} \in \mathbb{R}^{(N+2)\times(N+2)}\,. \tag{A.9}$$

Here, the matrices are of size $(N+2)\times(N+2)$ whereas the dashed box is a $N \times N$ matrix. For the sake of clarity, all matrix entries which are zero are represented by blank fields.

A.1 General boundary conditions

Although the derivatives are already properly discretized, the boundary conditions for the specific problem remain to be defined. A common ansatz are the general (mixed) *Dirichlet* and *von Neumann boundary conditions* [260, 262]

$$\alpha_{\mathrm{lo}}\, u(k = k_{\mathrm{lo}}) + \beta_{\mathrm{lo}}\, \frac{\mathrm{d}u(k)}{\mathrm{d}k}\bigg|_{k=k_{\mathrm{lo}}} = \gamma_{\mathrm{lo}} \qquad \text{and} \qquad \alpha_{\mathrm{hi}}\, u(k = k_{\mathrm{hi}}) + \beta_{\mathrm{hi}}\, \frac{\mathrm{d}u(k)}{\mathrm{d}k}\bigg|_{k=k_{\mathrm{hi}}} = \gamma_{\mathrm{hi}}\,. \quad \text{(A.10)}$$

Here, α_{lo}, β_{lo}, and γ_{lo} are constants constituting the boundary conditions for the lowest (lo) index. The constants α_{hi}, β_{hi}, and γ_{hi} are the respective equivalents for the highest (hi) index. In general, these indices are outside the normal domain, i.e., for a problem consisting of grid points $\{1, \ldots, N\}$ they are fixed at index positions 0 and $N + 1$ such that $u_{\mathrm{lo}} = u_0$ and $u_{\mathrm{hi}} = u_{N+1}$. Since the excitonic eigenfunctions are continuous at the boundaries, it may be assumed that the grid points at the boundaries are identical to their neighbors, i.e.,

$$u_0 = u_1 \quad \text{and} \quad u_{N+1} = u_N\,. \quad \text{(A.11)}$$

Inserting these conditions into Eq. (A.5), leads to boundary conditions for the second-order derivative

$$u_2 - u_1 \qquad \text{for matrix line 1}\,, \quad \text{(A.12)}$$

$$u_{N-1} - u_N \qquad \text{for matrix line } N\,. \quad \text{(A.13)}$$

With conditions (A.11), similar boundary conditions for the first-order derivative (A.6) arise. With these results, the matrix representations can be cast back into $N \times N$ matrix forms

$$\mathbf{M}^{(1)}_{\triangle_k} = \frac{1}{2\,\delta k} \begin{pmatrix} -1 & 1 & & & & & 0 \\ -1 & 0 & 1 & & & & \\ & -1 & 0 & 1 & & & \\ & & \ddots & \ddots & \ddots & & \\ & & & \ddots & \ddots & \ddots & \\ & & & & -1 & 0 & 1 \\ 0 & & & & & -2 & 2 \end{pmatrix} \in \mathbb{R}^{N\times N}\,, \quad \text{(A.14)}$$

and

$$\mathbf{M}^{(2)}_{\triangle_k} = \frac{1}{(\delta k)^2} \begin{pmatrix} -1 & 1 & & & & & 0 \\ 1 & -2 & 1 & & & & \\ & 1 & -2 & 1 & & & \\ & & \ddots & \ddots & \ddots & & \\ & & & \ddots & \ddots & \ddots & \\ & & & & 1 & -2 & 1 \\ 0 & & & & & 1 & -1 \end{pmatrix} \in \mathbb{R}^{N\times N}\,, \quad \text{(A.15)}$$

where an equidistant grid with continuous domain of definition is assumed, i.e., $\delta k = \mathrm{const.}$ for all grid points.

A.2 Angular-dependent part

The quantum-state number λ of the excitonic eigenfunctions and eigenvalues introduced in Sec. 5.1 implicitly contains the principal quantum number n_λ and the magnetic quantum number m_λ, i.e., the projection of the angular momentum. For clarification, both the principal quantum number and the magnetic quantum number are explicitly labeled with index λ here. These indices may be dropped if the connection becomes clear from the context. In App. B, e.g., the explicit distinction is needed since mixed terms of different states arise. The excitonic wavefunctions in momentum-space representation can then be expanded in terms of the radial and the angular contribution as

$$\phi_\lambda(\mathbf{k}) = \bar{\phi}_\lambda(|\mathbf{k}|)\, \mathrm{e}^{\mathrm{i}m_\lambda \varphi_\mathbf{k}} \tag{A.16}$$

where the radial part $\bar{\phi}_\lambda(|\mathbf{k}|)$ is indicated by the bar. For s-like states, i.e., $m_\lambda = 0$, the angular part vanishes and a spherically symmetric wavefunction appears. Applying the angular-dependent part $\triangle_{\varphi_\mathbf{k}} = \frac{1}{k^2}\frac{\partial^2}{\partial \varphi_\mathbf{k}^2}$ of the Laplace operator (A.1) to Eq. (A.16) leads to

$$\triangle_{\varphi_\mathbf{k}}\, \phi_\lambda(\mathbf{k}) = \bar{\phi}_\lambda(|\mathbf{k}|)\, \triangle_{\varphi_\mathbf{k}}\, \mathrm{e}^{\mathrm{i}m_\lambda \varphi_\mathbf{k}} = -\frac{m_\lambda^2}{k^2}\, \phi_\lambda(\mathbf{k})\,, \tag{A.17}$$

showing that the angular-dependent part can be written as a diagonal $N \times N$ matrix

$$\mathbf{M}_{\triangle_{\varphi_\mathbf{k}}} = -m_\lambda^2 \begin{pmatrix} \frac{1}{k_1^2} & & & & & & 0 \\ & \frac{1}{k_2^2} & & & & & \\ & & \frac{1}{k_3^2} & & & & \\ & & & \ddots & & & \\ & & & & \ddots & & \\ & & & & & \frac{1}{k_{N-1}^2} & \\ 0 & & & & & & \frac{1}{k_N^2} \end{pmatrix} \in \mathbb{R}^{N\times N}\,. \tag{A.18}$$

Matrix (A.18) directly reveals that the harmonic potential in the total-system Hamiltonian (5.4) is not angular-dependent for radially symmetric (s-like) states.

B

Diffusive scattering model

This appendix briefly discusses the main issues of the diffusive scattering models introduced in connection with the diffusive exciton scattering and the excitation-induced dephasing (EID). The analysis is presented in a completely generic format using a complex-valued ansatz without restricting the formalism to the low-density case, i.e., the representation distinguishes between left- and right-handed wavefunctions and their complex conjugate.

B.1 Diffusive exciton scattering

In Sec. 5.2, the Coulomb-scattering matrix

$$\varepsilon_{\alpha,\beta}^{\lambda,\nu}(|\mathbf{K}|) = \gamma\Big[r_{\alpha,\beta}^{\lambda,\nu}(0) - r_{\alpha,\beta}^{\lambda,\nu}(|\mathbf{K}|)\Big] \tag{B.1}$$

with overall scattering strength γ and momentum exchange $\mathbf{K}$ in the Coulomb-scattering process is introduced. It contains the matrix element

$$r_{\alpha,\beta}^{\lambda,\nu}(|\mathbf{K}|) = \frac{1}{2\pi}\int \Big[r_{\alpha}^{\lambda}(\mathbf{K})\Big]^{\star} r_{\beta}^{\nu}(\mathbf{K})\,\mathrm{d}\varphi_{\mathbf{K}} \tag{B.2}$$

and overlap integral

$$r_{\alpha}^{\lambda}(\mathbf{K}) = \sum_{\mathbf{k}} \left[\phi_{\lambda}^{\mathrm{L}}\left(\mathbf{k}\right)\right]^{\star} \phi_{\alpha}^{\mathrm{R}}\left(\mathbf{k}+\mathbf{K}\right)\,, \tag{B.3}$$

compare also Ref. [59] and supplemental material for more details. The derivation of the scattering matrix is non-trivial and needs careful treatment of all relations between the different angles. In general, a derivation in Cartesian coordinates is easier and less defective but a representation using the polar-coordinate system offers more insight into the different physical relations and eventually leads to helpful analytic results and simplifications. Thus, this supplement will concentrate on the derivation in polar coordinates applying a generic complex ansatz for the angular dependency without a-priori restrictions to a simple real-valued ansatz. The generic ansatz is needed for a more detailed understanding of the problem and for the correct normalization of the wavefunctions and the scattering contributions.

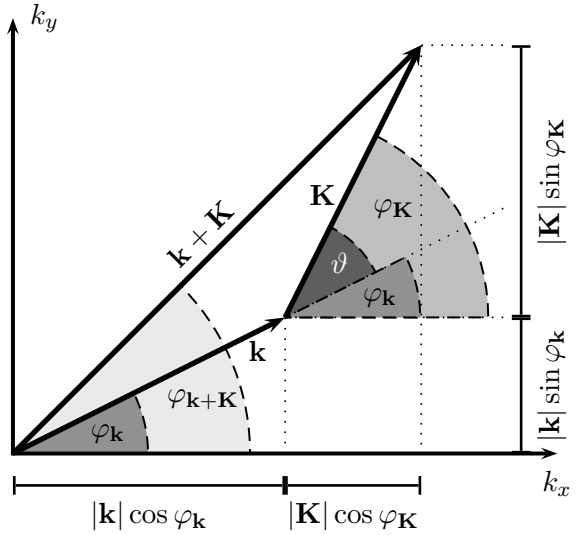

Figure B.1 | Illustration of the relationships between wavevector k and scattering wavevector K. The angles of both vectors against the *x*-axis are denoted by $\varphi_{\mathbf{k}}$ and $\varphi_{\mathbf{K}}$, and the difference angle is denoted by $\vartheta = \varphi_{\mathbf{K}} - \varphi_{\mathbf{k}}$. Same angles are highlighted by the same shadings. The different segments in *x*- and *y*-direction are also labeled at the bottom and the right side. All scattering vectors **K** are considered in the calculations.

Starting from Eq. (B.3) and applying separation (A.16), yields

$$\begin{aligned} r_\alpha^\lambda(\mathbf{K}) &= \sum_{\mathbf{k}} \left[\phi_\lambda^{\mathrm{L}}(\mathbf{k})\right]^\star \phi_\alpha^{\mathrm{R}}(\mathbf{k}+\mathbf{K}) = \sum_{\mathbf{k}} \left[\bar{\phi}_\lambda^{\mathrm{L}}(|\mathbf{k}|)\right]^\star \mathrm{e}^{-\mathrm{i}m_\lambda\varphi_\mathbf{k}}\, \bar{\phi}_\alpha^{\mathrm{R}}(|\mathbf{k}+\mathbf{K}|)\, \mathrm{e}^{\mathrm{i}m_\alpha\varphi_{\mathbf{k}+\mathbf{K}}} \\ &= \int k\,\mathrm{d}k \int \mathrm{d}\varphi_\mathbf{k} \left[\bar{\phi}_\lambda^{\mathrm{L}}(|\mathbf{k}|)\right]^\star \bar{\phi}_\alpha^{\mathrm{R}}(|\mathbf{k}+\mathbf{K}|)\ \mathrm{e}^{-\mathrm{i}m_\lambda\varphi_\mathbf{k}} \left[\cos\varphi_{\mathbf{k}+\mathbf{K}} + \mathrm{i}\sin\varphi_{\mathbf{k}+\mathbf{K}}\right]^{m_\alpha} . \end{aligned} \tag{B.4}$$

Figure B.1 illustrates the angular relations between the wavevector $\mathbf{k}$ and the scattering vector $\mathbf{K}$ where $\varphi_\mathbf{k}$, $\varphi_\mathbf{K}$, and $\varphi_{\mathbf{k}+\mathbf{K}}$ denote the angles between the x-axis and $\mathbf{k}$, $\mathbf{K}$, and $\mathbf{k}+\mathbf{K}$, respectively. Basic geometric relations, see the labels of segments at the bottom and right side in Fig. B.1, show that the angular part in Eq. (B.4) containing the angle $\varphi_{\mathbf{k}+\mathbf{K}}$ of the resulting vector can be expanded to

$$\begin{aligned} \mathrm{e}^{\pm\mathrm{i}\varphi_{\mathbf{k}+\mathbf{K}}} &= \cos(\pm\varphi_{\mathbf{k}+\mathbf{K}}) + \mathrm{i}\sin(\pm\varphi_{\mathbf{k}+\mathbf{K}}) = \cos(\varphi_{\mathbf{k}+\mathbf{K}}) \pm \mathrm{i}\sin(\varphi_{\mathbf{k}+\mathbf{K}}) \\ &= \frac{|\mathbf{k}|\cos\varphi_\mathbf{k} + |\mathbf{K}|\cos\varphi_\mathbf{K}}{|\mathbf{k}+\mathbf{K}|} \pm \mathrm{i}\,\frac{|\mathbf{k}|\sin\varphi_\mathbf{k} + |\mathbf{K}|\sin\varphi_\mathbf{K}}{|\mathbf{k}+\mathbf{K}|} \\ &= \frac{1}{|\mathbf{k}+\mathbf{K}|}\left[|\mathbf{k}|\mathrm{e}^{\pm\mathrm{i}\varphi_\mathbf{k}} + |\mathbf{K}|\mathrm{e}^{\pm\mathrm{i}\varphi_\mathbf{K}}\right] \end{aligned} \tag{B.5}$$

where the plus and minus argumentation is true for p-like states due to the characteristics of cosine and sine, i.e., $\cos(-\vartheta) = \cos(\vartheta)$ and $\sin(-\vartheta) = -\sin(\vartheta)$, and the fact that $m = \pm 1$ for p-like states. Equation (B.5) shows that this procedure leads to a separation with respect to the angle $\varphi_{\mathbf{k}+\mathbf{K}}$ into terms depending on $\varphi_\mathbf{k}$ and $\varphi_\mathbf{K}$, respectively. Inserting this result into Eq. (B.4) yields

$$r_\alpha^\lambda(\mathbf{K}) = \int k\,\mathrm{d}k \int \mathrm{d}\varphi_\mathbf{k} \left[\bar{\phi}_\lambda^{\mathrm{L}}(|\mathbf{k}|)\right]^\star \bar{\phi}_\alpha^{\mathrm{R}}(|\mathbf{k}+\mathbf{K}|)\ \mathrm{e}^{-\mathrm{i}m_\lambda\varphi_\mathbf{k}} \left[\frac{|\mathbf{k}|\mathrm{e}^{\mathrm{i}m_\alpha\varphi_\mathbf{k}} + |\mathbf{K}|\mathrm{e}^{\mathrm{i}m_\alpha\varphi_\mathbf{K}}}{|\mathbf{k}+\mathbf{K}|}\right]^{|m_\alpha|} . \tag{B.6}$$

It is important to emphasize that Eq. (B.6) only applies for $m_\alpha \in \{-1, 0, +1\}$, i.e., s- and p-like states. This is why $|m_\alpha|$ is formally introduced in the exponent of Eq. (B.6). The angular-integration variable is now substituted by $\vartheta = \varphi_\mathbf{K} - \varphi_\mathbf{k}$ denoting the angle between $\mathbf{k}$ and $\mathbf{K}$. This substitution does not change the limits for a full-turn integration of a periodic integrand. With this, the integral may be written as

$$r_\alpha^\lambda(\mathbf{K}) = \int k\,\mathrm{d}k \int \mathrm{d}\vartheta \left[\bar{\phi}_\lambda^{\mathrm{L}}(|\mathbf{k}|)\right]^\star \bar{\phi}_\alpha^{\mathrm{R}}(|\mathbf{k}+\mathbf{K}|)\ A_{\alpha,\lambda}^{\mathbf{k},\mathbf{K}}(\vartheta) \tag{B.7}$$

with the angular-dependent integrand

$$A_{\alpha,\lambda}^{\mathbf{k},\mathbf{K}}(\vartheta) \equiv \mathrm{e}^{-\mathrm{i}m_\lambda(\varphi_\mathbf{K}-\vartheta)} \left[\frac{|\mathbf{k}|\mathrm{e}^{\mathrm{i}m_\alpha(\varphi_\mathbf{K}-\vartheta)} + |\mathbf{K}|\mathrm{e}^{\mathrm{i}m_\alpha\varphi_\mathbf{K}}}{|\mathbf{k}+\mathbf{K}|}\right]^{|m_\alpha|} . \tag{B.8}$$

To simplify this integral further, the symmetries of the trigonometrical functions in the complex exponential functions must be taken into consideration. The bracketed term in Eq. (B.8) with power of $|m_\alpha|$ vanishes for a s-like right-handed excitonic wavefunction and contributes with the power of $|m_\alpha| = |\pm 1| = 1$ for p-like states. While a simple result is obtained if $m_\alpha = 0$, the situation appears to be more complicated for a p-like state where the bracketed term contributes to the angular integral. Then, many different combinations of angular-dependent contributions appear. At this point, it proves to be very useful to make use of the relations of sine and cosine in combination with an integral over the complete period of 2π. Like the right-handed wavefunction depends on $\cos\vartheta$, the factor $|\mathbf{k}+\mathbf{K}| = \sqrt{k^2 + K^2 + 2kK\cos\vartheta}$ in Eq. (B.5) is also an even function in ϑ. Thus, only those contributions of the complex exponential functions containing $\cos^j\vartheta\,\sin^{2j}\vartheta$, $j \in \mathbb{N}^0$, will lead to a contribution of the ϑ-integral whereas the terms with odd powers of $\sin\vartheta$ will vanish. A case-by-case analysis of Eq. (B.8) yields four simplified results when considering the conditions stated above and restricting the analysis to s- and p-like states. With these considerations, the final result for arbitrary mixtures of s- and p-like states assumes the generic form

$$r_{\alpha}^{\lambda}(\mathbf{K}) \quad = \mathscr{R}_{\alpha}^{\lambda}(|\mathbf{K}|)\, \mathrm{e}^{\mathrm{i}(m_{\alpha}-m_{\lambda})\varphi_{\mathbf{K}}} \tag{B.9}$$

with radial contribution

$$\mathscr{R}_{\alpha}^{\lambda}(|\mathbf{K}|) \equiv \int k\, \mathrm{d}k \int \mathrm{d}\vartheta \, \left[\bar{\phi}_{\lambda}^{\mathbf{L}}\left(|\mathbf{k}|\right)\right]^{\star} \bar{\phi}_{\alpha}^{\mathbf{R}}\left(|\mathbf{k}+\mathbf{K}|\right) \, M_{|m_{\lambda}|,|m_{\alpha}|}^{\mathbf{k},\mathbf{K}}(\vartheta) \tag{B.10}$$

and matrix $\mathrm{M} \equiv \begin{pmatrix} M_{0,0}\, M_{0,1} \\ M_{1,0}\, M_{1,1} \end{pmatrix} = \begin{pmatrix} 1 & \frac{|\mathbf{k}|\cos\vartheta + |\mathbf{K}|}{|\mathbf{k}+\mathbf{K}|} \\ \cos\vartheta \, \frac{|\mathbf{K}|\cos\vartheta + |\mathbf{k}|}{|\mathbf{k}+\mathbf{K}|} \end{pmatrix}$.

Generic angular-dependent scattering-matrix element for *s*- and *p*-like states

The diffusive scattering matrix (B.1) is calculated by the difference between the unscattered case with vanishing scattering momentum, i.e., $\hbar\mathbf{K} = \mathbf{0}$, and the $\mathbf{K}$-dependent scattering-matrix element. For arbitrary scattering momenta and with the restriction to s- and p-like states, integral (B.2) can easily be evaluated yielding

$$\begin{aligned} r_{\alpha,\beta}^{\lambda,\nu}(|\mathbf{K}|) &= \frac{1}{2\pi} \int \mathrm{d}\varphi_{\mathbf{K}} \left[r_{\alpha}^{\lambda}(\mathbf{K})\right]^{\star} r_{\beta}^{\nu}(\mathbf{K}) \\ &= \frac{1}{2\pi} \mathscr{R}_{\alpha}^{\lambda}(|\mathbf{K}|)\, \mathscr{R}_{\beta}^{\nu}(|\mathbf{K}|) \int \mathrm{d}\varphi_{\mathbf{K}}\, \mathrm{e}^{\mathrm{i}(m_{\lambda}-m_{\alpha}+m_{\beta}-m_{\nu})\varphi_{\mathbf{K}}} \\ &= \begin{cases} 0 & \text{if } (m_{\lambda}-m_{\alpha}+m_{\beta}-m_{\nu}) \neq 0 \\ \mathscr{R}_{\alpha}^{\lambda}(|\mathbf{K}|)\, \mathscr{R}_{\beta}^{\nu}(|\mathbf{K}|) & \text{if } (m_{\lambda}-m_{\alpha}+m_{\beta}-m_{\nu}) = 0 \end{cases} . \end{aligned} \tag{B.11}$$

This shows that $r_{\alpha,\beta}^{\lambda,\nu}(|\mathbf{K}|)$ corresponds to the bare radial part of $r_{\alpha}^{\lambda}(\mathbf{K})$ and $r_{\beta}^{\nu}(\mathbf{K})$, respectively, if the magnetic quantum numbers sum up to zero. In all other cases, it does not contribute. In the special case of vanishing scattering momentum ($\hbar\mathbf{K} = \mathbf{0}$), only the radial part remains. Applying the generalized orthogonality relations, compare Eq. (5a) of Paper [IV], the radial parts reduce to the simple expression

$$\mathscr{R}_{\alpha}^{\lambda}(0) = \delta_{\lambda,\alpha} \tag{B.12}$$

which reflects the above-mentioned conservation of the magnetic quantum numbers. Implementing these findings, the diffusive scattering matrix (B.1) can finally be formulated as

$$\varepsilon_{\alpha,\beta}^{\lambda,\nu}(|\mathbf{K}|) = \gamma\Big[r_{\alpha,\beta}^{\lambda,\nu}(0) - r_{\alpha,\beta}^{\lambda,\nu}(|\mathbf{K}|)\Big] = \gamma\Big[\delta_{\lambda,\alpha}\, \delta_{\nu,\beta} - \mathscr{R}_{\alpha}^{\lambda}(|\mathbf{K}|)\, \mathscr{R}_{\beta}^{\nu}(|\mathbf{K}|)\Big] \tag{B.13}$$

illustrating that only the radial parts of the scattering matrix contribute while the angle of $\mathbf{K}$ does not play a role. Against the background that diffusive Coulomb scattering only redistributes the excitons to new momenta, Eq. (B.13) consistently reflects the physical scattering effects.

These results directly reproduce the physical character of the transition amplitude described by the overlap integral (B.3): For transitions between different exciton states $\lambda \neq \alpha$, Eq. (B.3) produces a vanishing result for $\mathbf{K} = \mathbf{0}$ since the wavefunctions are orthogonal. Coulomb scattering, however, always entails a momentum exchange via a scattering momentum $\hbar\mathbf{K} > \mathbf{0}$ such that the overlap integral takes a finite value. Thus, Coulomb scattering generates mixtures of the "pure" states of λ- and α-excitons. This fact clearly reveals that diffusive Coulomb scattering is capable to enable an effective coupling between $2p$ and $2s$ states. If the $2p$ state is populated, e.g., by applying a $1s$-to-$2p$ transition induced by a THz pulse to transfer NIR-interband generated $1s$ excitons to the $2p$ state, Coulomb scattering may lead to scattering of this $2p$ population to the $2s$ state. This eventually results in an effective $1s$-to-$2s$-state transfer, circumventing the usual selection rules for THz transitions.

B.2 Diffusive model for excitation-induced dephasing (EID)

The coherent polarization, compare Eq. (1) of Paper [VI], vanishes not only radiatively but also nonradiatively via scattering processes. In general, it it not sufficient to restrict these processes to a mere phenomenological contribution but rather describe them via a microscopic-scattering model

$$\Gamma_{\mathbf{k}} \equiv \sum_{\mathbf{k}',\mathbf{q}\neq\mathbf{0}} V_{\mathbf{q}} \left[c^{\mathbf{q},\mathbf{k}',\mathbf{k}}_{v,v,v,c} + c^{\mathbf{q},\mathbf{k}',\mathbf{k}}_{v,c,c,c} - \left(c^{\mathbf{q},\mathbf{k}',\mathbf{k}}_{c,v,v,v} + c^{\mathbf{q},\mathbf{k}',\mathbf{k}}_{c,c,c,v} \right)^{\star} \right] \tag{B.14}$$

which affects all momentum states by coupling the Coulomb interaction to coherent-carrier correlations. Equation (B.14) is taken from Eq. (117) of Ref. [24]. As already outlined in Sec. 5.1.2, the most accurate approach is to calculate at the level of the *second-Born–Markov approximation* providing results which are suitable even for high-precision design studies for research and industrial applications [263–265]. Owing to mathematical and numerical complexity, it is desirable to formulate a model that is easier to handle but includes the important symmetries of the Coulomb-induced scattering processes, i.e., total-polarization conservation via $\sum_{\mathbf{k}} \Gamma_{\mathbf{k}} = 0$ which is satisfied by the momentum-dependent scattering (B.14). This diffusive character redistributes the microscopic polarizations, similar to the diffusive exciton scattering derived in Sec. B.1. Clearly, a bare phenomenological dephasing constant is not capable of fulfilling this important relation. A possible ansatz for a diffusive dephasing is

$$\Gamma_{\mathbf{k}} = -\mathrm{i}\gamma \left[P_{\mathbf{k}} - \frac{1}{2\pi} \int \mathrm{d}\vartheta \; P_{\mathbf{k}+\mathbf{K}} \right] \tag{B.15}$$

with constant γ, coherent polarization $P_{\mathbf{k}}$, and angle $\vartheta = \varphi_{\mathbf{K}} - \varphi_{\mathbf{k}}$ between carrier momentum $\hbar\mathbf{k}$ and scattering momentum $\hbar\mathbf{K}$. Separating the radial and the angular part by using the general ansatz $P_{\mathbf{k}} = \bar{P}_{|\mathbf{k}|} \, \mathrm{e}^{\mathrm{i}m\varphi_{\mathbf{k}}}$, the expansion (B.5) may be adopted when considering only s- and p-like states. This leads to

$$\Gamma_{\mathbf{k}} = -\mathrm{i}\gamma \left[\bar{P}_{|\mathbf{k}|} \, \mathrm{e}^{\mathrm{i}m\varphi_{\mathbf{k}}} - \frac{1}{2\pi} \int \mathrm{d}\vartheta \; \bar{P}_{|\mathbf{k}+\mathbf{K}|} \left[\frac{|\mathbf{k}| + |\mathbf{K}| \mathrm{e}^{\mathrm{i}m\vartheta}}{|\mathbf{k}+\mathbf{K}|} \, \mathrm{e}^{\mathrm{i}m\varphi_{\mathbf{k}}} \right]^{|m|} \right] , \; m \in \{-1, 0, +1\} . \tag{B.16}$$

Distinguishing again between both considered symmetries and utilizing the trigonometrical relations of the last section, the scattering for s-like states ($m = 0$) reads

$$\Gamma_{\mathbf{k}} = -\mathrm{i}\gamma \left[\bar{P}_{|\mathbf{k}|} - \frac{1}{2\pi} \int \mathrm{d}\vartheta \; \bar{P}_{|\mathbf{k}+\mathbf{K}|} \right] \tag{B.17}$$

and for p-like states ($m = \pm 1$)

$$\Gamma_{\mathbf{k}} = -\mathrm{i}\gamma \left[\bar{P}_{|\mathbf{k}|} - \frac{1}{2\pi} \int \mathrm{d}\vartheta \; \bar{P}_{|\mathbf{k}+\mathbf{K}|} \frac{|\mathbf{k}| + |\mathbf{K}| \cos\vartheta}{|\mathbf{k}+\mathbf{K}|} \right] \mathrm{e}^{\pm\mathrm{i}\varphi_{\mathbf{k}}} \tag{B.18}$$

where only the radial part contributes to the eigenvalue problem. The diffusive scattering $\Gamma_{\mathbf{k}}$ enters the semiconductor Bloch equations via $\Gamma_{\mathbf{k}} = \sum_{\mathbf{k}'} \gamma_{\mathbf{k},\mathbf{k}'} P_{\mathbf{k}'}$ after Eq. (B.16) is represented in matrix form. As elaborated in Ref. [124], the scattering approximation in the generalized Wannier equations (5.7) and (5.8), originating from the exciton-correlation dynamics (2.28), follows from neglecting coupling among doublets and to six-point terms. Beyond the second-Born approach, the doublet structure is fully included while triplets are treated on the scattering level. Owing to the Fermionic structure, a consistent description then introduces six- and eight-point correlations leading to complicated mixtures of scattering between singlets and true excitons. Decent approximation schemes are presented in Ref. [124]. In this thesis, the diffusive scattering model is applied, which consistently describes the state-dependent broadening effects.

C

Influence of orbital symmetry on the Coulomb-matrix element

In Chap. 5, terahertz transitions between s- and p-like states are investigated. This gives rise to substantial changes of the excitonic eigenvalue problem not only in the scattering contributions, compare Sec. B.2, but also of the Coulomb-matrix element in Eqs. (5.7) and (5.8). This supplement briefly sketches the modifications of the Coulomb-matrix element to correspond to the energy levels within the subshell. The procedure is very similar to the argumentation of App. B.

The emerging Coulomb sums in Eqs. (5.7) and (5.8) contain the excitonic wavefunctions (A.16). Without loss of generality, the two-dimensional case is presented here such that the sum reads

$$\sum_{\mathbf{k}'} V_{\mathbf{k}-\mathbf{k}'}\, \phi_\nu(\mathbf{k}') = \sum_{\mathbf{k}'} V_{\mathbf{k}-\mathbf{k}'}\, \bar{\phi}_\nu(|\mathbf{k}'|)\, \mathrm{e}^{\mathrm{i}m_\nu \varphi_{\mathbf{k}'}} = \frac{\mathscr{L}^2}{4\pi^2} \int \bar{\phi}_\nu(|\mathbf{k}'|)\, V^{m_\nu}_{\mathbf{k}-\mathbf{k}'}\, k' \mathrm{d}k' \tag{C.1}$$

with the angular-integrated Coulomb-matrix element

$$V^{m_\nu}_{\mathbf{k}-\mathbf{k}'} \equiv \int V_{\mathbf{k}-\mathbf{k}'}\, \mathrm{e}^{\mathrm{i}m_\nu \varphi_{\mathbf{k}'}}\, \mathrm{d}\varphi_{\mathbf{k}'} = \int V_{\mathbf{k}-\mathbf{k}'}\, \mathrm{e}^{\mathrm{i}m_\nu (\varphi_{\mathbf{k}}+\vartheta)}\, \mathrm{d}\vartheta = \mathrm{e}^{\mathrm{i}m_\nu \varphi_{\mathbf{k}}} \int V_{\mathbf{k}-\mathbf{k}'}\, \cos(m_\nu \vartheta)\, \mathrm{d}\vartheta\,. \tag{C.2}$$

Here, $\vartheta = \varphi_{\mathbf{k}'} - \varphi_{\mathbf{k}}$ denotes the angle between $\mathbf{k}'$ and $\mathbf{k}$; compare Fig. B.1 and substitute $\mathbf{K} \to \mathbf{k}'$ to correspond to the derivation presented here. Following the same argumentation as in App. B, the complex part of the exponential function vanishes and only the cosine remains. This representation shows that the effective Coulomb-matrix element for different magnetic quantum numbers varies in a modulation $\cos(m_\nu \vartheta)$ which is 1 for s-like states and $\cos\vartheta$ for p-like states. Depending on the effective Coulomb-matrix element used, the excitonic eigenvalue problem will then lead to s-like or p-like radial solutions, respectively.

The Inner Horizon VI

See page XLIV for reference.

Bibliography and References

This chapter lists the sources and references cited in this thesis. Additional references and annotations are given on page XLIV.

[1] H. Haug and S. W. Koch, *Quantum Theory of the Optical and Electronic Properties of Semiconductors*, 5th ed. (World Scientific, Singapore, 2009) – ISBN 981-283-883-X.

[2] M. Kira and S. W. Koch, *Semiconductor Quantum Optics*, 1st ed. (Cambridge Univ. Press, Cambridge (England, UK), 2011) – ISBN 978-0-521-87509-7.

[3] J. Jeong, N. Aetukuri, T. Graf, T. D. Schladt, M. G. Samant, and S. S. P. Parkin, "Suppression of Metal-Insulator Transition in VO_2 by Electric Field-Induced Oxygen Vacancy Formation ", Science **339**, 1402 (2013).

[4] D. Takahashi, "IBM creates liquid-based transistors that can process data like the human brain", press article (March 21, 2013), venturebeat.com, available online (retrieved September 22, 2013), `http://venturebeat.com/2013/03/21/ibm-creates-liquid-based-transistors-that-can-process-data-like-the-human-brain`.

[5] N. Ernst, "IBM schaltet mit Nanolitern", press article (March 22, 2013), golem.de, available online (retrieved September 22, 2013), `http://www.golem.de/news/halbleiter-ibm-schaltet-mit-nanolitern-1303-98341.html`.

[6] J. B. H. Peek, J. W. M. Bergmans, J. A. M. M. van Haaren, F. Toolenaar, and S. G. Stan, *Origins And Successors Of The Compact Disc: Contributions of Philips to Optical Storage*, 1st ed., Philips Research Book Series, Vol. 11 (Springer Netherlands, Dordrecht (Netherlands), 2009) – ISBN 978-9048181544.

[7] C. Borchard-Tuch, "Blu-Ray Disc", Chemie in unserer Zeit **40**, 269 (2006).

[8] G. Wong, "Inside Solid State Drives (SSDs)", in *SSD Market Overview*, Springer Series in Advanced Microelectronics, Vol. 37, edited by R. Micheloni, A. Marelli, and K. Eshghi (Springer Netherlands, Dordrecht (Netherlands), 2013) pp. 1–17, – ISBN 978-94-007-5145-3.

[9] V. Ferretti, *Dictionary of Electronics, Computing, Telecommunications and Media* (Springer, Berlin, Heidelberg (Germany), 2004) – ISBN 978-3540406938.

[10] H. Goldstein, "Too little, too soon [solid-state flash memories]", Spectrum, IEEE **43**, 30 (2006).

[11] J. Shinar, *Organic Light-Emitting Devices: A Survey* (Springer, Berlin, Heidelberg (Germany), 2004) – ISBN 978-0387953434.

[12] C. W. Tang and S. A. Van Slyke, "Organic electroluminescent diodes", Appl. Phys. Lett. **51**, 913 (1987).

[13] H. Lee, I. Park, J. Kwak, D. Y. Yoon, and C. Lee, "Improvement of electron injection in inverted bottom-emission blue phosphorescent organic light emitting diodes using zinc oxide nanoparticles", Appl. Phys. Lett. **96**, 153306 (2010).

[14] M. Vogel, "Helles Licht aus dünnen Schichten", Physik Journal **12**, 50 (March 2013).

[15] J. Harpe and M. van Wichen, "Philips creates the world's most energy-efficient warm white LED lamp", press release (April 11, 2013), Royal Philips Electronics, available online (retrieved September 22, 2013), http://www.newscenter.philips.com/main/standard/news/press/2013/20130411-philips-creates-the-world-s-most-energy-efficient-warm-white-led-lamp.wpd.

[16] J. Harpe and M. van Wichen, "Details of the 200 lm/W TLED lighting technology breakthrough unraveled", press release (April 11, 2013), Royal Philips Electronics, available online (retrieved September 22, 2013), http://www.newscenter.philips.com/main/standard/news/articles/20130411-details-of-the-200lm-w-tled-lighting-technology-breakthrough-unraveled.wpd.

[17] N. Ernst, "Daten mit 3 GBit/s aus LED-Lampen", press article (April 8, 2013), golem.de, available online (retrieved September 22, 2013), http://www.golem.de/news/fraunhofer-hhi-daten-mit-3-gbit-s-aus-led-lampen-1304-98575.html.

[18] S. Anthony, "Researchers create 3Gbps LiFi network with LED bulbs", press article (April 5, 2013), extremeTech.com, available online (retrieved September 22, 2013), http://www.extremetech.com/computing/152740-researchers-create-3gbps-lifi-network-with-led-bulbs.

[19] W. Pluta, "Daten aus der Deckenlampe", press article (September 9, 2011), golem.de, available online (retrieved September 22, 2013), http://www.golem.de/1109/86194.html.

[20] R. Sagotra and R. Aggarwal, "Visible Light Communication", Int. J. Eng. Trends Technol. (IJETT) **4**, 403 (2013).

[21] H. M. Gibbs, G. Khitrova, and S. W. Koch, "Exciton–polariton light–semiconductor coupling effects", Nature Photon. **5**, 273 (2011).

[22] C. Lange, N. S. Köster, S. Chatterjee, H. Sigg, D. Chrastina, G. Isella, H. von Känel, M. Schäfer, M. Kira, and S. W. Koch, "Ultrafast nonlinear optical response of photoexcited Ge/SiGe quantum wells: Evidence for a femtosecond transient population inversion", Phys. Rev. B **79**, 201306 (2009).

[23] F. Blanchard, D. Golde, F. H. Su, L. Razzari, G. Sharma, R. Morandotti, T. Ozaki, M. Reid, M. Kira, S. W. Koch, and F. A. Hegmann, "Effective Mass Anisotropy of Hot Electrons in Nonparabolic Conduction Bands of n-Doped InGaAs Films Using Ultrafast Terahertz Pump-Probe Techniques", Phys. Rev. Lett. **107**, 107401 (2011).

[24] M. Kira and S. W. Koch, "Many-body correlations and excitonic effects in semiconductor spectroscopy", Prog. Quantum Electron. **30**, 155 (2006).

[25] H. Stolz, *Time-Resolved Light Scattering from Excitons* (Springer, Berlin, Heidelberg (Germany), 1994) – ISBN 978-0387579467.

[26] A. Thränhardt, C. Ell, S. Mosor, G. Rupper, G. Khitrova, H. M. Gibbs, and S. W. Koch, "Interplay of phonon and disorder scattering in semiconductor quantum wells", Phys. Rev. B **68**, 035316 (2003).

[27] P. Bozsoki, P. Thomas, M. Kira, W. Hoyer, T. Meier, S. W. Koch, K. Maschke, I. Varga, and H. Stolz, "Characterization of Disorder in Semiconductors via Single-Photon Interferometry", Phys. Rev. Lett. **97**, 227402 (2006).

[28] P. Bozsoki, M. Kira, W. Hoyer, T. Meier, I. Varga, P. Thomas, and S. W. Koch, "Microscopic modeling of photoluminescence of strongly disordered semiconductors", J. Lumin. **124**, 99 (2007).

[29] W. Hoyer, M. Kira, and S. W. Koch, "Influence of Coulomb and phonon interaction on the exciton formation dynamics in semiconductor heterostructures", Phys. Rev. B **67**, 155113 (2003).

[30] P. Borri, W. Langbein, J. M. Hvam, and F. Martelli, "Well-width dependence of exciton-phonon scattering in $In_xGa_{1-x}As/GaAs$ single quantum wells", Phys. Rev. B **59**, 2215 (1999).

[31] B. Mieck, H. Haug, W. A. Hügel, M. F. Heinrich, and M. Wegener, "Quantum-kinetic dephasing in resonantly excited semiconductor quantum wells", Phys. Rev. B **62**, 2686 (2000).

[32] H. W. Wyld, Jr. and B. D. Fried, "Quantum mechanical kinetic equations", Ann. Phys. (NY) **23**, 374 (1963).

[33] J. Čížek, "On the Correlation Problem in Atomic and Molecular Systems. Calculation of Wavefunction Components in Ursell-Type Expansion Using Quantum-Field Theoretical Methods", J. Chem. Phys. **42**, 4256 (1966).

[34] G. D. Purvis III and R. J. Bartlett, "A full coupled-cluster singles and doubles model: The inclusion of disconnected triples", J. Chem. Phys. **76**, 1910 (1982).

[35] J. Fricke, "Transport Equations Including Many-Particle Correlations for an Arbitrary Quantum System: A General Formalism", Ann. Phys. (NY) **252**, 479 (1996).

[36] M. Kira, W. Hoyer, and S. W. Koch, "Excitons and Luminescence in Semiconductor Heterostructures", Nonlin. Opt. (Mclc) Sec. B **29**, 481 (2002).

[37] M. Kira and S. W. Koch, "Microscopic theory of optical excitations, photoluminescence, and terahertz response in semiconductors", Eur. Phys. J. D **36**, 143 (2005).

[38] M. Kira and S. W. Koch, "Cluster-expansion representation in quantum optics", Phys. Rev. A **78**, 022102 (2008).

[39] P. Borri, W. Langbein, S. Schneider, U. Woggon, R. L. Sellin, D. Ouyang, and D. Bimberg, "Ultralong Dephasing Time in InGaAs Quantum Dots", Phys. Rev. Lett. **87**, 157401 (2001).

[40] Y.-Z. Ma, M. W. Graham, G. R. Fleming, A. A. Green, and M. C. Hersam, "Ultrafast Exciton Dephasing in Semiconducting Single-Walled Carbon Nanotubes", Phys. Rev. Lett. **101**, 217402 (2008).

[41] J. Brandt, P. Felbier, D. Fröhlich, C. Sandfort, M. Bayer, and H. Stolz, "Temperature dependence of homogeneous broadening of the $1s$ paraexciton in Cu_2O", Phys. Rev. B **81**, 155214 (2010).

[42] R. P. Stanley, J. Hegarty, R. Fischer, J. Feldmann, E. O. Göbel, R. D. Feldman, and R. F. Austin, "Hot-exciton relaxation in $Cd_xZn_{1-x}Te/ZnTe$ multiple quantum wells", Phys. Rev. Lett. **67**, 128 (1991).

[43] N. Balkan, *Hot Electrons in Semiconductors: Physics and Devices* (Oxford Univ. Press, Oxford (UK), 1998) – ISBN 978-0198500582.

[44] T. Kampfrath, L. Perfetti, F. Schapper, C. Frischkorn, and M. Wolf, "Strongly Coupled Optical Phonons in the Ultrafast Dynamics of the Electronic Energy and Current Relaxation in Graphite", Phys. Rev. Lett. **95**, 187403 (2005).

[45] U. Woggon, F. Gindele, O. Wind, and C. F. Klingshirn, "Exchange interaction and phonon confinement in CdSe quantum dots", Phys. Rev. B **54**, 1506 (1996).

[46] H. Zhao, S. Moehl, and H. Kalt, "Coherence Length of Excitons in a Semiconductor Quantum Well", Phys. Rev. Lett. **89**, 097401 (2002).

[47] T. Feldtmann, *Influence of phonons on semiconductor quantum emission*, PhD thesis, Philipps-Universität Marburg, Department of Physics and Material Sciences Center, Marburg (Germany) (2009).

[48] T. Feldtmann, M. Kira, and S. W. Koch, "Theoretical analysis of higher-order phonon sidebands in semiconductor luminescence spectra", J. Lumin. **130**, 107 (2010).

[49] T. Feldtmann, M. Kira, and S. W. Koch, "Phonon sidebands in semiconductor luminescence", Phys. Status Solidi B **246**, 332 (2009).

[50] A. Chernikov, T. Feldtmann, S. Chatterjee, M. Koch, M. Kira, and S. W. Koch, "Time-resolved phonon-sideband spectroscopy", Solid State Commun. **150**, 1733 (2010).

[51] S. Chatterjee, C. Ell, S. Mosor, G. Khitrova, H. M. Gibbs, W. Hoyer, M. Kira, S. W. Koch, J. P. Prineas, and H. Stolz, "Excitonic Photoluminescence in Semiconductor Quantum Wells: Plasma versus Excitons", Phys. Rev. Lett. **92**, 067402 (2004).

[52] C. Weisbuch, M. Nishioka, A. Ishikawa, and Y. Arakawa, "Observation of the coupled exciton–photon mode splitting in a semiconductor quantum microcavity", Phys. Rev. Lett. **69**, 3314 (1992).

[53] R. Houdré, C. Weisbuch, R. P. Stanley, U. Oesterle, P. Pellandini, and M. Ilegems, "Measurement of Cavity-Polariton Dispersion Curve from Angle-Resolved Photoluminescence Experiments", Phys. Rev. Lett. **73**, 2043 (1994).

[54] M. Kira, F. Jahnke, S. W. Koch, J. D. Berger, D. V. Wick, T. R. Nelson, G. Khitrova, and H. M. Gibbs, "Quantum Theory of Nonlinear Semiconductor Microcavity Luminescence Explaining "Boser" Experiments", Phys. Rev. Lett. **79**, 5170 (1997).

[55] G. Khitrova, D. V. Wick, J. D. Berger, C. Ell, J. P. Prineas, T. R. Nelson, O. Lyngnes, H. M. Gibbs, M. Kira, F. Jahnke, S. W. Koch, W. W. Rühle, and S. Hallstein, "Excitonic Effects, Luminescence, and Lasing in Semiconductor Microcavities", Phys. Status Solidi B **206**, 3 (1998).

[56] M. S. Skolnick, T. A. Fisher, and D. M. Whittaker, "Strong coupling phenomena in quantum microcavity structures", Semicond. Sci. Technol. **13**, 645 (1998).

[57] G. Khitrova, H. M. Gibbs, F. Jahnke, M. Kira, and S. W. Koch, "Nonlinear optics of normal-mode-coupling semiconductor microcavities", Rev. Mod. Phys. **71**, 1591 (1999).

[58] G. Khitrova, H. M. Gibbs, M. Kira, S. W. Koch, and A. Scherer, "Vacuum Rabi splitting in semiconductors", Nature Phys. **2**, 81 (2006).

[59] W. D. Rice, J. Kono, S. Zybell, S. Winnerl, J. Bhattacharyya, H. Schneider, M. Helm, B. Ewers, A. Chernikov, M. Koch, S. Chatterjee, G. Khitrova, H. M. Gibbs, L. Schneebeli, B. Breddermann, M. Kira, and S. W. Koch, "Observation of Forbidden Exciton Transitions Mediated by Coulomb Interactions in Photoexcited Semiconductor Quantum Wells", Phys. Rev. Lett. **110**, 137404 (2013).

[60] J. M. J. Madey, "Stimulated Emission of Bremsstrahlung in a Periodic Magnetic Field", J. Appl. Phys. **42**, 1906 (1971).

[61] J. Urata, M. Goldstein, M. F. Kimmitt, A. Naumov, C. Platt, and J. E. Walsh, "Superradiant Smith-Purcell Emission", Phys. Rev. Lett. **80**, 516 (1998).

[62] M. Abo-Bakr, J. Feikes, K. Holldack, G. Wüstefeld, and H.-W. Hübers, "Steady-State Far-Infrared Coherent Synchrotron Radiation detected at BESSY II", Phys. Rev. Lett. **88**, 254801 (2002).

[63] J. Feldhaus, J. Arthur, and J. B. Hastings, "X-ray free-electron lasers", J. Phys. B **38**, S799 (2005).

[64] J. Faist, F. Capasso, D. L. Sivco, C. Sirtori, A. L. Hutchinson, and A. Y. Cho, "Quantum Cascade Laser", Science **264**, 553 (1994).

[65] B. S. Williams, S. Kumar, H. Callebaut, Q. Hu, and J. L. Reno, "Terahertz quantum-cascade laser operating up to 137 K", Appl. Phys. Lett. **83**, 5142 (2003).

[66] M. Kira, W. Hoyer, T. Stroucken, and S. W. Koch, "Exciton Formation in Semiconductors and the Influence of a Photonic Environment", Phys. Rev. Lett. **87**, 176401 (2001).

[67] M. Kira, W. Hoyer, and S. W. Koch, "Microscopic theory of the semiconductor terahertz response", Phys. Status Solidi B **238**, 443 (2003).

[68] R. H. M. Groeneveld and D. Grischkowsky, "Picosecond time-resolved far-infrared experiments on carriers and excitons in GaAs-AlGaAs multiple quantum wells", J. Opt. Soc. Am. B **11**, 2502 (1994).

[69] J. Černe, J. Kono, M. S. Sherwin, M. Sundaram, A. C. Gossard, and G. E. W. Bauer, "Terahertz Dynamics of Excitons in GaAs/AlGaAs Quantum Wells", Phys. Rev. Lett. **77**, 1131 (1996).

[70] R. A. Kaindl, M. A. Carnahan, D. Hagele, R. Lovenich, and D. S. Chemla, "Ultrafast terahertz probes of transient conducting and insulating phases in an electron-hole gas", Nature (London) **423**, 734 (2003).

[71] M. Kira, W. Hoyer, and S. W. Koch, "Terahertz signatures of the exciton formation dynamics in non-resonantly excited semiconductors", Solid State Commun. **129**, 733 (2004).

[72] P. H. Siegel, "Terahertz technology in biology and medicine", IEEE Trans. Microw. Theory Techn. **52**, 2438 (2004).

[73] C. H. Chen, *Ultrasonic and Advanced Methods for Nondestructive Testing and Material Characterization* (World Scientific, Singapore, 2007) – ISBN 978-9812704092.

[74] H. Welker, "Über neue halbleitende Verbindungen I", Z. f. Naturforschung **7a**, 744 (1952).

[75] H. Welker, "Über neue halbleitende Verbindungen II", Z. f. Naturforschung **8a**, 248 (1953).

[76] *Strahlungsphysik im optischen Bereich und Lichttechnik – Benennung der Wellenlängenbereiche*, Norm DIN 5031-7 (Jan. 1984).

[77] T. Kleine-Ostmann, P. Knobloch, M. Koch, S. Hoffmann, M. Breede, M. Hofmann, G. Hein, K. Pierz, M. Sperling, and K. Donhuijsen, "Continuous-wave THz imaging", Electron. Lett. **37**, 1461 (2001).

[78] M. Scheller, J. M. Yarborough, J. V. Moloney, M. Fallahi, M. Koch, and S. W. Koch, "Room temperature continuous wave milliwatt terahertz source", Opt. Express **18**, 27112 (2010).

[79] N. W. Ashcroft and D. N. Mermin, *Solid State Physics*, 1st ed. (Brooks Cole, 1976) – ISBN 978-0030839931.

[80] G. Czycholl, *Theoretische Festkörperphysik*, 3rd ed. (Springer, Berlin, Heidelberg (Germany), 2007) – ISBN 978-3-540-74789-5.

[81] M. Kira, F. Jahnke, W. Hoyer, and S. W. Koch, "Quantum theory of spontaneous emission and coherent effects in semiconductor microstructures", Prog. Quantum Electron. **23**, 189 (1999).

[82] W. Hoyer, *Quantentheorie zu Exzitonbildung und Photolumineszenz in Halbleitern*, PhD thesis, Philipps-Universität Marburg, Department of Physics and Material Sciences Center, Marburg (Germany) (2002).

[83] J. T. Steiner, *Microscopic Theory of Linear and Nonlinear Terahertz Spectroscopy of Semiconductors*, PhD thesis, Philipps-Universität Marburg, Department of Physics and Material Sciences Center, Marburg (Germany) (2008).

[84] R. Winkler, *Spin–orbit Coupling Effects in Two-Dimensional Electron and Hole Systems*, 1st ed. (Springer, Berlin, Heidelberg (Germany), 2003) – ISBN 978-3540011873.

[85] R. Danneau, O. Klochan, W. R. Clarke, L. H. Ho, A. P. Micolich, M. Y. Simmons, A. R. Hamilton, M. Pepper, D. A. Ritchie, and U. Zülicke, "Anisotropic Zeeman Splitting In Ballistic One-Dimensional Hole Systems", AIP Conf. Proc. **893**, 699 (2007).

[86] L. C. Andreani, F. Tassone, and F. Bassani, "Radiative lifetime of free excitons in quantum wells", Solid State Commun. **77**, 641 (1991).

[87] F. Bloch, "Über die Quantenmechanik der Elektronen in Kristallgittern", Z. Phys. **52**, 555 (1929).

[88] C. Cohen-Tannoudji, B. Diu, and F. Laloe, *Quantum Mechanics: Volume 1*, 1st ed. (John Wiley & Sons Inc., New York (USA), 1977) – ISBN 978-0471164333.

[89] L. D. Landau and E. M. Lifshitz, *Course of Theoretical Physics, Vol. 3 : Quantum Mechanics (Non-Relativistic Theory)*, 3rd ed. (Butterworth Heinemann, Oxford (UK), 1981) – ISBN 978-0750635394.

[90] M. Schäfer, M. Werchner, W. Hoyer, M. Kira, and S. W. Koch, "Quantum theory of luminescence in multiple-quantum-well Bragg structures", Phys. Rev. B **74**, 155315 (2006).

[91] M. Schäfer, W. Hoyer, M. Kira, S. W. Koch, and J. V. Moloney, "Influence of dielectric environment on quantum-well luminescence spectra", J. Opt. Soc. Am. B **25**, 187 (2008).

[92] M. Schäfer, *Microscopic Theory of Coherent and Incoherent Optical Properties of Semiconductor Heterostructures*, PhD thesis, Philipps-Universität Marburg, Department of Physics and Material Sciences Center, Marburg (Germany) (2008).

[93] J. C. Maxwell, "A Dynamical Theory of the Electromagnetic Field", Phil. Trans. R. Soc. London **155**, 459 (1865).

[94] M. Kira, *Complementary Quantum Dynamics* (University of Helsinki, 1995) – ISBN 951-45-7213-0.

[95] E. Merzbacher, *Quantum Mechanics*, 3rd ed. (John Wiley & Sons, New York (USA), 1998) – ISBN 978-0471887027.

[96] M. Born, E. Wolf, A. B. Bhatia, P. C. Clemmow, D. Gabor, A. R. Stokes, A. M. Taylor, P. A. Wayman, and W. L. Wilcock, *Principles of Optics: Electromagnetic Theory of Propagation, Interference and Diffraction of Light*, 7th ed. (Cambridge Univ. Press, Cambridge (England, UK), 1999) – ISBN 978-0521642224.

[97] M. Göppert-Mayer, "Über Elementarakte mit zwei Quantensprüngen", Ann. Phys. (Leipzig) **9**, 273 (1931).

[98] M. O. Scully and M. S. Zubairy, *Quantum Optics* (Cambridge Univ. Press, Cambridge (England, UK), 1997) – ISBN 978-0521435956.

[99] J. R. Danielson, Y.-S. Lee, J. P. Prineas, J. T. Steiner, M. Kira, and S. W. Koch, "Interaction of Strong Single-Cycle Terahertz Pulses with Semiconductor Quantum Wells", Phys. Rev. Lett. **99**, 237401 (2007).

[100] D. Golde, M. Kira, and S. W. Koch, "Terahertz response of a two-dimensional electron gas", in *Proc. SPIE*, Vol. 6892 (2008) p. 68921F.

[101] S. Schmitt-Rink, D. A. B. Miller, and D. S. Chemla, "Theory of the linear and nonlinear optical properties of semiconductor microcrystallites", Phys. Rev. B **35**, 8113 (1987).

[102] J. I. Frenkel, "On the Transformation of light into Heat in Solids. I", Phys. Rev. **37**, 17 (1931).

[103] N. Donlagic and T. Östreich, "Excitonic effects in optically excited semiconductors with LO-phonon coupling", Phys. Rev. B **59**, 7493 (1999).

[104] D. Kirk and W.-M. W. Hwu, *Programming Massively Parallel Processors: A Hands-On Approach (Applications of GPU Computing Series)* (Morgan Kaufman Publ. Inc., Burlington, MA (USA), 2010) – ISBN 978-0123814722.

[105] W. E. Nagel, D. H. Kröner, and M. M. Resch, *High Performance Computing in Science and Engineering '12: Transactions of the High Performance Computing Center, Stuttgart (HLRS) 2012* (Springer, Berlin, Heidelberg (Germany), 2013) – ISBN 978-3642333736.

[106] Y. Uejima and R. Maezono, "GPGPU for orbital function evaluation with a new updating scheme", J. Comput. Chem. **34**, 83 (2013).

[107] M. Kira and S. W. Koch, "Quantum-optical spectroscopy of semiconductors", Phys. Rev. A **73**, 013813 (2006).

[108] M. Kira, S. W. Koch, R. P. Smith, A. E. Hunter, and S. T. Cundiff, "Quantum spectroscopy with Schrodinger-cat states", Nature Phys. **7**, 799 (2011).

[109] M. Mootz, M. Kira, and S. W. Koch, "Sequential build-up of quantum-optical correlations", J. Opt. Soc. Am. B **29**, A17 (2012).

[110] M. Lindberg and S. W. Koch, "Effective Bloch equations for semiconductors", Phys. Rev. B **38**, 3342 (1988).

[111] J. I. Frenkel, "On the Transformation of Light into Heat in Solids. II", Phys. Rev. **37**, 1276 (1931).

[112] J. I. Frenkel, "On the absorption of light and the trapping of electrons and positive holes in crystalline dielectrics", Phys. Z. Sowjetunion **9**, 158 (1936).

[113] G. H. Wannier, "The Structure of Electronic Excitation Levels in Insulating Crystals", Phys. Rev. **52**, 191 (1937).

[114] J. J. Hopfield, "Theory of the Contribution of Excitons to the Complex Dielectric Constant of Crystals", Phys. Rev. **112**, 1555 (1958).

[115] R. Elliott, "Theory of excitons", in *Polarons and Excitons*, edited by C. Kuper and G. Whitefield (Oliver & Boyd, Edinburgh (Scotland, UK), 1963) pp. 269–293.

[116] R. S. Knox, "Theory of excitons", in *Solid State Physics*, supplement 5, edited by F. Seitz and D. Turnbull (Acad. Press, New York (USA), 1963).

[117] D. L. Dexter and R. S. Knox, *Excitons* (Interscience Pubn., New York (USA), 1965).

[118] S. W. Koch, T. Meier, W. Hoyer, and M. Kira, "Theory of the optical properties of semiconductor nanostructures", Physica E **14**, 45 (2002).

[119] M. Kira and S. W. Koch, "Exciton-Population Inversion and Terahertz Gain in Semiconductors Excited to Resonance", Phys. Rev. Lett. **93**, 076402 (2004).

[120] S. W. Koch, M. Kira, G. Khitrova, and H. M. Gibbs, "Semiconductor excitons in new light", Nature Mater. **5**, 523 (2006).

[121] M. Kira, F. Jahnke, and S. W. Koch, "Microscopic Theory of Excitonic Signatures in Semiconductor Photoluminescence", Phys. Rev. Lett. **81**, 3263 (1998).

[122] A. Thränhardt, S. Kuckenburg, A. Knorr, T. Meier, and S. W. Koch, "Quantum theory of phonon-assisted exciton formation and luminescence in semiconductor quantum wells", Phys. Rev. B **62**, 2706 (2000).

[123] J. Szczytko, L. Kappei, J. Berney, F. Morier-Genoud, M. T. Portella-Oberli, and B. Deveaud, "Determination of the Exciton Formation in Quantum Wells from Time-Resolved Interband Luminescence", Phys. Rev. Lett. **93**, 137401 (2004).

[124] W. Hoyer, M. Kira, and S. W. Koch, "Influence of bound and unbound electron-hole-pair populations on the excitonic luminescence in semiconductor quantum wells", arXiv:cond-mat/0604349 [cond-mat.mes-hall](2006).

[125] K. Siantidis, V. M. Axt, and T. Kuhn, "Dynamics of exciton formation for near band-gap excitations", Phys. Rev. B **65**, 035303 (2001).

[126] W. Hoyer, C. Ell, M. Kira, S. W. Koch, S. Chatterjee, S. Mosor, G. Khitrova, H. M. Gibbs, and H. Stolz, "Many-body dynamics and exciton formation studied by time-resolved photoluminescence", Phys. Rev. B **72**, 075324 (2005).

[127] I. Galbraith, R. Chari, S. Pellegrini, P. J. Phillips, C. J. Dent, A. F. G. van der Meer, D. G. Clarke, A. K. Kar, G. S. Buller, C. R. Pidgeon, B. N. Murdin, J. Allam, and G. Strasser, "Excitonic signatures in the photoluminescence and terahertz absorption of a $GaAs/Al_xGa_{1-x}As$ multiple quantum well", Phys. Rev. B **71**, 073302 (2005).

[128] E. M. Gershenzon, G. N. Goltsman, and M. G. Ptitsina, "Investigation of free excitons in Ge and their condensation at submillimeter waves", J. Exp. Theor. Phys. (JETP) (orig.: Zh. Eksp. Teor. Fiz. (ZhETF)) **43 (orig.: 70)**, 116 (orig.: 224) (1976).

[129] T. Timusk, H. Navarro, N. O. Lipari, and M. Altarelli, "Far-infrared absorption by excitons in silicon", Solid State Commun. **25**, 217 (1978).

[130] C. I. Ivanov, H. Barentzen, and M. Girardeau, "On the theory of dense exciton systems", Physica A **140**, 612 (1987).

[131] M. Kira, F. Jahnke, and S. W. Koch, "Ultrashort pulse propagation effects in semiconductor microcavities", Solid State Commun. **102**, 703 (1997).

[132] R. Huber, F. Tauser, A. Brodschelm, M. Bichler, G. Abstreiter, and A. Leitenstorfer, "How many-particle interactions develop after ultrafast excitation of an electron-hole plasma", Nature (London) **414**, 286 (2001).

[133] M. Kubouchi, K. Yoshioka, R. Shimano, A. Mysyrowicz, and M. Kuwata-Gonokami, "Study of Orthoexciton-to-Paraexciton Conversion in Cu_2O by Excitonic Lyman Spectroscopy", Phys. Rev. Lett. **94**, 016403 (2005).

[134] M. Jörger, T. Fleck, C. F. Klingshirn, and R. von Baltz, "Midinfrared properties of cuprous oxide: High-order lattice vibrations and intraexcitonic transitions of the $1s$ paraexciton", Phys. Rev. B **71**, 235210 (2005).

[135] S. Leinß, T. Kampfrath, K. v. Volkmann, M. Wolf, J. T. Steiner, M. Kira, S. W. Koch, A. Leitenstorfer, and R. Huber, "Terahertz Coherent Control of Optically Dark Paraexcitons in Cu_2O", Phys. Rev. Lett. **101**, 246401 (2008).

[136] A. D. Jameson, J. L. Tomaino, Y.-S. Lee, J. P. Prineas, J. T. Steiner, M. Kira, and S. W. Koch, "Transient optical response of quantum well excitons to intense narrowband terahertz pulses", Appl. Phys. Lett. **95**, 201107 (2009).

[137] M. Wagner, H. Schneider, D. Stehr, S. Winnerl, A. M. Andrews, S. Schartner, G. Strasser, and M. Helm, "Observation of the Intraexciton Autler-Townes Effect in GaAs/AlGaAs Semiconductor Quantum Wells", Phys. Rev. Lett. **105**, 167401 (2010).

[138] B. Ewers, N. S. Köster, R. Woscholski, M. Koch, S. Chatterjee, G. Khitrova, H. M. Gibbs, A. C. Klettke, M. Kira, and S. W. Koch, "Ionization of coherent excitons by strong terahertz fields", Phys. Rev. B **85**, 075307 (2012).

[139] J. L. Tomaino, A. D. Jameson, Y.-S. Lee, G. Khitrova, H. M. Gibbs, A. C. Klettke, M. Kira, and S. W. Koch, "Terahertz Excitation of a Coherent Λ-Type Three-Level System of Exciton-Polariton Modes in a Quantum-Well Microcavity", Phys. Rev. Lett. **108**, 267402 (2012).

[140] C. N. Böttge, *Phonon-assistierte Lasertätigkeit in Mikroresonatoren*, Diploma thesis, Philipps-Universität Marburg, Department of Physics and Material Sciences Center, Marburg (Germany) (2009).

[141] E. M. Purcell, "Spontaneous emission probabilities at radio frequencies", Phys. Rev. **69**, 681 (1946).

[142] D. Kleppner, "Inhibited Spontaneous Emission", Phys. Rev. Lett. **47**, 233 (1981).

[143] E. Yablonovitch, "Inhibited Spontaneous Emission in Solid-State Physics and Electronics", Phys. Rev. Lett. **58**, 2059 (1987).

[144] F. Jahnke, M. Kira, S. W. Koch, G. Khitrova, E. K. Lindmark, T. R. Nelson, Jr., D. V. Wick, J. D. Berger, O. Lyngnes, H. M. Gibbs, and K. Tai, "Excitonic Nonlinearities of Semiconductor Microcavities in the Nonperturbative Regime", Phys. Rev. Lett. **77**, 5257 (1996).

[145] C. W. Litton, D. C. Reynolds, T. C. Collins, and Y. S. Park, "Exciton–LO-Phonon Interaction and the Anti-Stokes Emission Line in CdS", Phys. Rev. Lett. **25**, 1619 (1970).

[146] S. Permogorov, "Hot excitons in semiconductors", Phys. Status Solidi B **68**, 9 (1975).

[147] S. Ramanathan, S. Bandyopadhyay, L. K. Hussey, and M. Munoz, "Observation of numerous E_2 mode phonon replicas in the room temperature photoluminescence spectra of ZnO nanowires: Evidence of strong deformation potential electron–phonon coupling", Appl. Phys. Lett. **89**, 143121 (2006).

[148] M. Soltani, M. Certier, R. Evrard, and E. Kartheuser, "Photoluminescence of CdTe doped with arsenic and antimony acceptors", J. Appl. Phys. **78**, 5626 (1995).

[149] C. F. Klingshirn, "Linear and nonlinear optics of wide-gap II-VI semiconductors", Phys. Status Solidi B **202**, 1521 (1997).

[150] M. Kozhevnikov, B. M. Ashkinadze, E. Cohen, and A. Ron, "LO-phonon sideband photoluminescence in pure GaAs", Solid State Commun. **106**, 73 (1998).

[151] X. B. Zhang, T. Taliercio, S. Kolliakos, and P. Lefebvre, "Influence of electron-phonon interaction on the optical properties of III nitride semiconductors", J. Phys. Condens. Matter **13**, 7053 (2001).

[152] H. Zhao, S. Moehl, and H. Kalt, "Energy relaxation during hot-exciton transport in quantum wells: Direct observation by spatially resolved phonon-sideband spectroscopy", Appl. Phys. Lett. **81**, 2794 (2002).

[153] L. T. Tan, R. W. Martin, K. P. O'Donnell, and I. M. Watson, "Photoluminescence and phonon satellites of single InGaN/GaN quantum wells with varying GaN cap thickness", Appl. Phys. Lett. **89**, 101910 (2006).

[154] D. G. Thomas, "The exciton spectrum of zinc oxide", J. Phys. Chem. Solids **15**, 86 (1960).

[155] A. Ashrafi and C. Jagadish, "Review of zincblende ZnO: Stability of metastable ZnO phases", J. Appl. Phys. **102**, 071101 (2007).

[156] A. Moezzi, A. M. McDonagh, and M. B. Cortie, "Zinc oxide particles: Synthesis, properties and applications", Chem. Eng. J. **185–186**, 1 (2012).

[157] B. K. Meyer, H. Alves, D. M. Hofmann, W. Kriegseis, D. Forster, F. Bertram, J. Christen, A. Hoffmann, M. Straßburg, M. Dworzak, U. Haboeck, and A. V. Rodina, "Bound exciton and donor-acceptor pair recombinations in ZnO", Phys. Status Solidi B **241**, 231 (2004).

[158] C. F. Klingshirn, "ZnO: Material, Physics and Applications", Chem. Phys. Chem **8**, 782 (2007).

[159] H. Morkoç and Ü. Özgür, *Zinc Oxide: Fundamentals, Materials and Device Technology*, 1st ed. (Wiley-VCH Verlag GmbH & Co. KGaA, Weinheim (Germany), 2009) – ISBN 3-527-40813-4.

[160] U. Ozgur, D. Hofstetter, and H. Morkoc, "ZnO Devices and Applications: A Review of Current Status and Future Prospects", Proc. IEEE **98**, 1255 (2010).

[161] Y. Segawa, H. Sun, T. Makino, M. Kawasaki, and H. Koinuma, "Exciton Related Stimulated Emission in ZnO-Based Multiple-Quantum Wells", Phys. Status Solidi A **192**, 14 (2002).

[162] U. Ozgur, Y. I. Alivov, C. Liu, A. Teke, M. A. Reshchikov, S. Dogan, V. Avrutin, S.-J. Cho, and H. Morkoc, "A comprehensive review of ZnO materials and devices", J. Appl. Phys. **98**, 041301 (2005).

[163] W. Shan, W. Walukiewicz, J. W. Ager III, K. M. Yu, H. B. Yuan, H. P. Xin, G. Cantwell, and J. J. Song, "Nature of room-temperature photoluminescence in ZnO", Appl. Phys. Lett. **86**, 191911 (2005).

[164] J. Pollmann and H. Büttner, "Effective Hamiltonians and binding energies of Wannier excitons in polar semiconductors", Phys. Rev. B **16**, 4480 (1977).

[165] S. W. Koch, private communication (2009).

[166] C. F. Klingshirn, private communication (2009).

[167] T. Hanada, in *Oxide and Nitride Semiconductors*, Advances in Materials Research, Vol. 12, edited by T. Yao and S.-K. Hong (Springer, Berlin, Heidelberg (Germany), 2009) pp. 1–19, – ISBN 978-3-540-88846-8.

[168] C. F. Klingshirn, A. Waag, A. Hoffmann, and J. Geurts, *Zinc Oxide: From Fundamental Properties Towards Novel Applications* (Springer, Berlin, Heidelberg (Germany), 2010) – ISBN 978-3642105760.

[169] W. Y. Liang and A. D. Yoffe, "Transmission spectra of ZnO single crystals", Phys. Rev. Lett. **20**, 59 (1968).

[170] R. Kuhnert and R. Helbig, "Vibronic structure of the green photoluminescence due to copper impurities in ZnO", J. Lumin. **26**, 203 (1981).

[171] S. J. Xu, S.-J. Xiong, and S. L. Shi, "Resonant coupling of bound excitons with LO phonons in ZnO: Excitonic polaron states and Fano interference", J. Chem. Phys. **123**, 221105 (2005).

[172] L. Li, H. Yang, G. Qi, J. Ma, X. Xie, H. Zhao, and F. Gao, "Synthesis and photoluminescence of hollow microspheres constructed with ZnO nanorods by H_2 bubble templates", Chem. Phys. Lett. **455**, 93 (2008).

[173] H. Fröhlich, "Interaction of electrons with lattice vibrations", Proc. R. Soc. Lond. **215**, 291 (1952).

[174] H. Fröhlich, "Electrons in lattice fields", Adv. Phys. **3**, 325 (1954).

[175] H. Haken, *Quantenfeldtheorie des Festkörpers* (Teubner, Stuttgart, 1973) – ISBN 3-519-03025-X.

[176] *Low-Dimensional Nitride Semiconductors*, edited by B. Gil, Series on Semiconductor Science and Technology (Oxford Univ. Press, Oxford (UK), 2002) – ISBN 978-0198509745.

[177] I. V. Bondarev, S. A. Maksimenko, G. Y. Slepyan, I. L. Krestnikov, and A. Hoffmann, "Exciton-phonon interactions and exciton dephasing in semiconductor quantum-well heterostructures", Phys. Rev. B **68**, 073310 (2003).

[178] W. A. Harrison, "Scattering of Electrons by Lattice Vibrations in Nonpolar Crystals", Phys. Rev. **104**, 1281 (1956).

[179] D. Braun, W. W. Rühle, C. Trallero-Giner, and J. Collet, "Spectroscopic determination of the optical deformation-potential constant in semiconductors", Phys. Rev. Lett. **67**, 2335 (1991).

[180] C. F. Klingshirn, *Semiconductor Optics*, 4$^{\text{th}}$ ed. (Springer, Berlin, Heidelberg (Germany), 2012) – ISBN 978-3-642-28361-1.

[181] P. Y. Yu and M. Cardona, *Fundamentals of Semiconductors: Physics and Materials Properties* (Springer, Berlin, Heidelberg (Germany), 2005) – ISBN 978-3540254706.

[182] S. Kalusniak, S. Sadofev, S. Halm, and F. Henneberger, "Vertical cavity surface emitting laser action of an all monolithic ZnO-based microcavity", Appl. Phys. Lett. **98**, 011101 (2011).

[183] T. Makino, C. H. Chia, N. T. Tuan, H. D. Sun, Y. Segawa, M. Kawasaki, A. Ohtomo, K. Tamura, and H. Koinuma, "Room-temperature luminescence of excitons in ZnO/(Mg, Zn)O multiple quantum wells on lattice-matched substrates", Appl. Phys. Lett. **77**, 975 (2000).

[184] H. D. Sun, Y. Segawa, M. Kawasaki, A. Ohtomo, K. Tamura, and H. Koinuma, "Phonon replicas in ZnO/ZnMgO multiquantum wells", J. Appl. Phys. **91**, 6457 (2002).

[185] X. Q. Gu, L. P. Zhu, Z. Z. Ye, H. P. He, Y. Z. Zhang, F. Huang, M. X. Qiu, Y. J. Zeng, F. Liu, and W. Jaeger, "Room-temperature photoluminescence from ZnO/ZnMgO multiple quantum wells grown on Si(111) substrates", Appl. Phys. Lett. **91**, 022103 (2007).

[186] B. Laumer, T. A. Wassner, F. Schuster, M. Stutzmann, J. Schormann, M. Rohnke, A. Chernikov, V. Bornwasser, M. Koch, S. Chatterjee, and M. Eickhoff, "Exciton confinement in homo- and heteroepitaxial ZnO/$Zn_{1-x}Mg_xO$ quantum wells with $x < 0.1$", J. Appl. Phys. **110**, 093513 (2011).

[187] W. von Sellmeier, "Zur Erklärung der abnormen Farbenfolge in Spectrum einiger Substanzen", Ann. Phys. (Leipzig) **143**, 272 (1871).

[188] C. W. Teng, J. F. Muth, Ü. Özgür, M. J. Bergmann, H. O. Everitt, A. K. Sharma, C. Jin, and J. Narayan, "Refractive indices and absorption coefficients of $Mg_xZn_{1-x}O$ alloys", Appl. Phys. Lett. **76**, 979 (2000).

[189] R. Schmidt, B. Rheinländer, M. Schubert, D. Spemann, T. Butz, J. Lenzner, E. M. Kaidashev, M. Lorenz, A. Rahm, H. C. Semmelhack, and M. Grundmann, "Dielectric functions (1 to 5 eV) of wurtzite $Mg_xZn_{1-x}O$ ($x \leq 0.29$) thin films", Appl. Phys. Lett. **82**, 2260 (2003).

[190] N. B. Chen, H. Z. Wu, D. J. Qiu, T. N. Xu, J. Chen, and W. Z. Shen, "Temperature-dependent optical properties of hexagonal and cubic $Mg_xZn_{1-x}O$ thin-film alloys", J. Phys. Condens. Matter **16**, 2973 (2004).

[191] Y. Merle d'Aubigné, A. Wasiela, H. Mariette, and T. Dietl, "Polariton effects in multiple-quantum-well structures of CdTe/$Cd_{1-x}Zn_xTe$", Phys. Rev. B **54**, 14003 (1996).

[192] L. Novotny, "Strong coupling, energy splitting, and level crossings: A classical perspective", Am. J. Phys. **78**, 1199 (2010).

[193] D. C. Reynolds, D. C. Look, D. N. Talwar, G. L. McCoy, and K. R. Evans, "Demonstration of semiconductor characterization by phonon sidebands in photoluminescence", Phys. Rev. B **51**, 2572 (1995).

[194] S. J. Xu, W. Liu, and M. F. Li, "Effect of temperature on longitudinal optical phonon-assisted exciton luminescence in heteroepitaxial GaN layer", Appl. Phys. Lett. **77**, 3376 (2000).

[195] J. Franck and E. G. Dymond, "Elementary processes of photochemical reactions", Trans. Faraday Soc. **21**, 536 (1926).

[196] E. Condon, "A Theory of Intensity Distribution in Band Systems", Phys. Rev. **28**, 1182 (1926).

[197] E. U. Condon, "Nuclear Motions Associated with Electron Transitions in Diatomic Molecules", Phys. Rev. **32**, 858 (1928).

[198] P. W. Atkins, *Molecular Quantum Mechanics*, 4$^{\text{th}}$ ed. (Oxford Univ. Press, Oxford (UK), 2004) – ISBN 978-0199274987.

[199] K. Huang and A. Rhys, "Theory of Light Absorption and Non-Radiative Transitions in F-Centres", Proc. R. Soc. Lond. A **204**, 406 (1950).

[200] R. L. Weiher and W. C. Tait, "Contribution of Excitons to the Edge Luminescence in Zinc Oxide", Phys. Rev. **166**, 791 (1968).

[201] E. Gross, S. Permogorov, and B. Razbirin, "Free exciton motion in crystals and exciton-phonon interaction", J. Phys. Chem. Solids **27**, 1647 (1966).

[202] R. Chen, D. Li, B. Liu, Z. Peng, G. G. Gurzadyan, Q. Xiong, and H. Sun, "Optical and Excitonic Properties of Crystalline ZnS Nanowires: Toward Efficient Ultraviolet Emission at Room Temperature", Nano Lett. **10**, 4956 (2010).

[203] F. Giustino, M. L. Cohen, and S. G. Louie, "Small phonon contribution to the photoemission kink in the copper oxide superconductors", Nature (London) **452**, 975 (2008).

[204] S. J. Xu, W. Liu, and M. F. Li, "Direct determination of free exciton binding energy from phonon-assisted luminescence spectra in GaN epilayers ", Appl. Phys. Lett. **81**, 2959 (2002).

[205] V. V. Ursaki, I. M. Tiginyanu, V. V. Zalamai, V. M. Masalov, E. N. Samarov, G. A. Emelchenko, and F. Briones, "Photoluminescence and resonant Raman scattering from ZnO-opal structures", J. Appl. Phys. **96**, 1001 (2004).

[206] B.-L. Gao, Y. Xiong, and S.-J. Xiong, "Collective mode and peak splitting in phonon sidebands from interaction of degenerate exciton states with longitudinal optical phonons", Phys. Rev. B **74**, 235102 (2006).

[207] S. Soha, Y. Alivov, Z. Fan, and M. Holtz, "Role of phonons in the optical properties of magnetron sputtered ZnO studied by resonance Raman and photoluminescence", J. Appl. Phys. **108**, 053507 (2010).

[208] W.-K. Hong, G. Jo, M. Choe, T. Lee, J. I. Sohn, and M. E. Welland, "Influence of surface structure on the phonon-assisted emission process in the ZnO nanowires grown on homoepitaxial films", Appl. Phys. Lett. **94**, 043103 (2009).

[209] A. W. E. Minnaert, A. Y. Silov, W. van der Vleuten, J. E. M. Haverkort, and J. H. Wolter, "Fröhlich interaction in InAs/GaAs self-assembled quantum dots", Phys. Rev. B **63**, 075303 (2001).

[210] T. Itoh, M. Nishijima, A. I. Ekimov, C. Gourdon, A. L. Efros, and M. Rosen, "Polaron and Exciton-Phonon Complexes in CuCl Nanocrystals", Phys. Rev. Lett. **74**, 1645 (1995).

[211] T. Usui, "Excitations in a High Density Electron Gas. I", Prog. Theor. Phys. **23**, 787 (1960).

[212] M. D. Girardeau, "Formulation of the Many-Body Problem for Composite Particles", J. Math. Phys. **4**, 1096 (1963).

[213] J. N. Ginocchio and C. W. Johnson, "Unified theory of fermion pair to boson mappings in full and truncated spaces", Phys. Rev. C **51**, 1861 (1995).

[214] S. Nomura and T. Kobayashi, "Exciton–LO-phonon couplings in spherical semiconductor microcrystallites", Phys. Rev. B **45**, 1305 (1992).

[215] A. V. Fedorov, A. V. Baranov, and K. Inoue, "Exciton–phonon coupling in semiconductor quantum dots: Resonant Raman scattering", Phys. Rev. B **56**, 7491 (1997).

[216] V. M. Fomin, V. N. Gladilin, J. T. Devreese, E. P. Pokatilov, S. N. Balaban, and S. N. Klimin, "Photoluminescence of spherical quantum dots", Phys. Rev. B **57**, 2415 (1998).

[217] C. Lange, N. S. Köster, S. Chatterjee, H. Sigg, D. Chrastina, G. Isella, H. von Känel, B. Kunert, and W. Stolz, "Comparison of ultrafast carrier thermalization in $Ga_xIn_{1-x}As$ and Ge quantum wells", Phys. Rev. B **81**, 045320 (2010).

[218] K. Reimann, R. A. Kaindl, and M. Woerner, "Optical deformation-potential scattering of holes in multiple quantum well structures", Phys. Rev. B **65**, 045302 (2001).

[219] W. Pötz and P. Vogl, "Theory of optical-phonon deformation potentials in tetrahedral semiconductors", Phys. Rev. B **24**, 2025 (1981).

[220] S.-H. Park and S.-L. Chuang, "Comparison of zinc-blende and wurtzite GaN semiconductors with spontaneous polarization and piezoelectric field effects", J. Appl. Phys. **87**, 353 (2000).

[221] S. Permogorov, "Optical emission due to exciton scattering by LO phonons in semiconductors", in *Excitons*, Modern Problems in Condensed Matter Sciences Series, edited by E. E. I. Rashba and M. D. Sturge (North-Holland Publ., 1982) – ISBN 978-0444862020.

[222] G. D. Mahan, *Many Particle Physics (Physics of Solids and Liquids)*, 3rd ed. (Springer, Berlin, Heidelberg (Germany)) – ISBN 978-0306463389.

[223] B. H. Loo, A. H. Francis, and K. W. Hipps, "Some aspects of electron–phonon interaction in the thermal modulation spectra of molecular crystals", J. Chem. Phys. **65**, 5068 (1976).

[224] A. A. Chernikov, *Time-resolved photoluminescence spectroscopy of semiconductors for optical applications beyond the visible spectral range*, PhD thesis, Philipps-Universität Marburg, Department of Physics and Material Sciences Center, Marburg (Germany) (2012).

[225] K. Takahashi, A. Yoshikawa, and A. Sandhu, *Wide Bandgap Semiconductors: Fundamental Properties and Modern Photonic and Electronic Devices* (Springer, Berlin, Heidelberg (Germany), 2007) – ISBN 978-3540472346.

[226] C. F. Klingshirn and H. Haug, "Optical properties of highly excited direct gap semiconductors", Phys. Rep. **70**, 315 (1981).

[227] F. Tassone, F. Bassani, and L. C. Andreani, "Resonant and surface polaritons in quantum wells", Il Nuovo Cimento D **12**, 1673 (1990).

[228] B. Deveaud, F. Clérot, N. Roy, K. Satzke, B. Sermage, and D. S. Katzer, "Enhanced radiative recombination of free excitons in GaAs quantum wells", Phys. Rev. Lett. **67**, 2355 (1991).

[229] F. Tassone, F. Bassani, and L. C. Andreani, "Quantum-well reflectivity and exciton–polariton dispersion", Phys. Rev. B **45**, 6023 (1992).

[230] L. C. Andreani, "Exciton–polaritons in superlattices", Phys. Lett. A **192**, 99 (1994).

[231] G. Panzarini and L. C. Andreani, "Double quantum well in a semiconductor microcavity: Three-oscillator model and ultrafast radiative decay", Phys. Rev. B **52**, 10780 (1995).

[232] J. Tignon, T. Hasche, D. S. Chemla, H. C. Schneider, F. Jahnke, and S. W. Koch, "Unified Picture of Polariton Propagation in Bulk GaAs Semiconductors", Phys. Rev. Lett. **84**, 3382 (2000).

[233] K.-H. Hellwege, O. Madelung, M. Schulz, H. Weiss, and I. Broser, *Landolt-Börnstein: Numerical Data and Functional Relationships in Science and Technology – New Series Group 3: Condensed Matter, Volume 17: Semiconductor Physics of II–VI and I–VII Compounds* (Springer, Berlin, Heidelberg (Germany), 1982) – ISBN 978-0387113081.

[234] O. Madelung, *Semiconductors – Basic Data* (Springer, Berlin, Heidelberg (Germany), 1996) – ISBN 978-3642976773.

[235] J. B. Stark, W. H. Knox, D. S. Chemla, W. Schäfer, S. Schmitt-Rink, and C. Stafford, "Femtosecond dynamics of excitons under extreme magnetic confinement", Phys. Rev. Lett. **65**, 3033 (1990).

[236] C. Stafford, S. Schmitt-Rink, and W. Schäfer, "Nonlinear optical response of two-dimensional magnetoexcitons", Phys. Rev. B **41**, 10000 (1990).

[237] S. Schmitt-Rink, J. B. Stark, W. H. Knox, D. S. Chemla, and W. Schäfer, "Optical properties of quasi-zero-dimensional magneto-excitons", Appl. Phys. A **53**, 491 (1991).

[238] H. A. Nickel, G. Kioseoglou, T. Yeo, H. D. Cheong, A. Petrou, B. D. McCombe, D. Broido, K. K. Bajaj, and R. A. Lewis, "Internal transitions of confined neutral magnetoexcitons in GaAs/$Al_xGa_{1-x}As$ quantum wells", Phys. Rev. B **62**, 2773 (2000).

[239] P. Zeeman, "On the influence of Magnetism on the Nature of the Light emitted by a Substance", Phil. Mag. **43**, 226 (1897).

[240] K. M. Rao and J. E. Sipe, "Coherent photocurrent control in a magnetic field through quantum interference", Phys. Rev. B **84**, 205313 (2011).

[241] W. Schäfer and M. Wegener, *Semiconductor Optics and Transport Phenomena*, 1st ed. (Springer, Berlin, Heidelberg (Germany), 2002) – ISBN 978-3540616146.

[242] E. Laguerre, "Sur l'intégral $\int_x^{+\infty} x^{-1}\,\mathrm{e}^{-x}\,\mathrm{d}x$", in *Oeuvres, Vol. 1. New York: Chelsea, pp. 428–437, (1971) [reprint],* Compt. Rend. Acad. Sci. Paris, Vol. 7 (Chelsea Pubn. Co., 1879) pp. 72–81.

[243] C. Hermite, "Sur un nouveau développement en série de fonctions", in *Oeuvres complètes, tome 2. Paris, pp. 293–308, (1908) [reprint],* Compt. Rend. Acad. Sci. Paris, Vol. 58 (Honoré Champion, 1864) pp. 93–100 and 266–273.

[244] T. Sandev and I. Petreska, "Selection rules for two-dimensional harmonic oscillator", Bull. Chem. Technol. Macedonia **24**, 143 (2005).

[245] F. Jahnke, M. Kira, and S. W. Koch, "Linear and nonlinear optical properties of excitons in semiconductor quantum wells and microcavities", Z. Phys. B: Condens. Matter **104**, 559 (1997).

[246] H. Wang, K. Ferrio, D. G. Steel, Y. Z. Hu, R. Binder, and S. W. Koch, "Transient nonlinear optical response from excitation induced dephasing in GaAs", Phys. Rev. Lett. **71**, 1261 (1993).

[247] T. Rappen, U.-G. Peter, M. Wegener, and W. Schäfer, "Polarization dependence of dephasing processes: A probe for many-body effects", Phys. Rev. B **49**, 10774 (1994).

[248] W. Schäfer, R. Lövenich, N. A. Fromer, and D. S. Chemla, "From Coherently Excited Highly Correlated States to Incoherent Relaxation Processes in Semiconductors", Phys. Rev. Lett. **86**, 344 (2001).

[249] W. W. Chow and S. W. Koch, *Semiconductor-Laser Fundamentals, Physics of the Gain Materials* (Springer, Berlin, Heidelberg (Germany), 1999) – ISBN 3-540-64166-1.

[250] J. Kono, M. Y. Su, J. Černe, M. S. Sherwin, S. J. A. Jr., T. Inoshita, T. Noda, and H. Sakaki, "Terahertz dynamics in confined magnetoexcitons", Physica B **249–251**, 527 (1998).

[251] Z. Barticevic, M. Pacheco, C. A. Duque, and L. E. Oliveira, "Intra-magnetoexciton transitions in semiconductor quantum wells", Mat. Res. Soc. Symp. Proc. **692**, H6.35.1 (2001).

[252] Z. Barticevic, M. Pacheco, C. A. Duque, and L. E. Oliveira, "Magnetoexciton transitions in GaAs–$Ga_{1-x}Al_x$ As quantum wells", J. Phys. Condens. Matter **14**, 1021 (2002).

[253] X. Mi, D. Li, F. Meng, and H. Zhao, "Magnetoabsorption spectra of magnetoexciton transitions in GaAs/$Ga_0.7Al_0.3$As quantum wells", Chin. Opt. Lett. **7**, 335 (2009).

[254] M. S. Salib, H. A. Nickel, G. S. Herold, A. Petrou, B. D. McCombe, R. Chen, K. K. Bajaj, and W. Schaff, "Observation of Internal Transitions of Confined Excitons in GaAs/AlGaAs Quantum Wells", Phys. Rev. Lett. **77**, 1135 (1996).

[255] H. Q. Hou, W. Staguhn, N. Miura, Y. Segawa, S. Takeyama, Y. Aoyagi, and J. M. Zhou, "Photoluminescence intensity of InGaAs/GaAs Strained quantum wells under high magnetic fields", Solid State Commun. **74**, 687 (1990).

[256] A. Wójs, J. J. Quinn, and P. Hawrylak, "Energy spectra and photoluminescence of charged magnetoexcitons", Physica E **8**, 254 (2000).

[257] S. Zybell, H. Schneider, S. Winnerl, M. Wagner, K. Kohler, and M. Helm, "Photoluminescence dynamics in GaAs/AlGaAs quantum wells under pulsed intersubband excitation", Appl. Phys. Lett. **99**, 041103 (2011).

[258] J. Bhattacharyya, M. Wagner, S. Zybell, S. Winnerl, D. Stehr, M. Helm, and H. Schneider, "Simultaneous time and wavelength resolved spectroscopy under two-colour near infrared and terahertz excitation", Rev. Sci. Instrum. **82**, 103107 (2011).

[259] J. Kono, M. Y. Su, T. Inoshita, T. Noda, M. S. Sherwin, J. S. J. Allen, and H. Sakaki, "Resonant Terahertz Optical Sideband Generation from Confined Magnetoexcitons", Phys. Rev. Lett. **79**, 1758 (Sep 1997).

[260] W. H. Press, S. A. Teukolsky, W. T. Vetterling, and B. P. Flannery, *Numerical Recipes: The Art of Scientific Computing*, 3rd ed. (Cambridge Univ. Press, Cambridge (England, UK)) – ISBN 978-0521880688.

[261] P. Deuflhard and M. Weiser, *Adaptive Numerical Solution of PDEs*, de Gruyter Textbook (De Gruyter, Berlin (Germany), 2012) – ISBN 978-3110283105.

[262] J. Stoer and R. Bulirsch, *Numerische Mathematik 2* (Springer, Berlin, Heidelberg (Germany)) – ISBN 978-3-540-23777-8.

[263] J. Hader, J. V. Moloney, M. Fallahi, L. Fan, and S. W. Koch, "Closed-loop design of a semiconductor laser", Opt. Lett. **31**, 3300 (2006).

[264] C. Bückers, E. Kühn, C. Schlichenmaier, S. Imhof, A. Thränhardt, J. Hader, J. V. Moloney, O. Rubel, W. Zhang, T. Ackemann, and S. W. Koch, "Quantum modeling of semiconductor gain materials and vertical-external-cavity surface-emitting laser systems", Phys. Status Solidi B **247**, 789 (2010).

[265] T. Lermer, A. Gomez-Iglesias, M. Sabathil, J. Muller, S. Lutgen, U. Strauss, B. Pasenow, J. Hader, J. V. Moloney, S. W. Koch, W. Scheibenzuber, and U. T. Schwarz, "Gain of blue and cyan InGaN laser diodes", Appl. Phys. Lett. **98**, 021115 (2011).

Additional References

Quote, logo, and triskelion on the quotation page by courtesy of ELUVEITIE (Winterthur, Switzerland) and according to

C. Glanzmann *et al.*, ELUVEITIE: *Everything remains (as it never was)* (Nuclear Blast, 2010).
C. Glanzmann *et al.*, ELUVEITIE: *Helvetios* (Nuclear Blast, 2012).

Artworks on the blank pages by courtesy of

Jens Lausen, Künstlerhaus Bergedorf, Hamburg (Germany)
and according to
Jens Lausen, *The Inner Horizon*, (Metropolitan Museum of Manila, Manila (the Philippines), 1992):
„Der innere und der äußere Horizont endigen in ein und derselben Linie."
as a homage to
Leonardo da Vinci, *A Treatise on Painting (Trattato della pittura, Codex Urbinus Latinus 1270)*.

Publications in peer-reviewed journals

The following part of this thesis contains a compilation of all associated publications, starting with a brief overview by presenting the corresponding abstracts. The papers are arranged according to the date of publication. Detailed information is given on the respective preceding cover page.

Paper I

Phys. Status Solidi C **8**, 1129–1132 (2011)

Plasma-related phonon-sideband emission in semiconductors

The phonon-assisted recombination in bulk II–VI semiconductors is analyzed by means of time-resolved photoluminescence spectroscopy. Experimental results on both CdS and CdSe clearly indicate that phonon-sideband emission is not exclusively attributed to the presence of excitons. The contributions of Coulomb-correlated electron–hole plasma to the phonon-assisted recombination may be significant, depending on the excitation conditions. This observation is supported by a microscopic many-particle theory of interacting electrons, phonons, and photons. Our theoretical approach generalizes previous investigations by including both correlated and uncorrelated luminescence sources. Our findings contradict and expand the traditional picture of phonon-sideband emission.

Paper II

Phys. Status Solidi C **8**, 1220–1223 (2011)

Phonon sidebands in the semiconductor microcavity luminescence

A microscopic theory is developed to study the optical properties of semiconductor systems with strong phonon coupling inside a cavity. The semiconductor luminescence equations are expanded to include the phonon-assisted contributions. Numerical investigations predict a considerably enhanced luminescence when the cavity resonance is shifted to coincide with the phonon sideband resonance.

Paper III

Phys. Rev. B **85**, 035201 (2012)

Phonon-assisted luminescence of polar semiconductors: Fröhlich coupling versus deformation-potential scattering

The origin of exciton–phonon interaction in polar semiconductors is investigated. The relative contributions of Fröhlich coupling and deformation potential scattering are identified by analyzing experimentally measured phonon-assisted luminescence using a rigorous many-body approach. Our experiment–theory comparison demonstrates that phonon scattering is significantly influenced by many-body interactions. Fröhlich interaction can be strongly suppressed for excitons even when it dominates electronic single particle scattering. The results show that deformation potential scattering dominates the exciton–phonon interaction in ZnO, whereas Fröhlich interaction prevails in CdS, and both coupling mechanisms yield almost equal contributions in ZnS.

Paper IV

Phys. Rev. B **85**, 094301 (2012)

Enhancement of the phonon-sideband luminescence in semiconductor microcavities

The influence of a semiconductor microcavity on the phonon-assisted photoluminescence is investigated by expanding the microscopic quantum-optical semiconductor luminescence equations. For the example of a ZnO-based system, strong enhancement but no normal-mode splitting of the phonon-sideband luminescence is predicted, even if the cavity becomes resonant with the first phonon sideband. For increasing cavity quality, it is shown that the intensity of the $1s$ resonance first increases due to the Purcell effect but then starts to decrease due to the transition into the nonperturbative regime, while the spectral integrated phonon-sideband intensity saturates.

Paper V

Phys. Status Solidi C **10**, 1218–1221 (2013)

Terahertz-induced effects on excitons in magnetic field

Terahertz-induced intra-exciton transitions are studied in semiconductor quantum-well systems under the influence of a constant magnetic field. A systematic description is developed to include carrier–carrier interactions, terahertz transitions, and magnetic-field effects to the exciton-correlation dynamics. When a magnetic field is present, the exciton states and energies are changed directly and parametrically via the center-of-mass momentum of excitons. The numerical results show that both effects influence the terahertz spectroscopy. Especially, the transition between $1s$- and $2p$-exciton states is shown to depend strongly on both magnetic field and center-of-mass momentum.

Paper VI

Phys. Status Solidi B **250**, 1768–1772 (2013)

Terahertz-induced exciton signatures in semiconductors

This paper discusses recent studies involving time-resolved optical and terahertz (THz) fields in the linear and nonlinear regime. An overview of the microscopic modeling scheme is presented and applied to analyze a variety of experimental results. The examples include coherent excitons in weak and strong THz fields, Rabi splitting and ionization of intra-excitonic transitions, THz studies in semiconductor microcavities, and the THz manipulation of excitonic transitions.

Paper VII

—submitted—

Magnetic control of Coulomb scattering and terahertz transitions among excitons

Time-resolved terahertz quenching studies of the magnetoexcitonic photoluminescence from GaAs/AlGaAs quantum wells are performed. A microscopic theory is developed to analyze the experiments. Detailed experiment–theory comparisons reveal a remarkable magnetic-field controllability of the Coulomb and terahertz interactions in the excitonic system.

PAPER I

A. Chernikov, **C. N. Böttge**, T. Feldtmann, S. Chatterjee, M. Koch, M. Kira, and S. W. Koch
Plasma-related phonon-sideband emission in semiconductors
Phys. Status Solidi C **8**, 1129–1132 (2011)

DOI: 10.1002/pssc.201000841

The Inner Horizon VII

See page XLIV for reference.

Phys. Status Solidi C **8**, No. 4, 1129–1132 (2011) / **DOI** 10.1002/pssc.201000841

physica status solidi c
www.pss-c.com
current topics in solid state physics

Plasma-related phonon-sideband emission in semiconductors

Alexej Chernikov*, Christoph N. Böttge, Thomas Feldtmann, Sangam Chatterjee, Martin Koch, Mackillo Kira, and Stephan W. Koch

Faculty of Physics and Material Sciences Center, Philipps-Universität Marburg, Renthof 5, 35032 Marburg, Germany

Received 13 August 2010, revised 5 October 2010, accepted 5 October 2010
Published online 21 February 2011

Keywords semiconductors, phonon sidebands, excitons, electron-hole plasma

* Corresponding author: e-mail alexej.chernikov@physik.uni-marburg.de, Phone: +49-(0)6421-2822121, Fax: +49-(0)6421-2827036

The phonon-assisted recombination in bulk II-VI semiconductors is analyzed by means of time-resolved photoluminescence spectroscopy. Experimental results on both CdS and CdSe clearly indicate that phonon-sideband emission is not exclusively attributed to the presence of excitons. The contributions of Coulomb-correlated electron-hole plasma to the phonon assisted recombination may be significant, depending on the excitation conditions. This observation is supported by a microscopic many-particle theory of interacting electrons, phonons, and photons. Our theoretical approach generalizes previous investigations by including both correlated and uncorrelated luminescence sources. Our findings contradict and expand the traditional picture of phonon-sideband emission.

1 Introduction Excitonic resonances usually dominate photoluminescence (PL) spectra of high-quality, direct-gap semiconductors [1]. For materials with strong electron-phonon coupling the spectra also feature one or more replicas of the main peak. These replicas are equidistantly spaced in energy, with the separation corresponding to the longitudinal-optical (LO) phonon energy. These additional emission lines are commonly referred to as phonon-sidebands (PSBs) [2–7]. Their origin is the radiative recombination of an electron-hole pair under the simultaneous emission of one or more LO-phonons. Traditionally, the appearance of the PSBs in the luminescence spectra is attributed to the presence of excitons [8]. Therefore, PSB-spectroscopy is often used in the literature to gain information about the excitonic properties of an excited semiconductor system [9–13]. However, already the PL at the main excitonic resonance does not necessarily require excitonic population, as was shown both theoretically [14] and experimentally [15]. In many cases, a Coulomb-correlated electron-hole plasma is the source of the PL at the exciton energy.

Here, we investigate the origin of the PSB-related emission for the typical direct semiconductors CdS and CdSe. Different excitation conditions are chosen, favoring or impeding exciton formation, respectively. For all conditions we measure pronounced PSBs with excitation-independent intensity-ratios. This observation seemingly contradicts the established theory and the accepted understanding of the physical nature of the PSB emission process. Carefully excluding trivial explanations, a fully microscopic theory is applied in order to explain the experimental findings, The theory incorporates interacting charge carriers, lattice vibrations, and light modes, including both correlated and uncorrelated emission sources. The generalization of the previous perturbative treatments shows that *excitons and plasma* contribute additively to the PSB signal.

2 Experimental detail The investigated materials are chemically synthesized, high-purity CdS and CdSe flakes of about 10 µm thickness. Time-resolved PL experiments are performed as function of excitation power and excitation energy at $T = 10\,\mathrm{K}$. A frequency-doubled 100 fs Ti:sapphire laser with a repetition rate of 80 MHz is used for excitation. The samples were mounted inside a He-flow microscopy cryostat. The PL emission was spectrally and temporally resolved with a standard streak camera setup, obtaining resolutions of 0.4 nm and 20 ps, respectively.

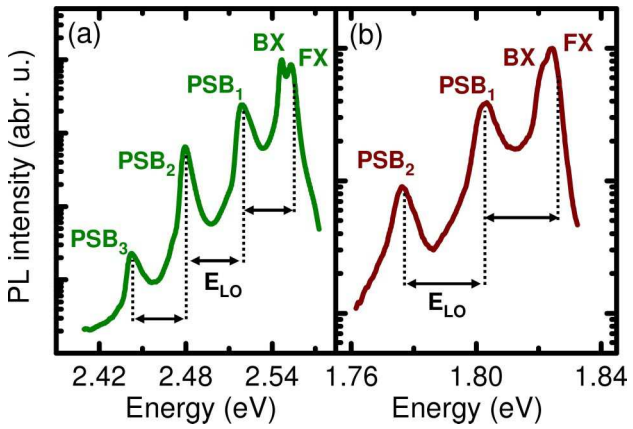

Figure 1 PL spectra of CdS (a) and CdSe (b) at $T = 10$ K for low excitation density and non-resonant excitation conditions at T = 10 K. Signatures of bound and free excitons as well as the corresponding phonon-sidebands are marked by BX, FX, and PSB, respectively.

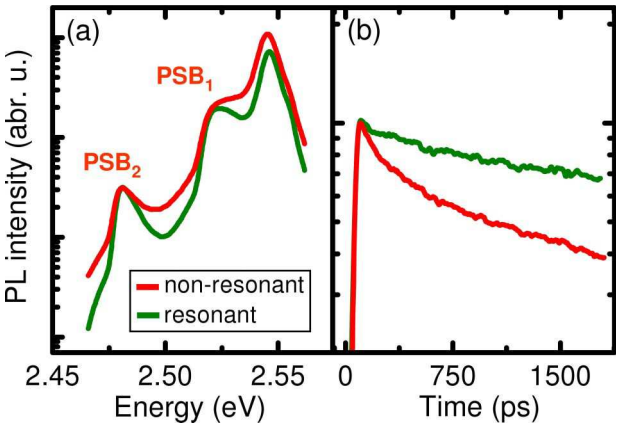

Figure 2 (a) PL spectra of CdS at high excitation density for the resonant (green) and non-resonant (red) excitation energies of 2.54 eV, and 2.85 eV, respectively. (b) Normalized time resolved luminescence of the second PSB. The lattice temperature is set to 10 K.

Details of the experiment are given here [16]. Low excitation results are always recovered after the application of high pump densities to ensure that the samples were not damaged during the experiments.

3 Results and discussion Figure 1 shows the time-integrated PL spectra of the CdS (a) and the CdSe (b) samples for a lattice temperature of T = 10 K. The data was taken for the non-resonant excitation at 2.85 eV and low excitation density of 10^{11} cm^{-2} photons per pulse. The dominant emission signatures at 2.547 eV and 2.553 eV for CdS, as well as 1.821 eV and 1.825 eV for CdSe are attributed to the zero phonon lines of the bound (BX) and free A-excitons (FX), respectively [2, 17, 18]. The FX emission originates mainly from the sample surface due to the well-known polariton propagation in the bulk crystals [1]. Additional peaks are observed at the low energy side of the spectrum. The respective intensities decrease with decreasing peak energy. The peaks are nearly equidistantly spaced with a separation of about 38 meV for CdS and 27 meV for CdSe, as are the separations between the first peak and the FX line. These energies correspond to the energies of the LO-phonons in these materials [17, 18]. Therefore, the peaks are unambiguously identified as the PSBs of the FX emission, commonly observed in the luminescence spectra of the wide-gap semiconductors [1]. In contrast to the FX emission, the PSB luminescence is only weakly affected by the polariton effects and thus originates from the entire excited bulk volume.

PL spectra of CdS are plotted in Fig. 2(a) for the resonant and non-resonant excitation at high pump densities in the range of 10^{14} cm^{-2} photons per pulse. We find pronounced PSBs in the emission spectra for both excitation conditions. Remarkably, the shape and the relative intensities of the sidebands are nearly independent of the excitation energy. Only a slight broadening due to the higher carrier temperature is observed for the non-resonant case. However, in stark contrast to the similar spectral line shape, a large difference in the PL dynamics of the PSBs is observed for the two different excitation conditions. The normalized PL time traces at the energy of the second PSB, are shown in Fig. 2(b). The signal decays monoexponentially in case of resonant excitation, as commonly expected for exciton-related PL [1]. For the non-resonant excitation conditions, the PL shows a more complicated nonexponential behavior. The PL decays fast after the excitation pulse, followed by a slower decay on a longer time scale.

Next, the dependence of the sideband PL on excitation density is studied under non-resonant excitation conditions. The PL transients for the pump densities between 10^{11} cm^{-2} and 10^{14} cm^{-2} photons per pulse are plotted in Fig. 3 for the second PSB of CdS (a) and CdSe (b). For both samples, we observe a single-exponential decay at low excitation densities, similar to the PL dynamics under the resonant excitation. As the pump power is increased, the PL dynamics show pronounced nonexponential behavior. To exclude any trivial effects of increasing non-radiative recombination, it is also necessary to look at the PL amplitudes. Figures 3(c) and (d) show the spectrally- and temporally-integrated PL intensity (full circles) and the PL intensity direct after the excitation (empty circles) as function of the pump-density for CdS and CdSe, respectively. The absolute intensity of the PL is directly proportional to the excitation density, while the initial PL intensity exhibits a pronounced super-linear increase. Non-radiative recombination via defects, Auger processes or "sideways-lasing" will lead to a pronounced sublinear behavior of the PL, which, however, we do not observe. A saturation of impurity-related non-radiative channels at

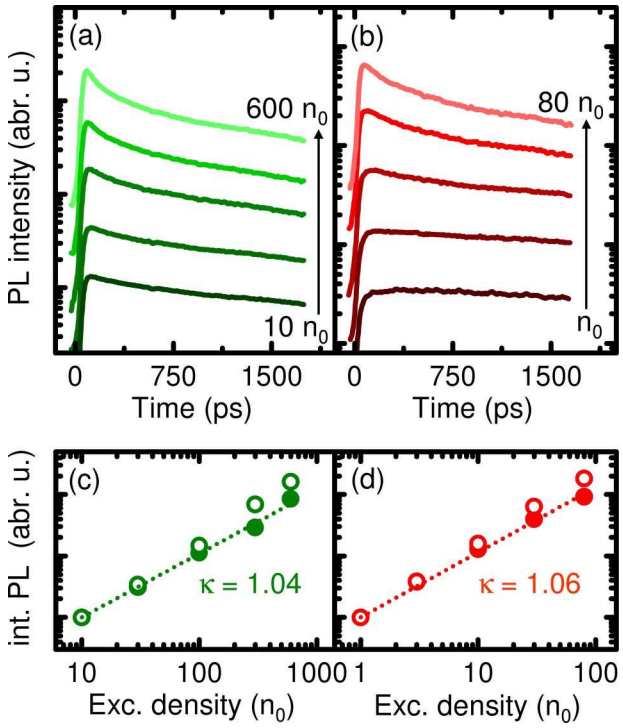

Figure 3 Time-resolved PSB_2 emission of CdS(a) and CdSe (b) as function of excitation power for a lattice temperature of T=10 K. The lowest excitation density is $n_0 = 10^{11}\,\mathrm{cm}^{-2}$ photons per pulse. The corresponding absolute PL intensities (full circles) and the PL amplitudes directly after the excitation (empty circles) of the second PSB are shown in (c) and (d) for CdS and CdSe, respectively. The dotted lines are fits with the power law $I_{PL} \propto I_{pump}^{\kappa}$.

higher pump densities, i.e. Shockley-Reed-Hall recombination, is also excluded due to the linear increase of the absolute PL intensity and shorter carrier lifetimes. Therefore, the enhancement of the decay rate for the increasing excitation densities is unambiguously attributed to faster radiative recombination and all other processes are excluded.

Since the recombination of an exciton produces a single photon, the radiative decay rate of excitons is independent of the exciton density. As long as the non-radiative contributions are independent from the carrier density, the corresponding PL decay should be single exponential. This scenario is expected to be valid for resonant or weak non-resonant excitations, favoring the formation of bound electron-hole pairs. Thus, we attribute the measured single exponential PL dynamics for resonant excitation as well as for non-resonant excitation with low pump densities to the decay of the excitons. However, the non-resonant excitation with high pump intensities enhances the PL decay greatly above the exciton-related level for both materials. Such density-dependent increase of the radiative recombination is a clear hallmark of plasma-related PL with the quadratical dependence of the decay rate on the carrier density. Usually, strong non-resonant excitations tend to produce electron-hole plasmas rather than extions [1]. The excitation-density threshold for the plasma-related dynamics in CdSe is one order of magnitude lower than in CdS, being consistent with the different exciton binding energies of 16 meV and 30 meV, respectively [18]. In the view of the presented experimental findings it is obviously interesting to study, whether the electron-hole plasma can produce the additional contributions to the sideband luminescence.

4 Theoretical description For the analysis of the exciton and plasma contributions to the sideband luminescence, the theory has to go beyond the earlier investigations, that describe the excited state of the semiconductor within a bosonic pair-state picture and treat PSBs perturbatively [8]. When the fermionic substructure of the electron-hole pairs is fully taken into account, the perturbational approach becomes very involved already for lower-order PSBs. In order to simplify the calculation, a unitary-transformation method is employed that enables us to treat the electron-phonon coupling non-perturbatively. The microscopic theory is developed in full detail in [19]. The semiconductor luminescence equations [20, 14] are extended by including phonon-assisted recombination processes. As it is explicitly shown in [21], this approach produces the PL spectra including PSBs of arbitrary order. At the same time, we can systematically compute the luminescence resulting from any quasi-stationary mixture of electron-hole plasma and excitons.

When only the dominant $1s$ excitonic resonance and its replicas are considered, the luminescence spectra assume the compact form $I(\omega) = \sum_{n=0}^{\infty} I^{(n)}(\omega)$. The luminescence intensity at the zero-phonon line ($n = 0$) and the n-th replica ($n = 1, 2, ...$) follows from

$$I^{(n)}(\omega) = \frac{1}{n!} Im \sum_{\mathbf{Q}} \frac{\mathcal{G}_{\mathbf{Q}}^{(n)} \left[\Delta N(\mathbf{Q}) + N_{\mathrm{eh}}(\mathbf{Q})\right]}{E(\mathbf{Q}) - n\hbar\Omega - \hbar\omega - i\gamma_n}. \quad (1)$$

Here, $\hbar\omega$ and $\hbar\Omega$ denote the photon and optical-phonon energy, respectively. The $1s$-exciton energy $E(\mathbf{Q}) = E_{1s} + \hbar^2|\mathbf{Q}|^2/2M$ contains the binding energy E_{1s} as well as the center-of-mass energy of excitons, $M = m_e + m_h$ being the sum of the electron and hole masses. Homogeneous line broadening is implemented via the phenomenological parameter γ_n that is fitted to the experiment. In accordance with the perturbative treatment, the weight factor $\mathcal{G}_{\mathbf{Q}}^{(n)}$ scales with the $2n$-th power of the absolute value of the electron-phonon coupling constant [21].

The luminescence formula (1) shows explicitly that both $1s$-excitons $\Delta N(\mathbf{Q})$ as well as a direct electron-hole plasma contribution

$$N_{\mathrm{eh}}(\mathbf{Q}) = \sum_{\mathbf{k}} |\phi(\mathbf{k})|^2 f^e_{\mathbf{k}+\mathbf{Q}_e} f^h_{\mathbf{k}-\mathbf{Q}_h} \quad (2)$$

act simultaneously as sources for the phonon-assisted emission. More specifically, the electron-hole plasma term contains the $1s$-exciton wave function $\phi(\mathbf{k})$ multiplied by a product of electron $f^e_{\mathbf{k}}$ and hole $f^h_{\mathbf{k}}$ distributions with momentum arguments shifted by $\mathbf{Q}_{e,h} = \mathbf{Q}\frac{m_{e,h}}{M}$. In particular, the plasma contribution is always present whenever the carrier system is excited from the semiconductor ground state. This yields an interesting prediction that excitonic luminescence [15] as well as the related sideband PL can equally well result from excitons or from the electron-hole plasma. In particular, the emergence of excitonic sidebands does not necessarily imply the presence of excitons.

Moreover, Eq. 1 makes a distinct prediction for the momentary radiative recombination rate of carrier excitations

$$r_{\mathrm{rad}} \equiv \sum_{n=0}^{\infty} \frac{\int d\omega\, I^{(n)}(\omega)}{n_{\mathrm{carr}}} = \Delta r^{1s}_{\mathrm{rad}} + r^{\mathrm{eh}}_{\mathrm{rad}} \qquad (3)$$

where $\int d\omega\, I^{(n)}(\omega)$ defines the rate of photons emitted (carriers recombined) and n_{carr} the number of carriers within the quasi-stationary many-body state. Since $1s$ excitons and electron-hole plasma appear additively in $I^{(n)}(\omega)$, we can separate the contributions resulting from the presence of $1s$ excitons [$\Delta N(\mathbf{Q})$] and the electron-hole plasma [$N_{\mathrm{eh}}(\mathbf{Q})$] in $\Delta r^{1s}_{\mathrm{rad}}$ and $r^{\mathrm{eh}}_{\mathrm{rad}}$, respectively. If the system contains 100% excitons, $\Delta r^{1s}_{\mathrm{rad}}$ is independent of the excitation level because exciton luminescence is linearly proportional to the exciton density. Thus, exciton-dominated sideband PL yields a strictly single-exponential decay, verifying our assumption above. At the same time, the plasma-related PSB emission is quadratic in density, leading to a density dependent recombination rate $r^{\mathrm{eh}}_{\mathrm{rad}}$. For high carrier densities the initial PL decay is very fast due to the non-linear enhancement of the excitonic resonances by the electron-hole plasma. As the carrier density successively decreases due to the carrier recombination, the plasma contributions, scaling quadratically with density, drop quickly below the exciton-related PL. Thus, the experiment exhibits a crossover from plasma- to exciton-dominated luminescence decay; the exciton-dominated PL results in the slower single-exponential decay shown in the low density case of Fig. 3. Similar observations resulting from the crossover from plasma to exciton dominated emission have been also made in microcavity quantum-dot luminescence [22]. Thus, the microscopic theory clearly predicts nonexponential decay dynamics, which provide the observed enhancement in the PL decay rates for the elevated carrier densities.

5 Conclusion In conclusion, we have presented the experimental evidence, supported by the theoretical analysis, that the emission at the exciton-phonon sideband resonances cannot be considered as an unambiguous evidence of an excitonic population. The PSB PL is significantly enhanced by the electron-plasma contribution under strong non-resonant excitation conditions. Our results contradict and expand earlier theoretical treatments, providing new insight in the interpretation of the phonon-assisted emission.

References

[1] C. F. Klingshirn, Semiconductor Optics, 2nd ed. (Springer, Berlin/Heidelberg/New York, 2007).
[2] C. W. Litton, D. C. Reynolds, T. C. Collins, and Y. S. Park, Phys. Rev. Lett. **25**, 1619 (1970).
[3] L. Eckey, J. C. Holst, P. Maxim, R. Heitz, A. Hoffmann, I. Broser, B. K. Meyer, C. Wetzel, E. N. Mokhov, and P. G. Baranov, Appl. Phys. Lett. **68**, 415 (1995).
[4] M. Lowisch, M. Rabe, B. Stegemann, F. Henneberger, M. Grundmann, V. Türck, and D. Bimberg, Phys. Rev. B **43**, R11074 (1996).
[5] U. Woggon, F. Gindele, O. Wind, and C. Klingshirn, Phys. Rev. B **54**, 1506 (1996).
[6] H. Zhao, S. Moehl, and H. Kalt, Phys. Rev. Lett. **89**, 0974011 (2002).
[7] C. Bekeny, T. Voss, H. Gafsi, J. Gutowski, B. Postels, M. Kreye, and A. Waag, J. Appl. Phys. **100**, 104317 (2006).
[8] S. Permogorov, Excitons (North-Holland, Amsterdam, 1982).
[9] R. P. Stanley, J. Hegarty, R. Fischer, J. Feldmann, E. O. Göbel, R. D. Feldman, and R. F. Austin, Phys. Rev. Lett. **67**, 128 (1991).
[10] N. Pelekanos, J. Ding, Q. Fu, A. V. Nurmikko, S. M. Durbin, M. Kobayashi, and R. L. Gunshor, Phys. Rev. B **43**(11), 9354–9357 (1991).
[11] J. H. Collet, H. Kalt, L. S. Dang, J. Cibert, K. Saminadayar, and S. Tatarenko, Phys. Rev. B **43**(8), 6843–6846 (1991).
[12] D. Kovalev, B. Averboukh, D. Volm, B. K. Meyer, H. Amano, and I. Akasaki, Phys. Rev. B **54**(4), 2518–2522 (1996).
[13] H. Zhao and H. Kalt, Phys. Rev. B **68**(12), 125309 (2003).
[14] M. Kira, F. Jahnke, and S. W. Koch, Phys. Rev. Lett. **81**(15), 3263–3266 (1998).
[15] S. Chatterjee, C. Ell, S. Mosor, G. Khitrova, H. M. Gibbs, W. Hoyer, M. Kira, S. W. Koch, J. P. Prineas, and H. Stolz, Phys. Rev. Lett. **92**(6), 067402 (2004).
[16] A. Chernikov, S. Horst, M. Koch, S. Chatterjee, T. A. Wassner, B. Laumer, and M. Eickhoff, J. Lumin. **130**, 2256 (2010).
[17] S. S. Prabhu, A. S. Vengurlekar, and J. Shah, Phys. Rev. B **53**(16), 10465 (1996).
[18] O. Madelung, Landolt-Boernstein: Numerical Data and Functional Relationships in Science and Technology (Springer, Berlin/Heidelberg/New York, 1982).
[19] T. Feldtmann, M. Kira, and S. W. Koch, Phys. Status Solidi B **246**(2), 332–336 (2009).
[20] M. Kira, F. Jahnke, S. W. Koch, J. D. Berger, D. V. Wick, T. R. Nelson, G. Khitrova, and H. M. Gibbs, Phys. Rev. Lett. **79**(25), 5170–5173 (1997).
[21] T. Feldtmann, M. Kira, and S. W. Koch, J. Lumin. **130**(1), 107–113 (2010).
[22] M. Schwab, H. Kurtze, T. Auer, T. Berstermann, M. Bayer, J. Wiersig, N. Baer, C. Gies, F. Jahnke, J. P. Reithmaier, A. Forchel, M. Benyoucef, and P. Michler, Phys. Rev. B **74**(4), 045323 (2006).

PAPER II

C. N. Böttge, T. Feldtmann, M. Kira, and S. W. Koch
Phonon sidebands in the semiconductor microcavity luminescence
Phys. Status Solidi C **8**, 1220–1223 (2011)

DOI: 10.1002/pssc.201000826

The Inner Horizon VIII

See page XLIV for reference.

Phys. Status Solidi C **8**, No. 4, 1220–1223 (2011) / **DOI** 10.1002/pssc.201000826

physica status solidi c
www.pss-c.com
current topics in solid state physics

Phonon sidebands in the semiconductor microcavity luminescence

Christoph N. Böttge*, Thomas Feldtmann, Mackillo Kira, and Stephan W. Koch

Department of Physics and Material Sciences Center, Philipps-University, Renthof 5, 35032 Marburg, Germany

Received 12 August 2010, accepted 11 September 2010
Published online 26 January 2011

Keywords phonon sidebands, semiconductor luminescence, dielectric environment

* Corresponding author: e-mail Christoph.Boettge@physik.uni-marburg.de, Phone: +49-6421-28-24217, Fax: +49-6421-28-27076

A microscopic theory is developed to study the optical properties of semiconductor systems with strong phonon coupling inside a cavity. The semiconductor luminescence equations are expanded to include the phonon-assisted contributions. Numerical investigations predict a considerably enhanced luminescence when the cavity resonance is shifted to coincide with the phonon sideband resonance.

1 Introduction The strong interaction between electrons and longitudinal optical (LO) phonons in materials like ZnO gives rise to pronounced phonon sidebands in the photoluminescence (PL) spectrum. Recent investigations are reported in Refs. [1,2]. To theoretically model the phonon-sideband emission, we have generalized the semiconductor luminescence equations (SLE) [3] by including the pertinent phonon-assisted processes. This approach allows us to compute both spontaneous and stimulated emission at the excitonic resonance and its first phonon sideband. In addition, we have developed an analytic model to describe phonon-assisted luminescence in a microcavity formed by distributed Bragg reflectors.

2 Theory

2.1 Hamiltonian For a complete quantum mechanical description we start from the general semiconductor Hamiltonian [3–5] $\hat{\mathcal{H}} = \hat{\mathcal{H}}_{\text{el}} + \hat{\mathcal{H}}_{\text{phon}} + \hat{\mathcal{H}}_{\text{em}} + \hat{\mathcal{H}}_{\text{el-el}} + \hat{\mathcal{H}}_{\text{el-phon}} + \hat{\mathcal{H}}_{\text{el-em}}$ where

$$\hat{\mathcal{H}}_{\text{el}} = \sum_{\lambda,\boldsymbol{k}} \epsilon_{\lambda,\boldsymbol{k}} \hat{a}^{\dagger}_{\lambda,\boldsymbol{k}} \hat{a}_{\lambda,\boldsymbol{k}} \,, \tag{1}$$

$$\hat{\mathcal{H}}_{\text{phon}} = \sum_{\boldsymbol{p},p_\perp} \hbar\Omega_{\boldsymbol{p},p_\perp} \left(\hat{D}^{\dagger}_{\boldsymbol{p},p_\perp} \hat{D}_{\boldsymbol{p},p_\perp} + \frac{1}{2} \right), \tag{2}$$

$$\hat{\mathcal{H}}_{\text{em}} = \sum_{\boldsymbol{q},q_\perp} \hbar\omega_{\boldsymbol{q},q_\perp} \left(\hat{B}^{\dagger}_{\boldsymbol{q},q_\perp} \hat{B}_{\boldsymbol{q},q_\perp} + \frac{1}{2} \right), \tag{3}$$

$$\hat{\mathcal{H}}_{\text{el-el}} = \frac{1}{2} \sum_{\substack{\lambda,\lambda' \\ \boldsymbol{k},\boldsymbol{k}' \\ \boldsymbol{q}\neq 0}} V_{|\boldsymbol{q}|} \hat{a}^{\dagger}_{\lambda,\boldsymbol{k}} \hat{a}^{\dagger}_{\lambda',\boldsymbol{k}'} \hat{a}_{\lambda',\boldsymbol{k}'+\boldsymbol{q}} \hat{a}_{\lambda,\boldsymbol{k}-\boldsymbol{q}} \,, \tag{4}$$

$$\hat{\mathcal{H}}_{\text{el-phon}} = \sum_{\lambda,\boldsymbol{k},\boldsymbol{p},p_\perp} \hbar\Omega_{\boldsymbol{p},p_\perp} \, g^{\lambda}_{\boldsymbol{p},p_\perp} \hat{a}^{\dagger}_{\lambda,\boldsymbol{k}-\boldsymbol{p}} \hat{a}_{\lambda,\boldsymbol{k}} \cdot \left(\hat{D}_{-\boldsymbol{p},-p_\perp} + \hat{D}^{\dagger}_{\boldsymbol{p},p_\perp} \right), \tag{5}$$

$$\hat{\mathcal{H}}_{\text{el-em}} = -\sum_{\boldsymbol{k},\boldsymbol{q},q_\perp} \mathrm{i} \left(\mathcal{F}_{\boldsymbol{q},q_\perp} \hat{a}^{\dagger}_{\text{c},\boldsymbol{k}+\boldsymbol{q}} \hat{a}_{\text{v},\boldsymbol{k}} + \mathcal{F}^{*}_{\boldsymbol{q},q_\perp} \hat{a}^{\dagger}_{\text{v},\boldsymbol{k}} \hat{a}_{\text{c},\boldsymbol{k}-\boldsymbol{q}} \right) \hat{B}_{\boldsymbol{q},q_\perp} + \text{h.c.} \tag{6}$$

The Hamiltonians $\hat{\mathcal{H}}_{\text{el}}$, $\hat{\mathcal{H}}_{\text{phon}}$, and $\hat{\mathcal{H}}_{\text{em}}$ describe the non-interacting charge carriers, lattice vibrations and light modes. The interacting parts of the electron-electron scattering, electron-phonon coupling, and the light-matter interaction are described by the last three Hamiltonians where $V_{|\boldsymbol{q}|}$, $g^{\lambda}_{\boldsymbol{p},p_\perp}$, and $\mathcal{F}_{\boldsymbol{q},q_\perp}$ are the matrix elements for Coulomb-, phonon-, and light-matter interac-

tion. The strength of the light-matter interaction is given by $\mathcal{F}_{\boldsymbol{q},\,q_\perp} := \mathscr{E}_{\boldsymbol{q},q_\perp}\bar{\boldsymbol{u}}_{\boldsymbol{q},q_\perp}\cdot\boldsymbol{d}_{\rm cv}$ with the vacuum-field amplitude $\mathscr{E}_{\boldsymbol{q},q_\perp}$ [3], the dipole matrix element $\boldsymbol{d}_{\rm cv}$ between valence and conduction band, and the overlap integral $\bar{\boldsymbol{u}}_{\boldsymbol{q},q_\perp}$ between the QW-confinement function and the light mode $\boldsymbol{u}_{\boldsymbol{q},q_\perp}(r_\perp)$. The mode functions are calculated using the transfer matrix method [3,4].

The Fermionic operators $\hat{a}^\dagger_{\lambda,\,\boldsymbol{k}}$ and $\hat{a}_{\lambda,\,\boldsymbol{k}}$ create or annihilate a Bloch electron with momentum $\hbar\boldsymbol{k}$, kinetic- or single-particle energy $\epsilon_{\lambda,\,\boldsymbol{k}} = \frac{\hbar^2\boldsymbol{k}^2}{2\,m^*}$, and effective mass m^* in band λ. Due to the strong confinement it is sufficient to consider only one valence band and one conduction band. The Bosonic system of phonons and photons is described by the creation (annihilation) operators $\hat{D}^\dagger_{\boldsymbol{p},\,p_\perp}$ ($\hat{D}_{\boldsymbol{p},\,p_\perp}$) for the phonons and $\hat{B}^\dagger_{\boldsymbol{q},\,q_\perp}$ ($\hat{B}_{\boldsymbol{q},\,q_\perp}$) for the photons. While the phonon operators describe phonons with momentum $\hbar\boldsymbol{p}$ and frequency $\Omega_{\boldsymbol{p},p_\perp}$, the photon operators create and destroy photons with momentum $\hbar\boldsymbol{q}$ and frequency $\omega_{\boldsymbol{q},q_\perp}$. Since optical phonons show a largely constant dispersion relation, it is justified to consider a constant phonon frequency $\Omega_{\boldsymbol{p},p_\perp} \simeq \Omega_{\rm LO}$.

2.2 Generalized SLE For a consistent description of the quantum mechanical light-matter interaction, we derive the semiconductor luminescence equations through the Heisenberg equations of motion $\mathrm{i}\hbar\partial_t\hat{O} = [\hat{O},\hat{H}]$ where $\hat{O}$ characterizes an arbitrary combination of operators describing electron-, phonon-, and photon interaction. Due to the many-body interaction N-particle operators couple to $(N+2)$-particle operators which yields an infinite hierarchy of equations. This *hierarchy problem* can be truncated by factorizing higher-order correlations with the so-called *cluster expansion* [4,6–10] where N-particle expectation values are factorized into single-particle terms (Singlets), coupled pairs (Doublets), and three-particle clusters (Triplets). A schematic illustration of this factorization scheme is shown in Fig. 1. Since we are investigating a quantum mechanical electron-photon-phonon process, we have to deal with three particles and it is sufficient to truncate the hierarchy problem at the triplet level.

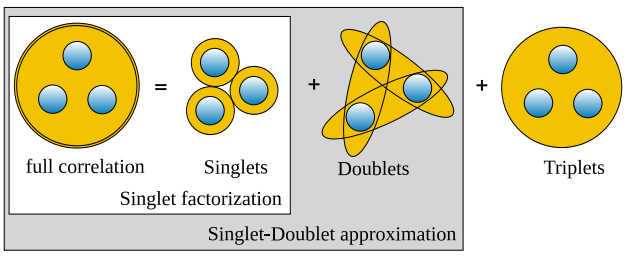

Figure 1 Schematic illustration of the cluster expansion. For a detailed description of the cluster-expansion representation see Ref. [6].

We obtain the following equations of motion where the single-photon correlations

$$\begin{aligned} &i\hbar\frac{\partial}{\partial t}\,\Delta\langle\hat{B}^\dagger_{\boldsymbol{q},\,q_\perp}\hat{B}_{\boldsymbol{q},\,q'_\perp}\rangle \\ &= \left(\hbar\omega_{\boldsymbol{q},\,q'_\perp} - \hbar\omega_{\boldsymbol{q},\,q_\perp}\right)\Delta\langle\hat{B}^\dagger_{\boldsymbol{q},\,q_\perp}\hat{B}_{\boldsymbol{q},\,q'_\perp}\rangle \\ &\quad + \mathrm{i}\mathcal{F}^*_{\boldsymbol{q},\,q'_\perp}\sum_{\boldsymbol{k}}\Pi^{\boldsymbol{k}}_{\boldsymbol{q},q_\perp} + \mathrm{i}\mathcal{F}_{\boldsymbol{q},\,q_\perp}\sum_{\boldsymbol{k}}\left(\Pi^{\boldsymbol{k}}_{\boldsymbol{q},q'_\perp}\right)^* \end{aligned} \tag{7}$$

are coupled to photon-assisted polarizations $\Pi^{\boldsymbol{k}}_{\boldsymbol{q},q_\perp} = \Delta\langle\hat{B}^\dagger_{\boldsymbol{q},\,q_\perp}\hat{v}^\dagger_{\boldsymbol{k}}\hat{c}_{\boldsymbol{k}+\boldsymbol{q}}\rangle$ whose equation of motion is represented by

$$\begin{aligned} &i\hbar\frac{\partial}{\partial t}\,\Delta\langle\hat{B}^\dagger_{\boldsymbol{q},\,q_\perp}\hat{v}^\dagger_{\boldsymbol{k}}\hat{c}_{\boldsymbol{k}+\boldsymbol{q}}\rangle \\ &= \left(\tilde{\epsilon}^{\rm e}_{\boldsymbol{k}+\boldsymbol{q}} + \tilde{\epsilon}^{\rm h}_{\boldsymbol{k}} - \hbar\omega_{\boldsymbol{q},\,q_\perp} - \mathrm{i}\gamma_0\right)\Delta\langle\hat{B}^\dagger_{\boldsymbol{q},\,q_\perp}\hat{v}^\dagger_{\boldsymbol{k}}\hat{c}_{\boldsymbol{k}+\boldsymbol{q}}\rangle \\ &\quad - \left(1 - f^{\rm e}_{\boldsymbol{k}+\boldsymbol{q}} - f^{\rm h}_{\boldsymbol{k}}\right)\Xi_{\rm ST}(\boldsymbol{k},\boldsymbol{q},q_\perp) + \Xi_{\rm SE}(\boldsymbol{k},\boldsymbol{q},q_\perp) \\ &\quad + \hbar\Omega_{\rm LO} \\ &\cdot\sum_{\boldsymbol{p},p_\perp}\Big[g^{\rm c}_{\boldsymbol{p},\,p_\perp}\Delta\langle\hat{B}^\dagger_{\boldsymbol{q},\,q_\perp}\left(\hat{D}^\dagger_{\boldsymbol{p},\,p_\perp} + \hat{D}_{-\boldsymbol{p},\,p_\perp}\right)\hat{v}^\dagger_{\boldsymbol{k}}\hat{c}_{\boldsymbol{k}+\boldsymbol{p}+\boldsymbol{q}}\rangle \\ &\quad - g^{\rm v}_{\boldsymbol{p},\,p_\perp}\Delta\langle\hat{B}^\dagger_{\boldsymbol{q},\,q_\perp}\left(\hat{D}^\dagger_{\boldsymbol{p},\,p_\perp} + \hat{D}_{-\boldsymbol{p},\,p_\perp}\right)\hat{v}^\dagger_{\boldsymbol{k}-\boldsymbol{p}}\hat{c}_{\boldsymbol{k}+\boldsymbol{q}}\rangle\Big]. \end{aligned} \tag{8}$$

For brevity, we introduced the new operators $\hat{a}^{(\dagger)}_{{\rm c},\boldsymbol{k}} \equiv \hat{c}^{(\dagger)}_{\boldsymbol{k}}$ and $\hat{a}^{(\dagger)}_{{\rm v},\boldsymbol{k}} \equiv \hat{v}^{(\dagger)}_{\boldsymbol{k}}$. Equation (8) describes correlated processes of the creation of a photon with momentum $\hbar\boldsymbol{q}$ whereas an electron-hole pair with the same momentum is annihilated and couples back via the stimulated emission source

$$\begin{aligned} \Xi_{\rm ST}(\boldsymbol{k},\boldsymbol{q},q_\perp) = \mathrm{i}\sum_{q'_\perp}\mathcal{F}_{\boldsymbol{q},\,q'_\perp}\;\Delta\left\langle\hat{B}^\dagger_{\boldsymbol{q},\,q_\perp}\hat{B}_{\boldsymbol{q},\,q'_\perp}\right\rangle \\ + \sum_{\boldsymbol{k}'}V_{|\boldsymbol{k}-\boldsymbol{k}'|}\Delta\left\langle\hat{B}^\dagger_{\boldsymbol{q},\,q_\perp}\hat{v}^\dagger_{\boldsymbol{k}'}\hat{c}_{\boldsymbol{k}'+\boldsymbol{q}}\right\rangle. \end{aligned} \tag{9}$$

The stimulated term $\sum_{q'_\perp}\Delta\langle\hat{B}^\dagger\hat{B}\rangle$ describes the dynamic interplay of field-field and field-particle correlations. Its influence on the luminescence spectrum under strong coupling conditions leads to the well-known normal-mode splitting [11–13]. In Eq. (8) we denote the renormalized single-particle energies by $\tilde{\epsilon}^\lambda_{\boldsymbol{k}} = \epsilon_{\lambda,\boldsymbol{k}} - \sum_{\boldsymbol{q}\neq 0}V_{|\boldsymbol{k}-\boldsymbol{q}|}f^\lambda_{\boldsymbol{q}}$, $\lambda = {\rm e},\,{\rm h}$, with the Coulomb matrix element $V_{|\boldsymbol{k}-\boldsymbol{q}|}$. For completeness, we want to mention the spontaneous emission source

$$\Xi_{\rm SE}(\boldsymbol{k},\boldsymbol{q},q_\perp) = \mathrm{i}\mathcal{F}_{\boldsymbol{q},\,q_\perp}\left(f^{\rm e}_{\boldsymbol{k}+\boldsymbol{q}}f^{\rm h}_{\boldsymbol{k}} + \sum_{\boldsymbol{k}'}c^{\boldsymbol{q},\boldsymbol{k},\boldsymbol{k}'}_{\rm X}\right) \tag{10}$$

which contains the single-particle contribution $f^{\mathrm{e}}f^{\mathrm{h}}$ and the truly correlated electron-hole pairs $c_{\mathrm{X}}^{\boldsymbol{q},\boldsymbol{k},\boldsymbol{k'}} = \Delta\langle\hat{c}^{\dagger}_{\boldsymbol{k'}}\hat{v}^{\dagger}_{\boldsymbol{k}}\hat{c}_{\boldsymbol{k}+\boldsymbol{q}}\hat{v}_{\boldsymbol{k'}-\boldsymbol{q}}\rangle$.

For a more detailed description of the SLE we refer to Refs. [3,4]. For this work, the last two lines in Eq. (8) are the most crucial expansion and form the additional phonon part of the common SLE. Here, one sums over all phonon momenta $\boldsymbol{p}$ of the phonon- and photon-assisted polarization. The expectation values of these polarizations have to be computed dynamically for which reason we derive the equations of motion in a completely analogous way to Eq. (8) with the difference that we now have to consider three-particle correlations.

2.3 Phonon-assisted contributions The Heisenberg equations of motion yield for the polarization term

$$
\begin{aligned}
&i\hbar\frac{\partial}{\partial t}\,\Delta\langle\hat{B}^{\dagger}_{\boldsymbol{q},\,q_\perp}\hat{D}^{\dagger}_{\boldsymbol{p},\,p_\perp}\hat{v}^{\dagger}_{\boldsymbol{k}}\hat{c}_{\boldsymbol{k}+\boldsymbol{p}+\boldsymbol{q}}\rangle\\
&= \left(\tilde{\epsilon}^{\mathrm{e}}_{\boldsymbol{k}+\boldsymbol{p}+\boldsymbol{q}} + \tilde{\epsilon}^{\mathrm{h}}_{\boldsymbol{k}} - \hbar\omega_{\boldsymbol{q},\,q_\perp} - \hbar\Omega_{\mathrm{LO}} - \mathrm{i}\gamma_1\right)\times\\
&\qquad \Delta\langle\hat{B}^{\dagger}_{\boldsymbol{q},\,q_\perp}\hat{D}^{\dagger}_{\boldsymbol{p},\,p_\perp}\hat{v}^{\dagger}_{\boldsymbol{k}}\hat{c}_{\boldsymbol{k}+\boldsymbol{p}+\boldsymbol{q}}\rangle\\
&\quad - \left(1 - f^{\mathrm{e}}_{\boldsymbol{k}+\boldsymbol{p}+\boldsymbol{q}} - f^{\mathrm{h}}_{\boldsymbol{k}}\right)\times\\
&\qquad \Bigg[\sum_{\boldsymbol{k'}} V_{|\boldsymbol{k}-\boldsymbol{k'}|}\quad \Delta\langle\hat{B}^{\dagger}_{\boldsymbol{q},\,q_\perp}\hat{D}^{\dagger}_{\boldsymbol{p},\,p_\perp}\hat{v}^{\dagger}_{\boldsymbol{k'}}\hat{c}_{\boldsymbol{k'}+\boldsymbol{p}+\boldsymbol{q}}\rangle\\
&\qquad + \mathrm{i}\sum_{q'_\perp}\mathcal{F}_{\boldsymbol{q}+\boldsymbol{p},\,q'_\perp}\,\Delta\langle\hat{D}^{\dagger}_{\boldsymbol{p},\,p_\perp}\hat{B}^{\dagger}_{\boldsymbol{q},\,q_\perp}\hat{B}_{\boldsymbol{q}+\boldsymbol{p},\,q'_\perp}\rangle\Bigg]\\
&\quad + \mathrm{i}\mathcal{F}_{\boldsymbol{q}}\Bigg(f^{\mathrm{h}}_{\boldsymbol{k}}\qquad \Delta\langle\hat{D}^{\dagger}_{\boldsymbol{p},\,p_\perp}\hat{c}^{\dagger}_{\boldsymbol{k}+\boldsymbol{q}}\hat{c}_{\boldsymbol{k}+\boldsymbol{p}+\boldsymbol{q}}\rangle -\\
&\qquad f^{\mathrm{e}}_{\boldsymbol{k}+\boldsymbol{p}+\boldsymbol{q}}\,\Delta\langle\hat{D}^{\dagger}_{\boldsymbol{p},\,p_\perp}\hat{v}^{\dagger}_{\boldsymbol{k}}\hat{v}_{\boldsymbol{k}+\boldsymbol{p}}\rangle\\
&\qquad + \sum_{\boldsymbol{k'}}\,\Delta\langle\hat{D}^{\dagger}_{\boldsymbol{p},\,p_\perp}\hat{c}^{\dagger}_{\boldsymbol{k'}}\hat{v}^{\dagger}_{\boldsymbol{k}}\hat{c}_{\boldsymbol{k}+\boldsymbol{p}+\boldsymbol{q}}\hat{v}_{\boldsymbol{k'}-\boldsymbol{q}}\rangle\Bigg). \qquad (11)
\end{aligned}
$$

The solutions of Eq. (11) enter the photon-assisted polarization from Eq. (8) as an additional part and are weighted with the phonon matrix elements $g^{\mathrm{c}}_{\boldsymbol{p},\,p_\perp}$ and $g^{\mathrm{v}}_{\boldsymbol{p},\,p_\perp}$ for the conduction and valence band, respectively. These matrix elements can either be calculated assuming Fröhlich or deformation potential coupling or a mixture of both. Equation (11) shows a similar structure as Eq. (8) and is coupled to the phonon-assisted single-photon correlations

$$
\begin{aligned}
&i\hbar\frac{\partial}{\partial t}\,\Delta\langle\hat{D}^{\dagger}_{\boldsymbol{p},\,p_\perp}\hat{B}^{\dagger}_{\boldsymbol{q},\,q_\perp}\hat{B}_{\boldsymbol{q}+\boldsymbol{p},\,q'_\perp}\rangle\\
&= \left(\hbar\omega_{\boldsymbol{q}+\boldsymbol{p},\,q'_\perp} - \hbar\omega_{\boldsymbol{q},\,q_\perp} - \hbar\Omega_{\mathrm{LO}}\right)\times\\
&\qquad \Delta\langle\hat{D}^{\dagger}_{\boldsymbol{p},\,p_\perp}\hat{B}^{\dagger}_{\boldsymbol{q},\,q_\perp}\hat{B}_{\boldsymbol{q}+\boldsymbol{p},\,q'_\perp}\rangle\\
&\quad + \mathrm{i}\mathcal{F}_{\boldsymbol{q},\,q_\perp}\quad\sum_{\boldsymbol{k}}\Delta\langle\hat{B}^{\dagger}_{\boldsymbol{q}+\boldsymbol{p},\,q'_\perp}\hat{D}_{\boldsymbol{p},\,p_\perp}\hat{v}^{\dagger}_{\boldsymbol{k}}\hat{c}_{\boldsymbol{k}+\boldsymbol{q}}\rangle^{*}\\
&\quad + \mathrm{i}\mathcal{F}^{*}_{\boldsymbol{q}+\boldsymbol{p},\,q'_\perp}\sum_{\boldsymbol{k}}\Delta\langle\hat{B}^{\dagger}_{\boldsymbol{q},\,q_\perp}\hat{D}^{\dagger}_{\boldsymbol{p},\,p_\perp}\hat{v}^{\dagger}_{\boldsymbol{k}}\hat{c}_{\boldsymbol{k}+\boldsymbol{p}+\boldsymbol{q}}\rangle. \qquad (12)
\end{aligned}
$$

Due to the fact that phonon- and photon-assisted polarizations appear again on the right-hand side of Eq. (11) and phonon-assisted photon-correlations on the right-hand side of Eq. (12), we have a closed set of equations. The correlation and driving terms in Eq. (11) can be computed analogously and have been solved in Markov approximation [14].

3 Results In order to investigate the influence of a cavity on the QW system, we embed the sample in a dielectric environment consisting of several layers with different refractive index to build a high-quality and high-reflecting resonator. The distributed Bragg layers act as mirrors that significantly influence the reflection and transmission of the whole heterostructure. Increasing the number of used DBR pairs leads to a higher reflectivity of the mirrors whereas an increase of the difference of the refractive indices enhances the reflectivity and broadens the stopband. To investigate the influence of the cavity on the zero phonon line (ZPL), i.e., the 1s exciton resonance, and the first phonon sideband (PSB_1) we shifted the cavity resonance to fit the according energy (see Fig. 2).

Because phonon-assisted emission and absorption take place on different sides of the excitonic resonance, we found that no normal-mode splitting occurs for the phonon sideband. This is in pronounced contrast to the usual case where the cavity mode coincides with the zero phonon line leading to strong qualitative changes in the spectra due to the normal-mode coupling. This is shown in Fig. 2a) where the solid black line depicts the photoluminescence spectrum with a cavity that is resonant with the 1s exciton peak. One observes a clear splitting into two peaks showing the well-known normal-mode coupling which is expected for this case. The light-shaded area shows the same calculation without a cavity. The reflectivity, i.e., the cavity resonance and the stopband of the semiconductor, is shown by the dark-shaded area. In contrast to this szenario, no normal-mode coupling is seen if the cavity is resonant with the first phonon sideband which is shown in Fig. 2b). Since the first phonon sideband arises at an energy which is $\hbar\Omega_{\mathrm{LO}}$ smaller than the excitonic resonance, no energy can be coupled back into the system and therefore no reabsorption can take place. Our numerical and analytical results con-

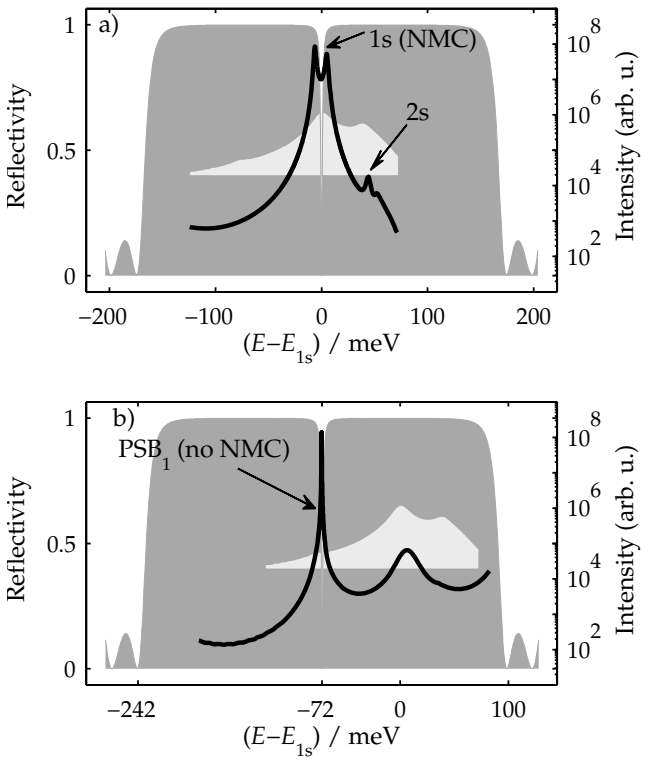

Figure 2 Splitting behavior of zero phonon line (ZPL) and first phonon sideband (PSB_1) for a cavity that is resonant to a) the 1s resonance (ZPL) and b) the PSB_1. Solid line: PL spectra with cavity (logarithmic scale). Light shaded area: PL spectra without cavity. Dark shaded area: Reflectivity (linear scale), i.e., the cavity resonance.

firm that the sideband intensity is strongly enhanced when the reflectivity of the mirrors reaches a critical value.

4 Summary A microscopic theory for the description of the phonon-assisted photoluminescence in a semiconductor has been developed by expanding the semiconductor luminescence equations to include also the phonon-assisted contributions. The calculations have been performed with and without a dielectric microcavity. Our results show the expected normal-mode splitting if the cavity mode coincides with the 1s exciton resonance. No splitting can be seen if the cavity mode is resonant with the first phonon sideband, however, the phonon-assisted luminescence is strongly enhanced in this case.

Acknowledgements Christoph N. Böttge wants to thank the International Research Training Group 790 *Electron-Electron Interactions in Solids* (Marburg–Budapest) for financial support.

References

[1] W. Shan et al., Appl. Phys. Lett. **86**, 19 (2005).
[2] T. Feldtmann, M. Kira, and S. W. Koch, Phys. Status Solidi B **246**, 2 (2009).
[3] M. Kira, F. Jahnke, W. Hoyer, and S. W. Koch, Prog. Quantum Electron. **23**, 6 (1999).
[4] M. Kira and S. W. Koch, Prog. Quantum Electron. **30**, 5 (2006).
[5] H. Haug and S. W. Koch, Quantum Theory of the Optical and Electronic Properties of Semiconductors (World Scientific Publishing Co. Pte. Ltd., Singapore, 2009).
[6] M. Kira and S. W. Koch, Phys. Rev. A **78**, 2 (2008).
[7] J. Čížek, J. Chem. Phys. **45**, 11 (1966).
[8] G. D. Purvis III, and R. J. Bartlett, J. Chem. Phys. **76**, 4 (1982).
[9] J. Fricke, Ann. Phys. **252**, 2 (1996).
[10] H. W. Wyld, Jr., and B. D. Fried, Ann. Phys. **23**, 3 (1963).
[11] C. Weisbuch, M. Nishioka, A. Ishikawa, and Y. Arakawa, Phys. Rev. Lett. **69**, 23 (1992).
[12] G. Khitrova, H. M. Gibbs, F. Jahnke, M. Kira, and S. W. Koch, Rev. Mod. Phys. **71**, 5 (1999).
[13] F. Jahnke, M. Kira, S. W. Koch, G. Khitrova, E. K. Lindmark, T. R. Nelson, Jr., D. V. Wick, J. D. Berger, O. Lyngnes, H. M. Gibbs, and K. Tai, Phys. Rev. Lett. **77**, 26 (1996).
[14] W. W. Chow and S. W. Koch, Semiconductor-Laser Fundamentals, Physics of the Gain Materials (Springer, Berlin, 1999).

PAPER III

A. Chernikov, V. Bornwasser, M. Koch, S. Chatterjee, **C. N. Böttge**, T. Feldtmann, M. Kira, S. W. Koch, T. Wassner, S. Lautenschläger, B. K. Meyer, and M. Eickhoff

Phonon-assisted luminescence of polar semiconductors: Fröhlich coupling versus deformation-potential scattering

Phys. Rev. B **85**, 035201 (2012)

DOI: 10.1103/PhysRevB.85.035201

The Inner Horizon IX

See page XLIV for reference.

Phonon-assisted luminescence of polar semiconductors: Fröhlich coupling versus deformation-potential scattering

A. Chernikov, V. Bornwasser, M. Koch, S. Chatterjee, C. N. Böttge, T. Feldtmann, M. Kira, and S. W. Koch
Faculty of Physics and Materials Sciences Center, Philipps-Universität Marburg, Renthof 5, D-35032 Marburg, Germany

T. Wassner
Walter Schottky Institut, Technische Universität München, Am Coulombwall 3, D-85748 Garching, Germany

S. Lautenschläger, B. K. Meyer, and M. Eickhoff
I. Physikalisches Institut, Justus-Liebig-Universität Gießen, Heinrich-Buff-Ring 16, D-35392 Gießen, Germany
(Received 1 August 2011; published 4 January 2012)

The origin of exciton-phonon interaction in polar semiconductors is investigated. The relative contributions of Fröhlich coupling and deformation potential scattering are identified by analyzing experimentally measured phonon-assisted luminescence using a rigorous many-body approach. Our experiment-theory comparison demonstrates that phonon scattering is significantly influenced by many-body interactions. Fröhlich interaction can be strongly suppressed for excitons even when it dominates electronic single particle scattering. The results show that deformation potential scattering dominates the exciton-phonon interaction in ZnO, whereas Fröhlich interaction prevails in CdS, and both coupling mechanisms yield almost equal contributions in ZnS.

DOI: 10.1103/PhysRevB.85.035201 PACS number(s): 78.47.jd, 63.20.kk, 78.55.Et

I. INTRODUCTION

Scattering between charge carriers and lattice vibrations is one of the elementary interactions in semiconductors. The microscopic understanding of this process is crucial for the analysis of a wide range of phenomena like cooling of a hot carrier system,[1–3] light–matter interaction,[4,5] and dephasing of coherent excitations,[6–8] to name only a few. Fröhlich interaction is presumably the most prominent carrier-phonon scattering mechanism.[9–11] It involves the direct coupling of the polarization of the lattice vibrations to the electron charge [Fig. 1(a)]. The dependence of the coupling strength on the quasimomentum **k** is qualitatively shown by the dark-gray area in Fig. 1(c). This interaction decays for large **k** and is, therefore, most efficient at transferring small momenta between electrons and phonons. In inorganic semiconductors, Fröhlich scattering is known to be of central importance in compound materials such as GaAs and GaP with polar contributions to atomic bonds,[12,13] and it is particularly strong in wide-gap materials, like CdS, ZnO, and GaN. Additionally, Fröhlich interaction is commonly applied to describe surface-related phonon scattering,[14] vibrational properties of low-dimensional systems,[15] and coupling to polarons.[16,17]

Generally, carrier-phonon interaction has to be considered in the presence of carrier-carrier Coulomb scattering. This leads to the formation of electron hole pairs, i.e., excitons,[18] observed in a wide range of materials such as organic and anorganic semiconductors,[13,19] polymers,[20] and many more. Also, in the case of the excitons, the Fröhlich interaction is commonly used to describe coupling to phonons.[21–24] However, the attractive electron-hole interaction should introduce significant modifications to the phonon scattering. While the Fröhlich coupling is strong for a single carrier, it may be much less efficient for a correlated many-body state. Thus, polar interaction between phonons and excitons should be at least partially canceled due to the opposite charges of electrons and holes within excitons. Indications for this behavior are observed and suggested in previous literature studies, e.g., on exciton-phonon scattering in confined quantum-dot systems.[25–27]

A second carrier-phonon scattering mechanism is based on the deformation of the atomic lattice by a phonon, leading to the indirect interaction with an electron via the modulations of the periodic lattice potential. This process is known as deformation potential scattering.[13,28,29] It dominates the electron-phonon coupling in nonpolar materials like Si or Ge.[12,30] The strength of the deformation potential scattering is essentially constant in **k** and leads to a relatively weak dependence of the coupling on the transferred momentum, see Fig. 1(c). Nevertheless, for small **k** values, the absolute interaction strength is considerably smaller compared to the Fröhlich interaction. However, this nonpolar coupling is only marginally changed for excitons or other correlated many-body states compared with the individual carrier interaction.

In this paper, we investigate the exciton-phonon scattering in three different polar semiconductors that are known for strong Fröhlich interaction between single charge carriers and phonons. We demonstrate that phonon scattering is significantly influenced by many-body interactions. Surprisingly, the Fröhlich coupling can be partially or even completely suppressed for exciton-phonon interactions, leaving deformation potential scattering as the dominant mechanism.

We have studied the phonon-assisted luminescence in order to identify the nature of the exciton-phonon interaction. This process is shown schematically in Fig. 1(d) in the polaron picture. The radiative recombination of excitons leads to the so-called zero-phonon line (ZPL) in the emission spectrum. The phonon-assisted radiative recombination, i.e., the simultaneous emission of a photon and one or several optical phonons, yields additional distinct spectral signatures, the so-called phonon sidebands (PSBs).[31,32] We exploit the differences between the two coupling mechanisms with respect to the interaction strength dependence on the transferred momentum by altering the carrier distribution in the reciprocal

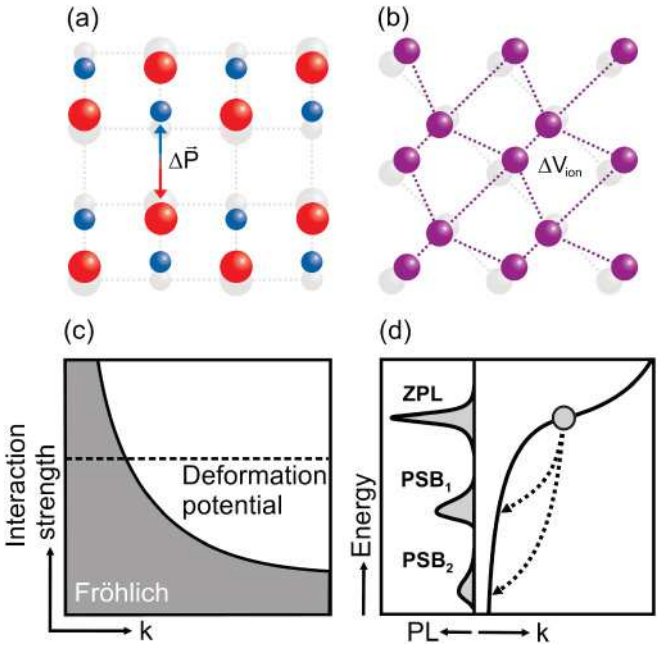

FIG. 1. (Color online) Schematic illustration of electron-phonon interaction mechanisms: polar Fröhlich coupling (a) and deformation potential scattering (b). The corresponding interaction strength is shown in (c) as a function of transferred quasimomentum **k**. Sketch of a phonon-sideband emission process in the polaron picture (d): The lower polariton branch is plotted on the right-hand side, the photoluminescence spectrum on the left.

space. Investigating the temperature dependence of the relative sideband ratios thus allows us to identify the role of Fröhlich versus deformation potential contributions to the exciton-phonon scattering processes.

II. THEORY

The Fröhlich-type carrier-LO phonon interaction stems from the relative displacements of oppositely charged ions within a unit cell, which produces a macroscopic polarization

$$\mathbf{P}(\mathbf{r}) = \frac{\hbar\Omega_{\mathrm{LO}}\epsilon_0}{e}\sum_{\mathbf{p}} g_{\mathbf{p}}^{\lambda}\frac{\mathbf{p}}{|\mathbf{p}|}\,\mathrm{e}^{\mathrm{i}\,\mathbf{p}\cdot\mathbf{r}}(D_{\mathbf{p}} - D_{-\mathbf{p}}^{\dagger}). \tag{1}$$

Here, $\frac{\mathbf{p}}{|\mathbf{p}|}(D_{\mathbf{p}} - D_{-\mathbf{p}}^{\dagger})$ describes the quantized form of induced displacement containing the Boson creation and annihilation operators $D_{\mathbf{p}}^{\dagger}$ and $D_{\mathbf{p}}$ for phonons with wave vector **p**. The associated polarization creates a macroscopic field via a Coulombic term. It is customary to express this via the band-independent Fröhlich matrix element[9]

$$\left|g_{\mathbf{p}}^{\lambda}\right|^2 = \frac{e^2}{\epsilon_0\mathcal{L}^3 2\hbar\Omega_{\mathrm{LO}}}\frac{1}{|\mathbf{p}|^2}\left[\frac{1}{\varepsilon(\infty)} - \frac{1}{\varepsilon(0)}\right], \quad \lambda = \{\mathrm{c}, \mathrm{v}\}, \tag{2}$$

where c and v represent conduction and valence band, respectively, and $\mathcal{L}^3$ is the normalization volume while ϵ_0 denotes the vacuum permittivity. It is also convenient to include dielectric constants for both high-frequency $\varepsilon(\infty)$ and low-frequency $\varepsilon(0)$ into $g_{\mathbf{p}}^{\lambda}$. The transferred momentum between the electron and LO phonon is denoted by **p**, and $\hbar\Omega_{\mathrm{LO}}$ is the respective energy of the phonon. These lattice vibrations couple with λ electrons having momentum **k**, which is described by the phonon-carrier interaction

$$H_{\mathrm{phon}} = \hbar\Omega_{\mathrm{LO}}\sum_{\lambda,\mathbf{k},\mathbf{p}} g_{\mathbf{p}}^{\lambda}\, a_{\lambda,\mathbf{k}-\mathbf{p}}^{\dagger} a_{\lambda,\mathbf{k}}(D_{-\mathbf{p}} - D_{\mathbf{p}}^{\dagger}), \tag{3}$$

where $a_{\lambda,\mathbf{k}}$ is a Fermion operator describing carriers.

The deformation-potential coupling originates from the variations of the bond lengths and angles that locally change the electronic band energies and lead to strongly band-dependent matrix elements. The resulting carrier-phonon interaction has the same form as Eq. (3); one just needs to replace $g_{\mathbf{p}}^{\lambda}$ by the deformation potential matrix element[33]

$$|g^{\lambda,\mathrm{def}}|^2 = \frac{1}{2\rho\mathcal{L}^3\hbar\Omega_{\mathrm{LO}}^3}\frac{(M_1+M_2)^2}{2M_1M_2}\frac{|d^{\lambda}|^2}{a^2}, \tag{4}$$

where ρ is the density of the material, M_1 and M_2 are the masses of the two different base atoms, d^{λ} is the optical deformation potential constant, and a is the lattice parameter.

In general, the deformation potentials are strongly band dependent. It can be shown that there is no deformation-potential interaction between conduction-band electrons and optical phonons in direct semiconductors, based on symmetry.[12,34] Therefore, d^{c} vanishes while d^{v} has a finite value in the range of some 10 eV and is also often denoted as $d_0 \equiv d^{\mathrm{v}}$ in the literature. The authors of Ref. 35 have used a tight-binding approach to calculate the deformation potentials for several semiconductors in diamond and zincblende structures and obtained a value of $d^{\mathrm{v}} = 39.8$ eV for ZnO and $d^{\mathrm{v}} = 23.7$ eV for CdS. The respective values must be converted from zincblende- to wurtzite-structure parameters for the comparison to our experimental data. These are derived using the relations of Ref. 36 where the authors have presented a general derivation of the deformation potentials in zincblende- and wurtzite-type semiconductors as well as a relation that connects both systems. The coupling constants for optical deformation potential scattering used in this work are $d_{\mathrm{ZnO}}^{\mathrm{v}} = 49.7$ eV and $d_{\mathrm{CdS}}^{\mathrm{v}} = 29.6$ eV.

The phonon sideband emission stems from phonon-assisted three-particle correlations that are systematically included with the semiconductor luminescence equations[37] as presented in the appendix. The resulting steady-state luminescence spectrum in free space follows from photon flux that is proportional to

$$I_{\mathrm{PL}}(\omega) = I_{\mathrm{ZPL}}(\omega) + I_{\mathrm{PSB}_1}(\omega) + I_{\mathrm{PSB}_2}(\omega), \tag{5}$$

where the ZPL, PSB_1, and PSB_2 contributions are simply summed over. When the 1*s*-exciton populations dominate over electron-hole plasma sources,[38] the ZPL spectrum follows from

$$I_{\mathrm{ZPL}}(\omega) = \mathrm{Im}\left[\frac{N_{\mathrm{ZPL}} - \delta N_{\mathrm{ZPL}}^{(1)} - \delta N_{\mathrm{ZPL}}^{(2)}}{E_{1s,\mathbf{0}} - \hbar\omega - \mathrm{i}\gamma_0}\right], \tag{6}$$

where the strength of the 1*s* emission —as in the case of our experiment— is defined by the exciton population $\Delta N_{1s,\mathbf{p}}$ at the vanishing momentum, i.e.,

$$N_{\mathrm{ZPL}} = \Delta N_{1s,\mathbf{0}}. \tag{7}$$

The emerging sidebands yield further corrections

$$\delta N^{(1)}_{\mathrm{ZPL}} = \sum_{\mathbf{Q}} \left| \frac{G^{1s,1s}_{\mathbf{Q}}}{\hbar\Omega - E^{\mathrm{CoM}}_{\mathbf{Q}}} \right|^2 \Delta N_{1s,\mathbf{Q}}, \tag{8}$$

$$\delta N^{(2)}_{\mathrm{ZPL}} = -\sum_{\mathbf{Q},\mathbf{p}} \sum_{\nu,\nu'} \frac{G^{1s,\nu}_{\mathbf{p}} G^{\nu,1s}_{\mathbf{Q}-\mathbf{p}}\, \Delta N_{1s,\mathbf{Q}}}{\left(2\hbar\Omega - E^{\mathrm{CoM}}_{\mathbf{Q}}\right)^2 \Delta E^{\nu,1s}_{\mathbf{p},\mathbf{0}}} \times \left[\frac{\left(G^{1s,\nu'}_{\mathbf{p}} G^{\nu',1s}_{\mathbf{Q}-\mathbf{p}}\right)^*}{\Delta E^{1s,\nu'}_{\mathbf{Q},\mathbf{p}}} + \frac{\left(G^{1s,\nu'}_{\mathbf{Q}-\mathbf{p}} G^{\nu',1s}_{\mathbf{p}}\right)^*}{\Delta E^{1s,\nu'}_{\mathbf{Q},\mathbf{Q}-\mathbf{p}}} \right]. \tag{9}$$

$\Delta N_{1s,\mathbf{q}}$ defines the center-of-mass distributions of $1s$ excitons and is assumed to follow the Bose-Einstein distribution. The corresponding exciton energy $E_{\nu,\mathbf{Q}} = E_\nu + \frac{\hbar^2\mathbf{Q}^2}{2M}$ is a sum of the exciton eigenenergy E_ν and the center-of-mass energy $E^{\mathrm{CoM}}_{\mathbf{Q}} = \frac{\hbar^2\mathbf{Q}^2}{2M}$ with the total electron-hole mass $M = m_{\mathrm{e}} + m_{\mathrm{h}}$. We also have identified the transition energy

$$\Delta E^{\nu,\nu'}_{\mathbf{Q},\mathbf{p}} \equiv \hbar\Omega - E_{\nu,\mathbf{Q}} + E_{\nu',\mathbf{p}}, \tag{10}$$

between the exciton state $(\nu,\mathbf{Q})$ and phonon-assisted transition to the exciton state $(\nu',\mathbf{p})$.

The exciton-phonon matrix elements are defined by

$$G^{\nu,\nu'}_{\mathbf{p}} = \hbar\Omega_{\mathrm{LO}} \sum_{\mathbf{k}'} \phi_\nu(\mathbf{k}' + \mathbf{p}_{\mathrm{e}}) \left[g^{\mathrm{c}}_{\mathbf{p}}\, \phi_{\nu'}(\mathbf{k}' + \mathbf{p}) - g^{\mathrm{v}}_{\mathbf{p}}\, \phi_{\nu'}(\mathbf{k}') \right]^\star, \tag{11}$$

where $\mathbf{p}_{\mathrm{e}} = \frac{m_{\mathrm{e}}}{m_{\mathrm{e}}+m_{\mathrm{h}}}\mathbf{p}$ and $\phi_\nu(\mathbf{k})$ is the low-density exciton wave function. In case phonon-matrix elements for the conduction and valence bands are equal—as it is for the Fröhlich interaction—Eq. (11) becomes

$$G^{\text{Fröhlich}}_{\mathbf{p}} = \hbar\Omega_{\mathrm{LO}} g_{\mathbf{p}} \sum_{\mathbf{k}'} \phi_\nu(\mathbf{k}' + \mathbf{p}_{\mathrm{e}}) [\phi_{\nu'}(\mathbf{k}' + \mathbf{p}) - \phi_{\nu'}(\mathbf{k}')]^\star. \tag{12}$$

This easily shows that one observes only a weak Fröhlich contribution of the phonon interaction especially for small phonon momenta $\mathbf{p}$. Since deformation potential has $d^{\mathrm{c}} = 0$ and $d^{\mathrm{v}} \neq 0$, it does not produce a reduction of phonon interaction for excitons. Therefore, the Fröhlich interaction couples excitons with phonons less efficiently than the deformation potential does.

We see from Eq. (6) that N_{ZPL} defines the strength of ZPL emission with phonon-assisted processes. Therefore, $\delta N^{(1)}_{\mathrm{ZPL}}$ and $\delta N^{(2)}_{\mathrm{ZPL}}$ provide corrections due to the presence of higher-order phonon-assisted processes. Since the ZPL is several orders of magnitude larger than the phonon sidebands, the introduced corrections have only a very slight influence on the ZPL emission. Furthermore, the energy denominators in Eqs. (8) and (9) depend only weakly on the phonon momenta, because the optical phonon energy is large compared with the energetic distance between the relevant excitonic resonances. It can be shown that the (ν,ν') combinations $(1s,1s)$ and $(1s,2p)$ especially show a significant scattering probability $|G^{\nu,\nu'}_{\mathbf{p}}|^2$.[39]

The phonon-sideband contributions up to the second sideband are similar to Eq. (6):

$$I_{\mathrm{PSB}_1}(\omega) = \mathrm{Im}\left[\sum_{\mathbf{Q}} \frac{N_{\mathrm{PSB}_1,\mathbf{Q}} - \delta N^{(2)}_{\mathrm{PSB}_1,\mathbf{Q}}}{E_{1s,\mathbf{Q}} - \hbar\Omega - \hbar\omega - \mathrm{i}\gamma_1} \right], \tag{13}$$

$$I_{\mathrm{PSB}_2}(\omega) = \mathrm{Im}\left[\sum_{\mathbf{Q}} \frac{N_{\mathrm{PSB}_2,\mathbf{Q}}}{E_{1s,\mathbf{Q}} - 2\hbar\Omega - \hbar\omega - \mathrm{i}\gamma_2} \right]. \tag{14}$$

The magnitude of the PSB resonances are defined by

$$N_{\mathrm{PSB}_1,\mathbf{Q}} = \left| \frac{G^{1s,1s}_{\mathbf{Q}}}{\hbar\Omega - E^{\mathrm{CoM}}_{\mathbf{Q}}} \right|^2 \Delta N_{1s,\mathbf{Q}}, \tag{15}$$

$$\delta N^{(2)}_{\mathrm{PSB}_1,\mathbf{Q}} = \sum_{\mathbf{p}} \frac{G^{1s,1s}_{\mathbf{Q}} G^{1s,1s}_{\mathbf{p}}\, \Delta N_{1s,\mathbf{Q}+\mathbf{p}}}{\left(2\hbar\Omega - E^{\mathrm{CoM}}_{\mathbf{Q}+\mathbf{p}}\right)\left(\hbar\Omega - E^{\mathrm{CoM}}_{\mathbf{Q}}\right) \Delta E^{1s,1s}_{\mathbf{Q}+\mathbf{p},\mathbf{Q}}} \times \sum_{\nu} \left[\frac{\left(G^{1s,\nu}_{\mathbf{Q}} G^{\nu,1s}_{\mathbf{p}}\right)^*}{\Delta E^{1s,\nu}_{\mathbf{Q}+\mathbf{p},\mathbf{Q}}} + \frac{\left(G^{1s,\nu}_{\mathbf{p}} G^{\nu,1s}_{\mathbf{Q}}\right)^*}{\Delta E^{1s,\nu}_{\mathbf{Q}+\mathbf{p},\mathbf{p}}} \right], \tag{16}$$

$$N_{\mathrm{PSB}_2,\mathbf{Q}} = \sum_{\mathbf{p}} \sum_{\nu,\nu'} \frac{G^{1s,\nu}_{\mathbf{p}} G^{\nu,1s}_{\mathbf{Q}-\mathbf{p}}\, \Delta N_{1s,\mathbf{Q}}}{\left(2\hbar\Omega - E^{\mathrm{CoM}}_{\mathbf{Q}}\right)^2 \Delta E^{1s,\nu}_{\mathbf{Q},\mathbf{p}}} \times \left[\frac{\left(G^{1s,\nu'}_{\mathbf{p}} G^{\nu',1s}_{\mathbf{Q}-\mathbf{p}}\right)^*}{\Delta E^{1s,\nu'}_{\mathbf{Q},\mathbf{p}}} + \frac{\left(G^{1s,\nu'}_{\mathbf{Q}-\mathbf{p}} G^{\nu',1s}_{\mathbf{p}}\right)^*}{\Delta E^{1s,\nu'}_{\mathbf{Q},\mathbf{Q}-\mathbf{p}}} \right]. \tag{17}$$

It is straightforward to show that the total PL, $\int I_{\mathrm{PL}}(\omega)\,\mathrm{d}\omega$, is not altered by the phonon-assisted processes. Therefore, $\delta N^{(1)}$ and $\delta N^{(2)}$ in Eqs. (6) and (13)–(14) just redistribute emission among the ZPL and PSBs through the phonon-assisted processes.

We also see from Eqs. (6)–(9) that phonon-assisted contributions change the ZPL via both $\delta N^{(1)}_{\mathrm{ZPL}}$ and $\delta N^{(2)}_{\mathrm{ZPL}}$ stemming from single- and two-phonon assisted processes, respectively. At the same time, the PSB_2 alters the PSB_1 via the $\delta N^{(2)}_{\mathrm{PSB}_1,\mathbf{Q}}$ contribution. The PSB_2 itself has only one phonon-assisted scattering source $N_{\mathrm{PSB}_2,\mathbf{Q}}$, since we include effects up to the second sideband, see Appendix A. Both the PSB_1 and PSB_2 spectra consist of a sum over exciton momentum in the Lorentzians. Therefore, the PSBs exhibit a broader spectrum at the high-energy tail than the ZPL. In particular, the slope of the high energy flank of the PSB_1 reflects the momentum-dependence of the carrier-phonon interaction, temperature of the system, available phase-space for the scattering process, and the dephasing constant γ_0. Due to nontrivial mixing of these effects, this slope is generally different for various PSBs. Therefore, the carrier temperature cannot be extracted from the fitting of the high-energy tail of a PSB by the Boltzmann function.

The intensities of PSB_1 and PSB_2 depend on the phonon-matrix elements G in the second and fourth power, respectively. Thus, the ratio between PSB_2 and PSB_1 emission is determined by the carrier temperature and by the dependence of G on the transferred momentum. As a result, one expects the $\mathrm{PSB}_2/\mathrm{PSB}_1$ ratio to decrease with increasing temperature for the momentum-dependent Fröhlich interaction since the corresponding phonon-matrix elements decrease for increasing momenta, c.f. Fig. 1. In the case of the momentum-free deformation potential, however, the phonon-matrix elements

are independent of the **p** and **Q** sums and become constant factors in Eqs. (15)–(17). Hence, the ratio PSB_2/PSB_1 does not depend on the transferred momenta and, therefore, on carrier temperature. Consequently, we expect a strongly temperature-dependent second-to-first sideband ratio for the Fröhlich scattering mechanism, while PSB_2/PSB_1 remains constant if deformation-potential coupling prevails. Thus, the carrier temperature dependence of the PSB-emission ratios offers an experimentally accessible method to identify the nature of the exciton-phonon interaction. In an experiment, the carrier temperature is easily controlled via lattice temperature and/or the excitation conditions.

III. EXPERIMENT

We perform lattice temperature-dependent measurements of the first and second PSB emission spectra for three different materials: ZnO, ZnS, and CdS. These are typical representatives for polar wide-gap semiconductors exhibiting strong electron-phonon and Coulomb-interaction effects.[12,13,32] The ZnO and ZnS samples are epitaxially grown 0.3-μm and 1-μm layers, respectively; for CdS, a chemically synthesized flake of about 10-μm thickness is investigated. Applying short-pulse interband excitation, we measure the time-resolved PL to ensure that only incoherent emission sources contribute to the signal. The second and third harmonic of a 100-fs Ti:sapphire laser with a repetition rate of 80 MHz are used for excitation. The photon energy is set to 2.9 eV in the case of CdS and to 4.1 eV for both other samples. The PL was spectrally and temporally dispersed in a standard streak camera setup,[38] obtaining resolutions of 0.4 nm and 5 ps, respectively. The phonon-sideband emission from the samples was studied as a function of lattice temperature and carrier density.

IV. RESULTS AND DISCUSSION

The time-integrated PL spectra of the CdS (a) and the ZnO (b) samples are shown in Fig. 2 at two different lattice temperatures of 10 K and 90 K in the spectral range of the first two PSBs. The well-known polariton propagation in bulk crystals leads to a strong dependence of the near band-edge PL on surface properties.[13] Therefore, we neglect the zero phonon line (ZPL) in our analysis and subtract it from the measured spectra. The data are then normalized to the PL of the second PSB for better comparison. As expected, the observed sidebands are shifted to lower energies with respect to the free exciton transitions at 2.553 eV and 3.378 eV in CdS and ZnO, respectively. The corresponding spectral intervals are multiples of LO-phonon energies of 38 meV in CdS and 72 meV in ZnO.[40] Additional weak signatures in the 10 K spectrum of the ZnO sample are identified as PSBs of donor-bound excitons.[41] Time resolved PL traces of the PSB_2 emission are shown in the insets of Fig. 1(a) and 1(b). The incident photon flux at the sample surface is set to $n_0 = 10^{11}$ photons/cm^2 per pulse. Taking into account the pump geometry and the absorption coefficients,[13,40] this corresponds to initially injected carrier densities of 3×10^{15} cm^{-3} and 2×10^{15}cm^{-3} for ZnO and CdS, respectively. All values are well below the respective Mott densities,[13,42] thus favoring the formation of excitons. In both samples, the emission dynamics

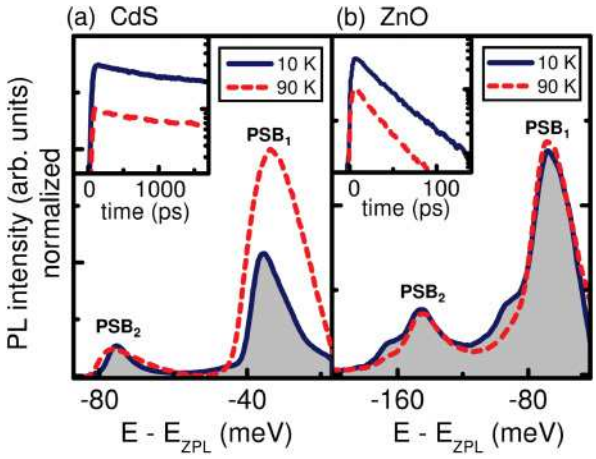

FIG. 2. (Color online) Time-integrated PL spectra of the first and the second PSB in CdS (a) and ZnO (b) at lattice temperatures of 10 K and 90 K. The inset shows the emission dynamics of the second PSB. The excitation density was $n_0 = 10^{11}$ photons/cm^2 per pulse.

are almost single exponential and do not change significantly with rising temperature. The data thus confirms exciton-related PL[13] and excludes thermal activation of additional recombination channels.

Our measurements clearly show that the ratio between the second and the first PSB strongly decreases in CdS, while it remains almost constant in ZnO when increasing the lattice temperature from 10 to 90 K. To quantify these differences, the measured temperature dependence of the PSB_2/PSB_1 intensity ratios for ZnO, ZnS, and CdS are plotted in Fig. 3(a). The corresponding theoretical results in Fig. 3(b) are obtained by calculating the contributions of Fröhlich and deformation-potential coupling. The comparison clearly shows that Fröhlich coupling dominates PSB scattering in CdS, whereas ZnO has the deformation potential coupling as the main exciton–phonon scattering process. At the same time, ZnS constitutes an intermediate case where both mechanisms equally contribute to the PSB emission.

Our findings are corroborated by the pump power dependence of the PSB luminescence. The carrier temperature rises for increasing excitation densities due to the formation of a nonequilibrium phonon population, leading to the well-known hot-phonon effect.[2] This provides an alternative way to alter the exciton distribution in favor of higher **k** values, i.e., momenta. Figure 4(a) shows the PSB_2/PSB_1 intensity ratios for ZnO (circles) and CdS (triangles) at 10 K as a function of excitation power. The resulting carrier density for the highest power applied is below 1×10^{18} cm^{-3} and, thus, still does not exceed the Mott density in both materials.[13,42] The PSB_2/PSB_1 ratio in ZnO increases only slightly for higher carrier densities. At the same time, the relative intensity of the second sideband decreases almost by a factor of two in the case of CdS. The pronounced density dependence of the PSB ratio therefore also influences the relative PL dynamics, see Figs. 4(b) and 4(c). The decay rates for the first and second PSB deviate from each other in the case of CdS [Fig. 4(c)] and are equal for the ZnO sample [Fig. 4(b)]. These results are fully consistent with temperature-dependent measurements, showing Fröhlich

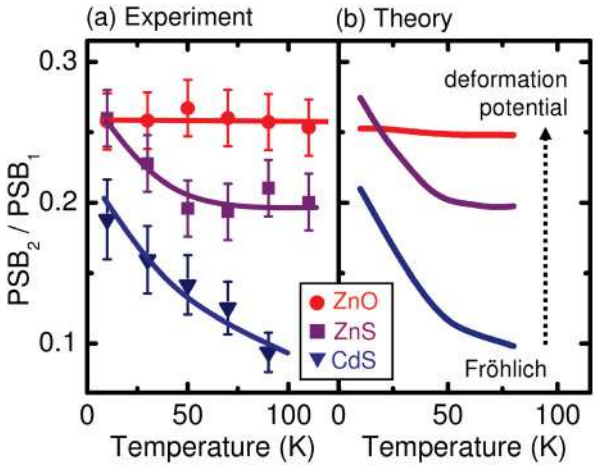

FIG. 3. (Color online) (a) Ratios of the second and first phonon sidebands as a function of lattice temperature for ZnO (circles), ZnS (squares), and CdS (triangles, top to bottom) for an excitation density of 10^{11} photons/cm^2 per pulse. The solid lines are given as guides to the eye. The corresponding results obtained from the many-body calculations are shown in (b).

behavior for the PSB emission in CdS and the deformation potential scattering in ZnO.

V. CONCLUSION

In conclusion, the exciton-phonon interaction mechanisms in polar semiconductors are studied theoretically and experimentally. A theoretical many-body approach is used to develop a straightforward way to identify the dominant scattering processes by the evaluation of phonon-assisted emission. The PSBs of ZnO, ZnS, and CdS are investigated by time-resolved PL spectroscopy as a function of temperature and excitation density. Fröhlich coupling governs the scattering in CdS, while deformation potential scattering turns out to be the dominant mechanism in ZnO. Both processes contribute about equally in ZnS. It is important to notice that our theory clearly shows that

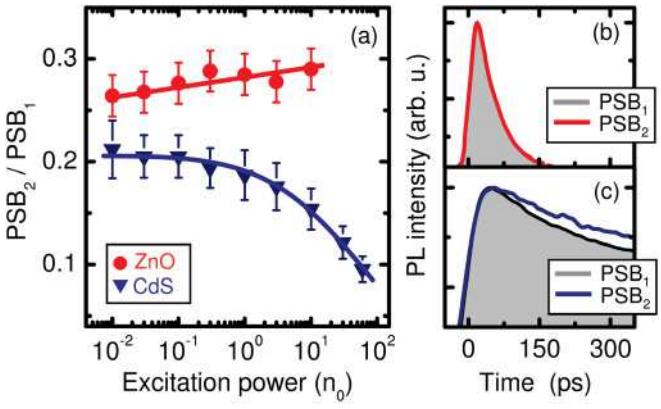

FIG. 4. (Color online) (a) Ratio of the second and first phonon sidebands as a function of excitation density at $T = 10$ K for ZnO (circles) and CdS (full triangles). Solid lines are guides to the eye. n_0 corresponds to the photon flux of 10^{11} photons/cm^2 per pulse. Normalized transients for ZnO (b) and CdS (c) of the first and second PSB are shown by solid lines and gray areas, respectively.

the scattering between a *single electron* and an optical phonon in all the studied cases is dominated by the Fröhlich interaction. However, particularly for ZnO, these contributions are suppressed by the strong Coulomb coupling of electrons and holes in excitons, rendering deformation potential scattering the overall dominant mechanism responsible for the sideband emission.

ACKNOWLEDGMENTS

A.C. and S.C. acknowledge helpful discussions with W. W. Rühle. Financial support by the German Science Foundation (DFG) and the German Ministry for Education and Research (BMBF) is gratefully acknowledged. C.B. thanks the International Research Training Group 790 *Electron-Electron Interactions in Solids* (Marburg-Budapest) for financial support.

APPENDIX: LOW-DENSITY EXCITON-DOMINATED PHONON SIDEBANDS

The description of phonon sideband luminescence is presented in Refs. 43 and 44 using the polaron picture and in Ref. 39 using the electron-hole picture. Within the applied theoretical approach, the semiconductor system as well as the carrier-carrier Coulomb-interaction and light-matter coupling mechanisms are treated microscopically using a quantized continuum model for the phonons. Both polaron and electron-hole treatments become rather cumbersome when resonances beyond the first sideband are evaluated. Therefore, we study here exciton-population dominated PSB_1 and PSB_2 when carrier densities are low. In this limiting case, we may start from a simplified system Hamiltonian

$$H = H_{\mathrm{X}} + H_{\mathrm{vib}} + H_{\mathrm{em}} + H_{\mathrm{X-vib}} + H_{\mathrm{X-em}}, \tag{A1}$$

where the noninteracting part contains

$$H_{\mathrm{X}} = \sum_{\nu,\mathbf{q}} E_{\nu,\mathbf{q}} X^{\dagger}_{\nu,\mathbf{q}} X_{\nu,\mathbf{q}}, \tag{A2}$$

with exciton operator $X_{\nu,\mathbf{q}}$ identified by state index ν and center-of-mass momentum $\hbar\mathbf{q}$. For elevated densities, H_{X} must be supplemented with additional pure carrier contributions,[37] and they can be ignored only at low densities. The free phonons and photons are described by

$$H_{\mathrm{vib}} = \sum_{\mathbf{p}} \hbar\Omega_{\mathrm{LO}} \left(D^{\dagger}_{\mathbf{p}} D_{\mathbf{p}} + \tfrac{1}{2} \right) \tag{A3}$$

and

$$H_{\mathrm{em}} = \sum_{\mathbf{q}} \hbar\omega_{\mathbf{q}} \left(B^{\dagger}_{\mathbf{q}} B_{\mathbf{q}} + \tfrac{1}{2} \right), \tag{A4}$$

where $\hbar\Omega_{\mathrm{LO}}$ is the LO-phonon energy and $\omega_{\mathbf{q}}$ sets the photon dispersion. Like always, phonon $D_{\mathbf{p}}$ and photon $B_{\mathbf{q}}$ are bosonic, while $X_{\nu,\mathbf{q}}$ is bosonic only approximately. For the low-density study performed here, we apply the bosonic approximation

$$[X_{\nu,\mathbf{Q}}, X^{\dagger}_{\nu',\mathbf{Q}'}]_- = \delta_{\nu,\nu'}\delta_{\mathbf{Q},\mathbf{Q}'}, \tag{A5}$$

$$[X_{\nu,\mathbf{Q}}, X_{\nu',\mathbf{Q}'}]_- = 0 = [X^{\dagger}_{\nu,\mathbf{Q}}, X^{\dagger}_{\nu',\mathbf{Q}'}]_-. \tag{A6}$$

In this situation, the exciton-phonon and exciton-photon interactions are described by

$$H_{\mathrm{X-vib}} = \sum_{\nu,\nu'} \sum_{\mathbf{Q},\mathbf{p}} G_{\mathbf{p}}^{\nu,\nu'} X_{\nu,\mathbf{Q}-\mathbf{p}}^{\dagger} X_{\nu',\mathbf{Q}} (D_{-\mathbf{p}} + D_{\mathbf{p}}^{\dagger}), \quad \text{(A7)}$$

$$H_{\mathrm{X-em}} = -\sum_{\nu,\mathbf{q}} \mathrm{i}[\mathcal{F}_{\nu,\mathbf{q}} X_{\nu,\mathbf{q}}^{\dagger} + \mathcal{F}_{\nu,\mathbf{q}}^{\star} X_{\nu',\mathbf{q}}] B_{\mathbf{q}} + \mathrm{h.c.}, \quad \text{(A8)}$$

respectively, where $G_{\mathbf{p}}^{\nu,\nu'}$ and $\mathcal{F}_{\nu,\mathbf{q}}$ determine exciton-phonon and exciton-light coupling matrix elements, respectively.

Computing the Heisenberg equation of motion, the incoherent photon flux follows from

$$I_{\mathrm{PL}}(\omega) = \frac{\partial}{\partial t} \Delta \langle B_{\mathbf{q}}^{\dagger} B_{\mathbf{q}} \rangle = \frac{2}{\hbar} \mathrm{Re}\Big[\sum_{\nu} \mathcal{F}_{\nu,\mathbf{q}}^{\star} \Pi_{\nu,\mathbf{q}}^{(0)} \Big]. \quad \text{(A9)}$$

This equation contains the photon-assisted polarization $\Pi_{\nu,\mathbf{q}}^{(0)} \equiv \Delta \langle B_{\mathbf{q}}^{\dagger} X_{\nu,\mathbf{q}} \rangle$. The corresponding phonon-assisted recombination correlations are $\Pi_{\nu,\mathbf{q};\mathbf{p}_1,\ldots,\mathbf{p}_n}^{(n)} \equiv \Delta \langle D_{\mathbf{p}_n}^{\dagger} \cdots D_{\mathbf{p}_1}^{\dagger} B_{\mathbf{q}}^{\dagger} X_{\nu,\mathbf{q}+\mathbf{p}_{1,n}} \rangle$, where $\mathbf{p}_{1,n} \equiv \sum_{j=1}^{n} \mathbf{p}_j$ is introduced to shorten the notation. The general equation of motion for $\Pi^{(n)}$ follows from

$$\begin{aligned} \mathrm{i}\hbar \frac{\partial}{\partial t} \Pi_{\nu,\mathbf{q};\mathbf{p}_1,\ldots,\mathbf{p}_n}^{(n)} &= (E_{\nu,\mathbf{q}+\mathbf{p}_{1,n}} - \hbar\omega_{\mathbf{q}} - n\hbar\Omega_{\mathrm{LO}})\, \Pi_{\nu,\mathbf{q};\mathbf{p}_1,\ldots,\mathbf{p}_n}^{(n)} \\ &\quad + \mathrm{i} \sum_{\nu'} \mathcal{F}_{\nu',\mathbf{q}}\, \Delta \big\langle D_{\mathbf{p}_n}^{\dagger} \cdots D_{\mathbf{p}_1}^{\dagger} X_{\nu',\mathbf{q}}^{\dagger} X_{\nu,\mathbf{q}+\mathbf{p}_{1,n}} \big\rangle \\ &\quad + \sum_{\nu',\mathbf{p}} G_{\mathbf{p}}^{\nu,\nu'}\, \Pi_{\nu',\mathbf{q};\mathbf{p},\mathbf{p}_1,\ldots,\mathbf{p}_n}^{(n+1)}. \end{aligned} \quad \text{(A10)}$$

Equations (A9) and (A10) have the structure of the *semiconductor luminescence equations*.[37] As an additional feature, phonon-assisted processes are now also included.

To solve ZPL, PSB_1, and PSB_2, we need to solve Eq. (A10) for $n = 0, 1$, and 2, respectively:

$$\begin{aligned} \mathrm{i}\hbar \frac{\partial}{\partial t} \Pi_{\nu,\mathbf{q}}^{(0)} &= (E_{\nu,\mathbf{q}} \Pi_{\nu,\mathbf{q}}^{(0)} - \hbar\omega_{\mathbf{q}} - \mathrm{i}\gamma^{(0)})\, \Pi_{\nu,\mathbf{q}}^{(0)} \\ &\quad + \mathrm{i}\mathcal{F}_{\nu,\mathbf{q}}^{\star}\, \Delta \langle X_{\nu,\mathbf{q}}^{\dagger} X_{\nu,\mathbf{q}} \rangle + \sum_{\nu',\mathbf{p}} G_{\mathbf{p}}^{\nu,\nu'} \Pi_{\nu',\mathbf{q};\mathbf{p}}^{(1)}, \end{aligned} \quad \text{(A11)}$$

$$\begin{aligned} \mathrm{i}\hbar \frac{\partial}{\partial t} \Pi_{\nu,\mathbf{q};\mathbf{p}_1}^{(1)} &= (E_{\nu,\mathbf{q}+\mathbf{p}_1} - \hbar\omega_{\mathbf{q}} - \hbar\Omega_{\mathrm{LO}} - \mathrm{i}\gamma^{(1)})\, \Pi_{\nu,\mathbf{q};\mathbf{p}_1}^{(1)} \\ &\quad + \mathrm{i} \sum_{\nu'} \mathcal{F}_{\nu',\mathbf{q}}^{\star}\, \Delta \big\langle D_{\mathbf{p}_1}^{\dagger} X_{\nu',\mathbf{q}}^{\dagger} X_{\nu,\mathbf{q}+\mathbf{p}_1} \big\rangle \\ &\quad + \sum_{\nu',\mathbf{p}} G_{\mathbf{p}}^{\nu,\nu'} \Pi_{\nu',\mathbf{q};\mathbf{p},\mathbf{p}_1}^{(2)}, \end{aligned} \quad \text{(A12)}$$

$$\begin{aligned} \mathrm{i}\hbar \frac{\partial}{\partial t} \Pi_{\nu,\mathbf{q};\mathbf{p}_1,\mathbf{p}_2}^{(2)} &= (E_{\nu,\mathbf{q}+\mathbf{p}_1} - \hbar\omega_{\mathbf{q}} - 2\hbar\Omega_{\mathrm{LO}} - \mathrm{i}\gamma^{(2)})\, \Pi_{\nu,\mathbf{q};\mathbf{p}_1,\mathbf{p}_2}^{(2)} \\ &\quad + \mathrm{i} \sum_{\nu'} \mathcal{F}_{\nu',\mathbf{q}}^{\star}\, \Delta \big\langle D_{\mathbf{p}_2}^{\dagger} D_{\mathbf{p}_1}^{\dagger} X_{\nu',\mathbf{q}}^{\dagger} X_{\nu,\mathbf{q}+\mathbf{p}_1+\mathbf{p}_2} \big\rangle, \end{aligned} \quad \text{(A13)}$$

where we have added dephasing $\gamma^{(n)}$ to describe scattering processes phenomenologically. For elevated densities, a $f^{\mathrm{e}} f^{\mathrm{h}}$ source also appears, giving rise to plasma-initiated emission at the excitonic ZPL and PSB_n resonances, c.f. Ref. 38.

The spontaneous-emission source terms that appear in Eqs. (A11)–(A13) take the form

$$\begin{aligned} \mathrm{i}\hbar \frac{\partial}{\partial t} \big\langle D_{\mathbf{p}_n}^{\dagger} \cdots D_{\mathbf{p}_1}^{\dagger} X_{\nu',\mathbf{q}}^{\dagger} X_{\nu,\mathbf{q}+\mathbf{p}_{1,n}} \big\rangle &= \big[E_{\nu,\mathbf{q}+\mathbf{p}_{1,n}} - E_{\nu',\mathbf{q}} - n\hbar\Omega_{\mathrm{LO}} - \mathrm{i}\eta_{\mathrm{X}}^{(n)}\big] \big\langle D_{\mathbf{p}_n}^{\dagger} \cdots D_{\mathbf{p}_1}^{\dagger} X_{\nu',\mathbf{q}}^{\dagger} X_{\nu,\mathbf{q}+\mathbf{p}_{1,n}} \big\rangle - \sum_{\nu'',\nu'''} \sum_{\mathbf{Q}} \sum_{j=1}^{n} \big(G_{\mathbf{p}_j}^{\nu''',\nu''}\big)^{\star} \\ &\quad \times \Big\langle \Big(\prod_{i\neq j}^{n} D_{\mathbf{p}_j}^{\dagger} \Big) X_{\nu'',\mathbf{Q}+\mathbf{p}_j}^{\dagger} X_{\nu''',\mathbf{Q}} X_{\nu',\mathbf{q}}^{\dagger} X_{\nu,\mathbf{q}+\mathbf{p}_{1,n}-\mathbf{p}_j} \Big\rangle \sum_{\nu''} \sum_{\mathbf{Q}} \big\langle D_{\mathbf{p}_n}^{\dagger} \cdots D_{\mathbf{p}_1}^{\dagger} (D_{\mathbf{Q}}^{\dagger} + D_{-\mathbf{Q}}) \\ &\quad \times \big[G_{\mathbf{Q}}^{\nu,\nu''} X_{\nu',\mathbf{q}}^{\dagger} X_{\nu'',\mathbf{q}+\mathbf{Q}+\mathbf{p}_{1,n}} - \big(G_{-\mathbf{Q}}^{\nu',\nu''}\big)^{\star} X_{\nu',\mathbf{q}-\mathbf{Q}}^{\dagger} X_{\nu,\mathbf{q}+\mathbf{p}_{1,n}} \big] \big\rangle, \end{aligned} \quad \text{(A14)}$$

where we again have added a dephasing $\eta_{\mathrm{X}}^{(n)}$ for each replica. We only consider those contributions to a given replica that are of the lowest order in the electron-phonon coupling constants. Therefore, we can neglect the last line of Eq. (A14) in the following analysis. Applying the cluster-expansion scheme[37,45–49] and solving Eq. (A14) in steady state, we obtain the form for phonon sidebands of arbitrary order

$$\begin{aligned} \big\langle D_{\mathbf{p}_n}^{\dagger} \cdots D_{\mathbf{p}_1}^{\dagger} X_{\nu',\mathbf{q}}^{\dagger} X_{\nu,\mathbf{q}+\mathbf{p}_{1,n}} \big\rangle &= \sum_{\mu_1,\ldots,\mu_{n-1}} \sum_{j_1=1}^{n} \sum_{\substack{j_2=1 \\ j_2\neq j_1}}^{n} \cdots \sum_{\substack{j_n=1 \\ j_n\neq j_1,\ldots,j_{n-1}}}^{n} \big(G_{\mathbf{p}_{j_1}}^{\nu',\mu_1}\big)^{\star} \big(G_{\mathbf{p}_{j_2}}^{\mu_1,\mu_2}\big)^{\star} \cdots \big(G_{\mathbf{p}_{j_n}}^{\mu_{n-1},\nu}\big)^{\star}\, \Delta N_{\nu,\mathbf{q}+\mathbf{p}_{1,n}} \\ &\quad \times \Big\{ \prod_{l=1}^{n} \big[E_{\nu,\mathbf{q}+\mathbf{p}_{1,n}} - E_{\mu_l,\mathbf{q}+\mathbf{p}_{j_1,j_l}} - l\hbar\Omega_{\mathrm{LO}} - \mathrm{i}\eta_{\mathrm{X}}^{(l)} \big] \Big\}^{-1}, \end{aligned} \quad \text{(A15)}$$

where we set $\mu_n = \nu'$. This expression identifies the exciton population

$$\Delta \langle X_{\nu,\mathbf{q}}^{\dagger} X_{\nu,\mathbf{q}} \rangle = \Delta N_{\nu,\mathbf{q}} \quad \text{(A16)}$$

as the source for the ZPL. In the same way, we find the PSB_1 and PSB_2 sources

$$\Delta\langle D^\dagger_{\mathbf{p}_1} X^\dagger_{\nu',\mathbf{q}} X_{\nu,\mathbf{q}+\mathbf{p}_1}\rangle = \frac{\left(G^{\nu',\nu}_{\mathbf{p}_1}\right)^\star \Delta N_{\nu,\mathbf{q}+\mathbf{p}_1}}{E_{\nu,\mathbf{q}+\mathbf{p}_1} - E_{\nu',\mathbf{q}} - \hbar\Omega_{\mathrm{LO}} - \mathrm{i}\eta^{(1)}_{\mathrm{X}}} \tag{A17}$$

and

$$\Delta\langle D^\dagger_{\mathbf{p}_2} D^\dagger_{\mathbf{p}_1} X^\dagger_{\nu',\mathbf{q}} X_{\nu,\mathbf{q}+\mathbf{p}_1+\mathbf{p}_2}\rangle = \sum_\mu \frac{\Delta N_{\nu,\mathbf{q}+\mathbf{p}_1+\mathbf{p}_2}}{E_{\nu,\mathbf{q}+\mathbf{p}_1+\mathbf{p}_2} - E_{\nu',\mathbf{q}} - 2\hbar\Omega_{\mathrm{LO}} - \mathrm{i}\eta^{(2)}_{\mathrm{X}}}$$
$$\times \left[\frac{\left(G^{\nu',\mu}_{\mathbf{p}_1}\right)^\star \left(G^{\mu,\nu}_{\mathbf{p}_2}\right)^\star}{E_{\nu,\mathbf{q}+\mathbf{p}_1+\mathbf{p}_2} - E_{\mu,\mathbf{q}+\mathbf{p}_1} - \hbar\Omega_{\mathrm{LO}} - \mathrm{i}\eta^{(1)}_{\mathrm{X}}} + \frac{\left(G^{\nu',\mu}_{\mathbf{p}_2}\right)^\star \left(G^{\mu,\nu}_{\mathbf{p}_1}\right)^\star}{E_{\nu,\mathbf{q}+\mathbf{p}_1+\mathbf{p}_2} - E_{\mu,\mathbf{q}+\mathbf{p}_2} - \hbar\Omega_{\mathrm{LO}} - \mathrm{i}\eta^{(1)}_{\mathrm{X}}} \right]. \tag{A18}$$

Respectively, these sources drive $\Pi^{(n)}$ as indicated in Eq. (A10). We see that $\Pi^{(0)}$ is coupled to $\Pi^{(1)}$ and $\Pi^{(2)}$. As we determine the steady state, we can determine the steady-state spectra (6), (13), and (14) defining ZPL, PSB_1, and PSB_2 spectra when the analysis includes $1s$ and $2p$ states. It is numerically confirmed that these contributions dominate the spectra under the conditions studied.

[1] R. P. Stanley, J. Hegarty, R. Fischer, J. Feldmann, E. O. Göbel, R. D. Feldman, and R. F. Austin, Phys. Rev. Lett. **67**, 128 (1991).

[2] *Hot Electrons in Semiconductors: Physics and Devices*, edited by N. Balkan (Clarendon Press, Oxford, 1998).

[3] T. Kampfrath, L. Perfetti, F. Schapper, C. Frischkorn, and M. Wolf, Phys. Rev. Lett. **95**, 187403 (2005).

[4] U. Woggon, F. Gindele, O. Wind, and C. Klingshirn, Phys. Rev. B **54**, 1506 (1996).

[5] H. Zhao, S. Moehl, and H. Kalt, Phys. Rev. Lett. **89**, 097401 (2002).

[6] P. Borri, W. Langbein, S. Schneider, U. Woggon, R. L. Sellin, D. Ouyang, and D. Bimberg, Phys. Rev. Lett. **87**, 157401 (2001).

[7] Y.-Z. Ma, M. W. Graham, G. R. Fleming, A. A. Green, and M. C. Hersam, Phys. Rev. Lett. **101**, 217402 (2008).

[8] J. Brandt, P. Felbier, D. Fröhlich, C. Sandfort, M. Bayer, and H. Stolz, Phys. Rev. B **81**, 155214 (2010).

[9] H. Froehlich, Adv. Phys. **3**, 325 (1954).

[10] H. Haken, *Quantenfeldtheorie des Festkoerpers* (Teubner, Stuttgart, 1973).

[11] F. Giustino, M. L. Cohen, and S. G. Louie, Nature (London) **452**, 975 (2008).

[12] P. Yu and M. Cardona, *Fundamentals of Semiconductors: Physics and Material Properties*, 3rd ed. (Springer-Verlag, Berlin, Heidelberg, New York, 2005).

[13] C. F. Klingshirn, *Semiconductor optics*, 2nd ed. (Springer, Berlin Heidelberg New York, 2007).

[14] W.-K. Hong, G. Jo, M. Choe, T. Lee, J. I. Sohn, and M. E. Welland, Appl. Phys. Lett. **94**, 043103 (2009).

[15] A. W. E. Minnaert, A. Y. Silov, W. van der Vleuten, J. E. M. Haverkort, and J. H. Wolter, Phys. Rev. B **63**, 075303 (2001).

[16] T. Itoh, M. Nishijima, A. I. Ekimov, C. Gourdon, A. L. Efros, and M. Rosen, Phys. Rev. Lett. **74**, 1645 (1995).

[17] S. J. Xu, S.-J. Xiong, and S. L. Shi, J. Chem. Phys. **123**, 221105 (2005).

[18] H. Haug and S. W. Koch, *Quantum Theory of the Optical and Electronic Properties of Semiconductors*, 5th ed. (World Scientific, Singapore, 2009).

[19] S. Blumstengel, S. Sadofev, C. Xu, J. Puls, and F. Henneberger, Phys. Rev. Lett. **97**, 237401 (2006).

[20] K. Minoshima, M. Taiji, K. Misawa, and T. Kobayashi, Phys. Chem. Lett. **218**, 67 (1994).

[21] S. J. Xu, W. Liu, and M. F. Li, Appl. Phys. Lett. **81**, 2959 (2002).

[22] V. Ursaki, I. Tiginyanu, V. Zalamai, V. Masalov, E. Samarov, G. Emelchenko, and F. Briones, J. Appl. Phys. **96**, 1001 (2004).

[23] B.-L. Gao, Y. Xiong, and S.-J. Xiong, Phys. Rev. B **74**, 235102 (2006).

[24] S. Sohai, Y. Alivov, Z. Fan, and M. Holtz, J. Appl. Phys. **108**, 053507 (2010).

[25] S. Nomura and T. Kobayashi, Phys. Rev. B **45**, 1305 (1992).

[26] A. V. Fedorov, A. V. Baranov, and K. Inoue, Phys. Rev. B **56**, 7491 (1997).

[27] V. M. Fomin, V. N. Gladilin, J. T. Devreese, E. P. Pokatilov, S. N. Balaban, and S. N. Klimin, Phys. Rev. B **57**, 2415 (1998).

[28] W. A. Harrison, Phys. Rev. **104**, 1281 (1956).

[29] D. Braun, W. W. Rühle, C. Trallero-Giner, and J. Collet, Phys. Rev. Lett. **67**, 2335 (1991).

[30] C. Lange, N. S. Köster, S. Chatterjee, H. Sigg, D. Chrastina, G. Isella, H. von Känel, B. Kunert, and W. Stolz, Phys. Rev. B **81**, 045320 (2010).

[31] C. W. Litton, D. C. Reynolds, T. C. Collins, and Y. S. Park, Phys. Rev. Lett. **25**, 1619 (1970).

[32] S. Permogorov, *Excitons* (North-Holland, Amsterdam, 1982), pp. 177–203.

[33] I. V. Bondarev, S. A. Maksimenko, G. Y. Slepyan, I. L. Krestnikov, and A. Hoffmann, Phys. Rev. B **68**, 073310 (2003).

[34] K. Reimann, R. A. Kaindl, and M. Woerner, Phys. Rev. B **65**, 045302 (2001).

[35] W. Pötz and P. Vogl, Phys. Rev. B **24**, 2025 (1981).

[36] S.-H. Park and S.-L. Chuang, J. Appl. Phys. **87**, 353 (2000).

[37] M. Kira, F. Jahnke, W. Hoyer, and S. W. Koch, Prog. Quant. Electron. **23**, 189 (1999).

[38] A. Chernikov, T. Feldtmann, S. Chatterjee, M. Koch, M. Kira, and S. W. Koch, Sol. Stat. Comm. **150**, 1733 (2010).

[39] T. Feldtmann, *Influence of Phonons on Semiconductor Quantum Emission*, Ph.D. thesis, Fachbereich Physik, Philipps-Universität Marburg, Germany, 2009.

[40] O. Madelung, *Landolt-Boernstein: Numerical Data and Functional Relationships in Science and Technology* (Springer, Berlin Heidelberg New York, 1982).

[41]B. K. Meyer, H. Alves, D. M. Hofmann, W. Kriegseis, D. Forster, F. Bertram, J. Christen, A. Hoffmann, M. Straßburg, M. Dworzak, U. Haboeck, and A. V. Rodina, Phys. Status Solidi B **241**, 231 (2004).
[42]C. Klingshirn and H. Haug, Phys. Rep. **70**, 315 (1981).
[43]T. Feldtmann, M. Kira, and S. W. Koch, Phys. Status Solidi B **246**, 332 (2009).
[44]T. Feldtmann, M. Kira, and S. W. Koch, J. Lumin. **130**, 107 (2010).
[45]M. Kira and S. W. Koch, Phys. Rev. A **78**, 022102 (2008).
[46]J. Čížek, J. Chem. Phys. **45**, 4256 (1966).
[47]G. D. Purvis III and R. J. Bartlett, J. Chem. Phys. **76**, 1910 (1982).
[48]J. Fricke, Ann. Phys. **252**, 479 (1996).
[49]H. Wyld Jr. and B. Fried, Ann. Phys. **23**, 374 (1963).

PAPER IV

C. N. Böttge, M. Kira, and S. W. Koch
Enhancement of the phonon-sideband luminescence in semiconductor microcavities
Phys. Rev. B **85**, 094301 (2012)

DOI: 10.1103/PhysRevB.85.094301

See page XLIV for reference.

Enhancement of the phonon-sideband luminescence in semiconductor microcavities

C. N. Böttge,* M. Kira, and S. W. Koch
Department of Physics and Material Sciences Center, Philipps-University of Marburg, Renthof 5, D-35032 Marburg, Germany
(Received 14 December 2011; published 5 March 2012)

The influence of a semiconductor microcavity on the phonon-assisted photoluminescence is investigated by expanding the microscopic quantum-optical semiconductor luminescence equations. For the example of a ZnO-based system, strong enhancement but no normal-mode splitting of the phonon-sideband luminescence is predicted, even if the cavity becomes resonant with the first phonon sideband. For increasing cavity quality, it is shown that the intensity of the 1*s* resonance first increases due to the Purcell effect but then starts to decrease due to the transition into the nonperturbative regime, while the spectral integrated phonon-sideband intensity saturates.

DOI: 10.1103/PhysRevB.85.094301 PACS number(s): 71.38.−k, 78.55.Cr, 42.79.Gn

I. INTRODUCTION

Zinc oxide (ZnO) exhibits a wide range of interesting properties. For example, its wide band gap that allows optical transitions in the blue/ultraviolet range could become important for semiconductor laser applications.[1,2] In optical experiments on ZnO, both the Coulomb and the electron–phonon interaction influence the resulting spectra. First of all, ZnO has a very large excitonic binding energy of about 60 meV,[3–5] which leads to strong excitonic signatures in the absorption and photoluminescence even at room temperature.[6–8] Moreover, due to its highly polar nature, the strong interaction between electrons and longitudinal-optical (LO) phonons in ZnO gives rise to pronounced phonon sidebands in the luminescence spectra.[4,8–16] Since the LO phonons have a discrete energy, phonon-assisted processes can create multiple replicas, i.e., phonon sidebands (PSBs) at distinct frequencies below the original excitonic resonance.[11,14,17] Traditionally, the excitonic resonance is called the zero-phonon line (ZPL).[12,15,18–21]

The emission properties of a quantum well (QW) can be strongly modified by its radiative environment, e.g., yielding the Purcell effect,[22] inhibited emission,[23] or the scenario of normal-mode coupling (NMC),[24–26] where the eigenmode of a high-quality microcavity and the exciton resonance are strongly coupled. Typically, such a microcavity is realized by growing distributed Bragg reflectors (DBRs) as mirrors around the QWs. For systems with strong PSBs, it is clearly interesting to study what happens to a PSB when it is coupled with a cavity mode. In ZnO, the first PSB lies 72 meV below the ZPL resonance, producing clearly separated PSB and ZPL features, which makes ZnO an attractive candidate for such investigations.

In this paper, we study how PSB luminescence is altered by an optical cavity. To develop a consistent microscopic theory of the sideband emission, we generalize the semiconductor luminescence equations (SLEs)[27–29] by fully including phonon-assisted processes. As an extension of our earlier work,[11,17] this approach allows us to compute both spontaneous and stimulated emission at the excitonic resonance and its first sideband. To corroborate our numerical results, we develop an analytic model to describe the main features of phonon-assisted luminescence in a cavity.

This paper is structured as follows. Section II presents the system Hamiltonian and Sec. III discusses the equations of motion used for the numerical and analytic calculations. Section IV reveals the principal effects of a dielectric environment. The analytic model is developed in Sec. V where the equations of motion are solved in a steady state. The appendices contain additional details of the exciton basis used and of the analytic model.

II. SYSTEM HAMILTONIAN

In our microscopic description of the optical properties, we start from the generic semiconductor Hamiltonian[27,29,30] for a two-band QW:

$$\begin{aligned} H = &\sum_{\lambda,\mathbf{k}} \epsilon_{\mathbf{k}}^{\lambda}\, a_{\lambda,\mathbf{k}}^{\dagger} a_{\lambda,\mathbf{k}} + \sum_{\mathbf{q}_{3D}} \hbar\omega_{\mathbf{q}_{3D}} \left(B_{\mathbf{q}_{3D}}^{\dagger} B_{\mathbf{q}_{3D}} + \frac{1}{2} \right) \\ &+ \sum_{\mathbf{p}_{3D}} \hbar\Omega_{\mathbf{p}_{3D}} \left(D_{\mathbf{p}_{3D}}^{\dagger} D_{\mathbf{p}_{3D}} + \frac{1}{2} \right) \\ &+ \frac{1}{2} \sum_{\lambda,\lambda'} \sum_{\mathbf{k},\mathbf{k}',\mathbf{q}\neq 0} V_{\mathbf{q}}\, a_{\lambda,\mathbf{k}}^{\dagger} a_{\lambda',\mathbf{k}'}^{\dagger} a_{\lambda',\mathbf{k}'+\mathbf{q}} a_{\lambda,\mathbf{k}-\mathbf{q}} \\ &+ \sum_{\lambda,\mathbf{k},\mathbf{p}_{3D}} \hbar\Omega_{\mathbf{p}_{3D}}\, g_{\mathbf{p}_{3D}}^{\lambda} a_{\lambda,\mathbf{k}-\mathbf{p}}^{\dagger} a_{\lambda,\mathbf{k}} \left(D_{-\mathbf{p}_{3D}} + D_{\mathbf{p}_{3D}}^{\dagger} \right) \\ &- \sum_{\mathbf{k},\mathbf{q}_{3D}} \mathrm{i} \left(\mathcal{F}_{\mathbf{q}_{3D}} a_{\mathrm{c},\mathbf{k}+\mathbf{q}}^{\dagger} a_{\mathrm{v},\mathbf{k}} + \mathcal{F}_{\mathbf{q}_{3D}}^{\star} a_{\mathrm{v},\mathbf{k}}^{\dagger} a_{\mathrm{c},\mathbf{k}-\mathbf{q}} \right) B_{\mathbf{q}_{3D}} + \mathrm{H.c.} \end{aligned} \tag{1}$$

Here, the electrons are described via the Fermionic operators $a_{\lambda,\mathbf{k}}^{\dagger}$ and $a_{\lambda,\mathbf{k}}$. The noninteracting parts contain the single-particle energy $\epsilon_{\mathbf{k}}^{\lambda}$ for an electron with momentum $\hbar\mathbf{k}$ in band λ, the photon energy $\hbar\omega_{\mathbf{q}_{3D}}$, and the phonon energy $\hbar\Omega_{\mathbf{p}_{3D}}$. We assume a sufficiently strong carrier confinement such that we only need to consider one conduction and valence band. We also use parabolic approximation $\epsilon_{\mathbf{k}}^{\lambda} = \frac{\hbar^2\mathbf{k}^2}{2m_{\lambda}}$ with the effective mass m_{λ} to describe excitations near the bottom of the bands. Since we are interested in longitudinal-optical phonons, with a constant dispersion relation, we set the phonon energy to a constant value of $\Omega_{\mathbf{p}_{3D}} \equiv \Omega$.

We consider here ZnO QWs where carriers are confined in the x-y plane. In this situation, it is beneficial to decompose the photon and phonon wave vectors into in-plane and z components, using $\mathbf{q}_{3D} = (\mathbf{q}, q_{\perp})$ and $\mathbf{p}_{3D} = (\mathbf{p}, p_{\perp})$. The corresponding subsystems are described by the Bosonic

creation (annihilation) operators $D^\dagger_{\mathbf{p}_{3D}}$ ($D_{\mathbf{p}_{3D}}$) for the phonons and $B^\dagger_{\mathbf{q}_{3D}}$ ($B_{\mathbf{q}_{3D}}$) for the photons. The remaining terms within H define the interactions of the carrier–photon–phonon system. More specifically, $V_{\mathbf{q}}$ is the Coulomb-matrix element, $\mathcal{F}_{\mathbf{q}_{3D}}$ defines the strength of the light-matter interaction, and $g^{\lambda}_{\mathbf{p}_{3D}}$ yields the carrier–phonon coupling. From those, $\mathcal{F}_{\mathbf{q}_{3D}} \equiv \mathscr{E}_{\mathbf{q}_{3D}}\mathbf{u}_{\mathbf{q}_{3D}} \cdot \mathbf{d}_{cv}$ contains the vacuum-field amplitude $\mathscr{E}_{\mathbf{q}_{3D}}$,[27] light mode strength $\mathbf{u}_{\mathbf{q}_{3D}}(r_\perp)$ at the QW position, and the dipole-matrix element $\mathbf{d}_{cv}$ for optical interband transitions in ZnO.

III. THEORY OF PHONON-SIDEBAND LUMINESCENCE

Due to the Coulomb- and quantum-optical interaction in Eq. (1), the operator dynamics yields the well-known hierarchy problem,[30] producing an infinite number of coupled equations. We truncate this hierarchy systematically using the so-called cluster-expansion approach[29,31–35] to the correlation dynamics. This approach expresses N-particle expectation values consistently in terms of all possible factorizations into single-particle quantities (singlets), two-particle correlations (doublets), three-particle correlations (triplets), and so on, up to correlated N-particle clusters. For example, a singlet level produces the semiconductor Bloch equations[30] that connect the classical light $\langle B_{\mathbf{q}}\rangle$ with polarization $P_{\mathbf{k}} = \langle a^\dagger_{v,\mathbf{k}} a_{c,\mathbf{k}}\rangle$ and densities $f^e_{\mathbf{k}} = \langle a^\dagger_{c,\mathbf{k}} a_{c,\mathbf{k}}\rangle$ and $f^h_{\mathbf{k}} = \langle a^\dagger_{v,\mathbf{k}} a_{v,\mathbf{k}}\rangle$.

For incoherent conditions, $\langle B_{\mathbf{q}}\rangle$ and $P_{\mathbf{k}}$ vanish. Therefore, incoherent light emission stems from doublet correlations, $\Delta\langle B^\dagger B\rangle = \langle B^\dagger B\rangle - \langle B^\dagger\rangle\langle B\rangle$, or higher-order correlations. We concentrate next exclusively on the incoherent regime where the photon number and its correlation are equal, i.e., $\Delta\langle B^\dagger B\rangle = \langle B^\dagger B\rangle$, because a singlet $\langle B\rangle$ vanishes. For the phonon-sideband analysis, we need to include contributions up to three-particle correlations to produce a closed set of equations describing the system consistently.

A. Semiconductor luminescence equations

The incoherent light emission follows from photon-number-like correlations,

$$i\hbar\frac{\partial}{\partial t}\Delta\langle B^\dagger_{\mathbf{q}_{3D}} B_{\mathbf{q},q'_\perp}\rangle = (\hbar\omega_{\mathbf{q},q'_\perp} - \hbar\omega_{\mathbf{q}_{3D}})\Delta\langle B^\dagger_{\mathbf{q}_{3D}} B_{\mathbf{q},q'_\perp}\rangle + i\sum_{\mathbf{k}}\left[\mathcal{F}^\star_{\mathbf{q},q'_\perp}\Pi_{\mathbf{k},\mathbf{q}_{3D}} + \mathcal{F}_{\mathbf{q}_{3D}}\Pi^\star_{\mathbf{k},\mathbf{q},q'_\perp}\right], \tag{2}$$

which are coupled to photon-assisted polarizations $\Pi_{\mathbf{k},\mathbf{q}_{3D}} \equiv \Delta\langle B^\dagger_{\mathbf{q}_{3D}} a^\dagger_{v,\mathbf{k}-\mathbf{q}_h} a_{c,\mathbf{k}+\mathbf{q}_e}\rangle$ where the photon momentum $\mathbf{q}$ is divided among the electron and hole according to $\mathbf{q}_e = \frac{m_e}{m_e+m_h}\mathbf{q}$ and $\mathbf{q}_h = \frac{m_h}{m_e+m_h}\mathbf{q}$. This defines the photon flux

$$I_{PL}(\omega_{\mathbf{q}_{3D}}) = \frac{\partial}{\partial t}\Delta\langle B^\dagger_{\mathbf{q}_{3D}} B_{\mathbf{q}_{3D}}\rangle = \mathrm{Re}\left[\sum_{\mathbf{k}}\mathcal{F}^\star_{\mathbf{q}_{3D}}\Pi_{\mathbf{k},\mathbf{q}_{3D}}\right], \tag{3}$$

which is proportional to the photoluminescence spectrum for quasistationary emission.[27] The corresponding equation of motion for the photon-assisted polarizations can be written as

$$\begin{aligned} i\hbar\frac{\partial}{\partial t}\Pi_{\mathbf{k},\mathbf{q}_{3D}} = {} & (\epsilon^\mu_{\mathbf{k}} + \epsilon^M_{\mathbf{q}} - \Sigma_{\mathbf{k},\mathbf{q}} - \hbar\omega_{\mathbf{q}_{3D}})\Pi_{\mathbf{k},\mathbf{q}_{3D}} \\ & - (1 - f^e_{\mathbf{k}+\mathbf{q}_e} - f^h_{\mathbf{k}-\mathbf{q}_h})\sum_{\mathbf{k}'} V_{\mathbf{k}-\mathbf{k}'}\Pi_{\mathbf{k}',\mathbf{q}_{3D}} \\ & - (1 - f^e_{\mathbf{k}+\mathbf{q}_e} - f^h_{\mathbf{k}-\mathbf{q}_h})\Delta\Omega_{\mathbf{q}_{3D}} + \Omega^{SE}_{\mathbf{k},\mathbf{q}_{3D}} \\ & + \hbar\Omega\sum_{\mathbf{p}_{3D}}\left[g^c_{\mathbf{p}_{3D}}(\Upsilon^{em}_{\mathbf{k},\mathbf{q}_{3D},\mathbf{p}_{3D}} + \Upsilon^{abs}_{\mathbf{k},\mathbf{q}_{3D},\mathbf{p}_{3D}}) \right. \\ & \left. - g^v_{\mathbf{p}_{3D}}(\Upsilon^{em}_{\mathbf{k}-\mathbf{p},\mathbf{q}_{3D},\mathbf{p}_{3D}} + \Upsilon^{abs}_{\mathbf{k}-\mathbf{p},\mathbf{q}_{3D},\mathbf{p}_{3D}})\right] + T[\Pi]. \end{aligned} \tag{4}$$

For parabolic bands, the sum of the single-particle energies $\epsilon^e_{\mathbf{k}+\mathbf{q}_e} + \epsilon^h_{\mathbf{k}-\mathbf{q}_h} = \epsilon^\mu_{\mathbf{k}} + \epsilon^M_{\mathbf{q}}$ can be decomposed into $\epsilon^\mu_{\mathbf{k}} = \frac{\hbar^2\mathbf{k}^2}{2\mu}$ and $\epsilon^M_{\mathbf{q}} = \frac{\hbar^2\mathbf{q}^2}{2M}$, where $\mu = (\frac{1}{m_e} + \frac{1}{m_h})^{-1}$ is the reduced mass and $M = m_e + m_h$ is the total mass. These energy terms appear in Eq. (4) together with the Coulomb renormalization,

$$\Sigma_{\mathbf{k},\mathbf{q}} \equiv \sum_{\mathbf{k}'} V_{\mathbf{k}-\mathbf{k}'}(f^e_{\mathbf{k}'+\mathbf{q}_e} + f^h_{\mathbf{k}'-\mathbf{q}_h}), \tag{5}$$

whenever carriers are excited in the system. Equations (2)–(4) constitute the principal structure of the semiconductor luminescence equations (SLEs),[27,29] where the explicit Coulomb sum yields excitonic resonances in the photoluminescence (PL). We have also included the phonon-assisted triplets

$$\Upsilon^{em}_{\mathbf{k},\mathbf{q}_{3D},\mathbf{p}_{3D}} = \Delta\langle B^\dagger_{\mathbf{q}_{3D}} D^\dagger_{\mathbf{p}_{3D}} a^\dagger_{v,\mathbf{k}-\mathbf{Q}_h} a_{c,\mathbf{k}+\mathbf{Q}_e}\rangle \tag{6}$$

and

$$\Upsilon^{abs}_{\mathbf{k},\mathbf{q}_{3D},\mathbf{p}_{3D}} = \Delta\langle B^\dagger_{\mathbf{q}_{3D}} D_{-\mathbf{p},p_\perp} a^\dagger_{v,\mathbf{k}-\mathbf{Q}_h} a_{c,\mathbf{k}+\mathbf{Q}_e}\rangle \tag{7}$$

that describe three-particle correlations due to phonon emission and absorption, respectively. Here, we introduced the center-of-mass momentum $\mathbf{Q} \equiv \mathbf{p} + \mathbf{q} = (\mathbf{p} + \mathbf{q})_e + (\mathbf{p} + \mathbf{q})_h$. The emerging correlations Υ generalize the SLEs to fully include phonon sidebands. The remaining triplet terms result from the Coulomb interaction. They do not directly participate in phonon-assisted processes but provide excitation-induced broadening and shifts of the emission resonances. The explicit format of the triplets $T[\Pi]$ is discussed in Ref. 29. In this paper, we treat these contributions at the level of a dephasing approximation, $T[\Pi] = -i\gamma_0\Pi_{\mathbf{k},\mathbf{q}_{3D}}$ defined by γ_0.

When a cavity is present, we must also include the stimulated feedback of light,

$$\Delta\Omega_{\mathbf{q}_{3D}} = i\sum_{q'_\perp}\mathcal{F}_{\mathbf{q},q'_\perp}\Delta\langle B^\dagger_{\mathbf{q}_{3D}} B_{\mathbf{q},q'_\perp}\rangle, \tag{8}$$

that yields the coupling between the different photon modes. This contribution in particular produces the well-known normal-mode splitting of excitonic resonances in high-quality cavities, which is also a focus of this study. The spontaneous emission itself is initiated by

$$\Omega^{SE}_{\mathbf{k},\mathbf{q}_{3D}} = i\mathcal{F}_{\mathbf{q}_{3D}}\left(f^e_{\mathbf{k}+\mathbf{q}_e} f^h_{\mathbf{k}-\mathbf{q}_h} + \sum_{\mathbf{k}'} c^{\mathbf{q},\mathbf{k},\mathbf{k}'}_X\right) \tag{9}$$

that is nonvanishing as soon as electrons and holes are present or when the system contains exciton correlations, $c_{\mathrm{X}}^{\mathbf{q},\mathbf{k},\mathbf{k}'} = \Delta\langle a^{\dagger}_{\mathrm{c},\,\mathbf{k}'+\mathbf{q}_{\mathrm{e}}} a^{\dagger}_{\mathrm{v},\,\mathbf{k}-\mathbf{q}_{\mathrm{h}}} a_{\mathrm{c},\,\mathbf{k}+\mathbf{q}_{\mathrm{e}}} a_{\mathrm{v},\,\mathbf{k}'-\mathbf{q}_{\mathrm{h}}}\rangle$.

Typically, the carrier distributions reach their quasiequilibrium form very rapidly via Coulomb and phonon scattering. In comparison, the spontaneous emission proceeds slowly on a nanosecond time scale such that both f^{λ} and c_{X} can be considered quasistationary when momentary PL spectra are analyzed. Therefore, we can choose them to be constant and can now concentrate on the new terms appearing in Eq. (4) to describe PSB luminescence. Technically, we must first determine Υ and then sum over all phonon momenta $\mathbf{p}$ of the phonon- and photon-assisted polarization. From these contributions, only Υ^{em} yields photon emission that is below the excitonic lines. We therefore construct the dynamics of Υ^{em} explicitly. The analysis of Υ^{abs} follows analogously; however, it is irrelevant for the PSBs studied here. The Υ^{abs} become important only if phonon absorption is relevant, requiring $k_{\mathrm{B}}T \gg \hbar\Omega$.

B. Phonon-assisted contributions

For a closed set of phonon-assisted semiconductor luminescence equations, we have to include the Υ^{em} dynamics. After deriving the Heisenberg equations of motion and taking the triplet level of the cluster expansion approach into account, we obtain

$$\begin{aligned}
\mathrm{i}\hbar\frac{\partial}{\partial t}\,\Upsilon^{\mathrm{em}}_{\mathbf{k},\mathbf{q}_{3\mathrm{D}},\mathbf{p}_{3\mathrm{D}}} &= \big(\epsilon^{\mu}_{\mathbf{k}} + \epsilon^{M}_{\mathbf{Q}} - \Sigma_{\mathbf{k},\mathbf{Q}} - \hbar\omega_{\mathbf{q},\,q_{\perp}} - \hbar\Omega\big)\Upsilon^{\mathrm{em}}_{\mathbf{k},\mathbf{q}_{3\mathrm{D}},\mathbf{p}_{3\mathrm{D}}} \\
&\quad - \big(1 - f^{\mathrm{e}}_{\mathbf{k}+\mathbf{Q}_{\mathrm{e}}} - f^{\mathrm{h}}_{\mathbf{k}-\mathbf{Q}_{\mathrm{h}}}\big)\left[\sum_{\mathbf{k}'} V_{\mathbf{k}-\mathbf{k}'}\,\Upsilon^{\mathrm{em}}_{\mathbf{k}',\mathbf{q}_{3\mathrm{D}},\mathbf{p}_{3\mathrm{D}}} + \mathrm{i}\sum_{q'_{\perp}} \mathcal{F}_{\mathbf{q}+\mathbf{p},\,q'_{\perp}}\Delta\big\langle D^{\dagger}_{\mathbf{p}_{3\mathrm{D}}} B^{\dagger}_{\mathbf{q}_{3\mathrm{D}}} B_{\mathbf{q}+\mathbf{p},\,q'_{\perp}}\big\rangle\right] \\
&\quad + \mathrm{i}\mathcal{F}_{\mathbf{q}_{3\mathrm{D}}}\left(f^{\mathrm{h}}_{\mathbf{k}-\mathbf{Q}_{\mathrm{h}}}\,\Xi^{\mathrm{c,\,c}}_{\mathbf{k},\mathbf{p}_{3\mathrm{D}},\mathbf{q}} - f^{\mathrm{e}}_{\mathbf{k}+\mathbf{Q}_{\mathrm{e}}}\,\Xi^{\mathrm{v,\,v}}_{\mathbf{k},\mathbf{p}_{3\mathrm{D}},\mathbf{0}} + \sum_{\mathbf{k}'}\,\Delta\big\langle D^{\dagger}_{\mathbf{p}_{3\mathrm{D}}} a^{\dagger}_{\mathrm{c},\,\mathbf{k}'-\mathbf{p}_{\mathrm{h}}} a^{\dagger}_{\mathrm{v},\,\mathbf{k}-\mathbf{Q}_{\mathrm{h}}} a_{\mathrm{c},\,\mathbf{k}+\mathbf{Q}_{\mathrm{e}}} a_{\mathrm{v},\,\mathbf{k}'-\mathbf{p}_{\mathrm{h}}-\mathbf{q}}\big\rangle\right) + Q[\Upsilon], \qquad (10)
\end{aligned}$$

where $\mathbf{Q} = \mathbf{p} + \mathbf{q}$ is again the center-of-mass momentum. The emerging quadruplets are presented only symbolically. They provide dephasing for the Υ^{em} processes, which is approximated via $Q[\Upsilon] = -\mathrm{i}\gamma_{\mathrm{l}}\Upsilon^{\mathrm{em}}_{\mathbf{k},\mathbf{q}_{3\mathrm{D}},\mathbf{p}_{3\mathrm{D}}}$. Equation (10) shows a similar structure as Eq. (4) and is coupled to the phonon-assisted two-photon correlations,

$$\begin{aligned}
\mathrm{i}\hbar\frac{\partial}{\partial t}\Delta\big\langle D^{\dagger}_{\mathbf{p}_{3\mathrm{D}}} B^{\dagger}_{\mathbf{q}_{3\mathrm{D}}} B_{\mathbf{q}+\mathbf{p},q'_{\perp}}\big\rangle &= (\hbar\omega_{\mathbf{q}+\mathbf{p},q'_{\perp}} - \hbar\omega_{\mathbf{q},q_{\perp}} - \hbar\Omega)\Delta\big\langle D^{\dagger}_{\mathbf{p}_{3\mathrm{D}}} B^{\dagger}_{\mathbf{q}_{3\mathrm{D}}} B_{\mathbf{q}+\mathbf{p},q'_{\perp}}\big\rangle \\
&\quad + \mathrm{i}\mathcal{F}_{\mathbf{q}_{3\mathrm{D}}}\sum_{\mathbf{k}}\big[\Upsilon^{\mathrm{abs}}_{\mathbf{k},(\mathbf{q}-\mathbf{p},q'_{\perp}),(-\mathbf{p},p_{\perp})}\big]^{\star} \\
&\quad + \mathrm{i}\mathcal{F}^{\star}_{\mathbf{q}+\mathbf{p},q'_{\perp}}\sum_{\mathbf{k}}\Upsilon^{\mathrm{em}}_{\mathbf{k},\mathbf{q}_{3\mathrm{D}},\mathbf{p}_{3\mathrm{D}}} \\
&\quad + \hbar\Omega\sum_{\lambda,\mathbf{k}} g^{\lambda}_{-\mathbf{p}_{3\mathrm{D}}}\Delta\big\langle B^{\dagger}_{\mathbf{q}_{3\mathrm{D}}} B_{\mathbf{q}+\mathbf{p},q'_{\perp}} a^{\dagger}_{\lambda,\mathbf{k}+\mathbf{p}} a_{\lambda,\mathbf{k}}\big\rangle. \qquad (11)
\end{aligned}$$

The appearing $\hbar\Omega\sum g^{\lambda}\langle B^{\dagger}Ba^{\dagger}_{\lambda}a_{\lambda}\rangle$ is a pure intraband process; its contribution to the photon emission scales as $(f^{\lambda})^2$.[36] For the low densities studied here, this contribution can therefore be dropped without affecting the results. The right-hand side of Eq. (10) additionally contains the contributions $\Xi^{\lambda,\lambda}_{\mathbf{k},\mathbf{p}_{3\mathrm{D}},\mathbf{q}}$ representing phonon-assisted scattering that initiate the correlations Υ^{em}. Since these evolve quickly into quasiequilibrium, we include them via their steady-state forms

$$\Delta\big\langle D^{\dagger}_{\mathbf{p}_{3\mathrm{D}}} a^{\dagger}_{\mathrm{c},\,\mathbf{k}-\mathbf{Q}_{\mathrm{h}}+\mathbf{q}} a_{\mathrm{c},\,\mathbf{k}+\mathbf{Q}_{\mathrm{e}}}\big\rangle = \frac{\hbar\Omega\,\big(g^{\mathrm{c}}_{\mathbf{p}_{3\mathrm{D}}}\big)^{\star} f^{\mathrm{e}}_{\mathbf{k}+\mathbf{Q}_{\mathrm{e}}}}{\epsilon^{\mathrm{e}}_{\mathbf{k}+\mathbf{Q}_{\mathrm{e}}} - \epsilon^{\mathrm{e}}_{\mathbf{k}-\mathbf{Q}_{\mathrm{h}}+\mathbf{q}} - \hbar\Omega - \mathrm{i}\eta_{\mathrm{e}}} + O(f^2), \qquad (12)$$

$$\Delta\big\langle D^{\dagger}_{\mathbf{p}_{3\mathrm{D}}} a^{\dagger}_{\mathrm{v},\,\mathbf{k}-\mathbf{Q}_{\mathrm{h}}} a_{\mathrm{v},\,\mathbf{k}+\mathbf{Q}_{\mathrm{e}}-\mathbf{q}}\big\rangle = \frac{\hbar\Omega\,\big(g^{\mathrm{v}}_{\mathbf{p}_{3\mathrm{D}}}\big)^{\star} f^{\mathrm{h}}_{\mathbf{k}-\mathbf{Q}_{\mathrm{h}}}}{\epsilon^{\mathrm{h}}_{\mathbf{k}-\mathbf{Q}_{\mathrm{h}}} - \epsilon^{\mathrm{h}}_{\mathbf{k}+\mathbf{Q}_{\mathrm{e}}-\mathbf{q}} - \hbar\Omega - \mathrm{i}\eta_{\mathrm{h}}} + O(f^2). \qquad (13)$$

Here, we have also neglected all nonlinear carrier distribution contributions because we analyze the PSB luminescence only for dilute densities with $f \ll 1$. For quasistationary situations, Eqs. (12) and (13) are a static source initiating Υ^{em} correlations. At this level, Eq. (10) contains only one additional unknown triplet source, $\Delta\langle D^{\dagger}a^{\dagger}_{\mathrm{v}}a^{\dagger}_{\mathrm{v}}a_{\mathrm{c}}a_{\mathrm{c}}\rangle$. This is also a steady-state source that can conveniently be treated after we introduce the exciton basis discussed in Appendix A. After these formal steps, we eventually obtain

$$\begin{aligned}
&\sum_{\mathbf{k}'}\Delta\big\langle D^{\dagger}_{\mathbf{p}_{3\mathrm{D}}} a^{\dagger}_{\mathrm{c},\,\mathbf{k}'-\mathbf{p}_{\mathrm{h}}} a^{\dagger}_{\mathrm{v},\,\mathbf{k}-\mathbf{Q}_{\mathrm{h}}} a_{\mathrm{c},\,\mathbf{k}+\mathbf{Q}_{\mathrm{e}}} a_{\mathrm{v},\,\mathbf{k}'-\mathbf{p}_{\mathrm{h}}-\mathbf{q}}\big\rangle \\
&= \big[\phi^{\mathrm{R}}_{1s,\,\mathbf{q}}(\mathbf{0})\big]^{\star}\phi^{\mathrm{R}}_{1s,\,\mathbf{q}+\mathbf{p}}(\mathbf{k})\frac{\hbar\Omega\,\Delta N_{1s,\mathbf{q}+\mathbf{p}}}{E_{1s,\mathbf{q}+\mathbf{p}} - E_{1s,\mathbf{q}} - \hbar\Omega - \mathrm{i}\eta_{\mathrm{X}}}\cdot\sum_{\mathbf{k}'}\phi^{\mathrm{L}}_{1s,\,\mathbf{q}}(\mathbf{k}'-\mathbf{p}_{\mathrm{h}})\big[g^{\mathrm{c}}_{\mathbf{p}_{3\mathrm{D}}}\phi^{\mathrm{R}}_{1s,\,\mathbf{q}+\mathbf{p}}(\mathbf{k}') - g^{\mathrm{v}}_{\mathbf{p}_{3\mathrm{D}}}\phi^{\mathrm{R}}_{1s,\,\mathbf{q}+\mathbf{p}}(\mathbf{k}'-\mathbf{p})\big]^{\star}, \qquad (14)
\end{aligned}$$

where $\phi^{\mathrm{L}}_{\nu,\mathbf{q}}(\mathbf{k})$ and $\phi^{\mathrm{R}}_{\nu,\mathbf{q}}(\mathbf{k})$ refer to left- and right-handed excitonic wave functions, respectively, with the eigenenergy $E_{\lambda,\mathbf{q}}$. The exciton wave function in $\mathbf{r}$-space origin is defined by

$$\phi^{\mathrm{R}}_{\nu,\mathbf{q}}(\mathbf{0}) \equiv \sum_{\mathbf{k}} \phi^{\mathrm{R}}_{\nu,\mathbf{q}}(\mathbf{k}). \tag{15}$$

Equation (14) also contains the exciton distribution $\Delta N_{1s,\mathbf{q}}$ that follows strictly from the exciton correlation c_{X}. To study quasiequilibrium conditions, we assume that $\Delta N_{1s,\mathbf{q}}$ follows a Bose–Einstein distribution. In reality, $\Delta N_{1s,\mathbf{q}}$ can have a significant hole burning[29] close to $\mathbf{q} = \mathbf{0}$. However, this does not effect Eq. (14) much because $\Delta N_{1s,\mathbf{q}}$ appears within an integral. The solutions of Eq. (10) enter the photon-assisted polarization from Eq. (4) as an additional source weighted by the phonon-matrix elements $g^{\mathrm{c}}_{\mathbf{p}_{3\mathrm{D}}}$ and $g^{\mathrm{v}}_{\mathbf{p}_{3\mathrm{D}}}$, which can either be calculated via Fröhlich coupling[37–40] or deformation potential,[40–42] or a mixture of both.[36]

In our numerical studies, the complete set of equations is evaluated fully dynamically by solving the equations of motion as shown above. Generally, $\Upsilon^{\mathrm{em}}_{\mathbf{k},\mathbf{q}_{3\mathrm{D}},\mathbf{p}_{3\mathrm{D}}}$ has a full vectorial dependence on all $\mathbf{k}$, $\mathbf{q}_{3\mathrm{D}}$, and $\mathbf{p}_{3\mathrm{D}}$ coordinates, i.e., Υ^{em} contains, in principle, also a dependence of angles between $\mathbf{k}$, $\mathbf{q}_{3\mathrm{D}}$, and $\mathbf{p}_{3\mathrm{D}}$. However, the photon momentum $\mathbf{q}_{3\mathrm{D}}$ is extremely small in the typical scale of carrier and phonon momenta. In addition, the introduction of center-of-mass decomposition shown in Eq. (5) separates the $\mathbf{k}$ and $\mathbf{p}_{3\mathrm{D}}$ dependencies into angle-independent $\epsilon^{\mu}_{\mathbf{k}}$ and $\epsilon^{M}_{\mathbf{Q}} \simeq \epsilon^{M}_{\mathbf{p}}$ parts. Therefore, the angle dependence of $\Upsilon^{\mathrm{em}}_{\mathbf{k},\mathbf{q}_{3\mathrm{D}},\mathbf{p}_{3\mathrm{D}}}$ stems directly from $f^{\lambda}_{\mathbf{k}\pm\mathbf{q}_{\lambda}}$ parts emerging in the driving source. For typical $\mathbf{k}$ and $\mathbf{Q} \simeq \mathbf{p}$ ranges of phonon-assisted processes, this angle dependence is very weak. Therefore, we can substitute $\Upsilon^{\mathrm{em}}_{\mathbf{k},\mathbf{q}_{3\mathrm{D}},\mathbf{p}_{3\mathrm{D}}} \to \Upsilon^{\mathrm{em}}_{|\mathbf{k}|,|\mathbf{q}_{3\mathrm{D}}|,|\mathbf{p}_{3\mathrm{D}}|}$ to accurately describe the main effects of phonon-assisted emission. In the computations, we discretize Υ^{em} to $40 \times 40 \times 100 = 1.6 \times 10^5$ elements, which makes the dynamical calculation very intricate and time consuming already for the first phonon sideband.

For the computation, we have used typical ZnO parameters. The effective polaron mass of the electrons in ZnO can be determined very precisely in cyclotron-resonance measurement giving $m^{\mathrm{e}}_{\mathrm{eff}} = 0.28 m_0$.[5,43] The effective mass of the holes is $m^{\mathrm{h}}_{\mathrm{eff}} = 0.59 m_0$,[5] which produces a reduced mass of $\mu = 0.19 m_0$. The material parameters of the ZnO-type QW are chosen to produce a band gap of $E_{\mathrm{gap}} = 3.37$ eV[3,5,44] and an exciton binding energy of $E_{\mathrm{B}} = 60$ meV. The energy of the longitudinal-optical phonons is $\hbar\Omega = 72$ meV and we use the deformation potential with a coupling constant of $d_0^{\mathrm{opt.\,def.}} = 50.6$ eV. The refractive index of ZnO is listed with values between 2.0 and 2.2 in the literature.[45–47] In this work, the refractive index of the QW is assumed to be $n = 2.2$.

IV. PRINCIPAL EFFECTS OF THE CAVITY

Even though ZnO microcavities have not yet been realized experimentally, sample growth techniques are developing in a direction where one can grow ZnO-type QWs between distributed Bragg reflector (DBR) mirror pairs constructed from alternating ZnO/$Mg_{0.36}Zn_{0.64}O$ layers. The refractive index profile in this study consists of several planar sections

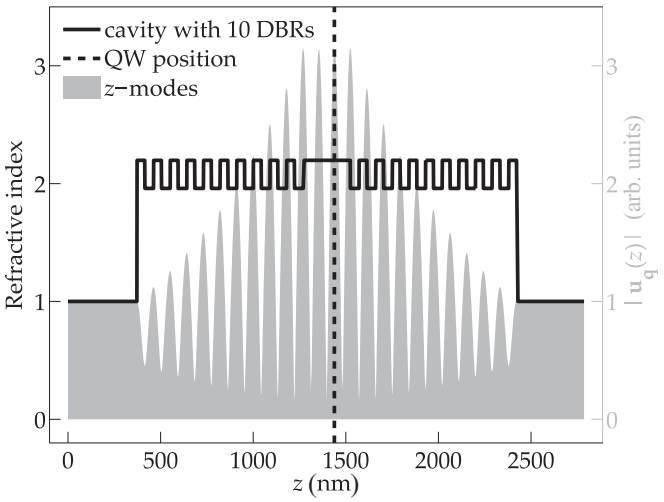

FIG. 1. Semiconductor microcavity structure. The refractive index profile of 10 ZnO/$Mg_{0.36}Zn_{0.64}O$ mirrors (black solid line) is shown together with an example of a resonant light mode $|\mathbf{u}_{\mathbf{q}}(z)|$ (shaded area). The quantum well is positioned at the mode maximum (dashed line) and the cavity has an optical thickness of $3/2\lambda$.

with piecewise constant $n = n(z)$. Each ZnO layer has the refractive index $n_{\mathrm{ZnO}} = 2.2$, while the $Mg_{0.36}Zn_{0.64}O$ layers have $n_{\mathrm{MgZnO}} = 1.96$.[46–49] For the cavity layer, we assume a material which shows the same refractive index as the ZnO-type QW itself to avoid reflections inside the sample structure. Figure 1 presents an exemplary microcavity $n(z)$ (solid line) and the mode function $u_{\mathbf{q}}(z)$ (shaded area) for the cavity resonance. The QW is positioned at the maximum of the mode function (dashed line).

The energetic position of the cavity resonance can be moved by adjusting the thickness of the $\lambda/4$ layers of the DBRs and the $3/2\lambda$ cavity layer, where λ is the wavelength of the cavity mode. Therefore, we can detune the cavity mode to be resonant either with the exciton resonance or the first PSB located at $E_{1s} - \hbar\Omega$. In the following, "1s cavity" refers to the case where the cavity is resonant with the 1s-exciton peak, i.e., the ZPL. The "phonon cavity" refers to a situation where the cavity is resonant with the PSB_1.

It is well known that the 1s cavity should produce a NMC splitting of the exciton peak into two peaks if the stimulated coupling between the light and the QW is strong enough.[24–26] Figure 2(a) shows the computed PL spectrum (black solid line) resulting from the 1s cavity. We have also plotted the bare cavity reflection (dark area) and the QW PL without the cavity (light-shaded area). The cavity mode and the 1s peak are clearly resonant, as they should be for the 1s-cavity configuration. The cavity in this example has 34 DBR layers producing a high 99.9% reflectivity for the mirrors.

As we compare the PL with (solid line) and without (light-shaded area) the cavity, we observe major qualitative changes. The 1s splits into two, as it should for the high-quality cavity, yielding the typical NMC scenario. At the same time, the overall level of the cavity PL is lower than without the cavity. Since NMC is the predominant process in this case, the phonon peak is very low. Other than that, the cavity does not modify the PSB_1 and the spectral shape of the emission at higher excitonic states. These aspects are studied further in Fig. 4.

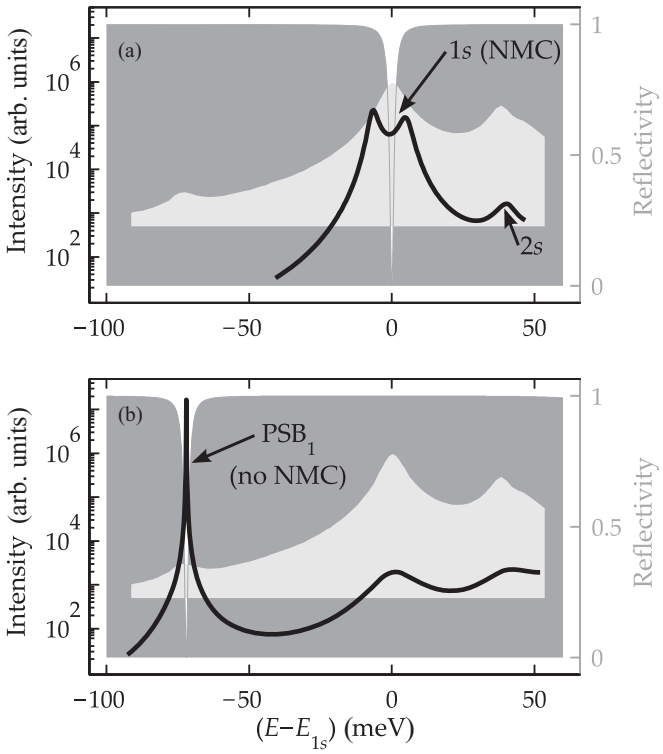

FIG. 2. Microcavity luminescence including the zero-phonon line (ZPL) and the first phonon sideband (PSB_1). The cavity is resonant with (a) the ZPL or (b) the PSB_1. The luminescence spectra with (solid line) and without (light area) cavity are compared with the reflectivity (dark area) of the bare cavity.

A completely different situation is observed in the phonon cavity where the cavity mode coincides with the first phonon sideband. In Fig. 2(b), we plot the resulting PL spectrum (solid line) showing that the phonon resonance is highly enhanced by the cavity, whereas the exciton resonance is suppressed. At the same time, the cavity PSB_1 does not produce a splitting of the emission resonance, indicating a fundamental difference between the 1*s*-cavity and the phonon–cavity coupling. For the 1*s* cavity, NMC follows from the reversible emission and absorption of light at the excitonic energy. For the phonon cavity, however, the cavity-PSB_1 coupling consists only of the photon emission part since one has only negligible phonon populations at low temperatures. Hence, there cannot be a reversible emission-absorption cycle and thus no NMC for the PSB.

A. Cavity effects vs mirror reflectivity

To verify that the phonon cavity does not produce NMC, we scan the PL spectra as a function of the DBR mirror pairs. This essentially increases the mirror reflectivity such that cavity effects become enhanced, producing a stronger coupling of the light modes to the material. Figure 3 shows the position of the emission peak(s) as a function of the DBR mirror pairs. One can clearly see that the 1*s* cavity produces a bifurcation of the 1*s* resonance into NMC splitting (solid line) as the mirror number is increased. At this point, the

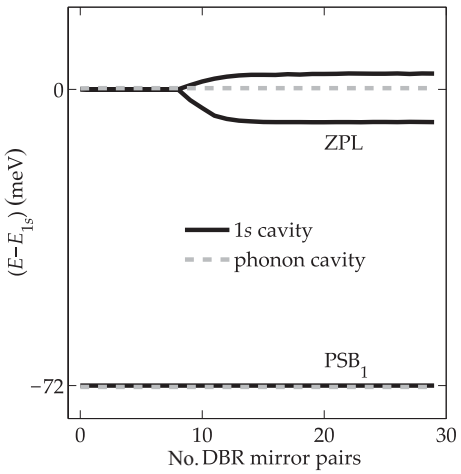

FIG. 3. Peak position in dependence of the number of DBR mirror pairs. The solid lines (dashed lines) indicate energies of the PL peaks for the 1*s* (phonon) cavity, respectively.

stimulated emission overcomes the spontaneous processes and the 1*s* resonance splits up into two peaks. The PSB_1 position, however, remains unchanged, indicating that the 1*s* cavity does not yield reversibility in this case. The phonon cavity produces a qualitatively very different behavior, as shown by the dashed lines. Neither the ZPL nor the PSB_1 positions are changed regardless of how strong the cavity becomes. This verifies that the PSB cannot yield to a reversible photon emission–absorption cycle due to a lack of phonon-assisted absorption, as discussed above.

The reversibility of the emission strongly alters the PL intensity, as seen in Fig. 2. To investigate this phenomenon further, in Fig. 4, we show the integrated PL around the 1*s*

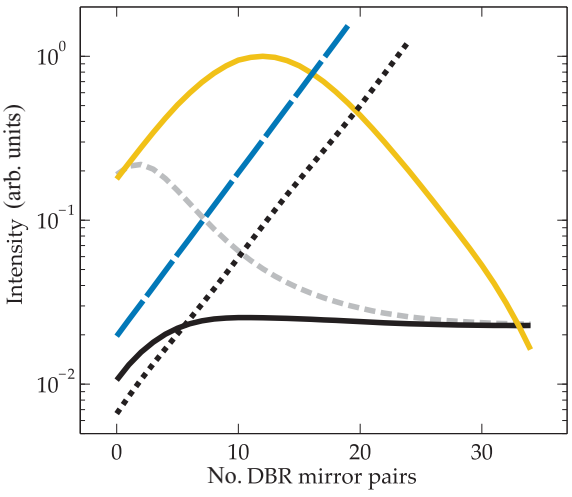

FIG. 4. (Color online) Intensity of the photoluminescence spectrum. The yellow (light gray) solid line shows the intensity of the exciton resonance for the 1*s* cavity, whereas the intensity of the phonon peak in the phonon cavity is shown by the black solid line. The short-dashed line shows the total intensity in the phonon cavity. The mode function maximum and the peak height of the first phonon sideband are indicated by the long-dashed (blue) and the dotted (black) lines, respectively.

(yellow solid line) and the PSB_1 (black solid line) resonances for the phonon cavity as a function of DBR mirror pairs. We also have defined the PSB_1 peak height (dotted line) and total integrated PL (dashed line) together with the mode strength $|u_{\mathbf{q}}|^2$ at the position of the QW.

In case of the $1s$ cavity, the intensity of ZPL emission (yellow solid line) first increases rapidly. However, the onset of reversibility starts to decrease the ZPL intensity assigning the regime of NMC. This transition takes place around 8 DBRs, which is the same threshold value producing NMC splitting in Fig. 3.

The phonon cavity produces a very different behavior. The integrated PSB_1 intensity (black solid line) first starts to increase slightly and then saturates to a constant level. In particular, we do not observe any decrease in the integrated PSB_1 intensity. At the same time, the PSB_1 peak height (dotted line) increases monotonously with the cavity mode strength (long-dashed blue line). These two observations mean that the cavity first enhances the PSB_1 via the Purcell effect. For an elevated number of DBR pairs, the PSB_1 narrows since the peak emission grows while the total emission saturates. Interestingly, the strong-cavity limit exclusively favors the PSB_1 emission over the ZPL emission because the integrated total PL (gray dashed line) and PSB_1 emission (black solid line) become equal.

V. ANALYTIC MODEL

To better understand the physical origin of the found effects, we develop an analytic model that captures the essence of the microcavity luminescence of the ZPL and PSB_1 emission. Here, we include only the $1s$ contributions and limit the investigation to dilute densities with $f^{\mathrm{e}} \ll 1$ and $f^{\mathrm{h}} \ll 1$. In this situation, it is beneficial to convert the full Eqs. (2), (4), (10), and (11) into the exciton basis,

$$\Pi^{X}_{\nu,\mathbf{q}_{3\mathrm{D}}} = \sum_{\mathbf{k}} \phi^{\star}_{\nu}(\mathbf{k})\, \Pi_{\mathbf{k},\mathbf{q}_{3\mathrm{D}}}, \tag{16a}$$

$$\Pi_{\mathbf{k},\mathbf{q}_{3\mathrm{D}}} = \sum_{\nu} \phi_{\nu}(\mathbf{k})\, \Pi^{X}_{\nu,\mathbf{q}_{3\mathrm{D}}}, \tag{16b}$$

and

$$\Upsilon^{X}_{\nu,\mathbf{p}_{3\mathrm{D}},\mathbf{q}_{3\mathrm{D}}} = \sum_{\mathbf{k}} \phi^{\star}_{\nu}(\mathbf{k})\, \Upsilon_{\mathbf{k},\mathbf{q}_{3\mathrm{D}},\mathbf{p}_{3\mathrm{D}}}, \tag{17a}$$

$$\Upsilon_{\mathbf{k},\mathbf{q}_{3\mathrm{D}},\mathbf{p}_{3\mathrm{D}}} = \sum_{\nu} \phi_{\nu}(\mathbf{k})\, \Upsilon^{X}_{\nu,\mathbf{p}_{3\mathrm{D}},\mathbf{q}_{3\mathrm{D}}}. \tag{17b}$$

For nonvanishing densities, one must distinguish the excitonic wave functions into left- and right-handed, i.e., $\phi^{\mathrm{L}}_{\nu,\mathbf{Q}}(\mathbf{k})$ and $\phi^{\mathrm{R}}_{\nu,\mathbf{Q}}(\mathbf{k})$. See the discussion in Appendix A for further details. Projecting the $1s$ component of Eq. (4) converts the principal structure of the SLE into

$$\mathrm{i}\hbar\frac{\partial}{\partial t}\Pi^{X}_{1s,\mathbf{q}_{3\mathrm{D}}} = [E_{1s,\mathbf{q}} - \hbar\omega_{\mathbf{q}_{3\mathrm{D}}} - \mathrm{i}\gamma_0]\Pi^{X}_{1s,\mathbf{q}_{3\mathrm{D}}} - \mathrm{i}\sum_{q'_{\perp}} \mathcal{F}^{1s}_{\mathbf{q},q'_{\perp}}\, \Delta\langle B^{\dagger}_{\mathbf{q}_{3\mathrm{D}}} B_{\mathbf{q},q'_{\perp}}\rangle + \mathrm{i}\mathcal{F}^{1s}_{\mathbf{q}_{3\mathrm{D}}} N_{1s,\mathbf{q}} + \hbar\Omega \sum_{\mathbf{p}_{3\mathrm{D}}} g^{1s,1s}_{\mathbf{p}_{3\mathrm{D}}}\, \Upsilon^{X}_{1s,\mathbf{p},\mathbf{q}_{3\mathrm{D}}}, \tag{18}$$

$$\mathrm{i}\hbar\frac{\partial}{\partial t}\Delta\langle B^{\dagger}_{\mathbf{q}_{3\mathrm{D}}} B_{\mathbf{q},q'_{\perp}}\rangle = \big(\hbar\omega_{\mathbf{q},q'_{\perp}} - \hbar\omega_{\mathbf{q}_{3\mathrm{D}}}\big)\Delta\langle B^{\dagger}_{\mathbf{q}_{3\mathrm{D}}} B_{\mathbf{q},q'_{\perp}}\rangle + \mathrm{i}\big[\mathcal{F}^{1s}_{\mathbf{q},q'_{\perp}}\big]^{\star}\Pi^{X}_{1s,\mathbf{q}_{3\mathrm{D}}} + \mathrm{i}\mathcal{F}^{1s}_{\mathbf{q}_{3\mathrm{D}}}\big[\Pi^{X}_{1s,\mathbf{q},q'_{\perp}}\big]^{\star}, \tag{19}$$

where the source term $N_{1s} = N^{\mathrm{eh}}_{1s} + \Delta N_{1s}$ is decomposed into a singlet and a correlated contribution. For low densities, the singlet part is proportional to $f^{\mathrm{e}} f^{\mathrm{h}}$ such that the spontaneous emission source follows mostly from the exciton distribution $N_{1s,\mathbf{q}} = \Delta N_{1s,\mathbf{q}}$ if it exists.[50] The quantity $\mathcal{F}^{1s}_{\mathbf{q}_{3\mathrm{D}}} \equiv \phi_{1s}(\mathbf{0})\,\mathcal{F}_{\mathbf{q}_{3\mathrm{D}}}$ defines the strength of the spontaneous emission.

Following the same derivation steps as in Eq. (18), the triplet source becomes

$$\mathrm{i}\hbar\frac{\partial}{\partial t}\Upsilon^{X}_{1s,\mathbf{p},\mathbf{q}_{3\mathrm{D}}} = \big[E_{1s,\mathbf{q}+\mathbf{p}} - \hbar\omega_{\mathbf{q}_{3\mathrm{D}}} - \hbar\Omega - \mathrm{i}\gamma_1\big]\Upsilon^{X}_{1s,\mathbf{p},\mathbf{q}_{3\mathrm{D}}} - \mathrm{i}\sum_{q'_{\perp}} \mathcal{F}^{1s}_{\mathbf{q}+\mathbf{p},q'_{\perp}}\, \Delta\langle D^{\dagger}_{\mathbf{p}_{3\mathrm{D}}} B^{\dagger}_{\mathbf{q}_{3\mathrm{D}}} B_{\mathbf{q}+\mathbf{p},q'_{\perp}}\rangle + \mathrm{i}\mathcal{F}^{1s}_{\mathbf{q}_{3\mathrm{D}}}\Delta N_{1s,\mathbf{p}_{3\mathrm{D}}}, \tag{20}$$

$$\begin{aligned}\mathrm{i}\hbar\frac{\partial}{\partial t}\Delta\langle D^{\dagger}_{\mathbf{p}_{3\mathrm{D}}} B^{\dagger}_{\mathbf{q}_{3\mathrm{D}}} B_{\mathbf{q}+\mathbf{p},q'_{\perp}}\rangle &= \big(\hbar\omega_{\mathbf{q}+\mathbf{p},q'_{\perp}} - \hbar\omega_{\mathbf{q}_{3\mathrm{D}}} - \hbar\Omega\big)\Delta\langle D^{\dagger}_{\mathbf{p}_{3\mathrm{D}}} B^{\dagger}_{\mathbf{q}_{3\mathrm{D}}} B_{\mathbf{q}+\mathbf{p},q'_{\perp}}\rangle \\ &\quad + \mathrm{i}\mathcal{F}^{1s}_{\mathbf{q}_{3\mathrm{D}}}\Delta\langle D^{\dagger}_{\mathbf{p}_{3\mathrm{D}}} B^{\dagger}_{\mathbf{q}+\mathbf{p},q'_{\perp}} X_{1s,\mathbf{q}}\rangle^{\star} + \mathrm{i}\big[\mathcal{F}^{1s}_{\mathbf{q}+\mathbf{p},q'_{\perp}}\big]^{\star}\Upsilon^{X}_{1s,\mathbf{p},\mathbf{q}_{3\mathrm{D}}}.\end{aligned} \tag{21}$$

The Υ^{X} dynamics contains a spontaneous phonon-assisted source,

$$\Delta N_{1s,\mathbf{p}_{3\mathrm{D}}} = \frac{\hbar\Omega\big[g^{1s,1s}_{\mathbf{p}_{3\mathrm{D}}}\big]^{\star}\Delta N_{1s,\mathbf{p}}}{E_{1s,\mathbf{p}} - E_{1s,\mathbf{0}} - \hbar\Omega} = \frac{\hbar\Omega\big[g^{1s,1s}_{\mathbf{p}_{3\mathrm{D}}}\big]^{\star}\Delta N_{1s,\mathbf{p}}}{\epsilon^{M}_{\mathbf{p}} - \hbar\Omega}, \tag{22}$$

where we have introduced the strength by the excitonic phonon-matrix element

$$g^{1s,1s}_{\mathbf{p}_{3\mathrm{D}}} = \sum_{\mathbf{k}'} \phi_{1s}(\mathbf{k}')\big[g^{\mathrm{c}}_{\mathbf{p}_{3\mathrm{D}}}\phi_{1s}(\mathbf{k}' + \mathbf{p}_{\mathrm{h}}) - g^{\mathrm{v}}_{\mathbf{p}_{3\mathrm{D}}}\phi_{1s}(\mathbf{k}' - \mathbf{p}_{\mathrm{e}})\big]^{\star}. \tag{23}$$

These contributions describe phonon-assisted processes between two exciton states.

A. Treatment of the stimulated parts

Even though the limitation to the $1s$-exciton contributions reduces the complexity of the phonon-assisted SLE considerably, Eqs. (18) and (20) still contain the nontrivial stimulated coupling via the $\sum \mathcal{F}\Delta\langle B^\dagger B\rangle$ and $\sum \mathcal{F}\Delta\langle D^\dagger B^\dagger B\rangle$ dependent contributions. To deal with these parts analytically, we introduce a scaled photon-operator and photon-assisted polarization

$$\bar{B}_{\mathbf{q},q_\perp'} \equiv \frac{B_{\mathbf{q},q_\perp'}}{\left[\mathcal{F}^{1s}_{\mathbf{q},q_\perp'}\right]^\star}, \tag{24}$$

$$\bar{\Pi}^X_{1s,\mathbf{q}_{3D}} \equiv \frac{\Pi^X_{1s,\mathbf{q}_{3D}}}{\mathcal{F}^{1s}_{\mathbf{q}_{3D}}}, \tag{25}$$

respectively. To solve Eqs. (18) and (19), we furthermore introduce collective operators

$$\bar{B}^\dagger_{\mathbf{q},\Sigma} \equiv \frac{1}{\mathcal{G}}\sum_{q_\perp'}\left[\mathcal{F}^{1s}_{\mathbf{q},q_\perp'}\right]^\star B^\dagger_{\mathbf{q},q_\perp'} = \frac{1}{\mathcal{G}}\sum_{q_\perp'}\left|\mathcal{F}^{1s}_{\mathbf{q},q_\perp'}\right|^2\bar{B}^\dagger_{\mathbf{q},q_\perp'}, \tag{26a}$$

$$\bar{B}_{\mathbf{q},\Sigma} \equiv \frac{1}{\mathcal{G}}\sum_{q_\perp'}\mathcal{F}^{1s}_{\mathbf{q},q_\perp'}B_{\mathbf{q},q_\perp'} = \frac{1}{\mathcal{G}}\sum_{q_\perp'}\left|\mathcal{F}^{1s}_{\mathbf{q},q_\perp'}\right|^2\bar{B}_{\mathbf{q},q_\perp'}. \tag{26b}$$

It is convenient to choose a normalization $\mathcal{G}$ such that $\bar{B}^\dagger_{\mathbf{q},\Sigma}$ and $\bar{B}_{\mathbf{q},\Sigma}$ satisfy Bosonic commutation relations. More specifically, we find Bosonic commutation $[\bar{B}_{\mathbf{q},\Sigma},\bar{B}^\dagger_{\mathbf{q}',\Sigma}]_- = 1$ if $\mathcal{G}^2 = \sum_{q_\perp}|\mathcal{F}^{1s}_{\mathbf{q},q_\perp}|^2$. To see the usefulness of the effective mode (26a) and (26b), we start by computing its dynamics from Eq. (19):

$$\begin{aligned}\mathrm{i}\hbar\frac{\partial}{\partial t}\Delta\langle\bar{B}^\dagger_{\mathbf{q},\Sigma}\bar{B}_{\mathbf{q},\Sigma}\rangle = {}& \frac{1}{\mathcal{G}^2}\sum_{q_\perp,q_\perp'}\left[\mathcal{F}^{1s}_{\mathbf{q},q_\perp}\right]^\star\mathcal{F}^{1s}_{\mathbf{q},q_\perp'}(\hbar\omega_{\mathbf{q},q_\perp'}-\hbar\omega_{\mathrm{cav}})\Delta\langle B^\dagger_{\mathbf{q},q_\perp}B_{\mathbf{q},q_\perp'}\rangle \\ &+\frac{1}{\mathcal{G}^2}\sum_{q_\perp,q_\perp'}\left[\mathcal{F}^{1s}_{\mathbf{q},q_\perp}\right]^\star\mathcal{F}^{1s}_{\mathbf{q},q_\perp'}(\hbar\omega_{\mathrm{cav}}-\hbar\omega_{\mathbf{q},q_\perp})\Delta\langle B^\dagger_{\mathbf{q},q_\perp}B_{\mathbf{q},q_\perp'}\rangle + 2\mathrm{i}\mathcal{G}\,\mathrm{Re}\big[\bar{\Pi}^X_{1s,\mathbf{q},\Sigma}\big],\end{aligned} \tag{27}$$

where we identified a collective photon-assisted contribution

$$\bar{\Pi}^X_{1s,\mathbf{q},\Sigma} \equiv \frac{1}{\mathcal{G}}\sum_{q_\perp'}\left|\mathcal{F}^{1s}_{\mathbf{q},q_\perp'}\right|^2\bar{\Pi}^X_{1s,\mathbf{q},q_\perp'}, \tag{28}$$

in analogy to Eq. (26a).

To study the case where the stimulated effects are particularly strong, we consider the situation of a planar semiconductor microcavity, as shown by the solid black line in Fig. 1. The cavity mode $|u_{\mathbf{q}}(z)|$ shown by the gray-shaded area is concentrated inside the cavity and the QW is positioned at one of the mode maxima, z_{QW}. The corresponding mode strength $|\mathcal{F}^{1s}_{\mathbf{q},q_\perp}|^2 \propto |u_{\mathbf{q},q_{\mathrm{cav}}}(z_{\mathrm{QW}})|^2$ forms a narrow peak around the cavity-mode energy $E_{\mathrm{cav}} = \hbar\omega_{\mathrm{cav}}$, whereas the area under $|\mathcal{F}^{1s}_{\mathbf{q},q_\perp}|^2$ remains unchanged when increasing the number of DBR layers, i.e., narrowing the peak width. Eventually, the cavity mode approaches a δ function as the cavity becomes stronger. Therefore, we can apply the *strong-cavity approximation* (SCA)

$$\sum_{q_\perp}\left|\mathcal{F}^{1s}_{\mathbf{q},q_\perp}\right|^2(\omega_{\mathbf{q},q_\perp}-\omega_{\mathrm{cav}})\odot_{\mathbf{q},q_\perp} = 0 \tag{29}$$

whenever $|\mathcal{F}^{1s}_{\mathbf{q},q_\perp}|^2$ is strongly peaked around ω_{cav} and the function $\odot_{\mathbf{q},q_\perp}$ is a slowly varying function around $\omega_{\mathbf{q},q_\perp} = \omega_{\mathrm{cav}}$. The SCA converts Eqs. (18) and (27) into

$$\mathrm{i}\hbar\frac{\partial}{\partial t}\Delta\langle\bar{B}^\dagger_{\mathbf{q},\Sigma}\bar{B}_{\mathbf{q},\Sigma}\rangle = 2\mathrm{i}\mathcal{G}\,\mathrm{Re}\big[\bar{\Pi}^X_{1s,\mathbf{q},\Sigma}\big], \tag{30}$$

$$\begin{aligned}\mathrm{i}\hbar\frac{\partial}{\partial t}\bar{\Pi}^X_{1s,\mathbf{q},\Sigma} = {}& [E_{1s,\mathbf{0}}-\hbar\omega_{\mathrm{cav}}-\mathrm{i}\gamma_0]\bar{\Pi}^X_{1s,\mathbf{q},\Sigma} \\ &+\mathrm{i}\,\mathcal{G}(\Delta N_{1s,\mathbf{0}}-\Delta\langle\bar{B}^\dagger_{\mathbf{0},\Sigma}\bar{B}_{\mathbf{0},\Sigma}\rangle) \\ &+\sum_{\mathbf{p}}\Delta\langle\bar{D}^\dagger_{\mathbf{p},\Sigma}\bar{B}^\dagger_{\mathbf{0},\Sigma}X_{\mathbf{p}}\rangle,\end{aligned} \tag{31}$$

where we defined a collective phonon operator

$$\bar{D}_{\mathbf{p},\Sigma} \equiv \sum_{p_\perp}\bar{D}_{\mathbf{p},p_\perp} \tag{32}$$

with

$$\bar{D}_{\mathbf{p},p_\perp} = \bar{D}_{\mathbf{p}_{3D}} \equiv \hbar\Omega\, g^{\nu,\nu'}_{\mathbf{p}_{3D}}D_{\mathbf{p}_{3D}}. \tag{33}$$

In the following, we study normal emission such that we can set $\mathbf{q} = \mathbf{0}$ in the photon operators. To keep the expressions brief, we introduce

$$\Delta^{\mathrm{ZPL}}_{\omega,\mathbf{p}} \equiv E_{1s,\mathbf{p}} - \hbar\omega_{\mathbf{0},q_\perp}, \tag{34a}$$

$$\Delta^{\mathrm{PSB},\pm}_{\omega,\mathbf{p}} \equiv E_{1s,\mathbf{p}} - \hbar\omega_{\mathbf{0},q_\perp} \pm \hbar\Omega, \tag{34b}$$

$$\Delta^{\mathrm{cav}}_{\omega} \equiv \hbar\omega_{\mathrm{cav}} - \hbar\omega_{\mathbf{0},q_\perp}, \tag{34c}$$

which define the exciton–light detuning ($\Delta^{\mathrm{ZPL}}_{\omega,\mathbf{p}}$), the PSB–light detuning ($\Delta^{\mathrm{PSB},\pm}_{\omega,\mathbf{p}}$), and the cavity–light detuning ($\Delta^{\mathrm{cav}}_{\omega}$), respectively. To solve the PL in the normal direction, we insert the transformations (26a), (26b), and (28) into Eqs. (18) and

(19). With similar steps as those producing Eqs. (30) and (31), we now obtain

$$\begin{aligned} i\hbar\frac{\partial}{\partial t}\begin{pmatrix} \bar{\Pi}^{X}_{1s,\mathbf{0},q_\perp} \\ \Delta\langle \bar{B}^{\dagger}_{\mathbf{0},q_\perp}\bar{B}_{\mathbf{0},\Sigma}\rangle \end{pmatrix} &= \mathbf{M}\begin{pmatrix} \bar{\Pi}^{X}_{1s,\mathbf{0},q_\perp} \\ \Delta\langle \bar{B}^{\dagger}_{\mathbf{0},q_\perp}\bar{B}_{\mathbf{0},\Sigma}\rangle \end{pmatrix} \\ &+ \begin{pmatrix} i\,\Delta N_{1s,\mathbf{0}} + \sum_{\mathbf{p}}\Delta\langle \bar{D}^{\dagger}_{\mathbf{p},\Sigma}\bar{B}^{\dagger}_{\mathbf{0},q_\perp}X_{\mathbf{p}}\rangle \\ i\left[\bar{\Pi}^{X}_{1s,\mathbf{0},\Sigma}\right]^{\star} \end{pmatrix}, \end{aligned} \tag{35}$$

where we have identified a 2×2 matrix,

$$\mathbf{M} = \begin{pmatrix} \Delta^{\mathrm{ZPL}}_{\omega,\mathbf{0}} - i\gamma_0 & -i\mathcal{G} \\ i\mathcal{G} & \Delta^{\mathrm{cav}}_{\omega} \end{pmatrix}. \tag{36}$$

The dynamics of Eq. (35) follows from a closed set of equations only in the absence of phonon effects.

Before we analyze the full PSB emission, we develop a suitable solution algorithm by solving Eqs. (30), (31), and (35) without phonons. We start from the steady state of Eq. (31), producing

$$\bar{\Pi}^{X}_{1s,\mathbf{0},\Sigma} = i\,\mathcal{G}\frac{\Delta\langle \bar{B}^{\dagger}_{\mathbf{0},\Sigma}\bar{B}_{\mathbf{0},\Sigma}\rangle - \Delta N_{1s,\mathbf{0}}}{E_{1s,\mathbf{0}} - \hbar\omega_{\mathrm{cav}} - i\gamma_0}. \tag{37}$$

This result implies that $\Delta\langle \bar{B}^{\dagger}_{\mathbf{0},\Sigma}\bar{B}_{\mathbf{0},\Sigma}\rangle$ is driven and a steady state is not reached unless we demand $\mathrm{Re}[\bar{\Pi}^{X}_{1s,\mathbf{q},\Sigma}] \equiv 0$; compare with Eq. (30). This leads to the constant collective photon-number correlation,

$$\Delta\langle \bar{B}^{\dagger}_{\mathbf{0},\Sigma}\bar{B}_{\mathbf{0},\Sigma}\rangle = \Delta N_{1s,\mathbf{0}}, \tag{38}$$

in the steady state. For this choice, $\bar{\Pi}^{X}_{1s,\mathbf{0},\Sigma}$ vanishes such that Eq. (35) becomes

$$\begin{aligned} i\hbar\frac{\partial}{\partial t}\begin{pmatrix} \bar{\Pi}^{X}_{1s,\mathbf{0},q_\perp} \\ \Delta\langle \bar{B}^{\dagger}_{\mathbf{0},q_\perp}\bar{B}_{\mathbf{0},\Sigma}\rangle \end{pmatrix} &= \mathbf{M}\begin{pmatrix} \bar{\Pi}^{X}_{1s,\mathbf{0},q_\perp} \\ \Delta\langle \bar{B}^{\dagger}_{\mathbf{0},q_\perp}\bar{B}_{\mathbf{0},\Sigma}\rangle \end{pmatrix} + \begin{pmatrix} i\,\Delta N_{1s,\mathbf{0}} \\ 0 \end{pmatrix}. \end{aligned} \tag{39}$$

This is now a typical linear equation driven by a known constant source $\Delta N_{1s,\mathbf{0}}$. Since $\mathbf{M}$ contains dephasing, Eq. (39) always evolves toward a steady state, yielding

$$\bar{\Pi}^{X}_{1s,\mathbf{0},q_\perp} = \frac{i\,\Delta N_{1s,\mathbf{0}}\,(\hbar\omega_{\mathbf{0},q_\perp} - \hbar\omega_{\mathrm{cav}})}{\det[\mathbf{M}]}, \tag{40}$$

where $\det[\mathbf{M}] = (E_{1s,\mathbf{0}} - \hbar\omega_{\mathbf{0},q_\perp} - i\gamma_0)(\hbar\omega_{\mathrm{cav}} - \hbar\omega_{\mathbf{0},q_\perp}) - \mathcal{G}^2$. To gain more insight, it is useful to rewrite the determinant via its roots:

$$\begin{aligned} \det[\mathbf{M}] &= \left(\Delta^{\mathrm{cav}}_{\omega} - \Delta_+\right)\left(\Delta^{\mathrm{cav}}_{\omega} - \Delta_-\right), \quad \text{with} \\ \Delta_\pm &= \tfrac{1}{2}\left(\Delta^{\mathrm{cav}}_{1s} + i\gamma_0 \pm \Omega^{\mathrm{cav}}_{1s}\right), \\ \Omega^{\mathrm{cav}}_{1s} &= \sqrt{4\mathcal{G}^2 + \left(\Delta^{\mathrm{cav}}_{1s} + i\gamma_0\right)^2}. \end{aligned} \tag{41}$$

By inserting Eqs. (41) into Eq. (40) and performing a partial-fraction decomposition, we can express $\bar{\Pi}^{X}_{1s,\mathbf{0},q_\perp}$ in terms of two individual Lorentzians,

$$\bar{\Pi}^{X}_{1s,\mathbf{0},q_\perp} = \frac{i\,\Delta N_{1s,\mathbf{0}}}{\Delta_+ - \Delta_-}\left(\frac{\Delta_-}{\Delta^{\mathrm{cav}}_{\omega} - \Delta_-} - \frac{\Delta_+}{\Delta^{\mathrm{cav}}_{\omega} - \Delta_+}\right). \tag{42}$$

We can now evaluate the steady-state photon flux (3) that defines the photoluminescence spectrum,

$$I^{\mathrm{ZPL}}_{\mathrm{PL}}(\omega_{\mathbf{0},q_\perp}) = \frac{2}{\hbar}\left|\mathcal{F}^{1s}_{\mathbf{0},q_\perp}\right|^2 \mathrm{Re}\left[\bar{\Pi}^{X}_{1s,\mathbf{0},q_\perp}\right] = \frac{2}{\hbar}\left|\mathcal{F}^{1s}_{\mathbf{0},q_\perp}\right|^2 \mathrm{Re}\left[\frac{i\,\Delta N_{1s,\mathbf{0}}}{\Delta_+ - \Delta_-}\left(\frac{\Delta_-}{\hbar\omega_{\mathrm{cav}} - \Delta_- - \hbar\omega_{\mathbf{0},q_\perp}} - \frac{\Delta_+}{\hbar\omega_{\mathrm{cav}} - \Delta_+ - \hbar\omega_{\mathbf{0},q_\perp}}\right)\right], \tag{43}$$

after the result (42) is used. We see now that the presence of a cavity splits the emission into two separate normal-mode coupling resonances centered at $\mathrm{Re}[\hbar\omega_{\mathrm{cav}} - \Delta_\pm]$. The corresponding width of the Lorentzians is defined by $\gamma_{0,\pm} = \mathrm{Im}[\Delta_\pm]$. Therefore, Eq. (43) provides an analytic model to study NMC PL.

The complete set including phonons is derived analogously by applying the new operator definitions and approximations several times to Eqs. (20) and (21), respectively. The results for the closed set of equations are presented in Appendix B. These equations will then evolve to a steady state.

B. Steady-state solution for the analytic model

The full analytic model, including PSB effects, is presented in Appendix B. We can apply the same derivation strategy as that which produces Eq. (43). Following this approach, the expression for the PL becomes

$$I_{\mathrm{PL}}(\omega_{\mathbf{0},q_\perp}) = \frac{2}{\hbar}\left|\mathcal{F}^{1s}_{\mathbf{0},q_\perp}\right|^2 \mathrm{Re}\left[\bar{\Pi}^{X,\,\mathrm{ZPL}}_{1s,\mathbf{0},q_\perp} + \bar{\Pi}^{X,\,\mathrm{PSB}}_{1s,\mathbf{0},q_\perp}\right]. \tag{44}$$

The ZPL contribution $\bar{\Pi}^{X,\,\mathrm{ZPL}}_{1s,\mathbf{0},q_\perp}$ is defined by Eq. (42). The corresponding PSB contributions result from

$$\bar{\Pi}^{X,\,\mathrm{PSB}}_{1s,\mathbf{0},q_\perp} = \frac{i[\mathcal{T}_1(\omega_{\mathbf{0},q_\perp}) - \mathcal{T}_2(\omega_{\mathbf{0},q_\perp})]\Delta^{\mathrm{cav}}_{\omega} - \frac{i\,\mathrm{Im}[\mathcal{T}_3] + \mathcal{T}_1(\omega_{\mathrm{cav}})}{\gamma_0}\mathcal{G}^2}{\mathcal{G}^2 - \left(\Delta^{\mathrm{ZPL}}_{\omega,\mathbf{0}} - i\gamma_0\right)\Delta^{\mathrm{cav}}_{\omega}}. \tag{45}$$

These contain the spectral function

$$\mathcal{T}_1(\omega_{\mathbf{0},q_\perp}) = \sum_{\mathbf{p}}\frac{\chi_{\mathbf{p}}}{\Delta^{\mathrm{PSB},-}_{\omega,\mathbf{p}} - i\gamma_1}, \tag{46}$$

with the oscillator strength

$$\begin{aligned} \chi_{\mathbf{p}} &\equiv \sum_{p_\perp}\hbar\Omega\, g^{1s,1s}_{\mathbf{p}_{3\mathrm{D}}}\Delta N_{1s,\mathbf{p}_{3\mathrm{D}}} = \frac{\xi_{\mathbf{p}}}{\hbar\Omega - \frac{\hbar^2\mathbf{p}^2}{2M}}, \\ \xi_{\mathbf{p}} &\equiv \Delta N_{1s,\mathbf{p}}\sum_{p_\perp}\left|\hbar\Omega\, g^{1s,1s}_{\mathbf{p}_{3\mathrm{D}}}\right|^2. \end{aligned} \tag{47}$$

The other spectral functions are

$$\mathcal{T}_2(\omega_{\mathbf{0},q_\perp}) = \frac{\chi_{\mathbf{0}}\left[\Delta_\omega^{\mathrm{cav}} - \hbar\Omega - \mathcal{G}\mathcal{R}\right]}{\mathcal{G}^2 - \left[\Delta_\omega^{\mathrm{cav}} - \hbar\Omega\right]\left[\Delta_{\omega,\mathbf{0}}^{\mathrm{PSB},-} - \mathrm{i}\gamma_1\right]}, \quad (48)$$

$$\mathcal{T}_3 = \chi_{\mathbf{0}}\,\hbar\Omega\,\frac{\Delta_{\omega,\mathbf{0}}^{\mathrm{PSB},+} - \Delta_\omega^{\mathrm{cav}} - \mathrm{i}\gamma_1}{\mathcal{S}_-}, \quad (49)$$

containing quantities

$$\mathcal{R} = \mathcal{G}\hbar\Omega\frac{\Delta_{\omega,\mathbf{0}}^{\mathrm{PSB},-} - \Delta_\omega^{\mathrm{cav}} - \mathrm{i}\gamma_1}{\mathcal{S}_+}, \quad (50)$$

$$S_\pm = \left[\Delta_{\omega,\mathbf{0}}^{\mathrm{PSB},-}\Delta_{\omega,\mathbf{0}}^{\mathrm{PSB},+} + 2\mathcal{G}^2 + \gamma_1^2\right]\hbar\Omega \pm 2\mathrm{i}\gamma_1[\mathcal{G}^2 - \hbar^2\Omega^2], \quad (51)$$

where $S_\pm$ has an analogous structure to Eq. (41).

In the case of the PSB cavity, $\hbar\omega_{\mathrm{cav}}$ is equal to the PSB_1 energy $E_{1s,\mathbf{0}} - \hbar\Omega$. As a result, the detunings (34b) reduce into

$$\Delta_{\omega,\mathbf{0}}^{\mathrm{PSB},-} \to \Delta_\omega^{\mathrm{cav}} \quad \text{and} \quad \Delta_{\omega,\mathbf{0}}^{\mathrm{PSB},+} = 2\hbar\Omega + \Delta_\omega^{\mathrm{cav}} \to 2\hbar\Omega, \quad (52)$$

where the limit applies close to the cavity resonance. Since the phonon energy is relatively large, we may additionally apply $\hbar\Omega \gg \mathcal{G}$, $\hbar\Omega \gg \Delta_\omega^{\mathrm{cav}}$, and $\hbar\Omega \gg \gamma_{\{0,1\}}$. By implementing these limits to Eqs. (45) and (46), and (48)–(51), we find

$$\mathrm{Re}\left[\bar{\Pi}_{1s,\mathbf{0},q_\perp}^{X,\ \mathrm{PSB}}\right] \to \frac{\gamma_1\left[\chi_{\mathbf{0}} + \sum_{\mathbf{p}}\chi_{\mathbf{p}}\right]}{\left(\Delta_\omega^{\mathrm{cav}}\right)^2 + \gamma_1^2}. \quad (53)$$

These results show very clearly that the PSB does not produce a splitting of the PSB resonance. Instead, the cavity enhances the PSB luminescence, which can be applied to increase the visibility of the PSB emission.

C. PL intensity

The fully analytic luminescence formula (44) can directly be applied to deduce the integrated PL. In order to characterize the overall ZPL and PSB luminescence, we integrate the ZPL and the PSB_1 parts of Eq. (44) separately, i.e.,

$$\mathscr{I}_{\{1s,\,\mathrm{ph}\}}^{\{\mathrm{ZPL},\,\mathrm{PSB}\}}(\eta) = \int_{-\infty}^{\infty} I_{\mathrm{PL}}^{\{\mathrm{ZPL},\,\mathrm{PSB}\}}(\omega)\,\mathrm{d}\omega, \quad (54)$$

where $\hbar\omega_{\mathrm{cav}}$ was chosen to coincide with the $1s$ cavity (subindex "$1s$") or the phonon cavity (subindex "ph"). For the mode function, we assume a Lorentzian

$$|u(\omega)|^2 = \frac{\mathcal{E}_0}{\pi}\frac{\eta}{(\hbar\omega - \hbar\omega_{\mathrm{cav}})^2 + \eta^2}, \quad (55)$$

where $\mathcal{E}_0$ is an amplitude with the unit of an energy so that the mode function is unitless, $\hbar\omega_{\mathrm{cav}}$ is again the resonance energy of the cavity mode, and η is the half width at half maximum (HWHM) of the assumed mode function.

In the case of a cavity which is resonant with the zero-phonon line, we find for the integrated ZPL,

$$\mathscr{I}_{1s}^{\mathrm{ZPL}}(\eta) = \frac{\mathcal{E}_0\eta\Delta N_{1s,\mathbf{0}}}{\eta^2 + \gamma_0\eta + \mathcal{G}^2} \to \frac{\mathcal{E}_0\eta}{\mathcal{G}^2}\Delta N_{1s,\mathbf{0}}. \quad (56)$$

This is linearly proportional to the cavity η. The overall NMC PL decreases for enhanced cavity in the $1s$-cavity case.

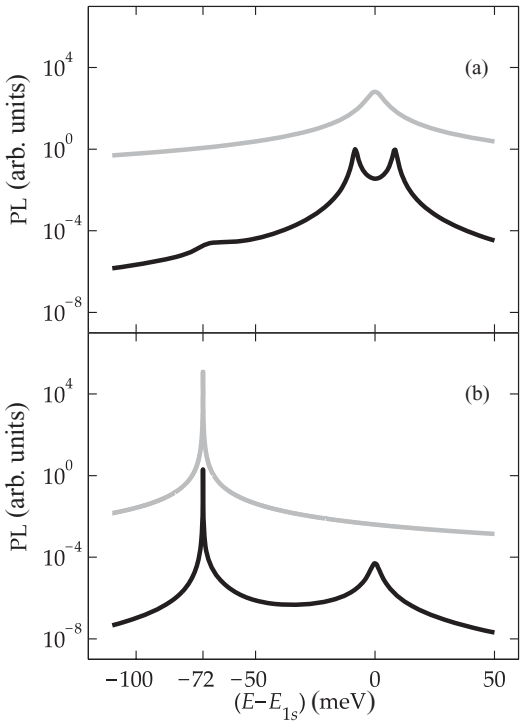

FIG. 5. Microcavity luminescence (black solid line) including the zero-phonon line (ZPL) and the first phonon sideband (PSB_1) calculated via the analytic model. The cavity is resonant with (a) the ZPL or (b) the PSB_1. The corresponding mode function is shown by the gray solid line.

For the phonon cavity, the first sideband PL integrates to

$$\mathscr{I}_{\mathrm{ph}}^{\mathrm{PSB}}(\eta) = \sum_{\mathbf{p}}\frac{\mathcal{E}_0\chi_{\mathbf{p}}[\Delta E_{\mathbf{p}}(\gamma_0+\eta) + (\gamma_1+\eta)\hbar\Omega]}{[(\Delta E_{\mathbf{p}})^2 + (\gamma_1+\eta)^2][(\gamma_0+\eta)^2 + \hbar^2\Omega^2]}, \quad (57)$$

where $\Delta E_{\mathbf{p}} \equiv E_{1s,\mathbf{p}} - E_{1s,\mathbf{0}}$. In the limit of $\eta \to 0$, we find for Eq. (57) that

$$\lim_{\eta\to 0}\mathscr{I}_{\mathrm{ph}}^{\mathrm{PSB}}(\eta) = \sum_{\mathbf{p}}\frac{\mathcal{E}_0\chi_{\mathbf{p}}[\Delta E_{\mathbf{p}}\,\gamma_0 + \gamma_1\hbar\Omega]}{[(\Delta E_{\mathbf{p}})^2 + \gamma_1^2]\hbar^2\Omega^2} \quad (58)$$

saturates to a constant level, unlike Eq. (56). In other words, Eqs. (56) and (58) confirm the numerical result in Fig. 6 that the cavity changes the exciton and the phonon resonance differently when it is tuned into the respective resonances.

To graphically illustrate the analytic result (44), we present in Fig. 5 the corresponding PL spectra for the $1s$ cavity and the phonon cavity. The black solid lines show the PL spectra and the gray solid lines show the corresponding mode function used in the calculation. We see that the results are qualitatively very similar to the full numerical analysis in Fig. 4. In particular, the $1s$ cavity produces a splitting of the PL resonances, whereas the phonon cavity enhances the PL at the sideband.

The analytic model can also be applied to derive the integrated spectra shown in Fig. 6. The yellow solid line represents the intensity of the ZPL photoluminescence using the $1s$ cavity, and the black solid line shows the PSB_1 photoluminescence for the phonon cavity. We see again that

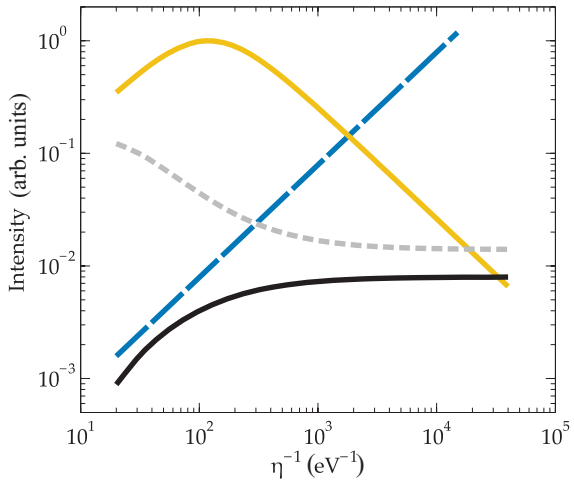

FIG. 6. (Color online) Intensity of the photoluminescence spectrum calculated with the analytic model. The yellow (gray) solid line shows the intensity of the exciton resonance using 1*s* cavity, whereas the intensity of the phonon peak with phonon cavity is represented by the black solid line. The short-dashed line (black) is the total intensity with phonon cavity. The mode function maximum is shown by the long-dashed line (blue). The top x axis indicates the number of DBR mirror pairs which correspond to the mode-function HWHM at the bottom x axis.

the ZPL intensity first increases but then starts decreasing at the point when the exciton resonance splits due to the transition into the nonperturbative regime. The saturation of the PSB_1 intensity for the narrow mode function shown by the black solid line can clearly be seen. The dashed gray line depicts the complete PL intensity using the phonon cavity, showing again that for a high reflectivity, the PSB_1 PL obviously dominates the system. The long-dashed blue line indicates an exponential increase of the mode function maximum. The x axis on the top of the figure shows the appropriate numbers of DBR mirror pairs, as used in the numerical studies, which correspond to the mode function's linewidth η on the bottom x axis.

VI. CONCLUSIONS

In this work, we have presented a microscopic many-body theory to describe phonon-assisted luminescence in a microcavity. In addition to a full numerical evaluation of the phonon-assisted semiconductor luminescence equations, we developed a rigorous analytic model. By introducing the strong-cavity approximation, we are able to find a consistent way to handle the stimulated parts in the semiconductor luminescence equations and formulate a closed analytical formula for the cavity PL. We find that the phonon-sideband luminescence is strongly enhanced if the cavity resonance is shifted to coincide with the first phonon-sideband resonance. With the help of the analytic model, it could be shown that the PL intensity first increases due to the Purcell effect, but then starts decreasing due to the transition into the nonperturbative regime if the cavity is resonant with the zero-phonon line. For a cavity that is resonant with the phonon sideband, the integrated PL saturates, which indicates a qualitative change in the cavity effects.

ACKNOWLEDGMENTS

This work is supported by the Deutsche Forschungsgemeinschaft. In particular, C.B. wants to thank the International Research Training Group 790 *Electron–Electron Interactions in Solids* (Marburg-Budapest) for financial support.

APPENDIX A: EXCITON BASIS

In this work, a generalized exciton basis is used to solve the analytic model as well as Eq. (14). We write the general exciton state ν as

$$|X_{\nu,\mathbf{Q}}\rangle = \sum_{\mathbf{k}} \phi_\nu(\mathbf{k})\, a^\dagger_{\mathrm{c},\,\mathbf{k}+\mathbf{Q}_\mathrm{e}} a_{\mathrm{v},\,\mathbf{k}-\mathbf{Q}_\mathrm{h}} |\mathrm{G}\rangle, \tag{A1}$$

where we introduced the center-of-mass momenta $\mathbf{Q}_{\{\mathrm{e,h}\}} = \frac{m_{\{\mathrm{e,h}\}}}{M}\mathbf{Q}$ and the total mass $M = m_\mathrm{e} + m_\mathrm{h}$ of an electron–hole pair, while the ground state of a semiconductor is characterized by a completely filled valence band and an empty conduction band via $|\mathrm{G}\rangle = \Pi_\mathbf{k} a^\dagger_{\mathrm{v},\,\mathbf{k}} |\mathrm{vac}\rangle$. By minimizing the energy of the carrier system in the low-density regime, the variational principle leads to a Hermitian eigenvalue problem for the *excitonic wave function* $\phi_\nu(\mathbf{k})$, which is represented by the so-called Wannier equation,

$$E_{\nu,\mathbf{Q}}\phi_\nu(\mathbf{k}) = \left(\varepsilon^\mathrm{e}_{\mathbf{k}+\mathbf{Q}_\mathrm{e}} + \varepsilon^\mathrm{h}_{\mathbf{k}-\mathbf{Q}_\mathrm{h}}\right)\phi_\nu(\mathbf{k}) - \sum_{\mathbf{k}'} V_{\mathbf{k}-\mathbf{k}'}\phi_\nu(\mathbf{k}'). \tag{A2}$$

Here, $E_{\nu,\mathbf{Q}} = \mathcal{E}_\nu + \frac{\hbar^2\mathbf{Q}^2}{2M}$ decomposes into the excitonic eigenenergy $\mathcal{E}_\nu$ and the center-of-mass energy of the electron–hole pair. A Fourier transformation into real space leads to the equation of the relative motion of the hydrogen atom. Since the problem is Hermitian, the eigenfunctions build a complete set of orthogonalized functions, which can be used to expand the linearized semiconductor Bloch equations to obtain an Elliott formula as an analytic result.

In the case of nonvanishing densities, the problem becomes non-Hermitian and it is helpful to introduce left- and right-handed eigenfunctions that solve the *excitonic eigenvalue equations*,

$$\begin{aligned} E_{\nu,\mathbf{Q}}\phi^\mathrm{R}_{\nu,\mathbf{Q}}(\mathbf{k}) = {} & \left(\tilde{\varepsilon}^\mathrm{e}_{\mathbf{k}+\mathbf{Q}_\mathrm{e}} + \tilde{\varepsilon}^\mathrm{h}_{\mathbf{k}-\mathbf{Q}_\mathrm{h}}\right)\phi^\mathrm{R}_{\nu,\mathbf{Q}}(\mathbf{k}) \\ & - \left(1 - f^\mathrm{e}_{\mathbf{k}+\mathbf{Q}_\mathrm{e}} - f^\mathrm{h}_{\mathbf{k}-\mathbf{Q}_\mathrm{h}}\right)\sum_{\mathbf{k}'} V_{\mathbf{k}-\mathbf{k}'}\phi^\mathrm{R}_{\nu,\mathbf{Q}}(\mathbf{k}'), \end{aligned} \tag{A3}$$

$$\begin{aligned} \left[\phi^\mathrm{L}_{\nu,\mathbf{Q}}(\mathbf{k})\right]^\star E_{\nu,\mathbf{Q}} = {} & \left[\phi^\mathrm{L}_{\nu,\mathbf{Q}}(\mathbf{k})\right]^\star\left(\tilde{\varepsilon}^\mathrm{e}_{\mathbf{k}+\mathbf{Q}_\mathrm{e}} + \tilde{\varepsilon}^\mathrm{h}_{\mathbf{k}-\mathbf{Q}_\mathrm{h}}\right) \\ & - \sum_{\mathbf{k}'}\left(1 - f^\mathrm{e}_{\mathbf{k}'+\mathbf{Q}_\mathrm{e}} - f^\mathrm{h}_{\mathbf{k}'-\mathbf{Q}_\mathrm{h}}\right)V_{\mathbf{k}-\mathbf{k}'}\phi^\mathrm{L}_{\nu,\mathbf{Q}}(\mathbf{k}'). \end{aligned} \tag{A4}$$

These eigenfunctions obey the *generalized orthogonality and completeness relations*

$$\sum_{\mathbf{k}} \left[\phi^\mathrm{L}_{\nu,\mathbf{Q}}(\mathbf{k})\right]^\star \phi^\mathrm{R}_{\nu',\mathbf{Q}}(\mathbf{k}) = \delta_{\nu,\nu'}, \tag{A5a}$$

$$\sum_{\nu} \left[\phi^\mathrm{L}_{\nu,\mathbf{Q}}(\mathbf{k})\right]^\star \phi^\mathrm{R}_{\nu,\mathbf{Q}}(\mathbf{k}') = \delta_{\mathbf{k},\mathbf{k}'}. \tag{A5b}$$

With this, one can define the *excitonic creation and annihilation operators*

$$X^{\dagger}_{\nu,\mathbf{Q}} = \sum_{\mathbf{k}} \phi^{\mathrm{L}}_{\nu,\mathbf{Q}}(\mathbf{k}) a^{\dagger}_{\mathrm{c},\mathbf{k}+\mathbf{Q}_{\mathrm{e}}} a_{\mathrm{v},\mathbf{k}-\mathbf{Q}_{\mathrm{h}}}, \tag{A6a}$$

$$X_{\nu,\mathbf{Q}} = \sum_{\mathbf{k}} \left[\phi^{\mathrm{L}}_{\nu,\mathbf{Q}}(\mathbf{k})\right]^{\star} a^{\dagger}_{\mathrm{v},\mathbf{k}-\mathbf{Q}_{\mathrm{h}}} a_{\mathrm{c},\mathbf{k}+\mathbf{Q}_{\mathrm{e}}}, \tag{A6b}$$

which can be inverted back to the single-particle basis via

$$a^{\dagger}_{\mathrm{c},\mathbf{k}+\mathbf{Q}_{\mathrm{e}}} a_{\mathrm{v},\mathbf{k}-\mathbf{Q}_{\mathrm{h}}} = \sum_{\nu} \left[\phi^{\mathrm{R}}_{\nu,\mathbf{Q}}(\mathbf{k})\right]^{\star} X^{\dagger}_{\nu,\mathbf{Q}}, \tag{A7a}$$

$$a^{\dagger}_{\mathrm{v},\mathbf{k}-\mathbf{Q}_{\mathrm{h}}} a_{\mathrm{c},\mathbf{k}+\mathbf{Q}_{\mathrm{e}}} = \sum_{\nu} \phi^{\mathrm{R}}_{\nu,\mathbf{Q}}(\mathbf{k})\ X_{\nu,\mathbf{Q}}. \tag{A7b}$$

In the low-density regime, it is justified to replace $\phi^{\{\mathrm{L,R}\}}_{\nu,\mathbf{Q}}(\mathbf{k})$ by $\phi_{\nu}(\mathbf{k})$.

APPENDIX B: ANALYTICAL MODEL

Applying the definitions (24)–(26b), (32), and (33), and the strong-cavity approximation introduced in Eq. (29), to Eqs. (20) and (21), we eventually compute the dynamic equations

$$\begin{aligned}
&\mathrm{i}\hbar\frac{\partial}{\partial t}\begin{pmatrix} \Delta\langle \bar{D}^{\dagger}_{\mathbf{p},\Sigma}\bar{B}^{\dagger}_{\mathbf{0},q_{\perp}}X_{\mathbf{p}}\rangle \\ \Delta\langle \bar{D}^{\dagger}_{\mathbf{0},\Sigma}\bar{B}^{\dagger}_{\mathbf{0},q_{\perp}}\bar{B}^{\dagger}_{\mathbf{0},\Sigma}\rangle \end{pmatrix} \\
&= \begin{pmatrix} \Delta^{\mathrm{PSB},-}_{\omega,\mathbf{p}} - \mathrm{i}\gamma_1 & -\mathrm{i}\,\mathcal{G}\delta_{\mathbf{p},\mathbf{0}} \\ \mathrm{i}\,\mathcal{G} & \Delta^{\mathrm{cav}}_{\omega} - \hbar\Omega \end{pmatrix} \cdot \begin{pmatrix} \Delta\langle \bar{D}^{\dagger}_{\mathbf{p},\Sigma}\bar{B}^{\dagger}_{\mathbf{0},q_{\perp}}X_{\mathbf{p}}\rangle \\ \Delta\langle \bar{D}^{\dagger}_{\mathbf{0},\Sigma}\bar{B}^{\dagger}_{\mathbf{0},q_{\perp}}\bar{B}^{\dagger}_{\mathbf{0},\Sigma}\rangle \end{pmatrix} \\
&\quad + \mathrm{i}\begin{pmatrix} \chi_{\mathbf{p}} \\ \Delta\langle \bar{D}^{\dagger}_{\mathbf{0},\Sigma}\bar{B}_{\mathbf{0},\Sigma}X^{\dagger}_{\mathbf{0}}\rangle \end{pmatrix}.
\end{aligned} \tag{B1}$$

Even though Eqs. (35) and (B1) have a much simpler format than the original equations, they still contain unknown collective contributions on the right-hand side. To solve these, we need to additionally evaluate

$$\begin{aligned}
&\mathrm{i}\hbar\frac{\partial}{\partial t}\Delta\langle \bar{D}^{\dagger}_{\mathbf{0},\Sigma}\bar{B}^{\dagger}_{\mathbf{0},\Sigma}\bar{B}_{\mathbf{0},\Sigma}\rangle \\
&= -\hbar\Omega\Delta\langle \bar{D}^{\dagger}_{\mathbf{0},\Sigma}\bar{B}^{\dagger}_{\mathbf{0},\Sigma}\bar{B}_{\mathbf{0},\Sigma}\rangle \\
&\quad + \mathrm{i}\,\mathcal{G}(\Delta\langle \bar{D}^{\dagger}_{\mathbf{0},\Sigma}\bar{B}_{\mathbf{0},\Sigma}X^{\dagger}_{\mathbf{0}}\rangle + \Delta\langle \bar{D}^{\dagger}_{\mathbf{0},\Sigma}\bar{B}^{\dagger}_{\mathbf{0},\Sigma}X_{\mathbf{0}}\rangle),
\end{aligned} \tag{B2}$$

$$\begin{aligned}
&\mathrm{i}\hbar\frac{\partial}{\partial t}\Delta\langle \bar{D}^{\dagger}_{\mathbf{0},\Sigma}\bar{B}_{\mathbf{0},\Sigma}X^{\dagger}_{\mathbf{0}}\rangle \\
&= [-E_{1s,\mathbf{0}} + \hbar\omega_{\mathrm{cav}} - \hbar\Omega - \mathrm{i}\gamma_1]\Delta\langle \bar{D}^{\dagger}_{\mathbf{0},\Sigma}\bar{B}_{\mathbf{0},\Sigma}X^{\dagger}_{\mathbf{0}}\rangle \\
&\quad + \mathrm{i}\,\mathcal{G}(\chi_{\mathbf{0}} - \Delta\langle \bar{D}^{\dagger}_{\mathbf{0},\Sigma}\bar{B}^{\dagger}_{\mathbf{0},\Sigma}\bar{B}_{\mathbf{0},\Sigma}\rangle),
\end{aligned} \tag{B3}$$

$$\begin{aligned}
&\mathrm{i}\hbar\frac{\partial}{\partial t}\Delta\langle \bar{D}^{\dagger}_{\mathbf{0},\Sigma}\bar{B}^{\dagger}_{\mathbf{0},\Sigma}X_{\mathbf{0}}\rangle \\
&= [E_{1s,\mathbf{0}} - \hbar\omega_{\mathrm{cav}} - \hbar\Omega - \mathrm{i}\gamma_1]\Delta\langle \bar{D}^{\dagger}_{\mathbf{0},\Sigma}\bar{B}^{\dagger}_{\mathbf{0},\Sigma}X_{\mathbf{0}}\rangle \\
&\quad + \mathrm{i}\,\mathcal{G}(\chi_{\mathbf{0}} - \Delta\langle \bar{D}^{\dagger}_{\mathbf{0},\Sigma}\bar{B}^{\dagger}_{\mathbf{0},\Sigma}\bar{B}_{\mathbf{0},\Sigma}\rangle),
\end{aligned} \tag{B4}$$

which are linear equations with damping and source terms that evolve into a steady state.

*christoph.boettge@physik.uni-marburg.de

[1] D. G. Thomas, J. Phys. Chem. Solids **15**, 86 (1960).
[2] A. Ashrafi and C. Jagadish, J. Appl. Phys. **102**, 071101 (2007).
[3] C. F. Klingshirn, Chem. Phys. Chem. **8**, 782 (2007).
[4] H. Morkoç and Ü. Özgür, *Zinc Oxide: Fundamentals, Materials and Device Technology*, 1st ed. (Wiley-VCH Verlag, Weinheim, 2009).
[5] B. K. Meyer, H. Alves, D. M. Hofmann, W. Kriegseis, D. Forster, F. Bertram, J. Christen, A. Hoffmann, M. Straßburg, M. Dworzak, U. Haboeck, and A. V. Rodina, Phys. Status Solidi B **241**, 231 (2004).
[6] U. Ozgur, Y. I. Alivov, C. Liu, A. Teke, M. A. Reshchikov, S. Dogan, V. Avrutin, S.-J. Cho, and H. Morkoc, J. Appl. Phys. **98**, 041301 (2005).
[7] Y. Segawa, H. Sun, T. Makino, M. Kawasaki, and H. Koinuma, Phys. Status Solidi A **192**, 14 (2002).
[8] W. Shan, W. Walukiewicz, J. W. Ager III, K. M. Yu, H. B. Yuan, H. P. Xin, G. Cantwell, and J. J. Song, Appl. Phys. Lett. **86**, 191911 (2005).
[9] W. Y. Liang and A. D. Yoffe, Phys. Rev. Lett. **20**, 59 (1968).
[10] S. J. Xu, S.-J. Xiong, and S. L. Shi, J. Chem. Phys. **123**, 221105 (2005).
[11] T. Feldtmann, M. Kira, and S. W. Koch, Phys. Status Solidi B **246**, 332 (2009).
[12] C. F. Klingshirn, Phys. Status Solidi B **202**, 1521 (1997).
[13] L. Li, H. Yang, G. Qi, J. Ma, X. Xie, H. Zhao, and F. Gao, Chem. Phys. Lett. **455**, 93 (2008).
[14] S. Ramanathan, S. Bandyopadhyay, L. K. Hussey, and M. Munoz, Appl. Phys. Lett. **89**, 143121 (2006).
[15] H. Zhao, S. Moehl, and H. Kalt, Appl. Phys. Lett. **81**, 2794 (2002).
[16] R. Kuhnert and R. Helbig, J. Lumin. **26**, 203 (1981).
[17] T. Feldtmann, M. Kira, and S. W. Koch, J. Lumin. **130**, 107 (2010).
[18] X. B. Zhang, T. Taliercio, S. Kolliakos, and P. Lefebvre, J. Phys. Condens. Matter **13**, 7053 (2001).
[19] M. Kozhevnikov, B. M. Ashkinadze, E. Cohen, and A. Ron, Solid State Commun. **106**, 73 (1998).
[20] M. Soltani, M. Certier, R. Evrard, and E. Kartheuser, J. Appl. Phys. **78**, 5626 (1995).
[21] L. T. Tan, R. W. Martin, K. P. O'Donnell, and I. M. Watson, Appl. Phys. Lett. **89**, 101910 (2006).
[22] E. M. Purcell, Phys. Rev. **69**, 681 (1946).
[23] E. Yablonovitch, Phys. Rev. Lett. **58**, 2059 (1987).
[24] C. Weisbuch, M. Nishioka, A. Ishikawa, and Y. Arakawa, Phys. Rev. Lett. **69**, 3314 (1992).
[25] G. Khitrova, H. M. Gibbs, F. Jahnke, M. Kira, and S. W. Koch, Rev. Mod. Phys. **71**, 1591 (1999).
[26] F. Jahnke, M. Kira, S. W. Koch, G. Khitrova, E. K. Lindmark, T. R. Nelson Jr., D. V. Wick, J. D. Berger, O. Lyngnes, H. M. Gibbs, and K. Tai, Phys. Rev. Lett. **77**, 5257 (1996).

[27]M. Kira, F. Jahnke, W. Hoyer, and S. W. Koch, Prog. Quantum Electron. **23**, 189 (1999).
[28]M. Kira, F. Jahnke, and S. W. Koch, Phys. Rev. Lett. **81**, 3263 (1998).
[29]M. Kira and S. W. Koch, Prog. Quantum Electron. **30**, 155 (2006).
[30]H. Haug and S. W. Koch, *Quantum Theory of the Optical and Electronic Properties of Semiconductors*, 5th ed. (World Scientific, Singapore, 2009).
[31]M. Kira and S. W. Koch, Phys. Rev. A **78**, 022102 (2008).
[32]J. Čížek, J. Chem. Phys. **45**, 4256 (1966).
[33]G. D. Purvis III and R. J. Bartlett, J. Chem. Phys. **76**, 1910 (1982).
[34]J. Fricke, Ann. Phys. (NY) **252**, 479 (1996).
[35]H. W. Wyld Jr. and B. D. Fried, Ann. Phys. (NY) **23**, 374 (1963).
[36]T. Feldtmann, Ph.D. thesis, Fachbereich Physik, Philipps-Universität Marburg, 2009.
[37]H. Fröhlich, Adv. Phys. **3**, 325 (1954).
[38]H. Fröhlich, Proc. R. Soc. London **215**, 291 (1952).
[39]H. Haken, *Quantenfeldtheorie des Festkörpers* (Teubner, Stuttgart, 1973).
[40]I. V. Bondarev, S. A. Maksimenko, G. Y. Slepyan, I. L. Krestnikov, and A. Hoffmann, Phys. Rev. B **68**, 073310 (2003).
[41]D. Braun, W. W. Rühle, C. Trallero-Giner, and J. Collet, Phys. Rev. Lett. **67**, 2335 (1991).
[42]W. A. Harrison, Phys. Rev. **104**, 1281 (1956).
[43]G. Coli and K. K. Bajaj, Appl. Phys. Lett. **78**, 2861 (2001).
[44]C. F. Klingshirn, Phys. Status Solidi B **244**, 3027 (2007).
[45]A. A. Serdobintsev, E. I. Burylin, A. G. Veselov, O. A. Kiryasova, and A. S. Dzhumaliev, Tech. Phys. **53**, 368 (2008).
[46]C. W. Teng, J. F. Muth, Ü. Özgür, M. J. Bergmann, H. O. Everitt, A. K. Sharma, C. Jin, and J. Narayan, Appl. Phys. Lett. **76**, 979 (2000).
[47]N. B. Chen, H. Z. Wu, D. J. Qiu, T. N. Xu, J. Chen, and W. Z. Shen, J. Phys. Condens. Matter **16**, 2973 (2004).
[48]R. Schmidt, B. Rheinländer, M. Schubert, D. Spemann, T. Butz, J. Lenzner, E. M. Kaidashev, M. Lorenz, A. Rahm, H. C. Semmelhack, and M. Grundmann, Appl. Phys. Lett. **82**, 2260 (2003).
[49]W. von Sellmeier, Ann. Phys. (Leipzig) **143**, 272 (1871).
[50]S. Chatterjee, C. Ell, S. Mosor, G. Khitrova, H. M. Gibbs, W. Hoyer, M. Kira, S. W. Koch, J. P. Prineas, and H. Stolz, Phys. Rev. Lett. **92**, 067402 (2004).

PAPER V

C. N. Böttge, B. Breddermann, L. Schneebeli, M. Kira, S. W. Koch,
J. Bhattacharyya, H. Schneider, and M. Helm

Terahertz-induced effects on excitons in magnetic field

Phys. Status Solidi C **10**, 1218–1221 (2013)

DOI: 10.1002/pssc.201200702

The Inner Horizon XI

See page XLIV for reference.

Phys. Status Solidi C **10**, No. 9, 1218–1221 (2013) / **DOI** 10.1002/pssc.201200702

physica status solidi c
www.pss-c.com
current topics in solid state physics

Terahertz-induced effects on excitons in magnetic field

C. N. Böttge[*,1], B. Breddermann[1], L. Schneebeli[1], M. Kira[1], S. W. Koch[1], J. Bhattacharyya[2], H. Schneider[2], and M. Helm[2]

[1] Department of Physics and Material Sciences Center, Philipps-University of Marburg, Renthof 5, 35032 Marburg, Germany
[2] Helmholtz-Zentrum Dresden-Rossendorf e.V., Institute of Ion Beam Physics and Materials Research, 01314 Dresden, Germany

Received 14 September 2012, accepted 11 March 2013
Published online 5 June 2013

Keywords magnetoexcitons, terahertz spectroscopy

[*] Corresponding author: e-mail Christoph.Boettge@physik.uni-marburg.de, Phone: +49-6421-28-24217, Fax: +49-6421-28-27076

Terahertz-induced intra-exciton transitions are studied in semiconductor quantum-well systems under the influence of a constant magnetic field. A systematic description is developed to include carrier–carrier interactions, terahertz transitions, and magnetic-field effects to the exciton-correlation dynamics.

When a magnetic field is present, the exciton states and energies are changed directly and parametrically via the center-of-mass momentum of excitons. The numerical results show that both effects influence the terahertz spectroscopy. Especially, the transition between $1s$- and $2p$-exciton states is shown to depend strongly on both magnetic field and center-of-mass momentum.

1 Introduction Recent investigations have provided abundant evidence [1–5] that terahertz (THz) fields can efficiently induce transitions between exciton states within semiconductors. Since the energetic range of THz fields ($1\,\mathrm{THz} \simeq 4\,\mathrm{meV}$) is three orders of magnitude smaller than the usual band-gap energies, a typical THz excitation cannot generate interband transitions [6]. However, such THz fields can induce modifications of the collective intraband excitations in semiconductors, which can significantly alter the optical properties [1,7–9].

While the binding energy of an exciton is a measure for the strength of the Coulomb interaction, its response to internal and external fields reveals facts about polarizability. Therefore, it is an interesting challenge to investigate how a magnetic field effects on excitons. When the magnetic field is strong, electronic states become strongly confined [10,11], allowing for investigations of the transition from systems without magnetic field to substantial confinement effects. At the limit of strong magnetic field, the eigenenergies are energetically equally spaced Landau orbitals. However, including the Coulomb interaction leads to the generation of so-called magnetoexcitons showing the well-known Zeeman splitting [12].

In this paper, we investigate how exciton and THz-induced intra-exciton transitions can be modified by applying an external magnetic field. For this purpose, we expand the theoretical description of Ref. [13] rigorously by fully including linear and nonlinear magnetic-field contributions to the total-system Hamiltonian. We show, both numerically and analytically, that these modifications change the exciton states, exciton-correlation dynamics, as well as the THz-transitions.

2 Theory Constant magnetic field $\boldsymbol{B}$ and THz field $\boldsymbol{E}_{\mathrm{THz}}$ can be simultaneously described through a common vector potential $\boldsymbol{A} = \boldsymbol{A}_{\mathrm{THz}} + \boldsymbol{A}_0$. More specifically, the THz field is transversal and we use its Coulomb-gauge form [14] $\boldsymbol{E}_{\mathrm{THz}} = -\frac{\partial}{\partial t}\boldsymbol{A}_{\mathrm{THz}}$. The magnetic field is presented using the symmetric gauge [15] $\boldsymbol{A}_0 = \frac{1}{2}\boldsymbol{B} \times \boldsymbol{r}$ defining $\boldsymbol{B} = \nabla \times \boldsymbol{A}_0$. We analyze here a situation where $\boldsymbol{B}$ is perpendicular to the quantum well (QW) that is in the x–y plane, i.e., $\boldsymbol{B} = B\boldsymbol{e}_z$.

The THz and magnetic-field effects enter only the kinetic-energy part of the system Hamiltonian where one implements the minimal substitution $\hat{\boldsymbol{p}} \to \hat{\boldsymbol{p}} + |e|\boldsymbol{A}$ for the momentum operator $\hat{\boldsymbol{p}}$. The elementary charge of elec-

trons is given by $-|e|$. The general system Hamiltonian $\hat{H}$ of the semiconductor system is presented, e.g., in Refs. [14, 13]. Besides $\boldsymbol{A}_{\mathrm{THz}}$ and $\boldsymbol{A}_0$ effects, it includes the lattice-periodic potential (producing the band structure), coupling to optical field, and the Coulomb- as well as the phonon-interaction effects. We analyze here a strongly confined QW where the many-body and THz excitations involve electrons only in one conduction and one valence band.

Under suitable conditions [16, 17], electrons in the conduction band and vacancies in the valence band, i.e., holes, form Coulomb-bound pairs, called the excitons. In many-body sense, excitons are two-particle correlations [13, 14]

$$c_{\mathrm{X}}^{\boldsymbol{Q},\boldsymbol{k}',\boldsymbol{k}} = \sum_{\lambda,\nu} \phi_{\lambda}^{\star}(\boldsymbol{k})\phi_{\nu}(\boldsymbol{k}')\,\Delta N_{\lambda,\nu,\boldsymbol{Q}} \tag{1}$$

where $\phi_{\nu}(\boldsymbol{k})$ is the exciton wavefunction of state ν, $\boldsymbol{k}$ is the relative-motion momentum, and $\boldsymbol{Q}$ is the center-of-mass (COM) momentum. The exciton populations are described by the diagonal elements $\Delta N_{\lambda,\lambda,\boldsymbol{Q}}$ while the off-diagonal elements describe both exciton-transition amplitudes and correlated electron–hole plasma.

The quantum-kinetics of $c_{\mathrm{X}}^{\boldsymbol{Q},\boldsymbol{k}',\boldsymbol{k}}$ is already derived in Ref. [13] and we only analyze here how the magnetic field modifies the THz-induced exciton transitions. More specifically, we start from the full quantum kinetics [13, 14] at the low-density limit:

$$\begin{aligned}\mathrm{i}\hbar\frac{\partial}{\partial t}\, c_{\mathrm{X}}^{\boldsymbol{Q},\boldsymbol{k}',\boldsymbol{k}} &= \left(\epsilon_{\boldsymbol{Q},\boldsymbol{k}',\boldsymbol{k}}(B) - \boldsymbol{j}_{\boldsymbol{k}'-\boldsymbol{k}}\cdot\boldsymbol{A}_{\mathrm{THz}}\right) c_{\mathrm{X}}^{\boldsymbol{Q},\boldsymbol{k}',\boldsymbol{k}} \\ &+ \sum_{\boldsymbol{k}''}\left(V_{\boldsymbol{k}''-\boldsymbol{k}}\, c_{\mathrm{X}}^{\boldsymbol{Q},\boldsymbol{k}',\boldsymbol{k}''} - V_{\boldsymbol{k}''-\boldsymbol{k}'}\, c_{\mathrm{X}}^{\boldsymbol{Q},\boldsymbol{k}'',\boldsymbol{k}}\right) \\ &+ S_{\mathrm{X}}^{\boldsymbol{Q},\boldsymbol{k}',\boldsymbol{k}} + T_{\mathrm{X}}^{\boldsymbol{Q},\boldsymbol{k}',\boldsymbol{k}}\end{aligned} \tag{2}$$

where $\epsilon_{\boldsymbol{Q},\boldsymbol{k}',\boldsymbol{k}}(B)$ includes the kinetic energy of electron–hole pairs, including the B-field effects due to the minimal substitution discussed above. The THz coupling is defined by the current-matrix element $\boldsymbol{j}_{\boldsymbol{k}} = -|e|\,\hbar\boldsymbol{k}/\mu$ where $\mu^{-1} = m_{\mathrm{e}}^{-1} + m_{\mathrm{h}}^{-1}$ is the reduced mass and m_{e} (m_{h}) is the effective electron (hole) mass [18]. The excitons follow from the so-called main-sum terms [13] that include the dominant Coulomb terms containing the Coulomb-matrix element $V_{\boldsymbol{k}}$. The single-particle source $S_{\mathrm{X}}^{\boldsymbol{Q},\boldsymbol{k}',\boldsymbol{k}}$ and the three-particle scattering terms $T_{\mathrm{X}}^{\boldsymbol{Q},\boldsymbol{k}',\boldsymbol{k}}$ are included here only symbolically because they are responsible for exciton formation and scattering effects, respectively. When exciton populations are strong, the contribution of the single-particle source to THz transitions is negligible [13]. The presented structure fully describes both THz- and magnetic-field effects at the low-density limit.

We analyze the magnetic-field effects where all excitations exist close to the Γ point. In this situation, the magnetic-field effects follow from the effective-mass approximation [19]. The homogeneous part of Eq. (2) then yields a generalized Wannier equation $\hat{H}\phi_{\lambda}(\boldsymbol{r}) = E_{\lambda}\,\phi_{\lambda}(\boldsymbol{r})$ where the Hamiltonian

$$\begin{aligned}\hat{H} = &\frac{\boldsymbol{p}_{\mathrm{e}}^2}{2m_{\mathrm{e}}} + \frac{\boldsymbol{p}_{\mathrm{h}}^2}{2m_{\mathrm{h}}} + |e|\left[\frac{\boldsymbol{A}(\boldsymbol{r}_{\mathrm{e}})\cdot\boldsymbol{p}_{\mathrm{e}}}{m_{\mathrm{e}}} - \frac{\boldsymbol{A}(\boldsymbol{r}_{\mathrm{h}})\cdot\boldsymbol{p}_{\mathrm{h}}}{m_{\mathrm{h}}}\right] \\ &+ \frac{e^2\boldsymbol{A}^2(\boldsymbol{r}_{\mathrm{e}})}{2m_{\mathrm{e}}} + \frac{e^2\boldsymbol{A}^2(\boldsymbol{r}_{\mathrm{h}})}{2m_{\mathrm{h}}} - V(\boldsymbol{r}_{\mathrm{e}} - \boldsymbol{r}_{\mathrm{h}})\end{aligned} \tag{3}$$

defines a two-body problem that is presented here in the real space; its Fourier transformation produces an integral equation for $\phi_{\lambda}(\boldsymbol{k})$. The Coulomb interaction is then $V(\boldsymbol{r}) = \frac{e^2}{4\pi\varepsilon_0\epsilon_{\mathrm{r}}|\boldsymbol{r}|}$ where ϵ_{r} is the relative permittivity. Since both electron and hole can move, Eq. (3) must be solved as a genuine two-body problem.

We start by converting Eq. (3) to relative and COM coordinates via $\boldsymbol{r} = \boldsymbol{r}_{\mathrm{e}} - \boldsymbol{r}_{\mathrm{h}}$ and $\boldsymbol{R} = \frac{m_{\mathrm{e}}}{M}\boldsymbol{r}_{\mathrm{e}} + \frac{m_{\mathrm{h}}}{M}\boldsymbol{r}_{\mathrm{h}}$ producing

$$\begin{aligned}\hat{H} = &-\frac{\hbar^2}{2M}\nabla_{\boldsymbol{R}}^2 - \frac{\hbar^2}{2\mu}\nabla_{\boldsymbol{r}}^2 - V(\boldsymbol{r}) \\ &- \mathrm{i}\hbar\left(\bar{\boldsymbol{\omega}}_{\mu}\cdot[\,\boldsymbol{R}\times\nabla_{\boldsymbol{r}}] + \bar{\boldsymbol{\omega}}_{M}\cdot[\,\boldsymbol{r}\times\nabla_{\boldsymbol{R}}]\right) \\ &- \mathrm{i}\hbar\tfrac{\bar{\boldsymbol{\omega}}_{\mathrm{e}}-\bar{\boldsymbol{\omega}}_{\mathrm{h}}}{2}\cdot[\,\boldsymbol{r}\times\nabla_{\boldsymbol{r}}] \\ &+ \tfrac{1}{2}\mu\bar{\boldsymbol{\omega}}_{\mu}^2(\boldsymbol{R}_{\parallel} + \boldsymbol{r}_{\parallel})^2 - \tfrac{3}{2}\mu\bar{\boldsymbol{\omega}}_{\mu}^2\tfrac{\mu}{M}\boldsymbol{r}_{\parallel}^2 \\ &- \tfrac{m_{\mathrm{h}}}{2}\,(\bar{\boldsymbol{\omega}}_{\mathrm{e}}\cdot\bar{\boldsymbol{\omega}}_{\mathrm{h}})(\boldsymbol{R}_{\parallel}\cdot\boldsymbol{r}_{\parallel})\end{aligned} \tag{4}$$

where we defined the following effective cyclotron frequencies: $\bar{\boldsymbol{\omega}}_{\mu} \equiv \frac{|e|\boldsymbol{B}}{2\mu}$, $\bar{\boldsymbol{\omega}}_{M} \equiv \frac{|e|\boldsymbol{B}}{2M}$ with total mass $M = m_{\mathrm{e}} + m_{\mathrm{h}}$, $\bar{\boldsymbol{\omega}}_{\mathrm{e}} = \frac{|e|\boldsymbol{B}}{m_{\mathrm{e}}}$, and $\bar{\boldsymbol{\omega}}_{\mathrm{h}} = \frac{|e|\boldsymbol{B}}{m_{\mathrm{h}}}$. This form corresponds to the Hamiltonian used by Schmitt-Rink *et al.* [20]. We see that the eigenvalue problem of Hamiltonian (4) cannot be solved with a simple separation of $\boldsymbol{r}$ and $\boldsymbol{R}$.

To solve this problem, we apply $\hat{H}' = \hat{U}\,\hat{H}\,\hat{U}^{\dagger}$ to the Hamiltonian (4) with the generalized Göppert-Mayer transformation [14,21] $\hat{U} = \exp\left[\frac{\mathrm{i}}{\hbar}|e|\,\boldsymbol{r}\cdot\boldsymbol{A}_0(\boldsymbol{R})\right]$, yielding

$$\begin{aligned}\hat{H}' = &\frac{\hat{\boldsymbol{p}}^2}{2\mu} + \frac{\hat{\boldsymbol{P}}^2}{2M} - V(\boldsymbol{r}) + \tfrac{\mu}{2}\bar{\boldsymbol{\omega}}_{\mu}^2\,\boldsymbol{r}_{\parallel}^2 \\ &+ \tfrac{|\bar{\boldsymbol{\omega}}_{\mathrm{e}}|-|\bar{\boldsymbol{\omega}}_{\mathrm{h}}|}{2}\hat{L}_z + \bar{\boldsymbol{\omega}}_{M}\cdot(\boldsymbol{r}\times\hat{\boldsymbol{P}})\end{aligned} \tag{5}$$

where $\boldsymbol{r}_{\parallel}$ is the in-plane component of $\boldsymbol{r}$ and $\hat{L}_z \equiv \boldsymbol{e}_z\cdot[\boldsymbol{r}\times\hat{\boldsymbol{p}}] = -\mathrm{i}\hbar\frac{\partial}{\partial\varphi}$ is the z component of the angular momentum defined with respect to the relative motion. The transformed Hamiltonian (5) corresponds to the model used by Nickel *et al.* [22] and its relative and COM coordinates are now separable because no mixed terms, between $\boldsymbol{r}$ and $\boldsymbol{R}$, appear anymore.

We may now seek the solution of the exciton problem $\hat{H}'\phi_{\lambda}(\boldsymbol{r},\boldsymbol{R}) = E_{\lambda}\,\phi_{\lambda}(\boldsymbol{r},\boldsymbol{R})$ with an ansatz $\phi_{\lambda}(\boldsymbol{r},\boldsymbol{R}) = \phi_{\lambda,\boldsymbol{Q}}(\boldsymbol{r})\,\mathrm{e}^{\mathrm{i}\boldsymbol{Q}\cdot\boldsymbol{R}}$ where the plane-wave part corresponds to the COM motion of the exciton. Analogously to the hydrogen problem [15], $\hat{L}_z$ commutes with $\hat{H}'$ such that it is beneficial to represent λ with the usual principal (n) and magnetic quantum number (m). As the main differences to the usual hydrogen problem, $\phi_{\lambda,\boldsymbol{Q}}$ depends parametrically on the COM-$\boldsymbol{Q}$ and the magnetic field lifts the degeneracy between the different m-quantum number states.

To understand the interplay of Coulomb and magnetic-field effects on excitons, one can combine the Coulomb and the harmonic-potential terms of Hamiltonian (5) into an effective potential

$$V_{\rm eff}(\boldsymbol{r}) = -V(\boldsymbol{r}) + \tfrac{\mu}{2}\bar{\omega}_\mu^2\, \boldsymbol{r}_\parallel^2 \,. \tag{6}$$

Without the magnetic field ($\bar{\boldsymbol{\omega}}_\mu \to \boldsymbol{0}$), $V_{\rm eff}(\boldsymbol{r})$ contains only the Coulomb attraction such that the eigenstates are the usual quantum-confined hydrogen states, cf. Ref. [14] for explicit examples. In this situation, the ground state is defined by the $1s$ ($n=1, m=0$) solution and the nearest excited states are defined by $2s$ ($n=2, m=0$) and $2p$ ($n=1, m=\pm1$). For a finite QW thickness, the $2s$ and $2p$ states are nearly degenerate. At the limit of dominating B-field, potential (6) produces the solutions of the harmonic oscillator. In the full problem, the Coulomb and B-field effects are mixed and the COM-$\boldsymbol{Q}$ alters further the solutions. For example, the $\hat{L}_z$ contribution within Eq. (5) shifts the $2p$-state energy by $\pm\hbar\frac{|\bar{\omega}_{\rm e}|-|\bar{\omega}_{\rm h}|}{2}$ for $m=\pm1$, which removes the degeneracy between the $2p_-$ ($m=-1$) and $2p_+$ ($m=+1$) states. The COM-$\boldsymbol{Q}$ produces an additional linear potential $\hbar\bar{\boldsymbol{\omega}}_M\cdot(\boldsymbol{r}\times\boldsymbol{Q})$ that essentially moves the center of the harmonic potential within $V_{\rm eff}(\boldsymbol{r})$.

To fully include these combined effects, we solve the eigenstates $\phi_{\lambda,\boldsymbol{Q}}(\boldsymbol{k})$ of Eq. (5) numerically in the $\boldsymbol{k}$ space. These can be then used to convert exciton-correlation dynamics (2) into the exciton basis:

$$\begin{aligned} \mathrm{i}\hbar\frac{\partial}{\partial t}\Delta N_{\lambda,\nu,\boldsymbol{Q}} = {} & [E_{\nu,\boldsymbol{Q}} - E_{\lambda,\boldsymbol{Q}} - \mathrm{i}\gamma(1-\delta_{\lambda,\nu})]\,\Delta N_{\lambda,\nu,\boldsymbol{Q}} \\ & + \sum_\beta [\boldsymbol{J}_{\lambda,\beta,\boldsymbol{Q}}\,\Delta N_{\beta,\nu,\boldsymbol{Q}} \\ & - \boldsymbol{J}_{\nu,\beta,\boldsymbol{Q}}\,\Delta N_{\lambda,\beta,\boldsymbol{Q}}]\cdot\boldsymbol{A}_{\rm THz} \end{aligned} \tag{7}$$

where we have simplified the three-particle scattering terms by a constant dephasing γ. The THz coupling follows from the transition-matrix element $\boldsymbol{J}_{\lambda,\nu,\boldsymbol{Q}} \equiv \sum_{\boldsymbol{k}} \phi^\star_{\lambda,\boldsymbol{Q}}(\boldsymbol{k})\,\boldsymbol{j}_{\boldsymbol{k}}\,\phi_{\nu,\boldsymbol{Q}}(\boldsymbol{k})$ and the total density of exciton correlations. We solve this numerically for a configuration where the system contains initially only $1s$ excitons while the THz field is applied to excite the system.

3 Results The derivations in Sec. 2 show that the electron–hole relative motion is significantly modified by the magnetic field because it generates new contributions to the Hamiltonian (5) that may dominate the exciton eigensystem. In addition, the COM motion of excitons influences parametrically the exciton energies and states. As the main effect, the degeneracy of $2p$ states is removed once the magnetic-field strength is increased.

The influence of magnetic field and COM motion is analyzed in Fig. 1 where we plot the computed eigenenergies for $E_{1s,\boldsymbol{Q}}$ (black line), $E_{2p_-,\boldsymbol{Q}}$ (thin orange line), and $E_{2p_+,\boldsymbol{Q}}$ (thick orange line). The vertical arrows indicate possible THz transitions. We have removed the trivial $\frac{\hbar^2\boldsymbol{Q}^2}{2M}$ dependence from these energies because it does not effect the energy differences observed by the THz transitions. Especially, this procedure removes the COM-$\boldsymbol{Q}$ dependence from the $1s$ state as expected based on Eq. (5).

However, the $2p_\pm$ states change significantly as we compare $\boldsymbol{Q}=\boldsymbol{0}\equiv\boldsymbol{Q}_0$ (solid lines) with $|\boldsymbol{Q}| = {}^2\!/_{a_0} \equiv \boldsymbol{Q}_2$ (dashed lines) where a_0 ist the Bohr radius of the exciton. In addition, we see that there is a clear energy splitting between $E_{2p_-,\boldsymbol{Q}}$ and $E_{2p_+,\boldsymbol{Q}}$ and that the splitting is asymmetric. More specifically, the $2p_+$ energy shifts much more from its zero-field value than the $2p_-$ state does. This follows from the interplay of kinetic energy and the $\hat{L}_z$ contribution within Eq. (5): Concerning the magnetic quantum number m, the kinetic energy contains a sign-independent m^2 part while $\hat{L}_z$ yields a sign-dependent $\pm\hbar m$ contribution. As these two contributions are combined, one finds an asymmetry between the $+|m|$ and the $-|m|$ solutions.

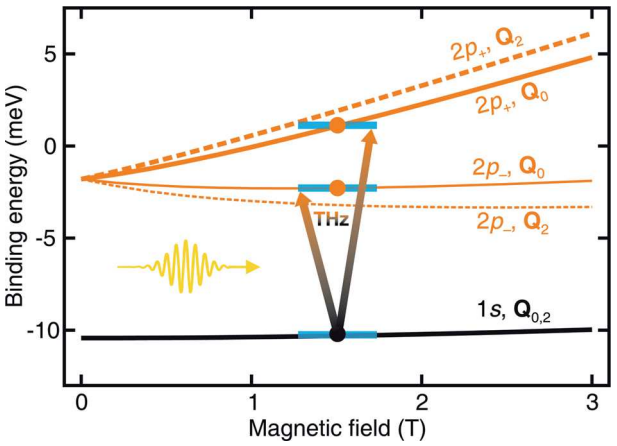

Figure 1 Shift of the $1s$ (black), $2p_-$ (thin orange), and $2p_+$ (thick orange) eigenenergies as function of magnetic-field for $\boldsymbol{Q}=\boldsymbol{0}$ ($\boldsymbol{Q}_0$, solid) and $|\boldsymbol{Q}| = {}^2\!/_{a_0}$ ($\boldsymbol{Q}_2$, dashed) at zero density. The incoming THz pulse (yellow) couples the $1s$ state to the $2p_\pm$ states (gradient-colored arrows, shown here for $\boldsymbol{Q}_0$).

Even though excitonic resonances in optical absorption spectrum originate exclusively from excitons with a vanishing COM momentum, this is not the case for THz-induced transitions because they involve $E_{1s,\boldsymbol{Q}}$ to $E_{2p_\pm,\boldsymbol{Q}}$ transitions with *all* COM-$\boldsymbol{Q}$ [23]. The specific wavefunctions involved determine the transition-matrix element $\boldsymbol{J}_{\lambda,\nu,\boldsymbol{Q}}$ [13] such that it is interesting to see how they are changed by the magnetic field and COM contributions. The left panel of Fig. 2 compares the $1s$ and $2p$ wavefunctions for $B=0\,\mathrm{T}$ (shaded area), $B=3\,\mathrm{T}$ ($\boldsymbol{Q}_0$, solid line) and ($\boldsymbol{Q}_2$, dashed line). In Fig. 2a, we see that the $1s$ state is hardly changed by the magnetic field indicating that the Coulomb effects outweigh the magnetic-field influence. Thus, the $1s$ wavefunction only slightly deviates for the magnetic fields investigated here. For p-like states, however, a magnetic field alters the wavefunction remarkably by concentrating it towards the origin, cf. Fig. 2b. This

confinement caused by the magnetic field is slightly diminished by a finite COM-$\boldsymbol{Q}$ as this leads to the additional linear potential, increasing the probability of finding the exciton at positions $\boldsymbol{r_Q} > \boldsymbol{r_0}$.

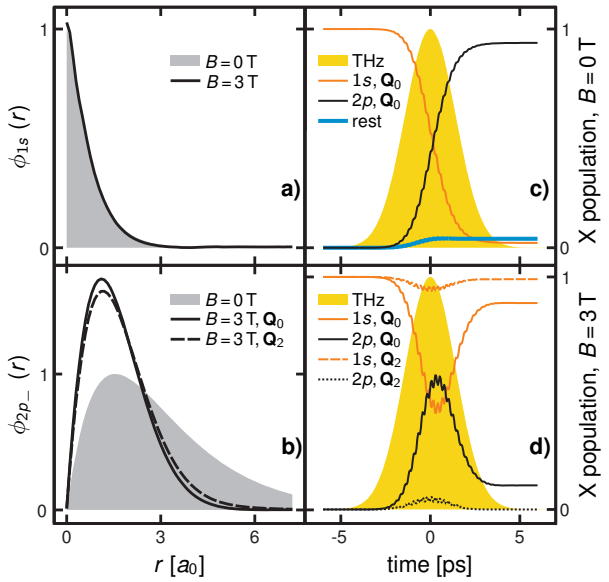

Figure 2 Left panel: Change of a) the $1s$ and b) the $2p_-$ wavefunction in dependence of magnetic field and COM momentum. Vanishing B-field (shaded) is compared to $B = 3\,\mathrm{T}$ for $\boldsymbol{Q}_0$ (solid). In frame b), the $2p_-$ wavefunction is slightly changed by the COM-$\boldsymbol{Q}$ (dashed). Right panel: $1s$- (orange), $2p_-$- (black), and higher-order (blue) carrier populations for c) $B = 0\,\mathrm{T}$ and d) $B = 3\,\mathrm{T}$. Only the lower $2p$ branch is taken into account here. The THz pulse is shown as shaded area.

To determine how the magnetic-field and COM effects influence the exciton dynamics, we analyze next how a THz pulse excites exciton correlations that initially occupy only the $1s$-exciton state. More specifically, we solve Eq. (7) numerically when a 3.3 ps long THz pulse is set to be resonant with the $1s$-to-$2p$ energy at 0 T. Figure 2c shows the THz pulse (shaded area), the $1s$ (orange line) as well as the $2p$ population (black line), and a population sum of all remaining exciton states (blue line); these 0 T computations are $\boldsymbol{Q}$ independent.

During the THz pulse, the $1s$ population decreases rapidly while the $2p$ population increases and the population transfer is nearly perfect after the pulse, indicating that the THz excitation is essentially a π pulse. In this situation, only a very small fraction of excitons go beyond the $1s$–$2p$ states such that we find a behavior analogous to a pure two-level system. Besides the usual state transfer in a two-level system [14], the populations show some wiggles due to the breakdown of the rotating-wave approximation; similar effects have been experimentally observed in Ref. [24].

A 3 T magnetic field is switched on in the computations of Fig. 2d where the state transfer of $\boldsymbol{Q}_0 = \boldsymbol{0}$ (solid lines) and $\boldsymbol{Q}_2 = {}^{2}/_{a_0}$ (dashed line) excitons is followed; the line colors and the THz pulse are otherwise the same as in Fig. 2c. We see that the magnetic field changes the state transfer dramatically; this decrease is particularly large for the moving $\boldsymbol{Q}_2$ excitons. This reduction is mainly explained by the magnetic-field induced $1s$–$2p_-$ detuning that is $0.55\,\mathrm{meV}$ for $\boldsymbol{Q}_0$ and $1.96\,\mathrm{meV}$ for $\boldsymbol{Q}_2$. Due to the large detuning, the upper branch, $2p_+$, is virtually not occupied (not shown).

4 Conclusion The electron–hole relative motion is significantly modified by an external magnetic field. As a main effect, the degeneracy of the $2p$ states is removed. This allows us to trace the $1s$–$2p_\pm$-population transfer for different configurations of the exciton states and eigenfunctions. The inclusion of center-of-mass momenta is of significant importance in the context of THz-induced population transfer leading to noticeable changes of the carrier populations. Therefore, the combination of optical pump and THz probe in connection with a magnetic field is a very sensitive spectroscopic tool to investigate correlated many-body systems.

Acknowledgements This work is supported by the Deutsche Forschungsgemeinschaft.

References

[1] J. Černe et al., Phys. Rev. Lett. **77**, 1131 (1996).
[2] S. Leinß et al., Phys. Rev. Lett. **101**, 246401 (2008).
[3] M. Wagner et al., Phys. Rev. Lett. **105**, 167401 (2010).
[4] B. Ewers et al., Phys. Rev. B **85**, 075307 (2012).
[5] J. L. Tomaino et al., Phys. Rev. Lett. **108**, 267402 (2012).
[6] C. N. Böttge et al., Phys. Status Solidi B **250**, 1768–1772 (2013).
[7] R. H. M. Groeneveld and D. Grischkowsky, J. Opt. Soc. Am. B **11**(12), 2502 (1994).
[8] S. W. Koch et al., Nature Mater. **5**(7), 523 (2006).
[9] A. D. Jameson et al., Appl. Phys. Lett. **95**(20), 201107 (2009).
[10] J. B. Stark et al., Phys. Rev. Lett. **65**, 3033 (1990).
[11] C. Stafford, S. Schmitt-Rink, and W. Schäfer, Phys. Rev. B **41**, 10000 (1990).
[12] P. Zeeman, Philos. Mag. **43**, 226 (1897).
[13] M. Kira and S. W. Koch, Prog. Quantum Electron. **30**, 155 (2006).
[14] M. Kira and S. W. Koch, Semiconductor Quantum Optics, 1st ed. (Cambridge Univ. Press, 2011).
[15] H. Haug and S. W. Koch, Quantum Theory of the Optical and Electronic Properties of Semiconductors, 5th ed. (World Scientific, Singapore, 2009).
[16] M. Kira et al., Phys. Rev. Lett. **87**, 176401 (2001).
[17] W. Hoyer, M. Kira, and S. W. Koch, Phys. Rev. B **67**, 155113 (2003).
[18] M. Kira, W. Hoyer, and S. W. Koch, Phys. Status Solidi B **238**(3), 443 (2003).
[19] K. M. Rao and J. E. Sipe, Phys. Rev. B **84**, 205313 (2011).
[20] S. Schmitt-Rink et al., Appl. Phys. A **53**, 491 (1991).
[21] M. Göppert-Mayer, Ann. Phys. (Leipzig) **9**(3), 273 (1931).
[22] H. A. Nickel et al., Phys. Rev. B **62**, 2773 (2000).
[23] M. Kira, W. Hoyer, and S. W. Koch, Solid State Commun. **129**(11), 733 (2004).
[24] J. R. Danielson et al., Phys. Rev. Lett. **99**, 237401 (2007).

PAPER VI

C. N. Böttge, S. W. Koch, L. Schneebeli, B. Breddermann, A. C. Klettke, M. Kira, B. Ewers, N. S. Köster, and S. Chatterjee

Terahertz-induced exciton signatures in semiconductors

Phys. Status Solidi B **250**, 1768–1772 (2013)

DOI: 10.1002/pssb.201200704

The Inner Horizon XII

See page XLIV for reference.

Phys. Status Solidi B **250**, No. 9, 1768–1772 (2013) / **DOI** 10.1002/pssb.201200704

physica status solidi b
www.pss-b.com
basic solid state physics

Invited Article

Terahertz-induced exciton signatures in semiconductors

C. N. Böttge, S. W. Koch*, L. Schneebeli, B. Breddermann, A. C. Klettke, M. Kira, B. Ewers, N. S. Köster, and S. Chatterjee

Department of Physics and Material Sciences Center, Philipps-University of Marburg, Renthof 5, 35032 Marburg, Germany

Received 14 September 2012, revised 14 February 2013, accepted 11 March 2013
Published online 19 June 2013

Keywords terahertz, Rabi splitting, microcavities, photoluminescence

* Corresponding author: e-mail Stephan.W.Koch@physik.uni-marburg.de, Phone: +49-6421-28-21336, Fax: +49-6421-28-27076

This paper discusses recent studies involving time-resolved optical and terahertz (THz) fields in the linear and nonlinear regime. An overview of the microscopic modeling scheme is presented and applied to analyze a variety of experimental results. The examples include coherent excitons in weak and strong THz fields, Rabi splitting and ionization of intra-excitonic transitions, THz studies in semiconductor microcavities, and the THz manipulation of excitonic transitions.

1 Introduction Optical spectroscopy is an indispensable tool for the analysis and control of many-body excitations in semiconductor heterostructures. Recently, the traditional interband studies have been supplemented and expanded due to the development of coherent terahertz (THz) sources. While typical band-gap energies are in the range of electron volts (eV), THz energies are in the range of milli-electron volts (meV). Since the internal energy structure of correlated semiconductor many-body states is in this meV range, THz spectroscopy is the ideal tool to probe these systems [1] and to induce controlled transitions [2] between the different states. Furthermore, the THz energy is far off-resonant with respect to the interband transitions in typical GaAs-like semiconductors such that the light–matter coupling in this spectral regime is governed by two- and more-particle correlation contributions. Hence, the combination of pulsed optical and THz fields allows not only for the creation of many-body excitations but also for the characterization of their dynamic evolution and the controlled manipulation of the involved quantum states.

If a resonant optical field, i.e., a field whose frequency is energetically close to the fundamental absorption edge, is used to excite a high-quality semiconductor, the ultrafast response is dominated by the induced excitonic polarization. Due to the light–matter coupling and the many-body interactions, the coherent polarization decays radiatively and is converted into incoherent quasi-particle excitations [3]. Depending on the excitation intensity, the resulting electron–hole populations exist in a variety of configurations such as Coulomb-bound pairs, i.e., as excitons, as plasma, or as a mixture of both.

Once the optical excitation is tuned energetically well above the band gap, the induced polarization decays rapidly into an incoherent electron–hole plasma [4]. The initially "hot" plasma loses some of its kinetic energy due to subsequent Coulomb and phonon interactions and cools towards the lattice temperature. In this process, some fraction of the excited carriers may bind into exciton populations [5]. To microscopically model the complex processes of nonequilibrium plasma relaxation and possible exciton formation [6], the Coulombic interaction between the charge carriers as well as the carrier–phonon scattering have to be included. The typical time scales for these processes range from a few femtoseconds for the carrier–carrier scattering [7] to nanoseconds for the interaction with acoustic phonons [8, 9]. The typical times for the carrier–LO-phonon scattering lie somewhere in between [10–12]. Due to the combination of all these effects, the quantitative prediction of the many-body state during and after this kinetic evolution is a highly non-trivial challenge.

2 Examples for weak optical and strong THz excitation spectroscopy As first example, we discuss a situation where a weak optical pulse predominantly generates an excitonic polarization and a strong THz pulse is applied to induce transitions among the excitonic states.

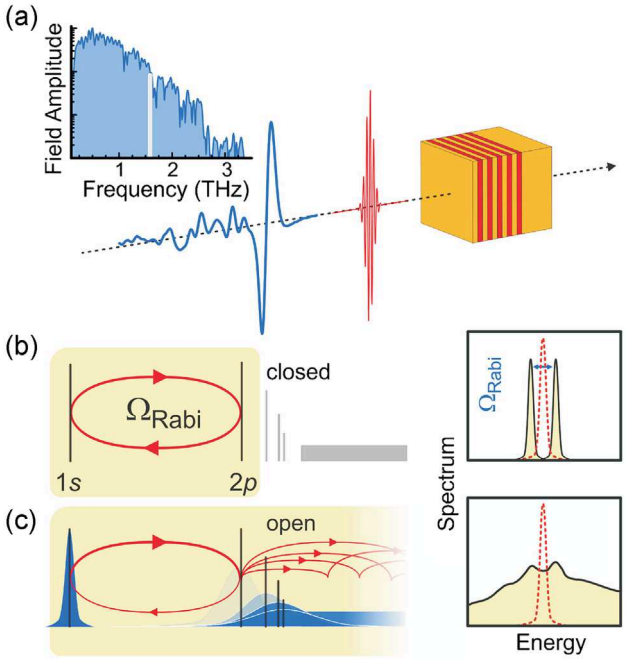

Figure 1 Two-level model for coherent coupling vs. full calculation including continuum of ionized states. **(a)** Time traces and Fourier transform of a THz pulse and bandwidth profile (inset). **(b)** Closed two-level system showing Rabi splitting (right). **(c)** Open system including effects beyond the Rabi-flopping scenario.

2.1 Coherent excitons in terahertz fields For a simple two-level system, it is well-known that sufficiently strong resonant excitation leads to the Rabi splitting of the levels [13, 14]. Even though excitons in semiconductors are far more complicated systems, one can also induce Rabi-splitting effects. For this purpose, one has to drive the optically pre-excited system with a THz pulse that is close to resonant with the intra-excitonic $1s$–$2p$ transition energy.

For strong THz fields, one can expect highly nonlinear phenomena due to the coherent coupling of the $1s$ polarization to the continuum of ionized exciton states. Figure 1 illustrates an experimental configuration to investigate such a situation. A weak optical and an intense THz pulse are incident perpendicularly to a quantum-well structure. An example of the time traces and Fourier transform of the THz pulse are displayed in Fig. 1**(a)**. The large bandwidth ensures sufficient overlap with the $1s$–$2p$-transition energy—here at 1.6 THz—indicated by the solid white line.

Ignoring the many-body interaction and strong-field effects, one might assume that the intra-excitonic $1s$–$2p$ transition forms a closed system that can be treated independently of all the higher states as illustrated by the yellow box in Fig. 1**(b)**. Resonant excitation with sufficiently strong THz fields should then lead to a clear Rabi splitting of the $1s$-exciton resonance, as shown schematically on the right-hand side of Fig. 1**(b)**. Experimental observations of the Rabi splitting are reported in Ref. [15] for strong narrow-band THz pulses. Detuning the THz frequency and the resonance

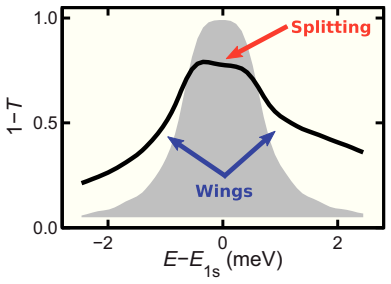

Figure 2 Computed THz-induced effects. The black solid line shows the full calculation of the transmission, plotted as $1 - T$. The shaded area shows the spectrum without THz. The upper arrow indicates the initiation of splitting of the $1s$-exciton peak and the two lower arrows highlight the pronounced wings arising due to ionization effects. According to Ref. [17].

frequency leads to the well-known anticrossing behavior of dressed states depending on the THz energy and intensity [15, 16]. Even though one can fit some features of such measurements to the results of a closed two-level model, one also observes significant deviations. Our fully microscopic treatment [17] attributes these effects to the breakdown of the rotating-wave approximation, the dynamical Franz–Keldysh effect, and exciton field ionization [18, 19].

As illustrated in Fig. 1**(c)**, the application of strong, short, pulses drives the system well beyond the Rabi-flopping scenario into the highly nonlinear regime, either directly (not shown here) or in a multi-step process. The effects are analyzed by applying a systematic microscopic many-body theory that self-consistently includes optical and THz fields as well as the microscopic quasi-particle interactions [18–21].

In Ref. [17], intense, single-cycle THz pulses have been used to resonantly drive the intra-excitonic $1s$–$2p$ transition. For sufficiently low THz fields, one observes a bleaching of the $1s$-exciton peak which evolves more and more into a significant splitting as the THz intensity is increased. By tracking the evolution from the weakly-coupled perturbative regime to extreme nonlinear THz optics, also ionization effects are revealed, see Fig. 2.

2.2 THz studies of optically resonant semiconductor microcavities Normal-mode coupling (NMC) occurs in a cavity with a resonance close to the excitonic $1s$-absorption peak of the quantum wells. This leads to a splitting of the excitonic peak into two new resonances [22, 23], the so-called exciton-polariton modes. Theoretical investigations of the THz properties of such systems predict that a suitably tuned THz field can induce transitions between each of the polaritonic normal-mode peaks and the exciton $2p$-state which is not directly coupled to the intracavity light field. This way, THz fields can be used for the coherent manipulation of the exciton-polariton states. Thus, the system described here shows a so-called Λ-configuration [24], or even more precisely, it is characterized as an *open* Λ-system due to the coupling to energetically higher excitonic and continuum states.

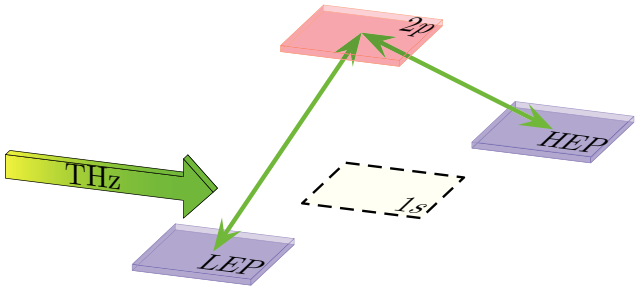

Figure 3 Schematic representation of 1s-exciton peak which splits into lower exciton-polariton (LEP) and higher exciton-polariton (HEP) mode. The THz pulse (left arrow) induces transitions between HEP (LEP) and the 2p level, shown by the thin arrows. According to Ref. [24].

In many aspects, this Λ-configuration is unique and different from the usual atomic Λ-systems where all levels are matter states. In semiconductor microcavities, all states of the ground state of the Λ system are induced by the optical excitation. In addition, only the 2p-state is a pure matter state while the two polariton states are mixed light–matter resonances which cannot be directly coupled by THz excitation since they result from the same excitonic state. Besides fundamental investigations of the coupling scenario under pulsed THz irradiation of different intensity and duration, there are considerable Λ-system applications such as THz-Stimulated Raman Adiabatic Passage (STIRAP) [25] and other coherent control techniques in semiconductor microcavities.

In the context of modeling Λ systems like discussed above, the many-body theory for the material excitations is extended by a self-consistent treatment of optical and THz fields. This theoretical description explains the generation of polarization by the optical field and finally the splitting into lower (LEP) and higher (HEP) exciton-polariton states when the system is coupled to a cavity. As the THz-transition matrix element shows p-like symmetry while the optical polarizations are s-like, i.e., spherically symmetric, the THz field enables the coupling of the polarization to the optically dark states, namely the 2p state. On the other hand, no coupling is observed between the LEP and HEP state confirming the realization of a Λ system. Figure 3 schematically depicts the three-level Λ-system configuration. The 1s-level splits into the lower exciton-polariton (LEP) and higher exciton-polariton (HEP) mode and is just indicated as a dashed level. The THz pulse, illustrated by the arrow on the left, induces transitions between the HEP (LEP) and the 2p level, but not between HEP and LEP.

For the detailed theory–experiment comparisons, it is necessary to carefully match the experimental configuration of the THz pulses and the microcavities used since these are highly-sensitive, nonlinear systems where small deviations in the actual system can lead to large differences in the spectroscopic results. As another interesting field of research, one can explore the influence of strong THz pulses which will be able to induce multiple THz-photon transitions. This introduces an efficient coupling also to energetically higher excitonic states. The theoretical modeling of a new class of microcavity systems where the normal-mode splitting exceeds the 1s–2p transition energy thus leads to specific systems which have recently been realized experimentally [26]. Based on the observations made so far, the simultaneous optical and THz excitation leads to state-coupling effects that are significantly different from pure matter systems such as atomic two-level systems.

2.3 THz manipulation of the secondary emission and the influence of magnetic fields Besides the effects of a semiconductor sample placed in a microcavity, one may also study the THz modifications of the optically induced secondary emission [27] from semiconductor quantum wells. To distinguish it from 'primary emission', i.e., the reflected and transmitted beams, the term 'secondary emission' comprises not only the incoherent photoluminescence (PL) but also the coherent emission after optical excitation into a direction deviating from that of the primary emission.

Since excitonic features significantly influence the semiconductor PL [5, 28, 29], strong THz fields can be used to modify the optical luminescence in semiconductors by transferring excitons into higher energy states and storing them there for an extended time [30]. If the THz excitation energy is chosen to be resonant with the 1s–2p-exciton transition, the 1s population is transferred into the optically dark 2p state, which partially depletes the 1s state resulting in a reduction of the respective PL intensity.

As already discussed in the context of the excitonic Rabi-splitting scenario, it is clear that the use of strong THz couples not only the two lowest energy levels but involves also the higher excitonic states. As a very intriguing extension of the THz-induced reduction of the optical PL from the 1s-exciton state, one may investigate the situation of short or even vanishing temporal delay between the optical and the THz pulses. This situation is still unexplored and it will be interesting to study how THz-induced changes to excitonic polarization, i.e., coherences, influence the secondary emission and the related many-body and quantum-optical effects [31].

Another interesting field of research involves the investigation of THz-induced effects in the presence of a magnetic field [32]. In this connection, the magnetic field changes the exciton states as well as the many-body interactions and the THz field can be applied both to probe the system and to induce further changes. Especially, the magnetic field can be used to shift the different excitonic resonances and lift the degeneracy caused by p-like states. For the treatment of this problem, it is necessary to solve the generalized excitonic Wannier equation, i.e., the non-Hermitian excitonic eigenvalue problem [4], in the presence of a magnetic field, using the resulting eigenfunctions as basis [33].

This work and concrete measurements shed new light on the level shift and manipulation of the excitonic wavefunctions and signatures in magnetic environments.

3 Theoretical techniques The basis of the microscopic theory is the semiconductor many-body Hamiltonian $\hat{H}$. Besides noninteracting electron and hole contributions, $\hat{H}$ includes the Coulomb interaction among the charge carriers, the carrier–phonon interaction as well as the light–matter coupling [4]. Starting from the Heisenberg equations of motion for the relevant operator combinations, we systematically truncate the infinite correlation hierarchy using the cluster-expansion approach as described in Ref. [4]. This way, we obtain semiconductor-Bloch-type equations including the THz contributions,

$$\begin{aligned}
\mathrm{i}\hbar\frac{\partial}{\partial t}P_{\boldsymbol{k}} &= \left[\epsilon_{\boldsymbol{k}} - \boldsymbol{j}_{\boldsymbol{k}}\cdot\boldsymbol{A}_{\mathrm{THz}} + \frac{|e|^2}{2\mu}\boldsymbol{A}_{\mathrm{THz}}^2\right]P_{\boldsymbol{k}} \\
&\quad - \left(1 - f_{\boldsymbol{k}}^{\mathrm{e}} - f_{\boldsymbol{k}}^{\mathrm{h}}\right)\Omega_{\boldsymbol{k}} + \Gamma_{\mathrm{v,c},\boldsymbol{k}}^{\mathrm{Coul}} + \Gamma_{\mathrm{v,c},\boldsymbol{k}}^{\mathrm{phon}}, \\
\mathrm{i}\hbar\frac{\partial}{\partial t}f_{\boldsymbol{k}}^{\mathrm{e}} &= 2\,\mathrm{Im}\left[P_{\boldsymbol{k}}\Omega_{\boldsymbol{k}}^{\star} + \Gamma_{\mathrm{c,c},\boldsymbol{k}}^{\mathrm{Coul}} + \Gamma_{\mathrm{c,c},\boldsymbol{k}}^{\mathrm{phon}}\right], \\
\mathrm{i}\hbar\frac{\partial}{\partial t}f_{\boldsymbol{k}}^{\mathrm{h}} &= 2\,\mathrm{Im}\left[P_{\boldsymbol{k}}\Omega_{\boldsymbol{k}}^{\star} - \Gamma_{\mathrm{v,v},\boldsymbol{k}}^{\mathrm{Coul}} - \Gamma_{\mathrm{v,v},\boldsymbol{k}}^{\mathrm{phon}}\right]. \qquad (1)
\end{aligned}$$

Here, $P_{\boldsymbol{k}}$ is the optical polarization for the momentum $\boldsymbol{k}$ and $\epsilon_{\boldsymbol{k}}$ is the renormalized kinetic electron–hole pair energy. The THz vector potential $\boldsymbol{A}_{\mathrm{THz}}$ couples to the current-matrix element $\boldsymbol{j}_{\boldsymbol{k}} = -|e|\,\hbar\boldsymbol{k}/\mu$, where μ is the reduced mass of an electron–hole pair, and causes ponderomotive contributions, scaling with the electron charge e and the reduced effective mass μ [21, 34]. The population of electrons (holes) in the conduction (valence) band is given by $f_{\boldsymbol{k}}^{\mathrm{e(h)}}$, while $\Omega_{\boldsymbol{k}}$ denotes the optical Rabi frequency. Phonon and dephasing contributions between valence band (v) and conduction band (c) are addressed by Γ^{phon} and Γ^{Coul}, respectively.

To study the optical and THz response in complicated optical systems like microcavities, it is important to dynamically take into account the transmission, reflection, and absorption of the different sample layers. Therefore, we solve Eqs. (1) self-consistently together with Maxwell's wave equation [35] describing the light propagation in the particular sample [36]. This includes backcoupling of the excited quantum wells on the electromagnetic fields. In this process, the matrix elements of the light–matter coupling at each position in the sample have to be taken into account. The secondary emission is solved from the semiconductor luminescence equations [37] and its extensions [31]. The THz fields generate polarizations in the sense of off-diagonal exciton correlations $\Delta n_{\lambda,\nu}$ through dipole coupling [4]. It is interesting to mention that the direct $1s$-to-$2s$ transition is dipole-forbidden whereas THz can induce dipole-allowed transitions between the $1s$ and $2p$ state. Furthermore, the three-particle scattering represented by the triplet contribution $T_{\mathrm{X}}^{\boldsymbol{q},\boldsymbol{k}',\boldsymbol{k}}$ breaks this symmetry producing scattering to the $2s$ state [30]. Since a simple dephasing model is not sufficient to treat the symmetry breaking, a more complex diffusive ansatz is needed [4].

The different features, like intra-excitonic carrier transfer and relaxation phenomena, can only be explained by fully microscopically examining the THz-field effects on the photogenerated electron–hole pairs. Once excitons are present, one has to include two-particle correlations $c_{\mathrm{X}}^{\boldsymbol{q},\boldsymbol{k}',\boldsymbol{k}} \equiv \Delta\langle\hat{a}_{\mathrm{c},\boldsymbol{k}}^{\dagger}\hat{a}_{\mathrm{v},\boldsymbol{k}-\boldsymbol{q}}^{\dagger}\hat{a}_{\mathrm{v},\boldsymbol{k}'}\hat{a}_{\mathrm{c},\boldsymbol{k}'+\boldsymbol{q}}\rangle$ between Fermionic creation (annihilation) $\hat{a}_{\lambda,\boldsymbol{k}}^{\dagger}$ ($\hat{a}_{\lambda,\boldsymbol{k}}^{\dagger}$) operators for carriers in band $\lambda = \{\mathrm{c}, \mathrm{v}\}$, respectively [4]. Here, $\boldsymbol{k}$ denotes the wavevector of each particle. The complete many-body dynamics of excitons is accessible via

$$\begin{aligned}
\mathrm{i}\hbar\frac{\partial}{\partial t}c_{\mathrm{X}}^{\boldsymbol{q},\boldsymbol{k}',\boldsymbol{k}} &= \left(\epsilon_{\boldsymbol{q},\boldsymbol{k}',\boldsymbol{k}} - \boldsymbol{j}_{\boldsymbol{k}'+\boldsymbol{q}-\boldsymbol{k}}\cdot\boldsymbol{A}_{\mathrm{THz}}\right)c_{\mathrm{X}}^{\boldsymbol{q},\boldsymbol{k}',\boldsymbol{k}} \\
&\quad + \left(1 - f_{\boldsymbol{k}}^{\mathrm{e}} - f_{\boldsymbol{k}-\boldsymbol{q}}^{\mathrm{h}}\right)\sum_{l} V_{l-\boldsymbol{k}}\, c_{\mathrm{X}}^{\boldsymbol{q},\boldsymbol{k}',l} \\
&\quad - \left(1 - f_{\boldsymbol{k}'+\boldsymbol{q}}^{\mathrm{e}} - f_{\boldsymbol{k}'}^{\mathrm{h}}\right)\sum_{l} V_{l-\boldsymbol{k}'}\, c_{\mathrm{X}}^{\boldsymbol{q},l,\boldsymbol{k}} \\
&\quad + S_{\mathrm{X}}^{\boldsymbol{q},\boldsymbol{k}',\boldsymbol{k}} + T_{\mathrm{X}}^{\boldsymbol{q},\boldsymbol{k}',\boldsymbol{k}}, \qquad (2)
\end{aligned}$$

where the renormalized energy of an electron–hole pair is denoted by $\epsilon_{\boldsymbol{q},\boldsymbol{k}',\boldsymbol{k}}$ and $V_{\boldsymbol{k}}$ is the Coulomb-matrix element. The single-particle source is given by $S_{\mathrm{X}}^{\boldsymbol{q},\boldsymbol{k}',\boldsymbol{k}}$ and the three-particle scattering is introduced via $T_{\mathrm{X}}^{\boldsymbol{q},\boldsymbol{k}',\boldsymbol{k}}$, $\boldsymbol{A}_{\mathrm{THz}}$ is the vector potential of the THz pulse, and $\boldsymbol{j}_{\boldsymbol{k}}$ is the current-matrix element. For explicit forms of S_{X} and T_{X}, consult Eq. (223) and App. D of Ref. [4]. It can be seen that the THz-current matrix element shows a p-like symmetry as mentioned earlier. Caused by the selection rules, there are dipole-allowed and dipole-forbidden transitions for THz radiation. The three-particle scattering needs a special treatment to consistently describe all the scattering processes [3].

4 Summary The substantial progress in research on THz physics opens a wide field of application possibilities. The fact that THz radiation is in the spectral range of intra-excitonic transitions leads to a variety of fascinating experiments and theoretical investigations. Owing to the development of Rabi splitting and the resonant excitation of the exciton-polariton polarization, completely new configurations become feasible. The appliance of external magnetic fields allows one to manipulate the excitonic configuration of the system opening a new interesting field of research. This provides the opportunity to design entirely novel concepts for THz applications.

Acknowledgements This work is supported by the Deutsche Forschungsgemeinschaft via the Research Training Group "Functionalization of Semiconductors" (RTG 1782). We gratefully acknowledge fruitful and stimulating collaborations with our experimental colleagues including (in alphabetical order) H. M. Gibbs, M. Helm, G. Khitrova, M. Koch, J. Kono, Y.-S. Lee, H. Schneider, and their respective research groups.

References

[1] M. Kira et al., Phys. Rev. Lett. **87**, 176401 (2001).
[2] M. Kira, W. Hoyer, and S. W. Koch, Solid State Commun. **129**(11), 733 (2004).
[3] M. Kira and S. W. Koch, Semiconductor Quantum Optics, 1st ed. (Cambridge Univ. Press, 2011).
[4] M. Kira and S. W. Koch, Prog. Quantum Electron. **30**, 155 (2006).
[5] S. W. Koch et al., Nature Mater. **5**(7), 523 (2006).
[6] W. Hoyer, M. Kira, and S. W. Koch, Phys. Rev. B **67**, 155113 (2003).
[7] M. P. Kesler and E. P. Ippen, Appl. Phys. Lett. **51**(22), 1765 (1987).
[8] P. K. Bhattacharya, Properties of III–V Quantum Wells and Superlattices (Institution of Engineering and Technology, 1996).
[9] T. Müller et al., Time-resolved measurement of intersubband population dynamics, in: Quantum Electronics and Laser Science Conference, 2002 (QELS '02), p. 262.
[10] K. T. Tsen et al., Appl. Phys. Lett. **68**(21), 2990 (1996).
[11] K. T. Tsen et al., Appl. Phys. Lett. **71**(13), 1852 (1997).
[12] K. T. Tsen and H. Morkoç, Phys. Rev. B **38**, 5615 (1988).
[13] L. C. Allen and J. H. Eberly, Optical Resonance and Two-Level Atoms (John Wiley & Sons Inc., 1975).
[14] H. Haug and S. W. Koch, Quantum Theory of the Optical and Electronic Properties of Semiconductors, 5th ed. (World Scientific, Singapore, 2009).
[15] M. Wagner et al., Phys. Rev. Lett. **105**, 167401 (2010).
[16] S. H. Autler and C. H. Townes, Phys. Rev. **100**, 703 (1955).
[17] B. Ewers et al., Phys. Rev. B **85**, 075307 (2012).
[18] J. R. Danielson et al., Phys. Rev. Lett. **99**, 237401 (2007).
[19] S. Leinß et al., Phys. Rev. Lett. **101**, 246401 (2008).
[20] A. D. Jameson et al., Appl. Phys. Lett. **95**, 201107 (2009).
[21] J. T. Steiner, M. Kira, and S. W. Koch, Phys. Rev. B **77**, 165308 (2008).
[22] G. Khitrova et al., Rev. Mod. Phys. **71**(5), 1591 (1999).
[23] G. Khitrova et al., Phys. Status Solidi B **206**(1), 3 (1998).
[24] J. L. Tomaino et al., Phys. Rev. Lett. **108**, 267402 (2012).
[25] J. Oreg, F. T. Hioe, and J. H. Eberly, Phys. Rev. A **29**, 690 (1984).
[26] E. Wertz et al., Appl. Phys. Lett. **95**, 051108 (2009).
[27] M. Kira, F. Jahnke, and S. W. Koch, Phys. Rev. Lett. **82**, 3544 (1999).
[28] S. Chatterjee et al., Phys. Rev. Lett. **92**, 067402 (2004).
[29] W. Hoyer et al., Phys. Rev. B **72**, 075324 (2005).
[30] W. D. Rice et al., Phys. Rev. Lett. **110**, 137404 (2013).
[31] M. Kira et al., Prog. Quantum Electron. **23**(6), 189 (1999).
[32] J. Černe et al., Phys. Rev. Lett. **77**, 1131 (1996).
[33] C. N. Böttge et al., Phys. Status Solidi C **10**, 1218 (2013) [same conference].
[34] M. Kira, W. Hoyer, and S. W. Koch, Phys. Status Solidi B **238**(3), 443 (2003).
[35] J. C. Maxwell, Philos. Trans. R. Soc. Lond. **155**, 459 (1865).
[36] F. Jahnke et al., Adv. Solid State Phys. **37**, 191 (1997).
[37] M. Kira et al., Phys. Rev. Lett. **79**, 5170 (1997).

